UNIVERSITA’ DEGLI STUDI DI PARMA

Dottorato di ricerca in Scienze chimiche

Ciclo XXIX (2014-2016)

MOLECULAR CONFINEMENT IN POROUS CRYSTALS

Coordinatore:
Chiar.mo Prof. Roberto Cammi

Tutor:
Chiar.mo Prof. Paolo Pelagatti

Dottorando: Davide Balestri

"The Wedding-Guest sat on a stone:

He cannot choose but hear;

And thus spake on that ancient man,

The bright-eyed Mariner. "

The Rime of the Ancient Mariner,

S. T. Coleridge

SUMMARY

1 Introduction

"Porosity is a way to do a lot with little."

"If I take a gram of MOF-200 and unravel it, it will cover many football fields, and that is the space you have for gases to assemble. [...] *It's like magic. Forty tons of MOFs is equal to the entire surface area of California."*

-Omar M. Yaghi-

1.1 Porous Materials

Nowadays, porous materials play a fundamental role in several areas of science and technology: from catalysis to petroleum refinement, from membranes for separation to adsorbents for gas storage and medicinal applications. According to the IUPAC definition[1], porous materials can be classified in three classes based on the dimension of their cavities: microporous ($d < 2.0$ nm), mesoporous ($2.0 < d < 50$ nm) and macroporous ($d > 50$nm).

The final material properties derive mainly by two factors: the pore architectures (dimension, shape, hydrophilicity, connectivity) and the pore distribution, which can be narrow or broad.[2] Herein is listed a series of families of porous materials, with their weaknesses and peculiar selling points.

1) **Zeolites and other porous silicates**

Zeolites are a class of microporous alluminosilicates which have found several commercial applications, owing to a very good thermal stability and the cheapness of the production process (optimized at industrial scale).[3,4] The morphology and surface area of the zeolites strongly depends upon the Si/Al ratio: this value affects also the charge balance of the overall structure, influencing the amount of ions trapped inside the pores. To obtain mesoporous cages, the inclusion of Ti in silicates has been studied: it is noteworthy to cite Ti-MCM-41[5] and Ti-SBA-15[6] materials, characterized by notably larger pores than common zeolites. In fact, Ti-MCM-41 shows cavities in the range 2-5 nm, while Ti-SBA-15 presents 6-15 nm cages. However, the increased pore dimension is usually connected to a low hydrothermal stability.[7]

2) Carbon nanotubes

Carbon nanotubes (CNTs) represent another well known class of porous materials. CNTs are an allotropic form of carbon and ideally, they can be assembled from sheets of graphite that have been rolled into a cylindrical shape. They can present different number of walls and consequently pore diameters: the smaller dimension reported is approximately 1 nm, observed for single walled nanotubes.[8] A wide number of applications of CNTs have been described, ranging from the assembly of sensors and electrodes[9] to the adsorption of a series of guests.[10,11]

3) Porous Organic Frameworks

The broad family of porous organic frameworks (POFs) can be divided in several subclasses, including the covalent organic frameworks (COFs), the porous aromatic frameworks (PAFs) and the metal organic frameworks (MOFs). The latter class, MOFs, will be discussed in details in the subsequent paragraph.

COFs are microcrystalline porous materials assembled via robust covalent bonding, composed by only light elements (C, H, N, B, and O).[12] In 2005, Yaghi and coworkers described the one-pot synthesis of the first COF material[13] : authors exploited the conversion of boronic acids to boronic anhydrides or esters, to produce COF-1 and COF-5, respectively, as displayed in Figure 1.1.

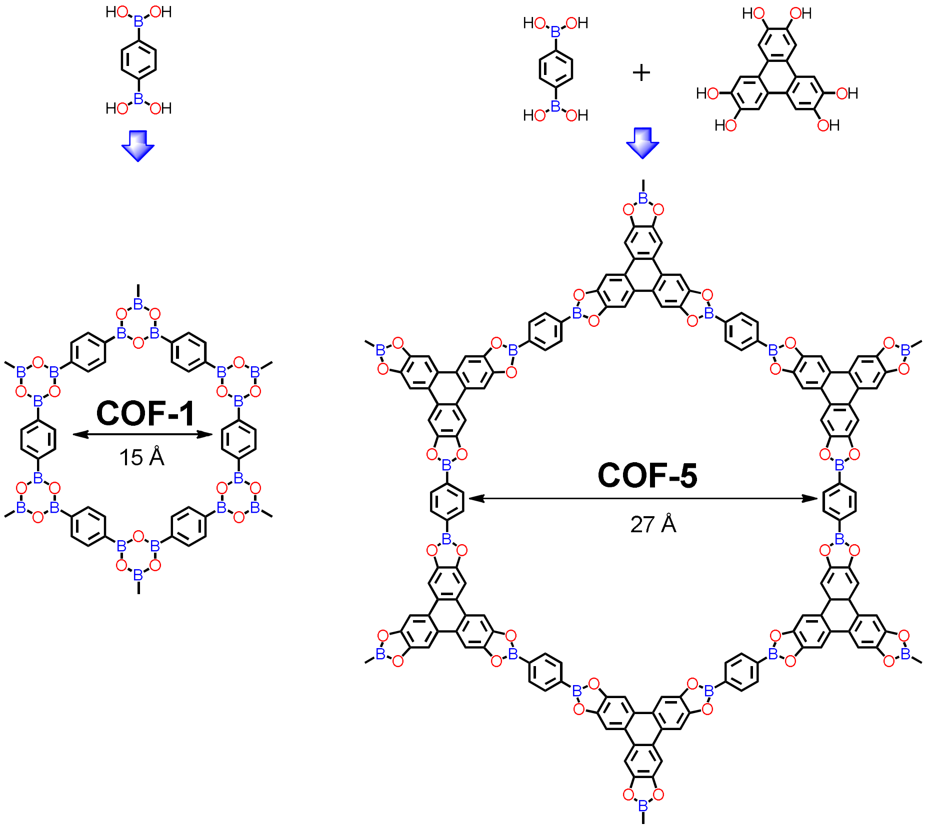

Figure 1.1 Two examples of COF assemblies: boronic anhydride (COF-1) and ester (COF-5)

The formation of strong covalent bonds between the organic building units leads to well-defined and predictable 2D/3D crystalline structures. The building unit length and shape is deeply reflected in the final material architecture, influencing respectively pore dimensions and final topology. In addition to the aforementioned boroxines, other frequent linking groups are imines[14], hydrazones[15] or triazines[16], which guarantee a rigid planar geometry.

More recently, in 2009, porous aromatic frameworks, **PAFs**, have been described.[17] For the synthesis of PAF-1[18], authors were inspired by the structure of the diamond, which presents carbon atoms tetrahedrally coordinated: the basic idea was to expand this network through the insertion of rigid phenyl rings into C-C diamond net.

PAFs are related to elevated surface area values and remarkable physicochemical stability: e.g. amorphous PAF-1 shows a huge Langmuir area, equal to 7000 m^2 g^{-1}, one of the highest values reported so far.

After this brief summary, it should be taken into account that none of the reported classes of materials can guarantee high performances for all applications. Hence, for our research goals we decided to focus our attention on **MOFs**, crystalline porous material built from the combination of bridging organic linkers with metal ions or clusters.[19] The inorganic part of the MOF it is commonly referred as secondary building units (SBUs). Yaghi defined SBUs as "*molecular complexes and cluster entities in which ligand coordination modes and metal coordination environments can be utilized in the transformation of these fragments into extended porous networks*".[20]

1.2 Metal Organic Frameworks

In 1999, a milestone in the history of porous materials was provided by Yaghi, with the synthesis of MOF-5 (or IR-MOF1).[21] The solvothermal reaction of Zn^{2+} ions with 1,4-benzene-di-carboxylate provided the very first example of a metal organic framework characterized by a permanent porosity (Figure 1.2).

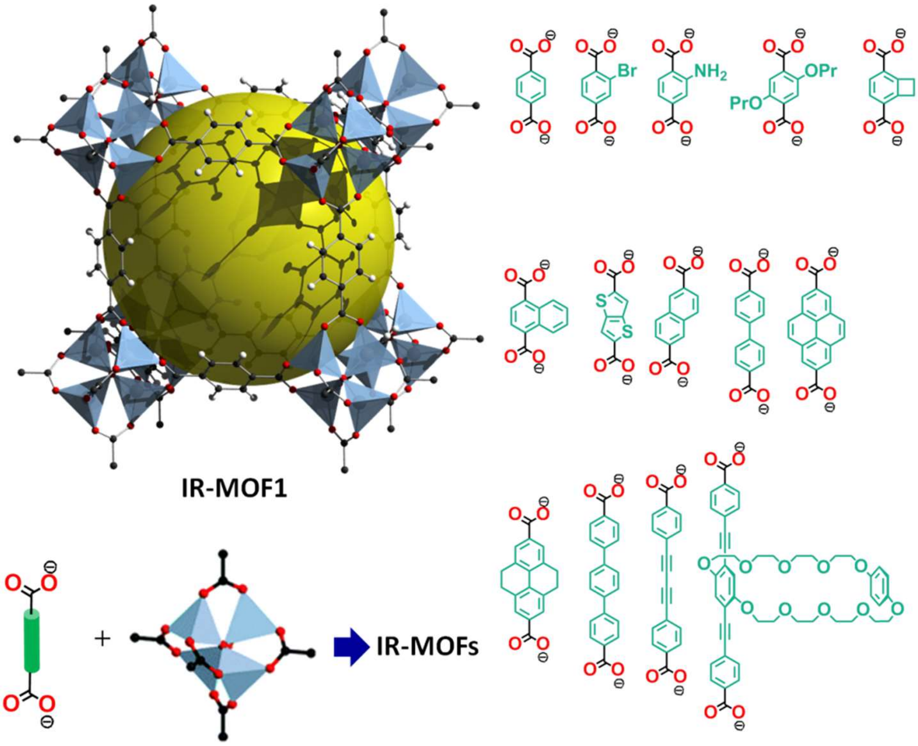

Figure 1.2: Top left: IR-MOF1 pore, Bottom left: combination of dicarboxylic ligand and Zn_4O cluster as the general isoreticular principle governing the IR-MOF series, Right: differences in the spacer length and substitution for some IR-MOF ligands.

MOF-5 exhibits a large Langmuir surface area (2900 m^2 g^{-1}) and a promising hydrogen storage uptake.[22] The feasibility of this approach paved the way for the synthesis of the large family of IR-MOF (Isoreticular Metal Organic Framework): maintaining the metallic Zn_4O SBU and the dicarboxylic coordinative function, a broad series of polymers can be simply obtained by tuning the length and the substitution of the aromatic spacer, as shown in Figure 1.2.[23,24]

The **isoreticular approach** can lead to a dramatic expansion of the MOF cavities: the most striking example is the pore expansion from the microporous hexagonal channels (14 Å wide) of Mg-IR-MOF-74-I up to a diameter of 98 Å for Mg-IR-MOF-74-XI.[25] In the last two decades, this field has shown an exponential growth in the variety and in the number of the described MOFs, crossing the boundary of 20000 structures[26] deposited on the Cambridge Structural Database in 2011.[27] It is noteworthy that two-third of the structural characterized MOFs are assembled exploiting robust carboxylate linkers.[28] This explosive expansion can be explained by the wide choice both in the linkers and in the metallic SBUs, leading to an accurate tuning of the final topology and porosity. A brief list of some common SBUs and ligand examples are listed in Figure 1.3 and Figure 1.4, respectively.

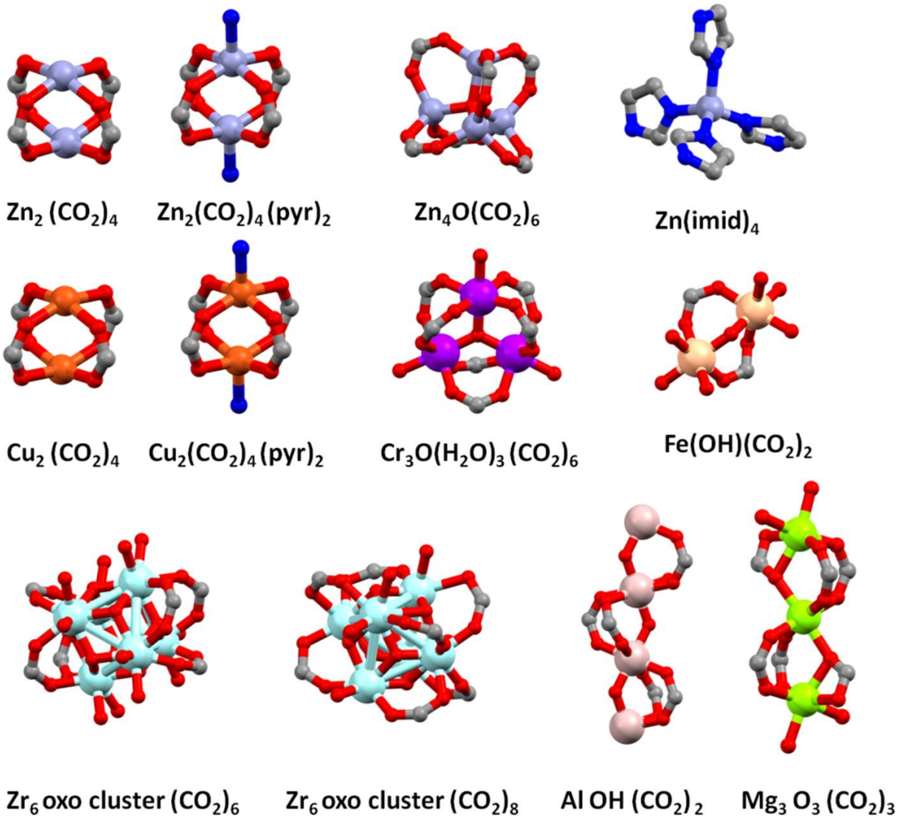

$Zn_2(CO_2)_4$ $Zn_2(CO_2)_4(pyr)_2$ $Zn_4O(CO_2)_6$ $Zn(imid)_4$

$Cu_2(CO_2)_4$ $Cu_2(CO_2)_4(pyr)_2$ $Cr_3O(H_2O)_3(CO_2)_6$ $Fe(OH)(CO_2)_2$

Zr_6 oxo cluster $(CO_2)_6$ Zr_6 oxo cluster $(CO_2)_8$ Al OH $(CO_2)_2$ $Mg_3O_3(CO_2)_3$

Figure 1.3 List of common secondary building units (SBUs) applied in MOF synthesis

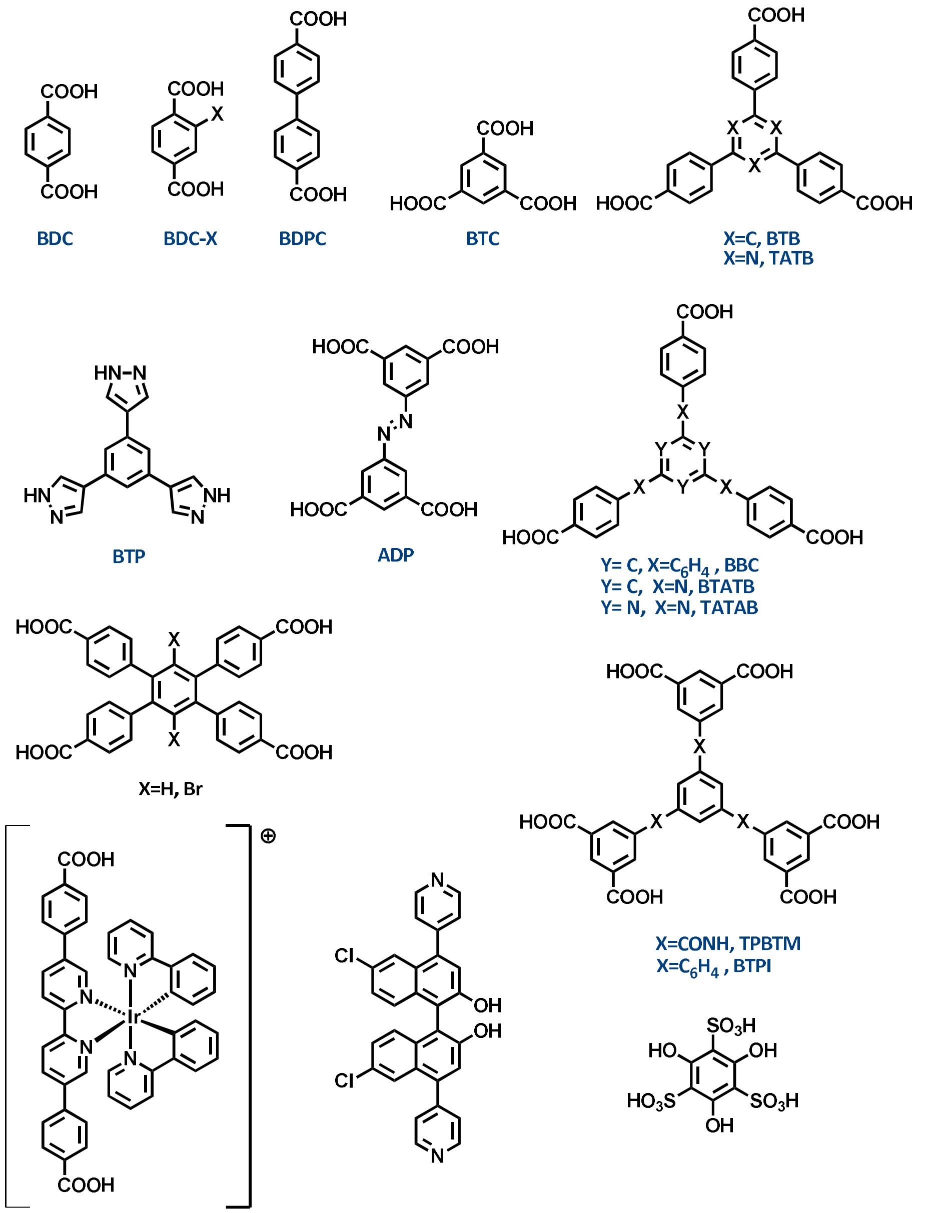

Figure 1.4 Examples of ligands employed in MOF synthesis, displaying a broad spectrum of topicity and functionalization (some popular acronyms are reported).

However, the ligand elongation is not always related to an increasing of the pore diameter: the **interpenetration** phenomenon should be taken into account.[29,30] In fact, if the cavity is sufficiently large to contain an additional framework, the formation of a second net is favoured from an energetic point of view. The occurring interpenetration leads to an advantageous filling of the void space: the resulting minimization of the system energy leads to a higher material stability. Several factors have been evaluated to reach a control over the degree of interpenetration : solvent change, [31,32] reaction temperature and concentration, [33,34,35] insertion of a photolabile protecting group[36] as well as the use of templating agents.[37] On the other hand, interpenetrated structures can present fascinating proprieties, due to the flexibility and the guest induced dynamic response of the framework.[38] It is worth mentioning the application of the pillared $Zn_2(bdc)_2(dpNDI)$ as a sensor for a series of substituted benzene derivatives (dpNDI = *N,N'*-di(4-pyridyl)-1,4,5,8-naphthalenediimide). Kitagawa[39] reported that the inclusion of several VOCs (volatile organic compounds) was correlated to peculiar emission colours, because of the guest-induced rearrangement of the MOF nets, based on framework sliding movements.

An alternative tool to modulate the pore and SBU features are the so called **Post Synthetic Modifications** (acronymized as PSM) [40,41,42] : this approach considers at first the MOF preparation and then the crystalline material is subjected to a chemical reaction to provide differently functionalized MOF. The reaction can involve the linker moieties (e.g. pending functional groups not involved in the coordination) or the metal SBUs (e.g transmetalation). One of the most useful application of PSM is the synthesis of novel MOFs which cannot be obtained by the direct solvothermal assembly of metal salt and linker.

The opportunity of reaching tailored functionalities by a careful MOF design has opened the doors to a plenty of applications in several fields, such as gas storage[43, 44], separation[45,46], heterogeneous catalysis[47], sensors,[48,49] proton conduction[50] and magnetism.[51] An overview of the applcations is reported in Table 1.1. One of the most studied fields is certainly the gas storage: in particular the selectivity towards H_2 , CH_4 and CO_2 trapping[52], [53] is of paramount importance, owing to the relevance that these gases have for both energetic and environmental issues. The first target is particularly challenging owing to the weak interactions between dihydrogen and MOF walls. To facilitate the research and application of hydrogen as an energy carrier, the US Department of Energy (DOE) has set the target loading for hydrogen storage apparatus: from 6.0 wt% by the year 2010 to 9.0 wt% within 2015.[54]

Property or application	**Compound**	**Achieved value or year of report**
Low Density [55]	MOF-399	0.126 g/cm^3
Highest reported value		
Pore aperture[25]	IRMOF-74-XI	98 Å
Number of linkers[56]	MTV-MOF-5	8
BET surface area[57]	NU-110	7140 m^2/g
Pore volume[58]	NU-110	4.40 cm^3/g
Hydrogen uptake[59]	NU-110	9.0 wt%
Methane uptake[60]	PCN-14	212 mg/g
Carbon dioxide uptake[61]	MOF-200	2347 mg/g
Charge mobility[62]	$Zn_2(TTFTB)$	0.2 cm^2/V·s
Lithium storage capacity[63]	$Zn_3(HCOO)_6$	560 mAh/g
Earliest report		
Catalysis by a MOF[64]	$Cd(BPy)_2(NO_3)_2$	1994
Asymmetric catalysis with a homochiral MOF[65]	POST-1	2000
MOF for magnetic resonance imaging[66]	MOF-73	2008

Table 1.1 General overview on properties and applications of metal-organic frameworks.

MOFs have also been investigated as possible host matrices for small molecules and as drug nano-carriers.[67] In 2006, Serre and coworkers observed a high Ibuprofen® loading inside Cr-based MIL-100 and MIL-101.[68] Authors estimated the inclusion of 92 Ibuprofen molecules inside the larger MOF cage. Two years later, a step forward in the study was provided[69]: optimization of the host-guest interactions was achieved with flexible MIL-53(Cr) and MIL-53(Fe) frameworks which allowed a controlled delivery of Ibuprofen®, associated to zero-order kinetics.

Remarkable results concerning encapsulation and subsequent guest release were also achieved with another very popular molecule, caffeine. In 2012, the caffeine confinement inside zeolitic imidazolate ZIF-8[70] was illustrated by Coronas [71] : the study showed an elevated loading (ca. 28 wt %) and a slow release, which reached completion after 27 days. An increased caffeine loading was reported by Serre [72] using MIL-100(Fe), which was associated to a ~ 50 wt % of caffeine loading, process which occurred very quickly. Authors furnished also a report upon the guest release in distilled water at pH = 6.3 and at a temperature of 37 °C: since the host architectures were preserved, the release process was ruled by the caffeine mobility and interactions with the MOF walls.

These studies were implemented with various computational studies aimed at identifying the best interactions responsible of the upload processes.[73,74]

1.3 The Crystalline Sponge Approach

“It’s an illuminating technique. It gives you information you didn’t have before and would be difficult to get in any other way,” Baran says. “There are limitations of this method, but I can’t think of a method or technique that doesn’t have limitations,” he says. “I think the technique has the potential to revolutionize the way we do chemistry, just like NMR did 60 years ago.”

Phil S. Baran talking about the Crystalline Sponge Method, from Chemical & Engeneering News, Volume 93 Issue 7 | pp. 29-30, February 16, 2015.

In 2013, Fujita and coworkers proposed for the first time the so called **crystalline sponge** device, which allowed the structural resolution of small molecules exploiting the inclusion of the same inside MOF pores.[75] This strategy has overcome an intrinsic Achilles’ heel of single crystal X-ray crystallography, the growth of a good quality single crystal of target substances for a structural determination.

Author’s choice fell upon MOF for their crystalline nature which allows to obtain highly ordered structures, joined with the possibility of engineering the final material features. In fact, a wide tunability of the pore sizes and properties of the host matrix (i.e. polarity and functional groups distribution) can be reached by a proper selection of the linkers and inorganic SBUs.

For the above described purpose, authors synthesized a microporous MOF (cavities 5 x 8 Å), generated from the self-assembly of ZnI_2 and the triptopic 2,4,6-tri-(4-pyridyl)-1,3,5-triazine (acronymized as tpt) to provide $[(ZnI_2)_3(tpt)_2 \cdot x(solvent)]$.[76]

Later on several efforts were made towards the method optimization[77,78] achieving other remarkable results. In 2014, Fujita reported a "snapshot" of a reaction intermediate[79] : nanoconfinement led to the observation of a highly unstable organometallic intermediate of a Pd-mediated aromatic bromination, intermediate which quickly dimerized under bulk reaction conditions. More recently, in 2016, two other insights, helpful to elucidate reaction pathways, were published: Honda and Fujita observed *in situ* the formation of a thiol Micheal adduct, by adding a thiol solution to a sponge@cyanoenone (the term sponge is referred to the host Metal-Organic-Framework). By a single crystal X-ray analysis, it was observed the transformation of the starting reagent, hosted into the cavities of the crystalline sponge, into the reaction adduct, exploiting a single-crystal-to single-crystal transformation[80]. The second example dealt with the confirmation of a *syn*-reaction mechanism for a metal-free olefin diboration reaction. Thanks to the crystalline sponge approach, the difficult experienced in defining the molecule conformation by NMR spectroscopy, due to a severe ^1H-^{11}B heteronuclear coupling, of the oily product was overcome.[81]

Another example of great interest is certainly the attribution of the absolute stereochemistry of molecules characterized by axial and planar chirality, illustrated by Fujita group in 2015.[82] The encapsulation of a chiral molecule led to a space group variation with respect to native sponge[83]: from the achiral C2/c group to the chiral space group *C*2 or *P*2$_1$. This, together with the anomalous scattering effect from ZnI_2 host fragment, was exploited for understanding the absolute guest configuration.

More recently, the crystalline sponge technique furnished the absolute structure of a marine natural product, named elatenyne. Although this molecule was isolated in 1986 and defined to be constituted by a simple 2,2'-bifuranyl backbone, its absolute configuration has been debated up to nowadays. The central core of elatenyne is featured by a pseudo-meso structure and a resulting specific rotation $[a]_D \cong 0$. MOF encapsulation, performed with only 100 μL of guest and subsequent X-Ray analysis solved this long-time question.[84]

A further remarkable outcome is the handling of hazardous compounds: encapsulation and structural characterization of explosive ozonides were realized without product isolation and avoiding any possible explosion risk.[85]

The Crystalline sponge method was recently employed successfully by other research groups: Buchwald revised the structure of a hypervalent iodine reagent, changing the previously attributed bond connectivity[86]. Baran and Blackmond, in collaboration with Fujita, managed to determine the regiochemistry of heterocyclic product deriving from a trifluoromethylation reaction.[87]

Taking into account the aforementioned examples, we decided to broaden the crystalline sponge approach to mesoporous MOFs, in order to move from single molecule entrapment to the inclusion of small molecular aggregates.

We have evaluated MOFs particularly suitable to investigate the effect of the encapsulation on crystallization process, especially regarding the first step of nucleation. It is important to underline that although many matrices are equally accessible as porous materials, MOFs exhibit a crystalline order, that should afford a rigorous control of the size, shape, and polymorph structure of the crystallizing nuclei. Therefore, the crystalline nature of MOFs can grant the use of single-crystal X-ray diffraction techniques to investigate the growing crystallizing nuclei.

It is rather known that the aggregation of nanosized clusters of atoms or molecules inside nanometric cavities, is marked with an alteration of the material macroscopic properties.[88]

More recently, significant progress in the understanding on crystallization phenomena in nanoconfined environment has been achieved through the development of polymeric non siliceous matrices, characterized by highly order cylindrical pores (diameters ranging from 10 to 100 nm).[89,90] Ward described the observation of peculiar phase behaviours, including the selective formation or stabilization of metastable phases,[91] size-dependent polymorphism,[92] and regulation of the nanocrystal orientation.[93]

The possibility of polymorphism regulation due to nanoconfinement is of high interest in various fields: remarkable examples comes from metallic sodium[94] and from pharmaceutical active molecules [95,96] nanoconfined in porous glasses or in mesoscopic cellular foams.

Hence, our final objectives were to investigate, from a structural point of view how a guest can be trapped inside a mesoporous MOF, paying particular attention on the type of non-covalent interactions which regulate the guest accommodation, and carefully studying possible intermolecular guest associations dictated by the nanoconfinement process. In principle, the confinement of a relatively high number of guest molecules could trigger on specific intermolecular contacts not possible, or disfavoured, in bulk solution, where the effect of the solvent must always be donsidered. This can have a profound effect on the polymorphism control for solid guests or, in the case of liquid guests, on the possibility of studying what it could be considered a primordial stage of crystallization of a liquid compound.

In addition, MOF can be designed to present coordinatively unsaturated metal centres or specific linker functionalities which could serve as anchoring sites for the incoming guest, thus promoting the early steps of the nanoconfined aggregation.

The leitmotiv of this thesis will be the study of the molecular encapsulation inside porous MOFs, employing different guest types, ranging from bio-mimetic organometallic complexes to biologically active small molecules.

In the next two chapters, the study of molecular trapping performed with already known mesoporous MOFs will be presented. These two MOFs derives from the self assembly of a tritopic carboxylic linker (TATB= 4,4′,4″-triazine-2,4,6-triyl-tribenzoic acid) with two different metal ions: Cu^{2+} (PCN-6′) and Zr^{4+}(PCN-777).

In particular, Chapter 2 will present results of nicotine inclusion inside PCN-6′, whereas Chapter 3 will discuss the successful confinement of biomimetic organic complexes and the heterogeneous catalytic proprieties of the resulting material.

Later on, we will move from already reported materials to novel MOFs. We designed *ex-novo* ligands with the aim of creating flexible frameworks, with walls decorated with amidic or aminic anchoring sites for the guests.

A small family of new ligands based on these considerations was prepared exploiting the Buchwald coupling protocol, fully characterized and successfully applied for the building of new MOFs. All these features joined with the activation study and their application as crystalline sponges for the inclusion of APIs (Active Pharmaceutical Ingredients), such as essential oils and 2,6-diidopropylphenol (Propofol®) will be discussed in Chapters 4 and 5.

2 Nicotine trapping inside mesoporous MOFs

"It's an odd case, Sir. Never come across a case of nicotine poisoning before in all my experience. No more has our Doctor Davis."

"I always thought it was a kind of disease you got from over-smoking."

"To tell the truth, so did I, Sir. But the doctor says that the pure alkaloid is an odourless liquid, and that a few drops of it are enough to kill a man almost instantaneously."

-Three Acts Tragedy, Agatha Christie-

2.1 Introduction

After a preliminary screening with a small library of APIs such as propofol, eugenol and carvacrol, our choice has fallen upon nicotine as valid guest. Nicotine is a potent alkaloid which is contained in tobacco (approximately 0.6-3.0% of the dry weight of tobacco) and acts as stimulant drug.[97] The nicotine activity seems to be related to its interactions with nicotinic acetylcholine receptors of the nervous system.[98]

Until the middle of 20th century, nicotine found a broad use also as insecticide agent.[99,100] However, the relative elevated cost compared to other synthetic pesticides and the high human[101] and mammalian toxicity (LD_{50}=50 mg/kg) strongly limited his application in the past few decades.[102]

It is noteworthy remember that the crystal structure of pure nicotine is still unknown: at low temperature nicotine presents a glassy transition and classical crystallization techniques have so far proved to be unsuccessful, although it has been successfully cocrystallized[103,104], complexed with metals[105] and confined into a micropourous crystalline sponge.[106]

All these intriguing features led us to focus our efforts on the possibility of stabilizing nicotine inside the crystalline matrix of PCN-6’ and studying possible aggregation phenomena: nanoconfinement experiments results will be discussed in details in the next paragraphs.

The hosting properties of PCN-6′ towards nicotine have already been reported in a previous PhD thesis produced in our group.[103] However, in this report the analytical characterization of the new material PCN-6′@nicotine is reported, with a more detailed quantification of the amount of loaded nicotine for each mass unit of PCN-6′.

2.2 PCN-6’: A mesoporous analogous of HKUST

PCN-6’ can be considered the isostructural expanded analogous of classical microporous HKUST.[107] The structural motif is based on the combination of Cu paddle-wheel nodes of the type [$Cu_2(COO)_4 \cdot 2H_2O$] with the tritopic ligand 4,4',4''-(1,3,5-triazine-2,4,6-triyl)tribenzoic acid, named as TATB (Figure 2.1). The resulting formula is $Cu_6(H_2O)_6(TATB)_4 \cdot DMF \cdot 12H_2O$.

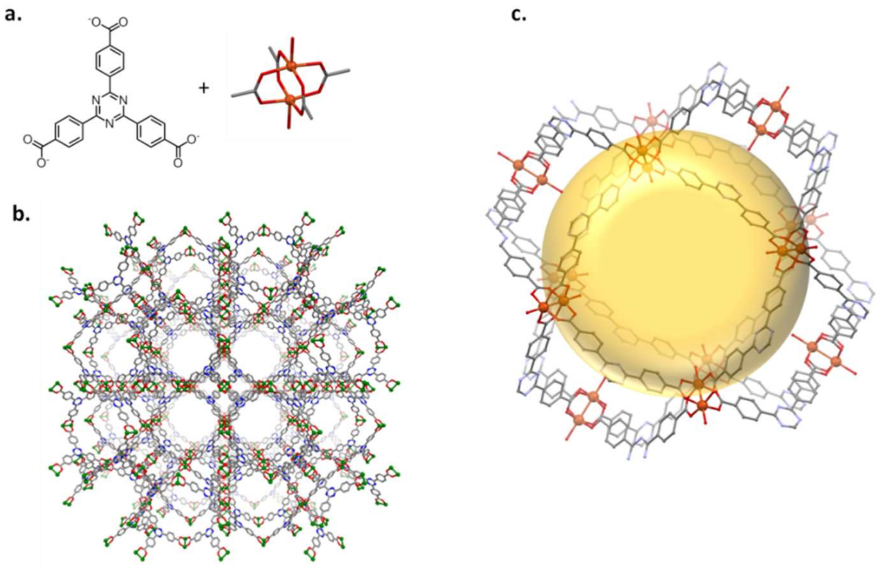

Figure 2.1 a) TATB ligand and the Cu paddle-wheel; b) view of the open channels in PCN-6’ framework; c) PCN-6’ pore: average sphere diameter 30Å.

As reported in Figure 2.1, the resulting framework displayed open wide channels of 21.4 Å x 21.4 Å (Cu···Cu distance) along crystallographic axes *a*, *b* and *c* and an internal mesoporous pore, with a 30 Å diameter (Cu···Cu distance).

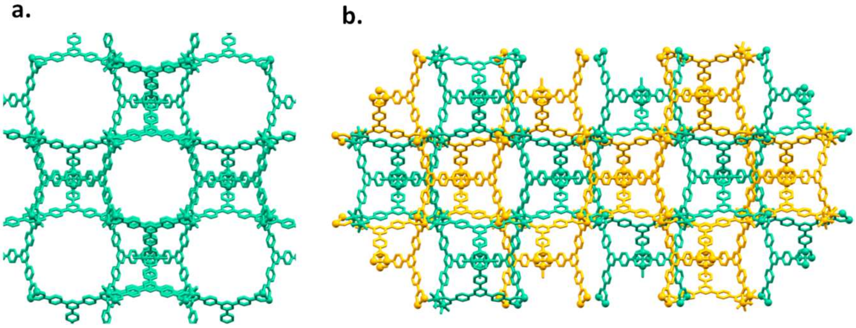

Figure 2.2 a) PCN-6' motif; b) PCN-6 motif: interpenetrated structure

The presence of large void cavities allowed the formation of an interpenetrated phase, known as PCN-6 [108] : its framework is represented in Figure 2.2. Despite interpenetration, PCN-6 maintained a considerable pore dimension suitable for the encapsulation studies. A comparison of the unit cell parameters of the two phases is given in Table 2.1.

	PCN-6'	PCN-6
Space group	Fm-3m	R-3m
a (Å)	46.636	32.968
b(Å)	46.636	32.968
c (Å)	46.636	80.783
α (°)	90	90
β(°)	90	90
γ(°)	90	120
Volume	101432	76039

Table 2.1 Comparison between the unit cell parameters for PCN-6' and PCN-6

Zhou reported that the solvothermal reaction of copper(II) nitrate with TATB ligand produced the interpenetrated PCN-6, while the addition of oxalic acid as templating agent provided only the non-interpenetrated PCN-6'.

Disappointingly, in our hand the proposed templating strategy failed: a certain fraction of interpenetrated PCN-6 as coproduct was always obtained. A mechanical separation of the two phases was barely impossible, as the crystals have the same size and morphology. Furthermore, the discrimination of the two phases by XRPD analysis was unfeasible since the two diffractograms are coincident. In the following, PCN-6' will indicate the mixture of the two different phases.

As for many mesoporous MOFs, PCN-6' is unstable in contact with water/moisture, but it is stable in several organic solvents, such as DMF, methanol, dichloromethane, acetonitrile, tetrahydrofuran. In addition, it is thermally robust, since decarboxylation processes start only above 350°C. These proprieties made PCN-6' a valuable candidate for the inclusion studies.

2.2.1 Synthesis of PCN-6'

PCN-6' was initially synthesized according to the procedure reported by Zhou.[107] In order to improve the dimension of the crystals of the final product, several variations of the solvothermal conditions were performed. It was observed that a higher concentration of the reactants was associated with the growing of bigger crystals. On the other hand, several drawbacks were associated to the modified method: the isolation of PCN-6′ crystals was a quite tedious procedure for the presence of two undesired by-products in the reaction tube. One of this by-product was identified as copper oxalate, which forms because of the presence of an excess of the templating oxalic acid in the reaction media. The other by-product appeared as solid microspheres whose preliminary analysis indicate to be likely composed by some inorganic Cu-containing phases, whose nature has not been defined (see Supplementary Materials for details). Furthermore, performing single-crystal X-ray diffraction measurements on crystals of PCN-6′, severe twinning problems were observed.

Hence, we took a step back to the published procedure, preferring to handle smaller crystals but of higher quality.

2.2.2 PCN-6’@nicotine

Nicotine was loaded into PCN-6′ crystals by soaking experiments. These consider the introduction of a weighed amount of PCN-6′ into a glass vial, crystals which are then covered with a measured volume of pure nicotine. The vial is then tightly capped and the soaking test was performed under static condition for a period of a week (see Experimental Part for further details). A long soaking time was chosen to allow equilibration thus reaching high loadings and making possible the best guest rearrangement inside PCN-6′ pores. One of the advantages deriving from the use of liquid guests is just the possibility to avoid the use of solvents for the guest dissolution. The solvent indeed must always be considered a competitor of the guest during the loading process, and its choice is far from being trivial. However, prior to the soaking experiments, to allow the entering of the guest molecules into the cavities of the MOF, the molecules of the solvent used for the MOF synthesis (DMF) that filled the pores must be removed. The activation of PCN-6’ by thermal heating led to an extensive loss of crystallinity, making unfeasible an X-Ray diffraction analysis of the loaded material. For this reason, the activation was performed by following a solvent exchange protocol. This procedure considers the crystals soaking in methanol for 24 hours at room temperature. Then, the supernatant is replaced with fresh methanol and the soaking is prolonged for additional 24 hours. Subsequently, the crystals underwent the same treatment with dichloromethane and were finally dried overnight under vacuum (< 10^{-3} Torr).

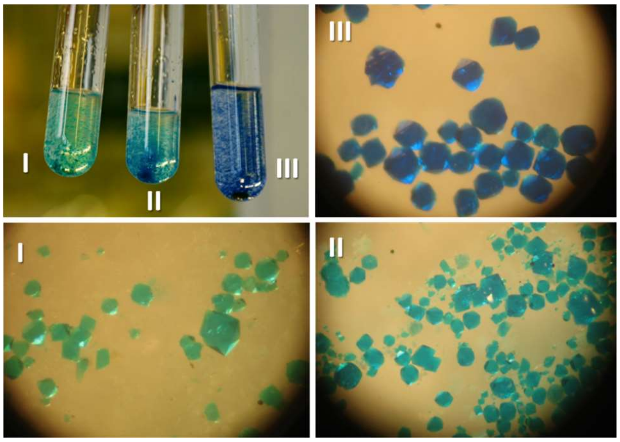

Figure 2.3 Chromatic changes underwent by crystals of PCN-6’ during the solvent exchange protocol: (I) as synthesized; (II) soaked in methanol; (III) soaked in dichloromethane. The purple crystals after vacuum treatment are not shown.

The chromatic variations observed during the solvent exchange protocol are ascribable to the different degrees of interactions between the solvent molecules and the walls of the MOF (see Figure 2.3). This phenomenon is not unexpected, and it has already been observed with other MOFs: Zhao *et al.* described a wide colour change for a Zn-based MOF. Authors attributed the chromatic variations to the charge transfer between *N,N′*-dimethylacetamide with a TATB unit.[109] After the vacuum treatment, the crystals became purple, indicating the complete removal of the solvent molecules.

Once activated, the crystals can be loaded by a simple soaking in neat nicotine. Addition of nicotine caused a very fast alteration of the crystal colour, which turned from purple to light green just in a few seconds. In this case, the chromatic change can be reasonably attributed to a variation of the coordination sphere of Cu. Thus, the coordination of nicotine through the pyridine ring can be regarded as the driving force of the inclusion process. The same colour changes were in fact observed performing soaking experiments of PCN-6′ crystals in dichloromethane or acetonitrile solutions of nicotine. Both solvents are much less coordinating than pyridine and cannot compete in completing the octahedral coordination geometry of the metal. The use of solvents is, however, expected to reduce the amount of loaded nicotine, since part of the free volume featuring the MOF will be occupied by solvent molecules.

Once loaded, the crystals of PCN-6’@nicotine were carefully washed with dichloromethane to remove the guest physically sorbed onto the crystals surface. The crystals were then characterized by SC-XRD, XRPD, TGA, and NMR analysis to quantify the amount of trapped guest.

2.2.3 X-Ray Diffraction Study

SC-XRD measurements were performed with synchrotron light radiation in order to obtain high resolution data and to understand whether the guest is ordered or partially organized inside the cavities. Diffraction experiments were conducted both by flash freezing of crystals at 100 K and by slow cooling, in order to allow the guest to equilibrate thus reaching an ordered disposition inside the cavities.

As previously mentioned, PCN-6'@nicotine crystals revealed to belong to two different families: trigonal or cubic (unit cell data previously reported in Table 2.1) corresponding to the coexistence of PCN-6 and PCN-6', respectively, in the isolated batch of crystals. Compared to PCN-6'@dichloromethane, higher electron densities were detected inside both PCN-6' and PCN-6 cavities, indicating the presence of many molecules of free nicotine. Disappointingly, we were only partially able to achieve our initial goal since no ordered guest clusters were revealed. For the guest molecules occupying the central part of the pore, a defined guest modeling was not possible, due to the disordered orientation of the trapped nicotine molecules.

The most remarkable result was obtained for interpenetrated PCN-6@nicotine: in this case, the position nearby copper atoms presented a residual distribution of electron density which could be modeled as a coordinated nicotine, as shown in Figure 2.4.

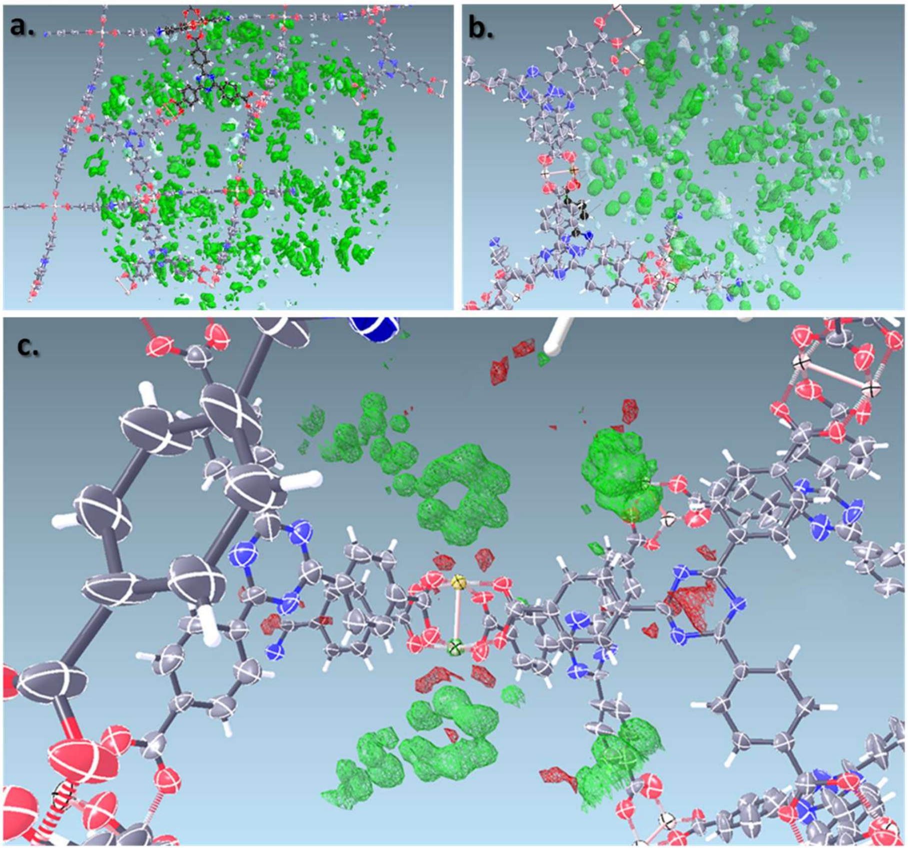

Figure 2.4 Residual electron density maps (contoured at 1.5 sigma) of: a) PCN-6@nicotine; b) PCN-6’@nicotine pore; c) zoom of PCN-6@nicotine, 6-membered ring of pyridine is clearly visible

2.2.4 Characterization of PCN-6’@nicotine

The preservation of the crystalline framework of PCN-6’ after nicotine inclusion was confirmed by XRPD analysis: a very good fit wass observed between the simulated diffractogram of PCN-6′ and the experimental trace collected for PCN-6’@nicotine (in Figure 2.5).

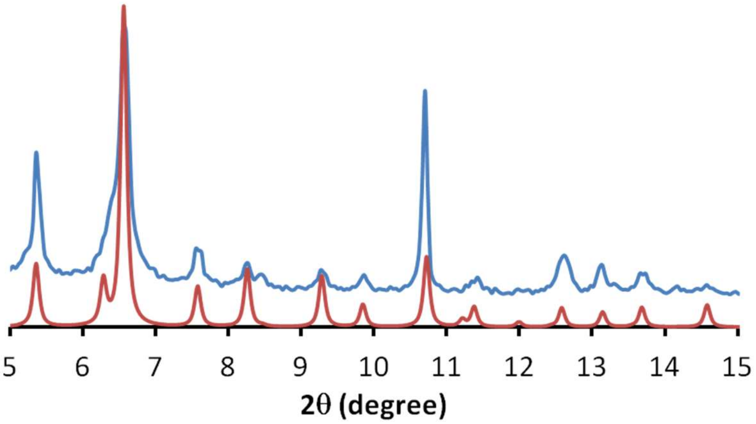

Figure 2.5: Comparison between the simulated (PCN-6’, red line) and experimental PCN-6’@nicotine (blue line) XRPD patterns.

This also pointed out an increased stability of PCN-6’@nicotine compared to native PCN-6’: in fact, the crystals of the latter are affected by a quick water adsorption with consequent loss of crystallinity, as previously described.

A first check on the PCN-6’ capability of trapping nicotine was provided by DIP-EI/MS and UV-VIS measurements.[103] An accurate study aimed at defining the amount of trapped nicotine was conducted by means of TGA and NMR analysis. Native PCN-6’ crystals, after activation, displayed almost no weight loss until MOF decarboxylation at 320°C, as illustrated in Figure 2.6. On the contrary, PCN-6’@nicotine showed an additional weight loss corresponding to 21% in the range from 180 to 240°C, attributed to nicotine extrusion from the crystals (green trace in Figure 2.6).

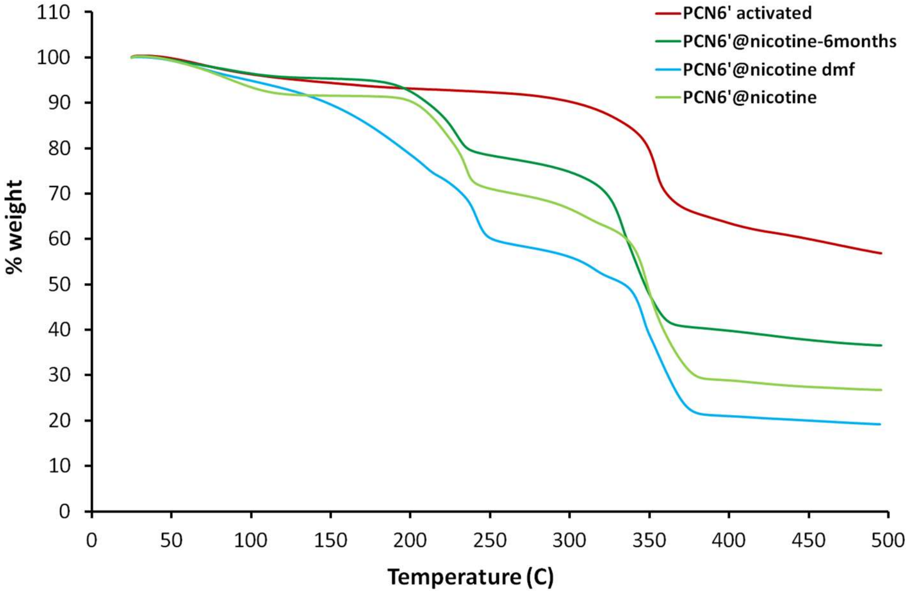

Figure 2.6: TGA traces of activated PCN6’ (red trace) and different PCN-6’ @nicotine samples corresponding to different loadings: 1 week of loading (green trace), 1 week of loading and 6 months of air exposure (dark green trace), not activated crystals from synthesis soaked in nicotine for 4 days (light blue trace).

The stability of PCN-6’@nicotine was confirmed repeating the TGA measurement after having stored the loaded crystals in the air for six months: a guest-release corresponding to 17% weight loss was observed (dark green trace in Figure 2.6). The high host-guest affinity was outlined by the result obtained with a nicotine soaking carried out without activating the PCN-6′crystals. A quick colour variation from light blue to green was observed once the guest was put in contact with the crystals of PCN-6′, and the TGA trace recorded on the same crystals, after 4 days of soaking, displayed a 15% weight loss in the temperature range 140-240°C. In this case, the observed slope is likely due to the contemporarily desorption of DMF and nicotine (light blue trace in Figure 2.6).

Despite the paramagnetic character of Cu(II), we considered the NMR spectroscopy a useful technique to complete the guest quantification. This method was in fact successfully used for the determination of the amount of solvent trapped inside Cu(II)-based MOFs by Yaghi and colleagues.[110] This approach proved to be much more convenient than elemental analysis owing to the rapid desolvation that mesoporous MOFs undergo at room temperature once removed from solvent.

Moreover, the application of NMR spectroscopy for the characterization of nicotine-Cu(II) molecular complexes has already been reported in literature.[111]

Then, some crystals of PCN-6′@nicotine were carefully washed with a minimum amount of acetone in order to remove the guest eventually sorbed on the crystals surface and subsequently digested in a mixture of TFA-d/DMSO-d. The resulting clear solution was first analysed by $^{13}C\{^{1}H\}$-NMR spectroscopy, in order to check the feasibility of the technique. Despite the presence of copper, we obtained satisfactory results, as furnished in Figure 2.7.

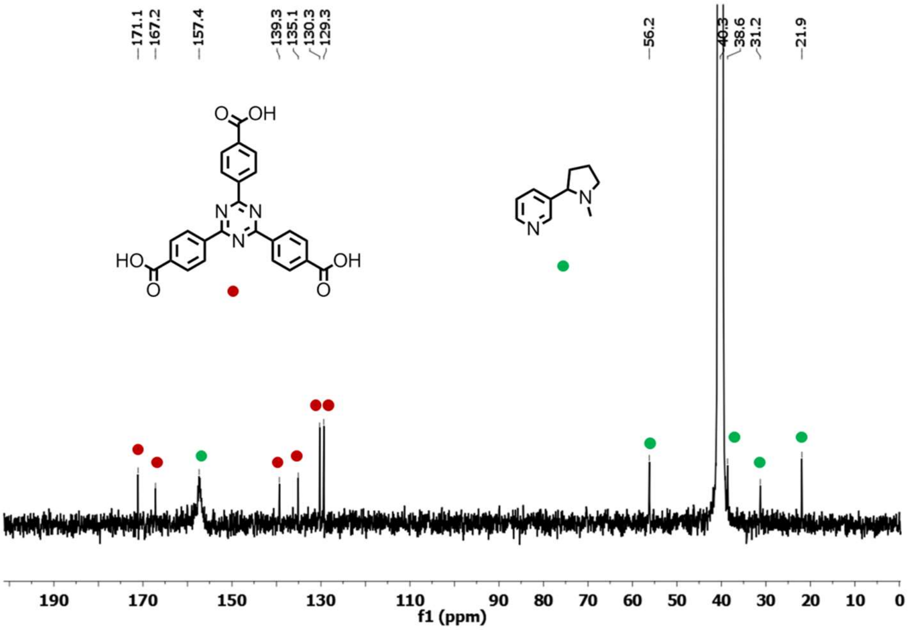

Figure 2.7 ^{13}C{^{1}H}-NMR (100 MHz, 0.5 mL DMSO-d, 20 μL TFA-d) of digested PCN-6’@nicotine: red dots for TATB peaks, green dots for nicotine peaks

In the interval 180-120 ppm the peaks belonging to TATB were visible. The pyridine signals were not well resolved, being fused in a broad signal. The line broadening is likely due to the presence of the paramagnetic metal ion. Moving toward the aliphatic carbons, we can recognize three signals at 56.2, 38.6 and 31.2 ppm, respectively, which can be assigned to CH_2 carbons of pyrrolidine. Finally, at 21.9 ppm the CH_3 peak is found.[112]

In order to define the TATB/nicotine ratio, the ^{1}H-NMR spectrum of the solution was collected (Figure 2.8).

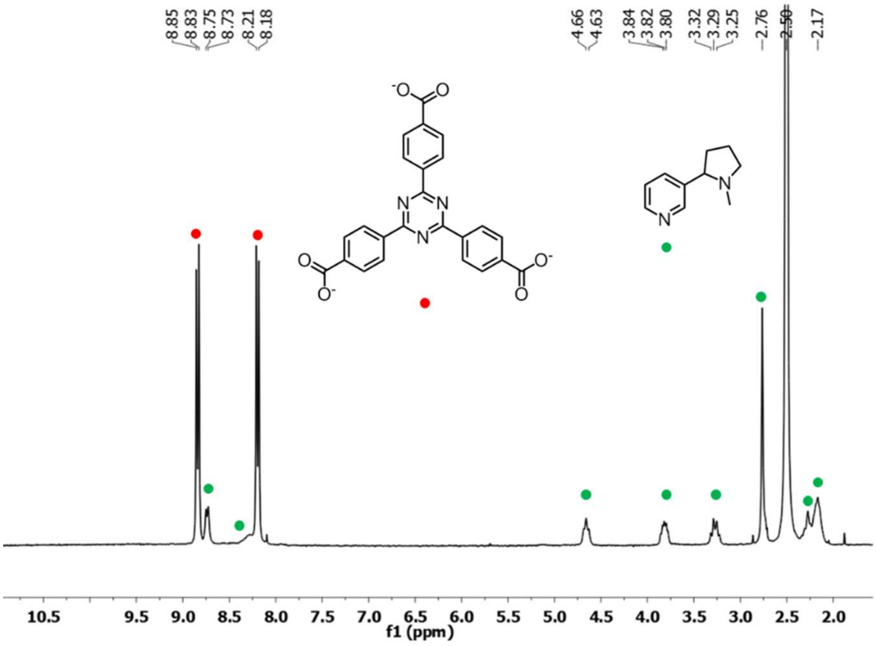

Figure 2.8 ^{1}H-NMR (300MHz, 0.5 mL DMSO-d, 20 μL TFA-d) of PCN-6'@nicotine: red dots for TATB protons, green dots for nicotine protons

The spectrum showed two sharp doublets corresponding to the 12 aromatic protons of TATB (8.84 and 8.20 ppm). Again, the pyridine gave rise to broad signals because of the presence of copper, and this hampered a rigorous attribution and integration of the signals. The line broadening points out that the py-nitrogen is still engaged into coordination with the metal. The two protons in *ortho* position with respect to the pyridine nitrogen are in fact not visible. The pseudo-doublet at 8.74 ppm can be attributed to the proton in *para* position, while the proton in *meta* was observed as a broad signal. In the aliphatic region, in the interval 4.7-2.1 ppm, the three broad multiplets and the two broad signals can be assigned to CH and CH_2 moieties of pyrrolidine ring, whereas the broad singlet at 2.76 ppm derives from the methyl protons (NC*H*$_3$).

For a reliable quantification of trapped nicotine, we chose the methyl group of pyrrolidine as a probe. Its peak multiplicity, singlet, corresponds to a higher signal over noise ratio, thus reducing the possible error during the area integration. The unambiguous assignment of the methyl signal was possible by a COSY experiment: no cross peaks were observed for the signal at 2.76 ppm (Figure 2.9).

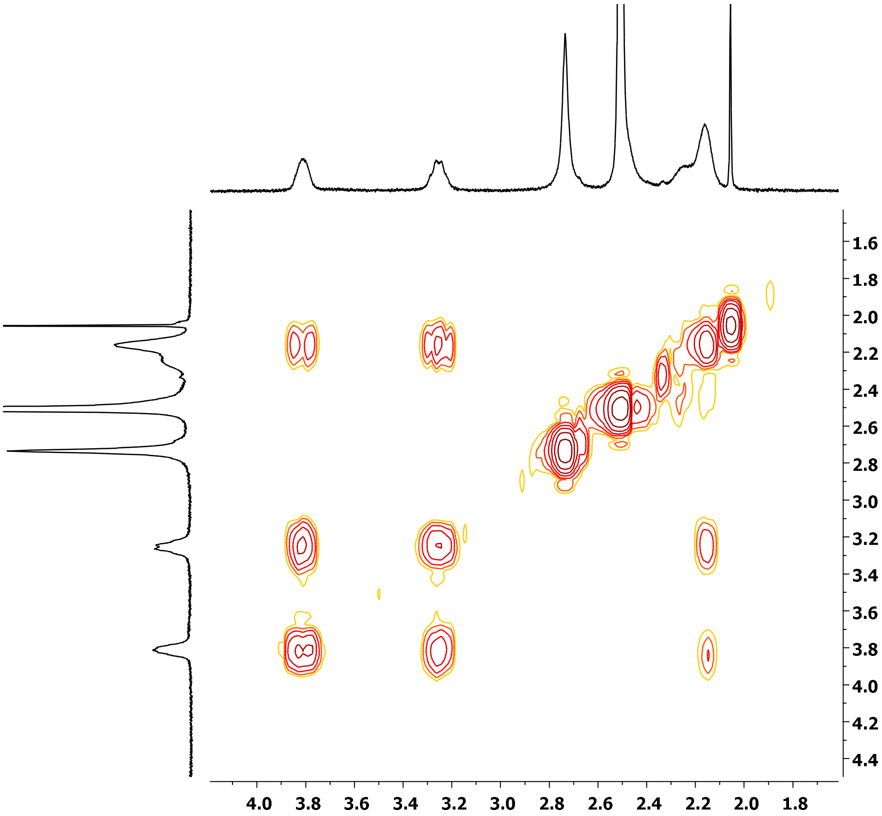

Figure 2.9 Expansion of the aliphatic region of the COSY spectrum of PCN-6´@nicotine (TFA-d/DMSO-d)

Taking into account the crystal structure of PCN-6´, we can consider that each pore is delimitated by eight molecules of TATB, corresponding to 96 aromatic protons and twelve Cu-paddle-wheels. For this reason, a normalized value of 48 protons is attributed to each doublet centred at 8.84 and 8.20 ppm in Figure 2.8. Hence, the integration area corresponding to the singlet belonging to the methyl group of the pyrrolidine ring corresponds to 21 molecules of nicotine included in each pore of the MOF, as reported in Table 2.2.

Sample	CH_3 integral value	Nicotine molecules for pore
PCN6’@nicotine (neat guest)	63	~21
PCN6’@nicotine (AcCN soaking solution)	40	~13
PCN6@nicotine (DCM soaking solution)	31	~10

Table 2.2 Summary of nicotine quantifications furnished by ^{1}H-NMR analysis

This leads to a unit formula of $Cu_6(TATB)_4 \cdot 10.5$nicotine for PCN-6′@nicotine. As expected, the amount of loaded nicotine decreased significantly when the soaking was performed with an acetonitrile solution (see entry 2, Table 2.2): CH_3CN molecules compete with nicotine to fill the cavities, for this reason only 13 molecules of nicotine are included in PCN-6’ pore. An additional lowering of the number of guest molecules is observed also in the soaking of the interpenetrated phase PCN-6: only 10 nicotines were estimated (entry 3, Table 2.2), corresponding to half the value observed for PCN-6’@nicotine. This is consistent with the presence of solvent molecules that act as competitors together with the reduced pore volume in the interpenetrated phase.

Taking a step back to the loading test performed in neat nicotine, comparing the amount of nicotine determined by NMR and TGA analysis a discrepancy can be found. In fact, the formula $Cu_6(TATB)_4 \cdot 10.5$ nicotine would correspond, for a complete thermally guest extrusion, to a calculated 44% of nicotine, against the 21% observed by TGA analysis conducted up to a temperature of 240 °C. In order to check if this temperature leads to the complete extrusion of nicotine, the ^{1}H-NMR spectrum of a sample of PCN-6′@nicotine already subjected to TGA analysis was recorded.

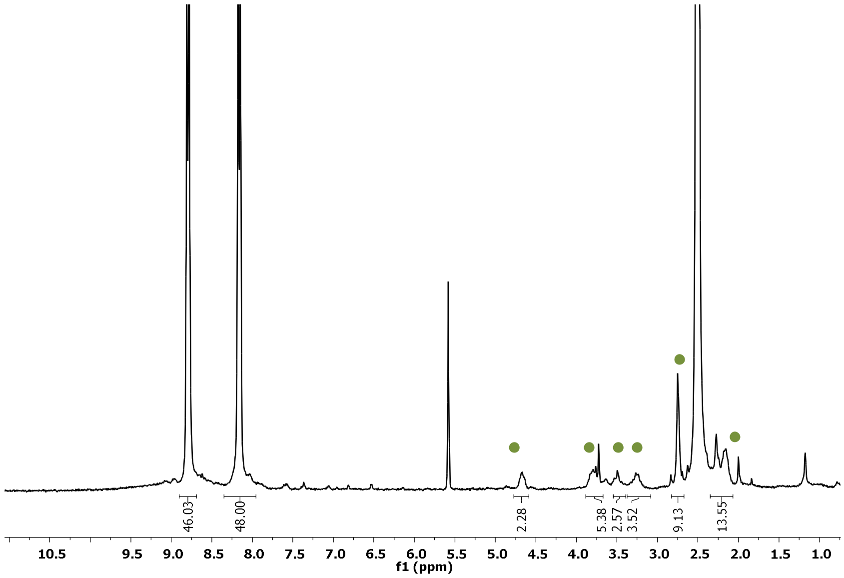

Figure 2.10 ^{1}H-NMR of digested PCN-6’@nicotine crystals after TGA heating ramp from 25 up to 240°C: nicotine protons are still present (green dots).

As illustrated in Figure 2.10, the NMR spectrum still indicates the presence of nicotine after the heating process. In view of these considerations, the TGA quantification has been revaluated considering also the weight loss in the interval from 180 to 320°C, obtaining an average 30% weight loss. The remaining discrepancy between TGA and NMR analysis points out that a further nicotine fraction is desorbed during the decarboxylative step (T> 320°C): this is consistent with the previously reported thermal behaviour of nicotine containing metal-complexes, which showed the nicotine release for temperature from 280 to 400°C. [113]

2.3 Experimental part

2.3.1 General Methods

^{1}H-NMR and ^{13}C{^{1}H}-NMR spectra were recorded on 400 MHz and 300 MHz Bruker instruments. Chemical shifts are reported in ppm relative to the solvent residual peak of $CDCl_3$ (δH 7.26, δC 77.0) or $(CD_3)_2SO$ (δH 2.50, δC 39.5). TFA-*d* is used for the digestion experiments. *J*-values are given in Hz and in the assignments the following notations have been used s = singlet, d = doublet, t = triplet, q = quartet, m = multiplet, br = broad, dd = doublet of doublets, bb = broad band.

EI(+)-MS spectra were collected with an ionising voltage of 70 eV by means of a Thermo DSQ II spectrometer equipped with a single quadrupole analyser. The analyses were conducted on solid samples by means of a DIP probe (direct insertion probe, flash thermolysis at 350 °C). IR spectra were obtained with a Thermo Scientific Nicolet 5PCFT-IR-ATR spectrometer (diamond crystal) in the 4000-400 cm^{-1} interval. Thermogravimetric analyses were performed on a PerkinElmer instrument (sample mass approx. 5-10 mg) at a heating rate of 10 °C min^{-1} in a temperature range from 25-500 °C. The measurement was performed at atmospheric pressure under flowing nitrogen (80 mL min^{-1}). Morphological analysis were conducted by an environmental scanning electron microscope (ESEM) Quanta^{TM} 250 FEG (FEI, Hillsboro, OR) equipped with an energy-dispersive spectrometer (EDS) for X-ray microanalysis (Bruker Nano GmbH, Berlin, Germany), operating with low-vacuum mode (70 Pa). ESPRIT 1.9

microanalysis software (Bruker Nano GmbH) was used for X-ray spectra acquisition and for digital element map. Morphological analysis were carried out with an accelerating voltage (HV) of 5.0 kV, while EDS analysis were conducted with a HV of 20.0 kV.

X-ray single crystal measurements were performed at *Elettra Sincrotrone* (Trieste, Italy) on beamline XRD1 at 100K under cold nitrogen flux. The source used for the analysis was a NdBFe Multipole Wiggler (Hybrid linear), 4.27 KeV with a power of 8.6 kW, a source size FWHM of 2.0 x 0.37 mm (0.7 x 0.2 mm FWHM beam size at sample) and photon flux 10^{12}-10^{13} ph/sec.

Soaked PCN-6'/PCN-6 crystals were taken directly from dichloromethane or nicotine and mounted with cryoloops (0.05-0.3 mm). Annealing trial was performed on mounted crystal dropping the temperature from r.t to 100 K, with a cooling rate of 2°C min^{-1}. Absorption correction was applied. Diffraction data were indexed, integrated, and scaled using CrysAlis software.[114] PCN6@nicotine structure was solved by direct methods using SHELXS[115] and refined by full-matrix least-squares on all F2 using SHELXL implemented in Olex2.[116] Anisotropic displacement parameters were refined except for hydrogen atoms. Nicotine molecule was refined as a rigid body.

2.3.2 Ligand Synthesis

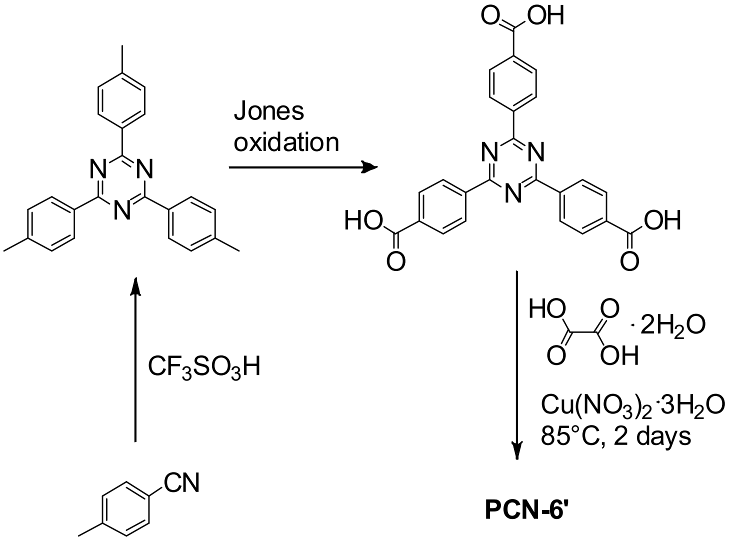

Scheme 2.1 General synthetic strategy for TATB and PCN-6'

2,4,6-tri-p-tolyl-1,3,5-triazine

CF_3SO_3H (10 g, 6.6 mmol) was added to a 50 mL one neck round bottomed flask, then *p*-tolunitrile (2.9 mL, 24.3 mmol) was added dropwise (exothermic reaction). Resulting orangish solution was stirred at room temperature overnight. Then, the reaction mixture was cooled to 0°C with an ice bath, then neutralized with NH_3. The precipitate was filtered under vacuum with a glass septum and washed with water (20 mL) and acetone (20 mL) and finally dried under vacuum. 2,4,6-tri-p-tolyl-1,3,5-triazine was obtained as a white solid (2.65 g, 7.6 mmol, y=93%).

Recrystallization procedure:

In a 100 mL one neck round bottomed flak 2,4,6-tri-p-tolyl-1,3,5-triazine (2.65 g, 7.6 mmol) was dissolved in toluene under reflux conditions. The resulting solution was cooled to -20°C, and crystallized product was isolated by filtration (2.56 g, 7.3 mmol, y= 95%).

^{1}H-NMR (300 MHz, $CDCl_3$) δ: 8.65 (d, 6H, *J*=8.4Hz, CH_{Ar}), 7.37 (d, 6H, *J*=8.4 Hz, CH_{Ar}), 2.48 (s, 9H, CH_3) ppm.

TATB-4,4',4''-(1,3,5-triazine-2,4,6-triyl)tribenzoic acid

To a 250 mL round bottomed flask acetic acid (40 mL), 2,4,6-tri-p-tolyl-1,3,5-triazine (1.5 g, 4.3 mmol) and H_2SO_4 (2.5 mL) were added, obtaining a pale yellow colour of the mixture. After cooling to 0°C with an ice bath, CrO_3 (3.9 g, 39 mmol, 9 equivalents) and acetic anhydride (2.4 mL) were added to provide a dark brown solution. Further 20 mL of acetic acid was added and the reaction was stirred at room temperature overnight.

Then, the reaction was quenched with distilled water (200 mL) obtaining the formation of a very fine product suspension. Resulting mixture was separated by centrifugation and carefully washed adding water, until no further precipitate formation was detected (deep green supernatant) and pale greenish solid. The isolated solid was carefully washed with water, followed by acetone and finally dried overnight under vacuum. TATB was obtained as off-white solid (1.31 g, 2.96 mmol, y= 86%).

Recrystallization procedure:

In a 100 mL round bottomed flask TATB (1.31 g, 2.96 mmol) was dissolved under magnetically stirring in DMF (65 mL) at 80°C. The limpid pale green solution was cooled to r.t and stored at -20°C overnight. Crystallized TATB was isolated by vacuum filtration with glass septum (1.07 g, 2.42 mmol, y=82%).

^{1}H-NMR (300 MHz, DMSO-*d*6) : *δ* 13.30 (br, COO*H*, 3H), 8.65 (d, CH_{Ar}, *J*= 8.2 Hz, 6H), 8.08 (d, CH_{Ar}, *J* = 8.2 Hz, 6H) ppm; ^{13}CNMR (75 MHz, DMSO-*d*6) : *δ* 170.4, 166.8, 138.6, 134.6, 129.7, 128.7 ppm

PCN-6' standard procedure

In a 16 mL pyrex tube TATB (20 mg, 0.044 mmol), $Cu(NO_3)_2{\cdot}3H_2O$ (52 mg, 0.214 mmol), and oxalic acid dihydrate (4 mg, 0.030 mmol) were added to DMF (3 mL). Then, the tube was tightly capped and heated at 80°C in a oily bath for 48 hours. NOTE: after few hours the formation of copper oxalate as a very fine pale blue powder was observed.

PCN-6' scaled up procedure

Scale up was performed in a 70 mL pyrex tube, head space and solvent volume were chosen in order to maintain the ratios employed for small scale reactions.

In a 70 mL pyrex tube TATB (70 mg, 0.16 mmol), $Cu(NO_3)_2$ $3H_2O$ (182 mg, 0.75 mmol), and oxalic acid dihydrate (14 mg, 0.11 mmol) were added to DMF (10.5 mL). Then, the tube was tightly capped and heated at 80°C in a oily bath for 48 hours.

	Metal Salt	TATB (mg)	Solvent/ Tube Vol (mL)	T (°C)	Comments
1	$Cu(NO_3)_2{\cdot}3H_2O$	10	1.5/10	80	Very small octahedral crystals
2	$Cu(NO_3)_2{\cdot}3H_2O$	10	1.5/10	110	Increased DMF degradation, slight reduced crystal quality
3	$Cu(NO_3)_2{\cdot}3H_2O$	20	1.5/10	85	Increased crystal dimension
4	$Cu(NO_3)_2{\cdot}3H_2O$	20	1.5/10	75	Lowering of T has no visible effect with respect to entry 3. Additional undesired byproducts
5	$Cu(NO_3)_2{\cdot}3H_2O$	40	1.5/10	85	Increased crystal dimension, but similar with respect to entry 3. Byproducts observed.
6	$Cu(NO_3)_2{\cdot}3H_2O$	20	3/16	75	Octahedral crystals
7	$Cu(NO_3)_2{\cdot}3H_2O$	80	4/16	85	Increased crystal dimension. Severe twinning problem and presence of by-product
8	$CuBr_2$	10	1.5/10	85	Longer reaction time and low amount of crystals formed
9	$CuBr_2$	20	1.5 /10	85	No variation with respect to entry 8
10	$Cu(NO_3)_2{\cdot}3H_2O$	135	12/70	80	Very small crystals
11	$Cu(NO_3)_2{\cdot}3H_2O$	70	10,5/70	80	Octahedral crystals

Table 2.3 Summary of the experimental conditions tested for the synthesis of PCN-6’.

PCN-6 general procedure:

In a 16 mL pyrex tube TATB (20 mg, 0.044 mmol) and $Cu(NO_3)_2 \cdot 3H_2O$ (52 mg, 0.214 mmol) were added to DMF (3 mL). Then, the tube was tightly capped and heated at 80°C in an oily bath for 48 hours. PCN-6 was obtained as a fine microcrystalline powder.

The tested reaction conditions are reported in Table 2.4 Summary of the experimental conditions tested for the synthesis of interpenetrated PCN-6.

TATB (mg)	Temp (°C)	Solvent/Tube Volume (mL)	Comments
20	75°C	3/16	microcrystalline powder
10	75°C	3/16	No significative variation
45	85°C	1.5 /10	No significative variation
80	80°C	3/16	No significative variation

Table 2.4 Summary of the experimental conditions tested for the synthesis of interpenetrated PCN-6.

Activation and Soaking with neat nicotine

PCN-6' and PCN-6 samples were activated following a solvent exchange protocol: as-synthesized crystals were soaked in methanol (10 mL for small scale synthesis) for 24 hours, then the solvent was discarded. Fresh methanol was subsequently added, and the crystals were allowed to soak for additional 24 hours. The same procedure was repeated with the subsequent treatment with dichloromethane (10 +10 mL), in order to remove methanol solvates. After 48 hours, the dichloromethane was removed by decanting and the sample was transferred in a Schlenk tube and dried overnight under dynamic vacuum (< 10^{-3} Torr) at room temperature.

After the evacuation, 10 mg of activated PCN-6’ crystals were dipped in neat nicotine (1 mL) under nitrogen flux. Then vial was tightly capped and the soaking was performed in static condition. After 1 week, nicotine was removed and crystal were carefully washed with acetone (1 mL) for two times, then dried under vacuum to provide PCN-6’@nicotine as green crystals.

2.4 Supplementary material

PCN-6’: attempts to characterize the by-products isolated during the scaled-up synthesis

The first by-product observed is a light blue powder identified as copper oxalate by IR spectroscopy, as shown in Figure 2.11.

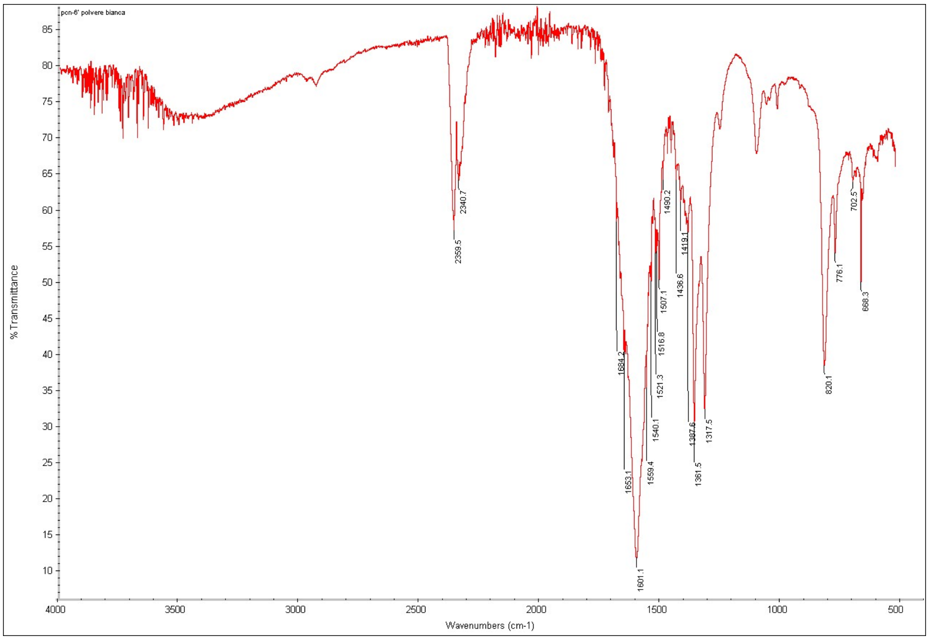

Figure 2.11 IR spectrum of one of the by-products isolated during the scaled-up synthesis of PCN-6′, identified as copper oxalate.

The second by-product proved to be a very tough and difficult-to-grind material, inhibiting a PXRD characterization. Morphological analysis performed with ESEM microscopy displayed a spherical shape of the particles (diameter ~100 μm), while the SEM microanalysis showed the presence of copper and oxygen (Figure 2.12).

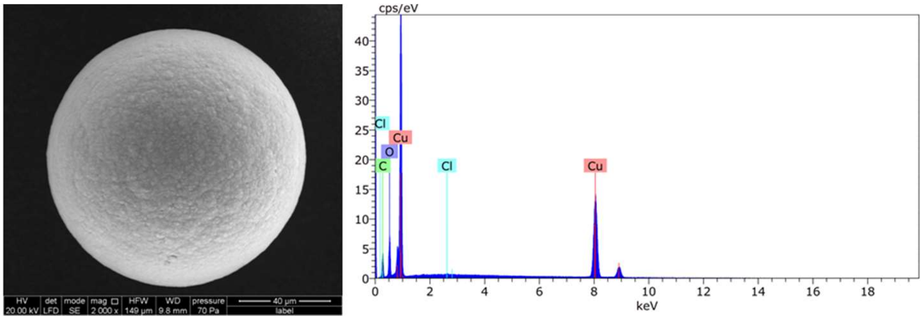

Figure 2.12 SEM imaging (left) and EDS spectrum (right) of the second by-product isolated during the scaled-up synthesis of PCN-6′.

Aging of PCN-6′@nicotine crystals

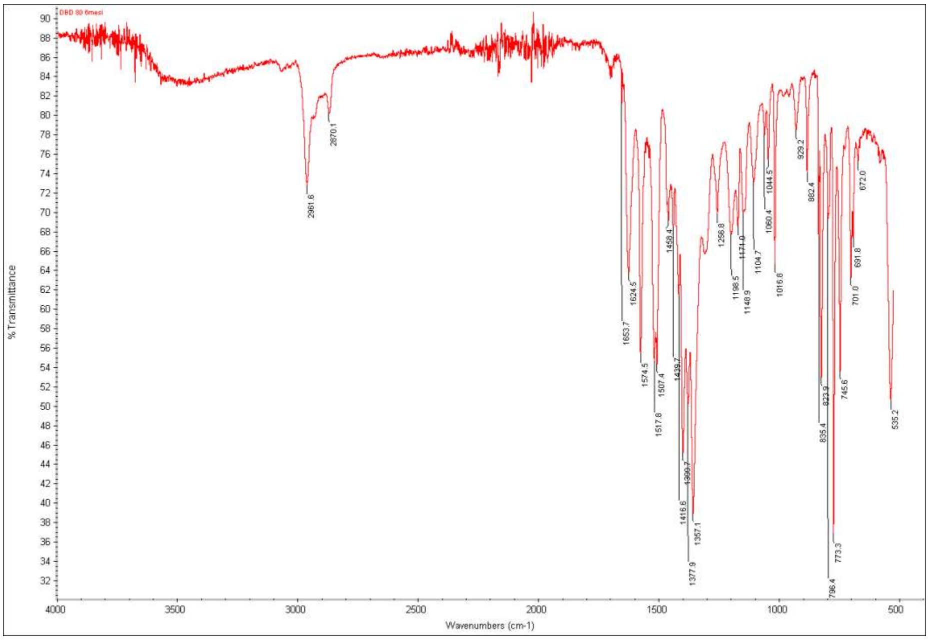

Figure 2.13 ATR-spectrum of PCN-6’@nicotine after a period of air exposure of six months: in the region from 3000 to 2800 cm^{-1} are clearly visible very strong CH vibrations related to nicotine guest.

3 Encapsulation of Metal Complexes into Mesoporous MOFs

Mi guardai intorno, e vidi in un angolo una comune pila a secco. Ecco quanto avremmo fatto: l'elettrolisi dell'acqua. […] *Presi acqua in un becher, vi sciolsi un pizzico di sale, capovolsi nel becher due barattoli da marmellata vuoti, trovai due fili di rame ricoperti di gomma, li legai ai poli della pila, e introdussi le estremità nei barattoli. Dai capi saliva una minuscola processione di bollicine* [...]

Era proprio idrogeno, dunque: lo stesso che brucia nel sole e nelle stelle, e dalla cui condensazione si formano in eterno silenzio gli universi.

-Il sistema periodico, Primo Levi-

3.1 Introduction: metal-complexes@MOF as heterogeneous catalysts

In the past few years, MOFs started to attract a broadening interest as possible hosts for metal catalysts. In fact, MOFs can be considered a complement of classical heterogeneous catalysts. On the one hand, zeolites are characterized by excellent thermal stability, suitable for high temperature catalysis reactions; on the other hand these materials are inadequate in terms of pore size tunability, which strongly limits the possible applications for solution catalysis. MOFs exhibit high surface area and a fine pore modulation, achieved through a suitable choice of metal SBUs and organic linkers.[117] In addition, the immobilization of transition metal catalysts allows to combine advantages of peculiar reactivity, typical of homogeneous processes, to the point of strength of heterogeneous systems (e.g: easy catalyst separation and recovery from reaction media).

One of the most used approach to bind a metal complex to MOF walls is post-synthetic modification (PSM). Lin et *al*. reported the inclusion of Pd/Ir complexes inside bpy-UiO.[118] Exploiting bi-pyridine moieties decorating the organic linkers, authors obtained the metal chelation thus providing a highly robust heterogeneous catalyst, more stable and active than the homogeneous analogous. The system bpy-UiO-Pd catalyzed the dehydrogenation of cyclohexenones to phenol derivatives, while bpy-UiO-Ir was a highly efficient catalyst for both borylation of aromatic rings and for *ortho*-silylation reactions.

In this field Zr-based MOFs have played a primary role [119], due to a great chemical 120, mechanical 121 and thermal stability of the frameworks under several experimental conditions. In 2013, Cohen *et al.* 122 illustrated a photocatalytic water splitting process employing UiO-66 decorated with a homo-binuclear iron complex. A mild PSM protocol allowed authors to substitute a 14% of starting BDC linkers with 1,4-dicarboxylbenzene-2,3-dithiolate bound to a homobinuclear [Fe-Fe] complex. The resulting heterogeneous catalyst proved to be three times more efficient with respect to the homogenous one, with 3.5 μmol of dihydrogen formed in 90 minutes ($[Ru(bpy)_3]^{2+}$ was added as photosensitizer). Similar results were published by Feng *et al.*123 using a zirconium porphyrin-containing MOF: Zn ion linked to the phorphyrinic core (tetrakis-4-carboxy-phenyl porphyrin, named as TCPP) acted as an anchoring sites for $[(SCH_2)_2\text{nicotinamide}]–[Fe_2(CO)_6]$. In this case, no addition of exogenous additives was required, as ZnTCPP-[Fe-Fe]acted both as photosensitizer and as catalyst. Irradiation at 420 nm for 2 hours produced 3.5 μmol of H_2: both higher performance and stability with respect to homogeneous system were confirmed.

Other highly stable MOFs containing metals different from Zr were used for this purpose: Fe-based MIL-101-NH_2, was functionalized by one pot condensation with $NiCl_2$ and pyridine carboxaldehyde, obtaining a diimino nickel complex. Resulting MIL-101-NH_2@Ni was applied for the selective dimerization of ethylene to 1-butene by Canivet *et al.*124

An alternative strategy is the prior inclusion of a metal complex into ligand skeleton, followed by MOF synthesis [125]: this protocol is possible only for complexes stable under solvothermal conditions. Taking a step back to hydrogen production, a Ru(II) complex was inserted in the ligand backbone obtaining the $Ru(tpy)_2$ linker, (tpy=bis(4'-(4-carboxyphenyl)-terpyridine) which was then used for the self-assembly of a Ti-based MOF. The resulting material, Ti-MOF-$Ru(tpy)_2$ was successfully tested for water reduction: a sacrificial electron source was added to the solution before irradiation with visible light.[126] All described pathways provided an immobilization of the guest complex through covalent bonding to MOF walls. To the best of our knowledge, no examples of metal catalysts not covalently linked to MOF hosts have so far been reported. For these reasons, we decided to focus our attention on the trapping of metal complexes taking advantage of hydrogen bonds and weak interactions as stabilizing forces. In theory, this approach can be advantageous from a synthetic point of view: after the choice of a suitable mesoporous MOF with pores larger enough to host the guest complex, a simple soaking experiment is required for encapsulation, avoiding complicated PSM steps. Absence of PSM and covalent bonding remove many limitations in the choice of the metal complex: we believe that this protocol could be further broadened in the future to a wider library of homogeneous metal catalysts. In order to make this strategy effective, possible leaching phenomena have to be verified. In this chapter we present in details the characterization and application of the host-guest systems composed by two already known mesoporous MOFs and two biomimetic Ni catalysts for the above described purpose. Metal complexes were kindly furnished by Dr. M. Gennari of the Department "CIRE- Chimie Inorganique REdox", Joseph Fourier University of Grenoble (France).

3.1.1 Bio-inspired Ni and Ni/Fe Complexes

Hydrogen evolution reaction (HER) involves the proton reduction in acidic media in the presence of an electrocatalyst, on the basis of the following reduction process:

$$2H^+ + 2e^- \rightarrow H_2$$

The presence of a catalyst is required to lowering the otherwise huge kinetic overpotential. Best performances were associated to Pt or other noble metal catalysts, however the scale up of hydrogen production entails the research of new low costing catalysts.[127] From this perspective, combination of catalyst with a porous host can enhance system performances and decrease the overpotential related problems, through a surface extension of catalytically active sites.

In this study, two bio-inspired Ni(II) complexes (Figure 3.1-a), active for H_2 evolution under homogeneous conditions, were chosen for the inclusion tests.

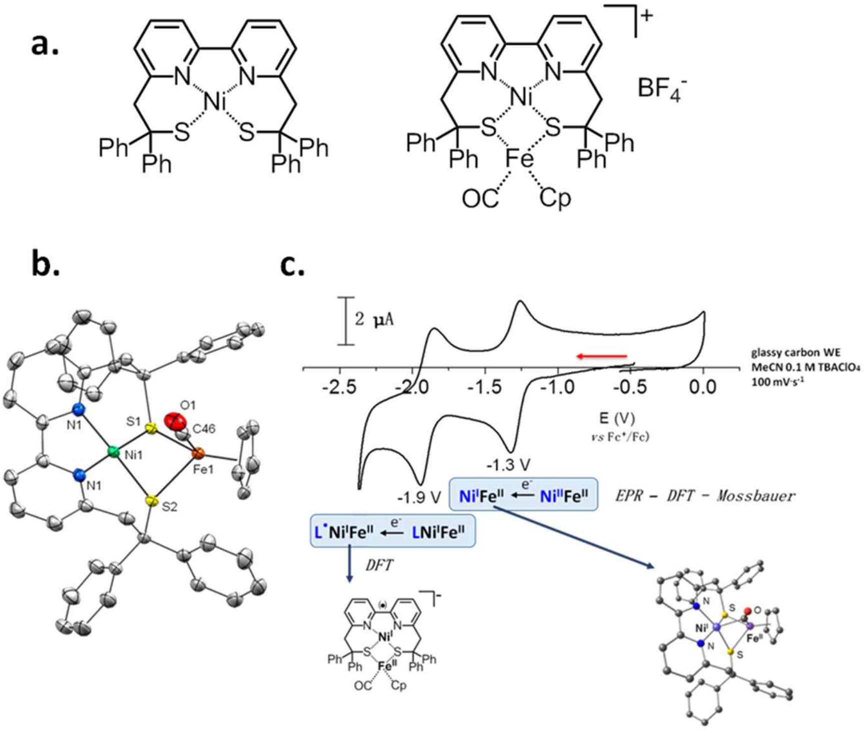

Figure 3.1: a) left NiL, right NiFeL; b) NiFeL X-ray structure; c) CV of NiFeL performed on GC electrode, with a 0.1 M TBAClO4 acetonitrile solution.

The first one, NiFeL is a hetero-binuclear nickel/iron complex which showed uncommon proprieties as proton reduction catalyst.[128] Peculiarity of this compound is the Ni-centred reactivity, which reproduces for the first time the activity of [NiFe] hydrogenase metallo-enzimes.[129] Since the crystal structure resolution of the enzyme, achieved in 1995,[130] the mechanism of action of [NiFe] hydrogenase has been widely studied.[131] Its active site is composed by a {Ni(cysteinate)$_4$} unit linked by two of these cysteinic residues to a {Fe^{II}(CN)$_2$(CO)} moiety. It is noteworthy that the observed Ni···Fe distance found in NiFeL is very similar to the one found in the enzyme:

2.90 Å for hydrogenase and 2.84 Å for NiFeL (determined by X-ray structure analysis, Figure 3.2-b).

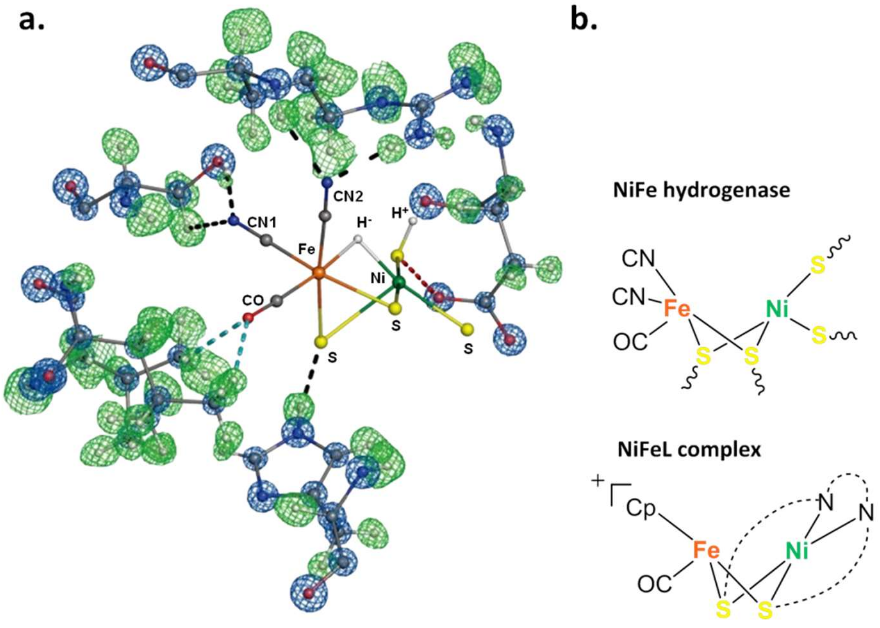

Figure 3.2 a) Active site of [NiFe] hydrogenase: electron density maps of the amino-acid residues that are hydrogen bonded to the active site; b) comparison between [NiFe] hydrogenase and NiFeL active sites.

Therefore, NiFeL proprieties can be explained by a fine complex design: bipyridine core allows the stabilization of low oxidation states, while phenylic substituents prevent thiolates oxidations. Starting from initial Ni(II), both Ni(I) and Ni(III) oxidation states are accessible during catalytic cycle.

The electrochemical proprieties of NiFeL are reported in fig. 3.1-c : CV performed on glassy-carbon (GC) electrode in MeCN 0.1 M $TBAClO_4$ ($TBAClO_4$ = tetrabutyl ammonium perchlorate, pointed out two different single electron reduction waves. The first one, at -1.3 V, corresponds to the reduction of Ni(II) to Ni(I), while the second wave at -1.9 V is associated with a super-reduced state $L^{\bullet}$Ni(I) with strong radical proprieties. This is then related with the transfer of an electron from Ni(I) to L.

Also the NiFeL precursor, named NiL [132], has been tested for H_2 production but it resulted less effective: authors observed 9 turnovers for NiL within 100 minutes, a significant lower value if compared with 16 turnovers observed with NiFeL within the same time.

Both complexes present a longest dimension of 14 Å (C*H*···C*H* distance between opposite phenyl rings, measured from X-ray crystalline structure): for a successful encapsulation of the two complexes a mesoporous host framework is then required. For this purpose, we selected two already known mesoporous MOFs, deriving from the self assembly of the same ligand (TATB= 4,4′,4″-triazine-2,4,6-triyl-tribenzoic acid) with two different metal cations: Cu^{2+} (PCN-6′) and Zr^{4+} (PCN-777). On the one hand we were interested on the possibility of a structural definition of confined guest into host cavities, on the other hand we aimed at testing the new material proprieties as heterogeneous catalyst, towards proton reduction. Finally, we were interested in the study of possible nanoconfinement effects: MOF could act as protective environment for the complex and could influence its proprieties, similarly to the pocket of the enzyme.

3.2 **PCN-6′: a suitable host with many limitations**

3.2.1 Trapping and evidence of encapsulation

Crystals of PCN-6’ were activated following the protocol previously described for the encapsulation of nicotine (solvent exchange protocol, then dried under vacuum overnight, see page 27). Activated crystals were soaked in a dichloromethane solution of the guest : 2.6 mM for NiL and 4.0 mM for NiFeL. The progress of the complex trapping could be conviniently monitored by UV-VIS spectroscopy, as outlined in Figure 3.3.a-b. UV-VIS spectra pointed out a gradual drop of the concentration of the soaking solution for both Ni complexes.

A proof of the inclusion of NiFeL was provided by IR spectroscopy , as shown in Figure 3.3.c.

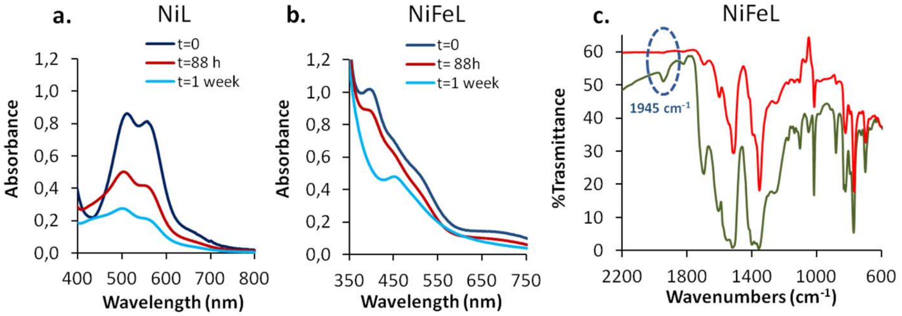

Figure 3.3 a) UV-VIS spectra of NiL solution in contact with crystals of PCN-6’ at different soaking times; b) UV-VIS spectra of NiFeL solution in contact with crystals of PCN-6’ at different soaking times; c) overimposition of the IR spectra of pristine PCN6’ (red line) and PCN6’ loaded with NiFeL complex (green line).

The IR spectrum of PCN-6’@NiFeL shows one CO stretching band at 1945cm^{-1}, a signal which is very similar to that of the starting complex: in fact, NiFeL displays a CO stretching frequency at 1929 cm^{-1}.

Hence, we procedeed to a more accurate quantification of the amount of NiL and NiFeL encapsuleted by ESEM-EDS mesaruments. SEM immaging allowed to recognize the integrity of loaded crystals, while EDS analysis provided S/Ni and Ni/Fe ratios, useful to evaluate the guest complexes preservation after the inclusion process.

Figure 3.4.a illustrates a first difference between native and loaded PCN-6’ crystals, once removed from solution: a massive cracking is clearly visible on pristine PCN-6’, while PCN-6’@NiFeL shows a smooth surface, indicating a higher stability of the MOF framework after encapsulation.

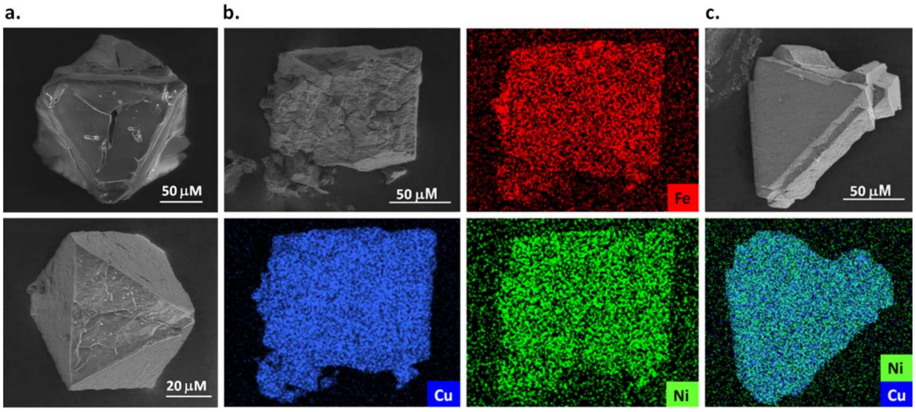

Figure 3.4 : a) Comparison between SEM images of crystals of pristine PCN-6’ (top) and PCN-6’@NiFeL (bottom) once removed from solution; b) SEM image and EDS maps of crystal section of PCN-6’@NiFeL; c) SEM image and the overlap of Ni and Cu EDS maps for an external section of PCN-6’@NiL.

Finally, EDS analysis was carried out both on the external crystal surfaces and both on the internal sections, after a carefully cutting of the crystals. EDS mapping showed a homogenous guest distribution inside crystals: the spot intensity is similar both on the external surface and on the internal crystal section. The distribution of the metals deriving from the guests is clearly visible in Figure 3.4.b-c. Also the line scan, carried out on the internal crystal section of two crystals of PCN-6'@NiL and PCN-6'@NiFeL gave a further confirmation of the uniformity of the guest distribution (see Experimental Part).

EDS elemental ratios give a precise hint on the amount of trapped complex and on its integrity. The S/Ni ratio found was very close to the 2:1 ratio expected for the intact complex: 2.4 for NiL and 2.2 for NiFeL respectively. Furthermore, based on the Cu/Ni ratio established by EDS analysis, it is possible to evaluate the avereage number of complexes encapsulated for each PCN-6' cavity.

Each pore of PCN-6′ is in fact composed by 12 copper paddle-wheel units, for a total of 24 copper atoms. Considering that the half of this Cu atoms is shared with the neighbouring cavities, internal walls of a single pore are decorated by 12 Cu atoms. The EDS analysis conducted on PCN-6'@NiL furnished a Cu/Ni ≅ 7, coherent with the trapping of 2 NiL entities for cavity. The EDS mesaurement conducted on PCN-6'@NiFeL furnished instead a Cu/Ni ≅ 13 congruent with 1 NiFeL molecule for each pore. The EDS metal ratios have been compared with the same values obtained by ICP analysis: a good fit is observed, as displayed in Figure 3.5. Here the amount of copper is normalized to 100, and the amounts of the other metals are reported accordingly.

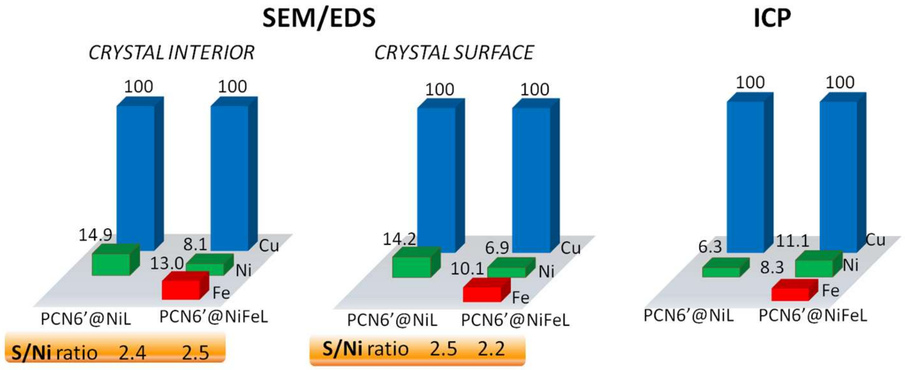

Figure 3.5 Comparison of the metal ratios determined with SEM/EDS and ICP analysis for PCN-6'@NiL and PCN-6' NiFeL

Afterwards, PCN-6'@NiL and PCN-6'@NiFeL were digested by treatment with a mixture of TFA-d/ DMSO-d. In both cases, the crystals dissolution was associated to the degradation of the host framework as well as that of the included complex. The resulting signals were are then related to free TATB and L (Figure 3.6).

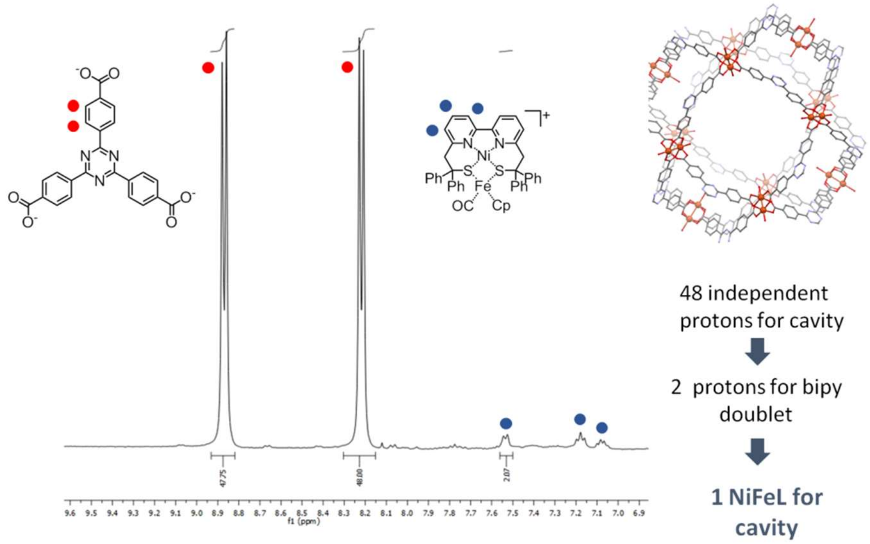

Figure 3.6: ^{1}H-NMR (400 MHz,TFA-d/DMSO-d) of PCN-6’@ NiFeL

From the integration areas of the signals belonging to TATB (the two doublets corresponding to the benzoate protons centred at about 8.9 and 8.2 ppm, Figure 3.6) and belonging to bipy ligand L (signals in the interval 7.6-7.0 ppm, Figure 3.6), an estimation of the number of NiFeL molecules for each MOF pore is then feasible. Assigning a normalized value of 48 protons to the area corresponding to each TATB signal (equivalent to the number of TATB protons which can be counted for each PCN-6′ cavity), the doublet at 7.55 ppm, associated to the two bipy protons adjacent to the N atoms, assumes a value exactly equal to 2, thus pointing out the presence of a single guest molecule for each pore. This value is in agreement with the Cu/Ni ratio obtained by EDS and ICP quantification. Unfortunately, digestion of PCN-6′@NiL in a mixture of TFA-d and DMSO-d led to very broad NMR signals, which do not allow a precise quantification of the host-guest ratio.

3.2.2 X-ray diffraction analysis

The nanoconfinement of Ni-containing complexes is associated with crystal chromatic variation, similarly to the behaviour observed for the trapping of nicotine. Once removed from the soaking solution, the loaded crystals present a blue colour, deeper with respect to the one which features the crystals of activated PCN-6’. Colour change becomes more pronounced after a short period of exposure to air: the crystals turn to deep green, colour which indicates the trapping of the Ni-complex (Figure 3.7).

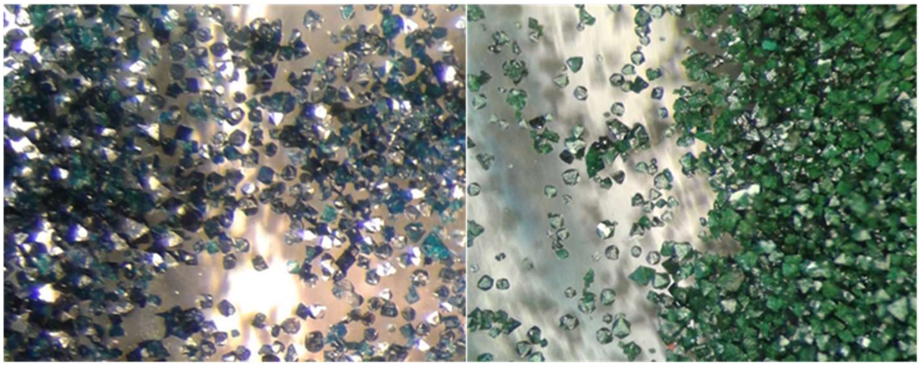

Figure 3.7 Optical microscope images of: PCN-6’@NiFeL from soaking solution (left) and air-exposed crystals of PCN-6’@NiFeL (right)

Loaded crystals were subjected to X-ray diffraction experiment by means of synchrotron light radiation (see experimental). From the analysis of the diffraction immages it was possible to confirm the integrity of the framework of PCN-6’ (Figure 3.8).

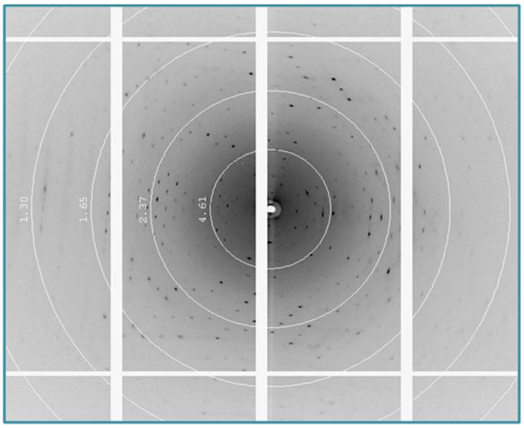

Reported in literature
a=b=c= 46.636(5) Å
α=β=γ=90°
Laue Class 2/m-3
*F*m-3-m, T =250K

Experimental data
a=b=c= 45.762(1) Å
α=β=γ=90°
Laue Class 2/m-3
F-lattice, T = 100K

Figure 3.8: Diffraction image of PCN-6’@NiFeL collected by synchroton radiation

Disappointingly, it was not possible to perform a structural refinement of the electron density map belonging to the trapped complex. The structural characterization is indeed hampered by the disorder of the guest and the solvent molecules (dichloromethane used for the soaking) confined in the cavities: differently from PCN-6’@nicotine, where the nicotine molecule is coordinated to the copper centres, PCN-6′@NiL and PCN-6′@NiFeL showed a random distribution of the encapsulated molecules, producing a liquid-like packing. Then, the high electron density deriving from the guest is splitted accordingly to the high symmetry of the cavities: all these factors inhibited a rigorous modelling of the confined guest complex.

3.2.3 Cyclic voltammetry

After having confirmed the accomplishment of the applied loading protocol and having defined the amount of trapped guest, the new material PCN-6′@NiFeL was tested as electrocatalyst for the proton reduction.

Then, PCN-6′@NiFeL was deposited on glassy carbon (GC) electrode (3 mm diameter) *via* drop casting technique, using a dichloromethane/PCN-6′@NiFeL suspension, which after deposition on the electrode, was allowed to evaporate overnight. A sufficiently stable suspension was obtained by sonication of a mixture of dichloromethane and PCN-6′@NiFeL for 5 minutes.

As expected, the CV experiments confirmed the red-ox activity of the host polymer: in the corresponding voltammogram a wave at -2.5 V related to the reduction of Cu(II) to Cu(I) was present, which brought to the collapse of the MOF net and consequently to a significant decrease of the current already after the 1st CV cycle (Figure 3.9).

Analogous degradation under application of a DC potential was described for HKUST [133]: under electrophoretic conditions the complete degradation of the crystals was observed. Further studies described a stepwise reduction of the parent Cu(II) into Cu(I) and formation of copper metal, as evidenced by TEM imaging. Formation of holes on the crystal surface and deposition of metallic copper was then observed.[134,135] The same behaviour can then be envisaged for

PCN-6′@NiFeL under CV conditions. For this reason PCN-6′@NiFeL was not further investigated.

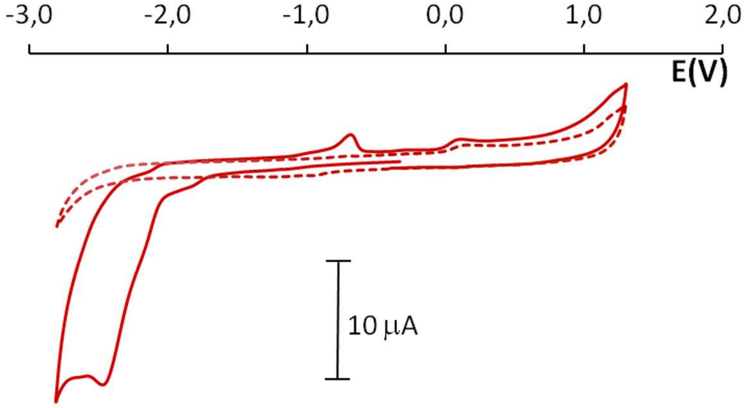

Figure 3.9 Cyclic Voltammetry performed with a GC electrode functionalized with PCN-6′@NiFeL. The first CV cycle corresponds to the solid line, while the second CV cycle corresponds to the dotted line. In this case the absence of signal is due to MOF degradation**.**

3.3 PCN-777: a well suited host

PCN-777 was synthesized according to the procedure reported by Zhou [136]: TATB linker and $ZrOCl_2{\cdot}8H_2O$ were dissolved in DMF and heated at 120°C, using TFA as acid modulator. PCN-777 was isolated as a very fine white powder by centrifugation and washed with DMF (4 times) and acetone (3 times). XRPD confirmed the purity of the phase obtained (see Supplementary Materials for further details).

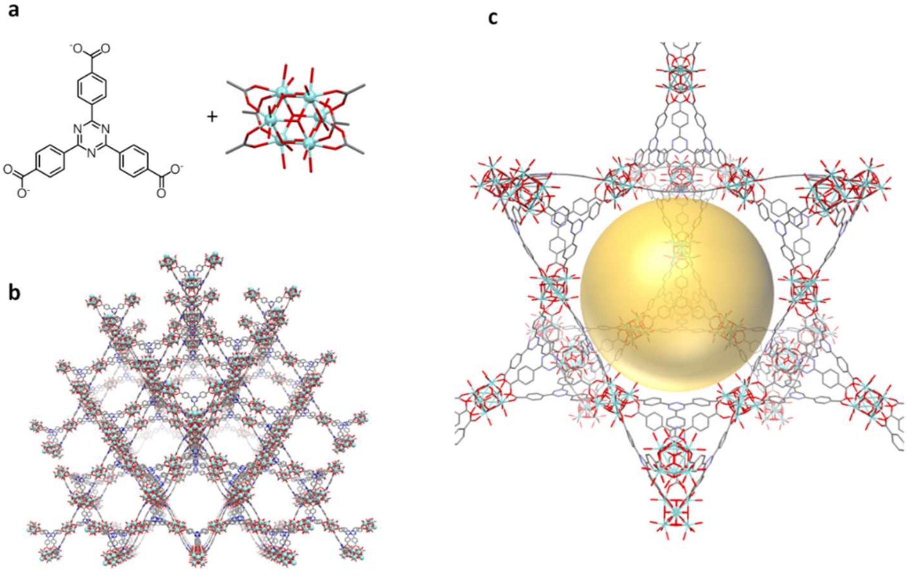

Figure 3.10 a)TATB ligand and Zr_6 cluster of PCN-777; b) PCN-777 framework; c) PCN-777 pore, average sphere diameter 38 Å

PCN-777 network is generated from the combination of tritopic TATB ligands and octahedral hexanuclear clusters of Zr(IV), as shown in Figure 3.10. The resulting overall formula is

$Zr_6(O)_4(OH)_{10}(H_2O)_6(TATB)_2$: each Zr(IV) cluster is coordinated by 6 carboxylates : Zr coordination sphere is completed by pending water and hydroxyl groups. PCN-777 exhibits the largest pore (∅= 38 Å) among zirconium-based MOFs, as shown in Figure 3.10.

In this case, a structural resolution from single crystal X-ray diffraction analysis is not possible owing to the very small size of the crystals (~nm dimensions). Despite this drawback, the host system presents several advantages with respect to PCN-6′. PCN-777 shows a higher chemical stability, starting form thermal proprieties: decarboxylation occurred at 330°C. In addition, Zhou reported that MOF is stable in water and also in acid (pH=3) and basic (pH=11) solution media. This behaviour is very rare for a mesoporous MOF and could be a great advantage for possible electrochemical applications. Authors outlined that this excellent stability can be explained by strong electrostatic interactions between the high positive charge density of Zr(IV) nodes and the negative charged TATB carboxylates. An additional key feature is the redox *inertia* of the Zr(IV) metal centres: differently from redox active Cu(II) present in PCN-6′, metal clusters of PCN-777 are not subjected to undesired redox processes during catalysis.

PCN-777 was thermally activated, by heating at 140°C at $5 \cdot 10^{-5}$ atm for 7 hours and effectiveness of the solvent removal was checked by DSC measurement. Then, the evacuated microcrystals were soaked in CH_2Cl_2 solutions of NiL and NiFeL, 4.0 mM and 2.6 mM respectively. After 1 week, the solutions were removed and the solids washed several times with dichloromethane. In comparison with pristine PCN-

777, the soaked samples clearly presented a peculiar colour change (as shown in Figure 3.11): brownish for PCN-777@NiFeL and light brown for PCN-777@NiL.

Figure 3.11 Left: native PCN-777; Middle: PCN-777@NiFeL; Right: PCN-777@NiL

The loading process was conveniently monitored by UV-Vis spectroscopy (Figure 3.12) following the diminishing of the concentration of the guest in the soaking solutions with time: after 88 hours, in the case of PCN-777@NiL, the absorbance of the surnatant solution was halved with respect to the starting one. Then, a constant but significant decreasing of the absorbance was observed during the next week. A different behaviour was instead observed with PCN-777@NiFeL. In fact, after 88 hours the absorbance of the surnatant solution was practically zeroed, observation that clearly points out a higher affinity of PCN-777 upon NiFeL uptake. This can be explained by the cooperative effects of both electrostatic and H-bond interactions. NiFeL complex bears an overall positive charge which can interact both with MOF carboxylates (negatively charged) or with aromatic rings of

TATB ligands (cation-π interaction). Moreover, the octahedral Zr_6-cluster is coordinated to several water molecules: these donor sites could be involved stabylizing intermolecular H-bond conctacts of the type Fe-CO···H-O.

IR measurements do not supply any useful information for PCN-777@NiL, with no significant variation with respect to the starting material. Instead, CO moiety linked to iron centre of NiFeL complex is a valid IR-probe of the occured encapsulation: loaded MOF reveals a diagnostic peak at 1939 cm^{-1}, with a frequence comparable to the observed with free NiFeL (1929 cm^{-1}).

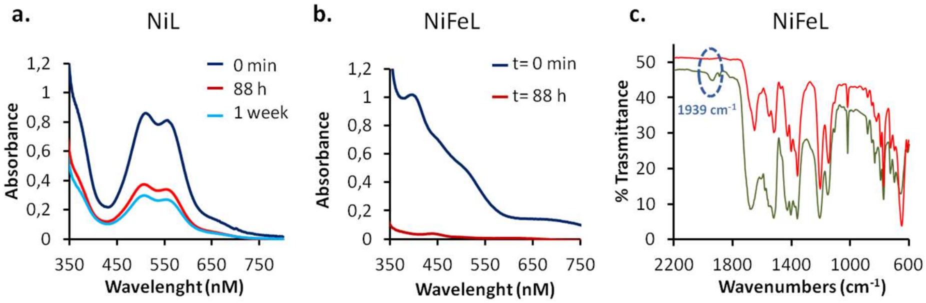

Figure 3.12 a) UV-VIS spectra of the NiL solution covering the microcrystals of PCN-777 after different soaking times ; b) UV-VIS spectra of NiFeL solution covering the microcrystals of PCN-777 after different soaking times; c) superimposition of the ATR spectrum of pristine PCN-777 (red trace) with IR spectrum (KBr pellet) of PCN-777@NiFeL (green curve).

Freeze-pump-thaw method turned out to be a more efficient and faster method for NiFeL trapping inside PCN-777 with respect to classical soaking strategy previously described. The general freeze-pump-thaw protocol involved the initial soaking of activated PCN-777 into a 10 mM NiFeL dichloromethane solution. Then, dynamic vacuum was applied for 15 minutes, followed by a final thawing under static vacuum (see Experimental Part for additional details). The main advantage of this approach is to promote the gas desorption from PCN-777 pores and thus favouring the guest entrance and diffusion.

Because of the more satisfying characterization data, we decided to focus our attention on PCN-777@NiFeL, the most promising system for host-guest chemistry.

Owing to the diamagnetic character of Zr(IV), it was possible to confirm the guest loading also by SS-NMR investigations (Figure 3.13).

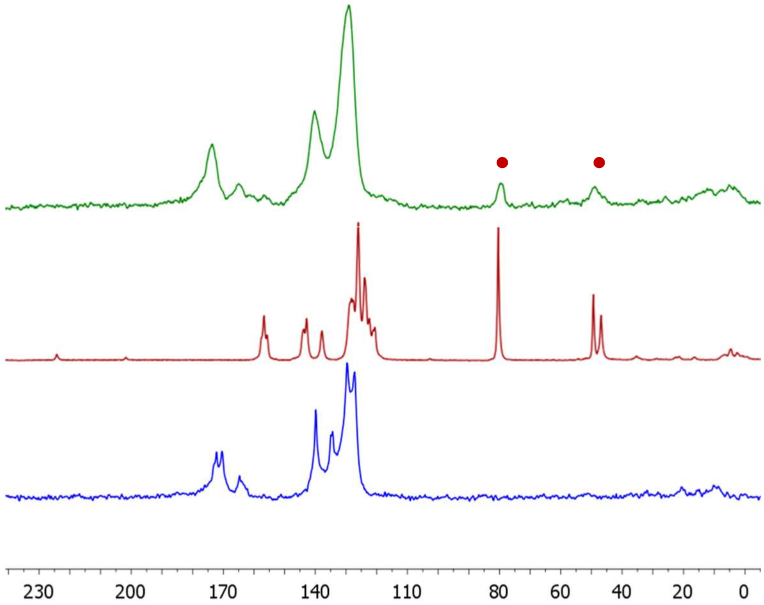

Figure 3.13: ^{13}C CP-MAS(12 kHz) NMR of NiFeL (red), pristine PCN-777 (blue) and PCN-777@ NiFeL (green)

^{13}C CP-MAS NMR of PCN-777@NiFeL provides strong evidences of the occurred inclusion: the aliphatic region of the spectrum is indeed characterized by peaks belonging to the CH_2 (80 ppm) and Cp (50 ppm) groups, which can be attributed to the encapsulated NiFeL complex. These signals are completely absent in the spectrum of pristine PCN-777, while are clearly visible in the spectrum of NiFeL.

As expected, a large decrease of the porosity, which was determined by N_2 sorption at 77 K (Figure 3.14).

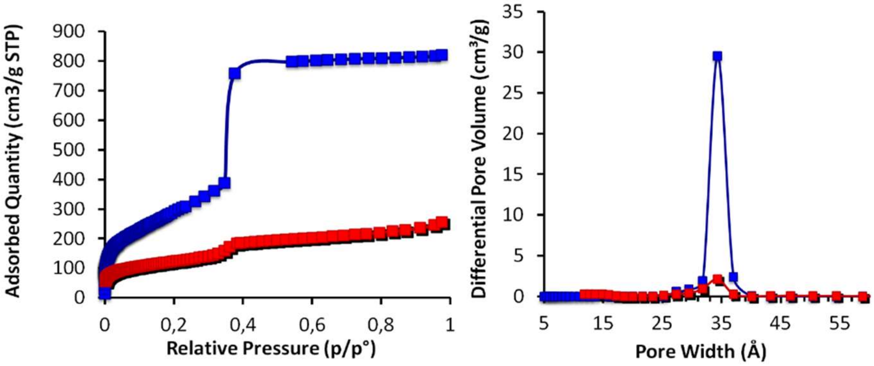

Figure 3.14: Left) N_2 adsorption isotherms recorded at 77 K up to 1 bar for: pristine PCN-777 (blue curve) and PCN-777@NiFeL (red curve); Right) pore size distribution for pristine PCN-777 (blue) and PCN-777@NiFeL (red).

Pristine PCN-777 showed a Type-IV[137] sorption behaviour, typical of mesoporous materials and an uptake of around 800 cm^3/g at 1 bar. The experimental Brunauer–Emmett–Teller (BET) surface area of PCN-777 is 1016,53 m^2/g. Then, we measured the porosity of PCN-777@NiFeL, calculating a BET surface equal to 439,29 m^2/g. This experimental evidence assesses that about a 60% of the starting pore volume is filled with NiFeL complexes.

A consistent decrease in the percentage of distribution of the pore volume at 34 Å, as furnished in figure 3.14, further confirmed that the majority of PCN-777 pores are occupied by NiFeL complex.

EDS mapping conducted on PCN-777@NiFeL shows a homogenous guest trapping: maps distributions of Zr, Ni and Fe in a solid sample of PCN-777@NiFeL are furnished in Figure 3.15.

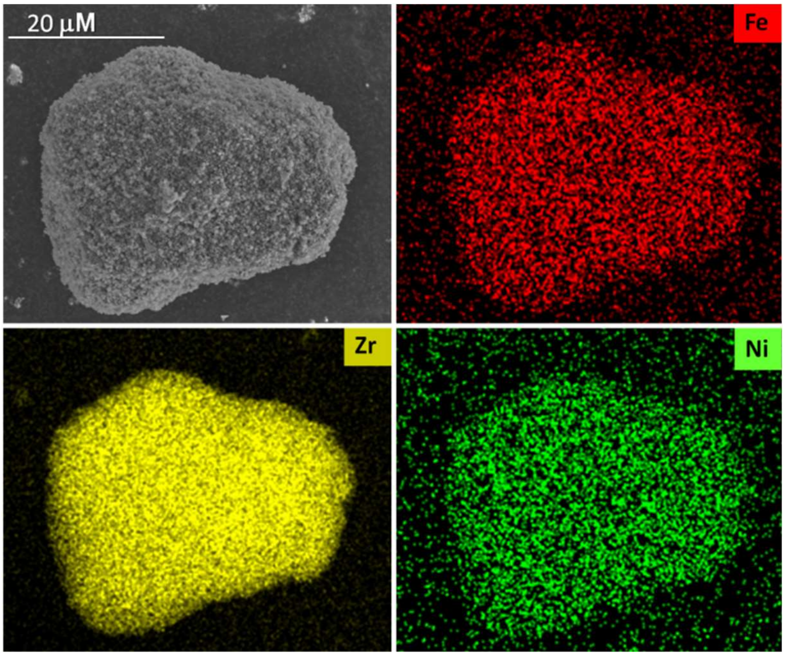

Figure 3.15 SEM image (top left) and EDS maps of PCN-777@NiFeL bulky nanocrystals.

Differently from PCN-6′@NiFeL, the microcrystalline nature of the sample does not allow to conduct the SEM-EDS analysis on a single crystal. However, the analysis performed on the bulk microcrystalline sample indicate a highly homogeneous distribution of intact NiFeL. In fact, the S/Ni average ratio of 1.9 obtained by microanalysis is in agreement with the integrity of the trapped complex (Figure 3.16).

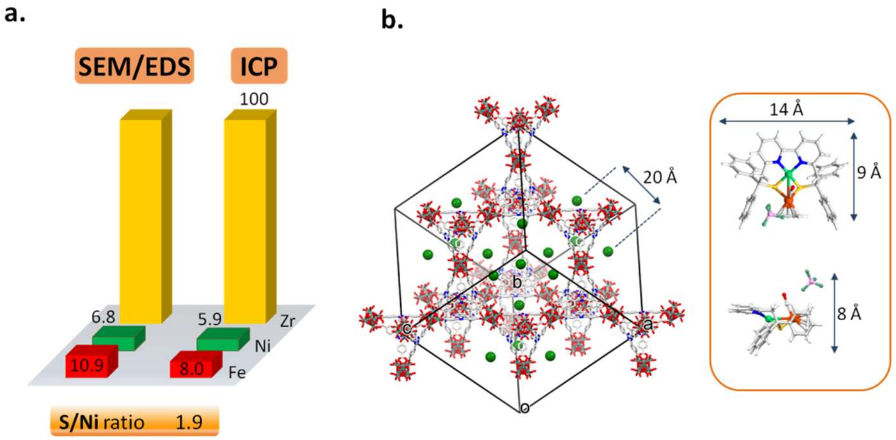

Figure 3.16: a) comparison between ICP and EDS quantifications for PCN-777@NiFeL; b) unit cell of PCN-777 with calculated cavities centroids, and NiFeL dimensions measured by X-ray crystal structure.

The Zr/Ni, Ni/Fe and Zr/Fe ratios found by ESEM-EDS analysis are in good agreement with the same ratios calculated from ICP analysis, as displayed in Figure 3.16.a. From the Zr/Ni and Zr/Fe average ratios, we can estimate how many guest molecules were encapsulated in each unit cell of PCN-777. PCN-777 unit cell comprises 16 Zr_6 clusters, which correspond to 96 Zr atoms: from Ni/Fe value we can extimate 8-10 NiFeL complex molecules per unit cell. Considering that in PCN-777 the cavities are more interconnected than in PCN-6′, calculating the centroids of the pores by Mercury[138] it was possible to locate 16 centroids/cell, spaced by ~20 Å. As outlined in Figure 3.16.b, the CH···CH distance between opposite phenyl rings of NiFeL is ~14Å. Hence, we can assume approximatively one NiFeL molecule per centroid. From this considerations, it is resonable to suppose that 10 of the 16 centroid positions can be occupied by NiFeL complexes, in agreement with the partial occupancy established by pore dustribution analysis (previously shown in Figure 3.14).

3.3.1 Thin film deposition on conductive glasses

In the past few years, for electrocatalytic purposes, several efforts have been directed towards the growth of homogenous MOF thin films over solid surfaces.[139] In principle, functionalization of conductive glasses, such as FTO (fluorine doped tin oxide) and ITO (indium tin oxide), with MOF films could pave the way for future applications in electronic devices, such as sensors or electrodes. Compared to the drop-casting technique, thin film deposition is related to several advantages, in particular it brings to a wider and more homogenous surface coverage, allowing at the same time a higher control on the film thickness. Furthermore, it should be recalled that the optimization of film thickness proves to be fundamental for electrocatalys: too thick layers are related to a substantial lack of conductivity.

Ott and Cohen recently reported a “bottom-up” approach to gain MOF films on conductive glasses: a solvothermal strategy was employed for the thin film growth of UiO-66[140] on FTO glasses.[141] The described protocol requires a initial soaking of the activated FTO in a solution of carboxylic linkers (1 mM, DMF) to generate a self-assembled monolayer (SAM) of MOF ligands. The SAM-decorated FTO is then added to a mixture of metal salt, organic linkers and acid modulator to obtain the final MOF films within 24 hours, under solvothermal conditions.

Similarly, Hupp described the deposition of FTO-NU-1000 films, subsequently used for the synthesis of NiS-NU-1000 hybrid material for hydrogen evolution.[142] However, in our hand this protocol proved to be unsuccessful for the deposition of high quality films of PCN-777: different concentrations of both ligand and metal salt were tested but highly irregular MOF depositions were always obtained (see Experimental Part for details).

Hence, we decided to exploit electrophoretic deposition (EPD) as an alternative approach, as proposed by Hupp *et al.*[143] Authors used a top-down pathway to achieve the film coating: thin films of NU-1000, UiO-66, MIL-53 and HKUST were obtained through the application of a DC electric field to a MOF suspension in a non-polar solvent, like toluene.

We considered two alternative routes to obtain PCN-777@NiFeL films:

- EPD of PCN-777, followed by activation and soaking in a NiFeL solution
- EPD of PCN-777@NiFeL

EPD of PCN-777 followed by activation and soaking in a NiFeL containing solution

In Figure 3.17, the results obtained with the EPD of activated PCN-777 for 90 minutes are provided. Despite an apparent film homogeneity observed by optical microscopy (Figure 3.17.a), ESEM analysis points out only a partial functionalization of FTO surface with large areas still exposed (Figure 3.17.b). This problem was overcome with longer deposition times (up to 5 hours) which brought to a complete surface covering.

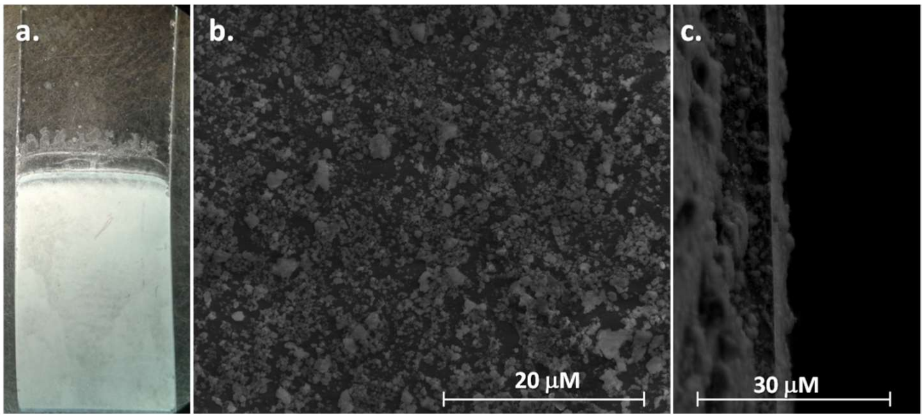

Figure 3.17. a) optical microscope image of PCN-777 film; b) SEM image of thin film; c) cross sectional image of PCN-777 thin film on FTO glass

No variation of microcrystallite morphology was observed with respect to bulky PCN-777. Cross-sectional ESEM image displays an average film thickness of 3 μm, a promising value from electrochemical applications (Figure 3.17.c).[141] Thereafter, the film obtained with this EPD pathway was washed several times with acetone and dried at 140 °C under vacuum ($5\cdot10^{-5}$ Torr). The activated film was subjected to freeze-thaw-pump technique with a dichloromethane solution of NiFeL (5.0 mM). Unfortunately, this method is associated with the mechanical removal of PCN-777 film from FTO glasses.

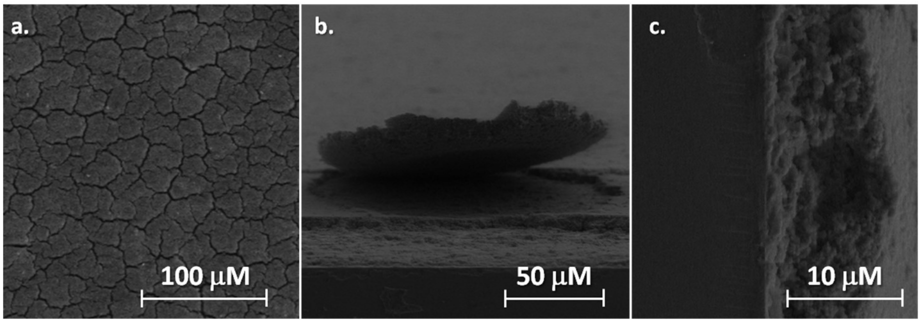

Figure 3.18 PCN-777@NiFeL deposited on FTO glass after the activation process and soaking: film cracking (a) and partial detachment of a portion of PCN-777 film (b); cross sectional image showing film thickness (c).

The loading was then attempted with classical soaking conditions, using a 5.0 mM dichloromethane solution of NiFeL for 72 hours. However, SEM imaging revealed an extensive film cracking, as shown in Figure 3.18.a. Activation conditions proved to be too harsh for the preservation of a complete film integrity. Furthermore, a partial film detachment from FTO surface was detected as shown in Figure 3.18.b. This phenomenon would seriously compromises the conductivity of the final film and the related electrochemical activity. An additional problem was the irregularity of the film thickness, ranging from 2 to 10 µm, depending on the spotted area. All these features combined with a lower NiFeL loading, as outlined by EDS measurement, led us to focus our attention on the second approach, described in the following paragraph.

EPD on PCN-777@NiFeL

At first, also the optimization of EPD approach on already loaded MOF proved to be tricky for several reasons, especially concerning the reproducibility and maintenance of PCN-777@NiFeL suspension for a sufficient period of time to gain a final good quality film. (see the Experimental Part for details). However, after optimization, it was possible to obtain good quality films. Best results were obtained from 180 minutes electrophoretic deposition. SEM imaging exhibited a low aspect ratio crystal morphology, as shown below in Figure 3.19.a.

This feature is also reported in literature for other Zr-based MOFs, like UiO-66.

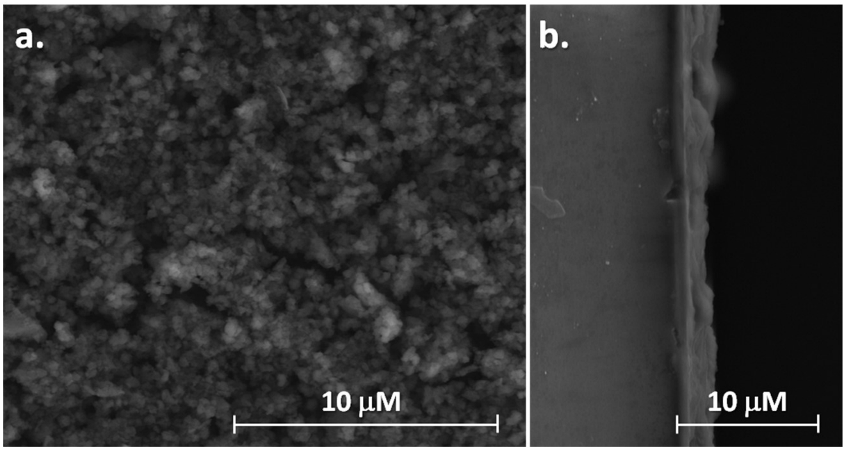

Figure 3.19. SEM images of PCN-777@NiFeL thin film after 180 minutes of EPD: crystal morphologies (a), and cross sectional image showing film thickness (b).

FTO decorated area (1,5 x 0,9 cm) is characterized by a homogenous coverage of glass surface, without cracking or residual exposed zones. Film thickness was estimated to be 2 μm by cross-sectional ESEM image (Figure 3.19.b.)

3.4 Electrochemical measurements

3.4.1 Drop casting on GC electrodes

Initially, we recorded the cyclic voltammetry (CV) of a MeCN 0.1 M $TBAClO_4$ solution by using a glassy carbon (GC) working electrode, previously modified by drop casting of a suspension of PCN-777@NiFeL in toluene.

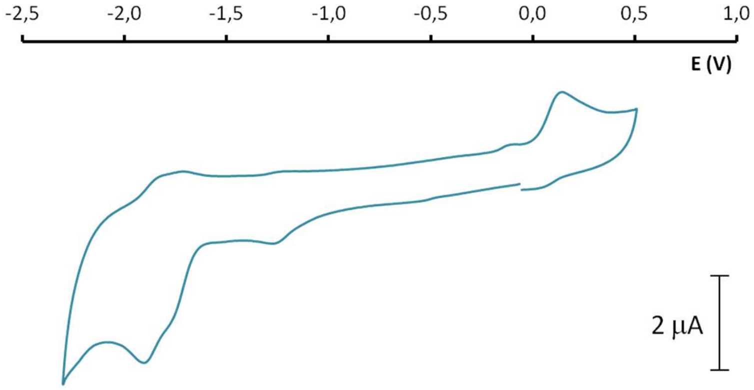

Figure 3.20: CV trace of PCN-777@NiFeL drop-casted on a GC working electrode in CH_3CN 0.1 M $TBAClO_4$

The analysis pointed out two different reduction systems (Figure 3.20): the first one at -1.3 V (Ag/Ag^+ 0.01 M in MeCN) corresponds to the red-ox process Ni(II)Fe(II) → Ni(I)Fe(II). Then, the second wave at -1.9 V corresponds to the reduction process Ni(I)Fe(II) → $L^{radical}$Ni(I)Fe(II). The same reduction processes were observed for the free guest, NiFeL, in MeCN solution (Figure 3.1). This confirms that NiFeL maintains its redox properties once incorporated into PCN-777. It should be noted that the second red-ox phenomenon displays a much greater intensity than the one characteristic of free NiFeL. This behaviour could be attributed to the reduction of water molecules trapped inside the MOF cavities. Then, we repeated CV measurements with different concentrations of Et_3NHBF_4 as weak acid, ranging from 1.0 mM to 5.0 mM ($TBAClO_4$, CH_3CN 0.1 M solution) as shown in Figure 3.21.

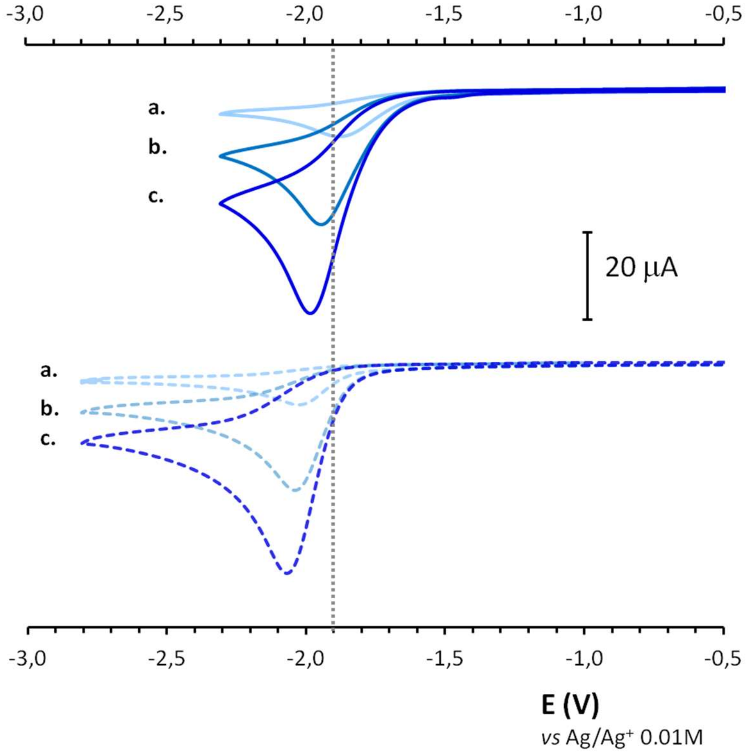

Figure 3.21 Comparison between GC-PCN-777@NiFeL (solid lines) and bare GC electrodes as reference (dotted curves) in CH_3CN 0.1 M $TBAClO_4$ with different Et_3NHBF_4 concentrations: a) 1.0 mM, b) 3.0 mM, c) 5.0 mM

A clear shift to lower potential values of the band associated with the second reduction was observed when PCN-777@NiFeL functionalized electrode was employed, compared to the bare GC electrode. Encouraged by this preliminary results we decided to optimize the electrode deposition protocol. Drop casting method is very simple and fast but presents several drawbacks. Thickness and uniformity of the resulting deposition are hard to control, and deposition is only possible for a limited coverage area. For these reasons we moved our attention to PCN-777@NiFeL deposited on conductive glasses (obtained as described in the previous paragraph, page 75).

3.4.2 Deposition on conductive glasses

Cyclic voltammetry was recorded on FTO/PCN-777@NiFeL thin films, employing a tetrabutylammonium terafluoroborate 0.1 M solution in CH_3CN. Performing repeated scans, a progressive lowering of signal is observed, together with a complete disappearing of the characteristic waves after 20 CV cycles. A possible mechanical film detachment was excluded , since the FTO-coating remained visibly unaltered after the CV experiment. An additional proof of the film integrity was provided by morphological SEM-analysis performed after the electrochemical tests. Hence, this lability is analogous to the one of the free NiFeL in the absence of a proton sourcen(Figure 3.22): after the double reduction processes, the complex is reduced to $L^{radical}$Ni(I)Fe(II), with strong radical features which cannot be stabilized through simply host-guest interactions.

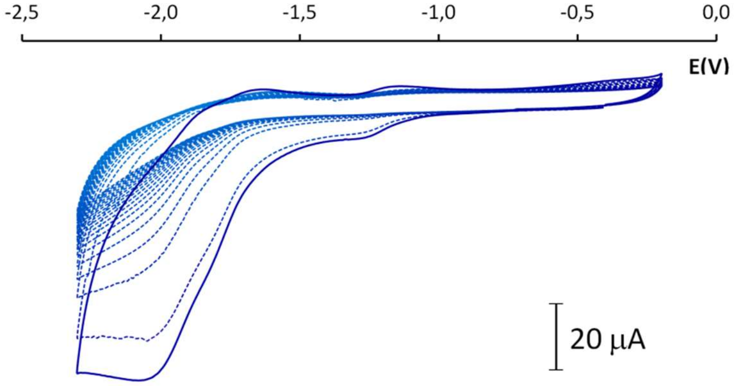

Figure 3.22: CV on FTO-PCN-777@NiFeL film (solid line) and subsequent 20 CV cycles (dotted lines) performed in acetonitrile in the presence of $TBABF_4$ (0.1 M) and in the absence of protic sources. Potential values are referred to Ag/Ag^+ 0.01 M in MeCN.

Hence, we evaluated the film performance for proton reduction. For this purpose, the weak acid $(Et)_3NH^+ BF_4^-$ (pk_a = 18.6 in CH_3CN)[144] was first used as proton source. Bare FTO glasses were used as references. Results are illustrated in Figure 3.23.

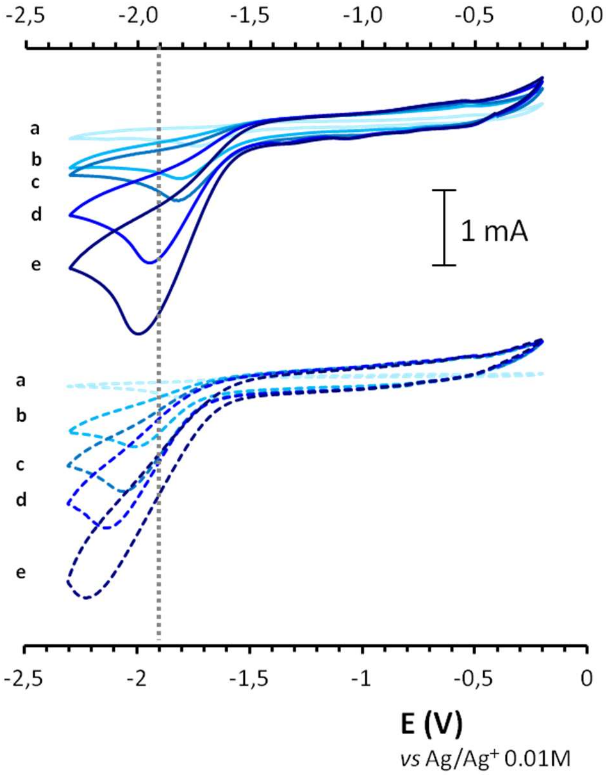

Figure 3.23 Comparison between FTO-PCN-777@NiFeL (solid lines) and bare FTO electrodes as references (dotted curves) in CH_3CN 0.1 M $TBABF_4$ with different Et_3NHBF_4 concentrations: a) 0.5 mM, b) 1.0 mM, c) 2.0 mM; d) 3.0 mM, e) 5.0 mM.

PCN-777@NiFeL coating shows a significant catalytic activity upon the addition of Et_3NHBF_4. As in the corresponding homogeneous system, under weak acid conditions we observed an electrocatalytic effect on the second reversible reduction wave (E_{cat}=2.0 V *versus* Ag/Ag^+).

Subsequently, we investigated the catalytic behaviour of the functionalized film under strong acidic conditions, by replacing $(Et)_3NHBF_4$ with $HBF_4 \cdot Et_2O$ (pKa= 0.1 in CH_3CN).[144] Also in this case, the FTO coverage is associated with a slight shift to less negative values of the proton reduction potential (Figure 3.24).

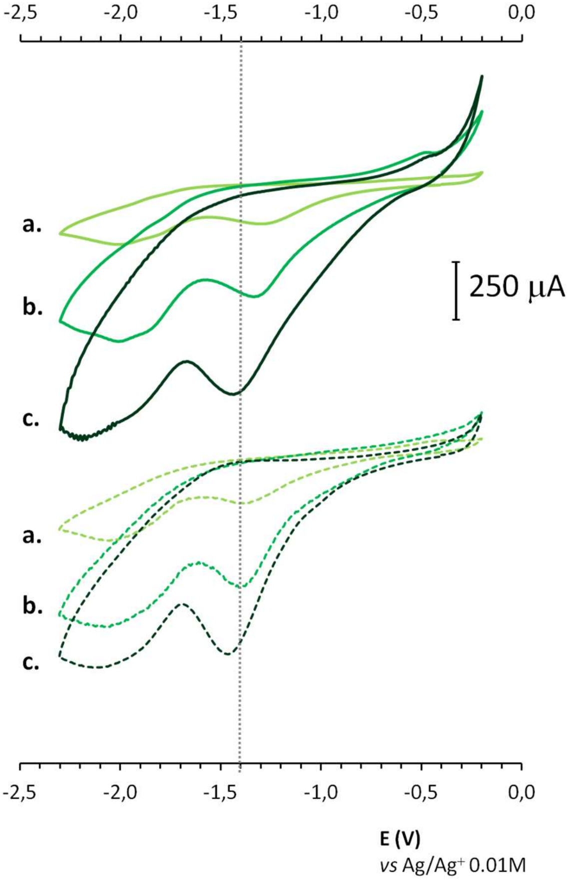

Figure 3.24 Comparison between FTO/PCN-777@NiFeL (solid lines) and bare FTO electrodes as references (dotted curves) in CH_3CN 0.1 M $TBABF_4$ with different HBF_4 concentrations: a) 0.5 mM, b) 1.0 mM, c) 2.0 mM.

Differently from weak acid working conditions, in this case it was possible to perform catalysis on the first reduction wave (-1.3 V).

Chronoamperometric experiments were performed on FTO-PCN-777@NiFeL in weak acid solution (acetonitrile 5.0 mM Et_3NHBF_4), working at -1.8 V for a period of 1000 sec. Results are plotted in Figure 3.25: increase of the current and of the charge flow are was revealed, in agreement with an electrocatalytic effect of PCN-777@NiFeL.

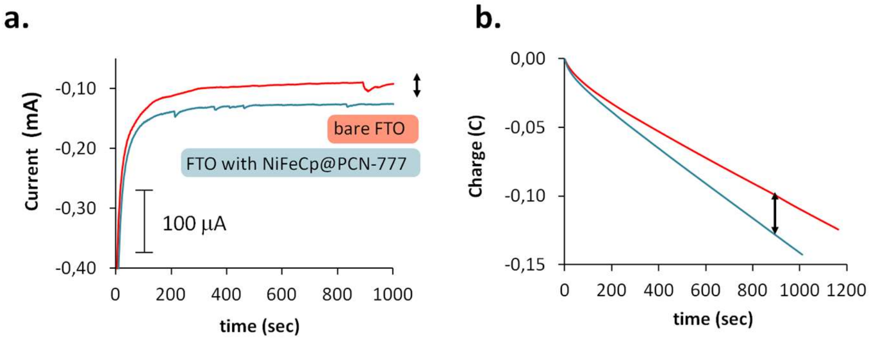

Figure 3.25 Weak acid conditions: comparison of current (a) and charge flow (b) with FTO-PCN-777@NiFeL (blue lines) and bare FTO glass as reference (red lines).

An analogous experiment was performed on FTO/PCN-777@NiFeL under strong acidic conditions (acetonitrile 2.0 mM $HBF_4{\cdot}Et_2O$) for a period of 1000 sec. The working potential was set at -1.2 V, corresponding to first wave reduction potential. Also in this case a slightly difference in current and charge intensity hints a catalytic effect of PCN-777@NiFeL film (Figure 3.26).

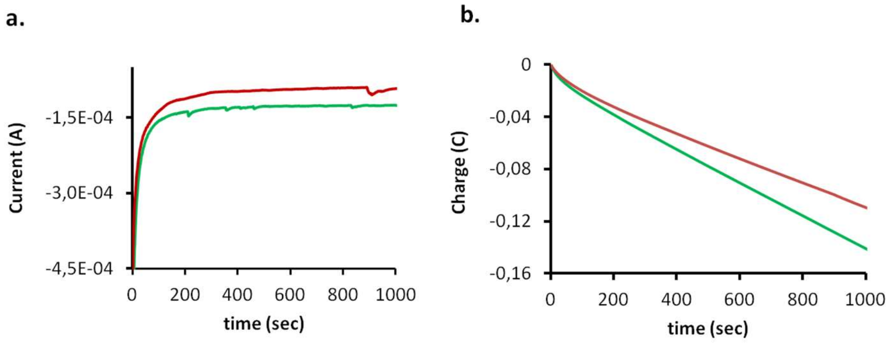

Figure 3.26 Strong acid condition: comparison of current (a) and charge flow (b) with FTO-PCN-777@NiFeL (green lines) and bare FTO glass as reference (red lines).

3.5 Experimental Part

General Methods

The NMR spectra were recorded on 400 MHz or 300 MHz Bruker instruments. The samples were digested in TFA-*d* (complete dissolution). Infrared Spectroscopy (ATR) were obtained with a Thermo Scientific Nicolet 5PCFT-ATR spectrophotometer, equipped with diamond or ZnSe crystal (4000-500 cm^{-1} interval).

Differential Scanning Calorimetry (DSC) was performed on a PerkinElmer DSC 6000 with a heating rate of 5°C min^{-1} in the temperature range from 25 to 445 °C. The samples (from 5 mg up to 12 mg) were sealed in a 50 µL aluminum pan. The measurement was performed at atmospheric pressure under a constant flow of nitrogen (20 mL min^{-1}).

Morphological analysis were conducted by an environmental scanning electron microscope (ESEM) Quanta^{TM} 250 FEG (FEI, Hillsboro, OR) equipped with an energy-dispersive spectrometer (EDS) for X-ray microanalysis (Bruker Nano GmbH, Berlin, Germany), operating with low-vacuum mode (70 Pa). ESPRIT 1.9 microanalysis software (Bruker Nano GmbH) was used for X-ray spectra acquisition and for digital element map. Morphological analysis were carried out with an accelerating voltage (HV) of 5.0 kV, while EDS analysis were conducted with a HV of 20.0 kV.

X-ray single crystal measurements were performed at *Elettra Sincrotrone* (Trieste, Italy) on beamline XRD1 at 100K under cold nitrogen flux. The source used for the analysis was a NdBFe Multipole Wiggler (Hybrid linear), 4.27 KeV with a power of 8.6 kW, a source size FWHM of 2.0 x 0.37 mm (0.7 x 0.2 mm FWHM beam size at sample) and photon flux 10^{12}-10^{13} ph/sec. Soaked PCN-6' crystals were taken directly from soaking dichloromethane solutions and mounted with cryoloops (0.05-0.3 mm).

Analysis of diffraction data and unit cell indexing were performed using CrysAlis software.[114]

Nitrogen adsorption-desorption isotherms at 77 K were performed using a Micromeritics analyzer ASAP 2020 HD up to 1 bar.

ICP-analysis were performed on ULTIMA 2 ICP-AES (HORIBA Jobin Yvon).

SS-NMR were recorded on Avance III 400 MHz Bruker equipped with a CP-MAS probe 4 mm BroadBand 1H / X(^{15}N - ^{31}P).

Electrochemical measurements were carried out in 0.1 M Bu_4NBF_4 MeCN solutions, under argon (glovebox) at room temperature, using a SP300 Bio-Logic potentiostat/galvanostat. A standard three electrode electrochemical cell was used for cyclic voltammetry experiments. Potentials were referred to an Ag/Ag^+, 0.01 M in MeCN reference electrode in MeCN +0.1 M Bu_4NBF_4. The working electrode was the FTO (fluorine doped tin oxide) glass covered with a film functionalized with PCN-777@NiFeL. The auxiliary electrode was a Pt wire in MeCN + 0.1 M Bu_4NBF_4 solution. A 0.5 M mother solution of Et_3NH^+ BF_4^- in acetonitrile (2 mL) was used for the stepwise additions of the weak acid, while a 0.5 M HBF_4 acetonitrile solution (2 mL) was employed for the stepwise addition of the strong acid. The additions were done by using a 100 μL Hamilton microsyringe.

PCN-6’ synthesis and activation

For synthesis details, see Experimental part of Chapter 2, page 46.

PCN-6’@NiL

All the loading procedures were performed under argon atmosphere (glovebox). Activated PCN-6’ sample (25 mg) was dipped in 4 mL of a NiL saturated dichloromethane solution (2.6 mM). The vial was tightly capped and PCN-6’ crystals were allowed to soak for 2 weeks. Then, the soaking solution was removed and the sample was quickly washed with dichloromethane (2 mL). PCN-6’@NiL was obtained as deep blue crystals, which turned to a deep green colour after a short period of air exposure.

PCN-6’@NiFeL

Crystals were loaded exploiting the same protocol applied for PCN-6’@NiL, with the only variation in the concentration of soaking solution: NiFeL 4 mM in dichloromethane. PCN-6’@NiFeL was obtained as deep blue crystals, which turned to a deep green colour after a short period of air exposure.

PCN-777 synthesis

In a 16 mL test tube, TATB (60 mg, 0.14 mmol), $ZrOCl_2 \cdot 8H_2O$ (200 mg, 1.12 mmol) were added to 12 mL DMF. Then, TFA (0.6 mL) was added as acid modulator and the resulting mixture was sonicated for 2 minutes. After having obtained a colourless solution, the tube was tightly capped and allowed to react under solvothermal condition at 120°C overnight. The very fine precipitate was washed with DMF (15 mL) for 4 times and centrifuged. Then other 3 washings with acetone (15 mL) were performed. After drying under vacuum PCN-777 was collected as a fine white powder.

Freeze pump thaw loading of NiFeL

200 mg of activated PCN-777 were placed in a 100 mL Schlenk flask under Ar flux. Then NiFeL (65 mg, 0.074 mmol) was dissolved in dichloromethane previously degassed in order to obtain a 10 mM solution: the resulting dark-brown solution was added to PCN-777. Then, the Schlenck flask was cooled with a liquid nitrogen bath, freezing the solvent. Then dynamic vacuum was applied for 15 minutes, followed by thawing under static vacuum for additional 15 minutes.

This cycle was repeated for 6 times, then the mixture was stirred at room temperature overnight .

Then the supernatant was decanted and PCN-777@NiFeL was separated from the solution. The resulting brown solid was washed with dichloromethane several times to remove completely the unloaded complex. PCN-777@NiFeL was collected by filtration on Millipore, and dried under vacuum to obtain a light brown homogeneous powder in quantitative yield.

FTO cleaning procedure A

Prior to functionalization, FTO glasses were washed with distilled water, ethanol and acetone under sonication (15 minutes per each solvent) and finally air dried.

FTO cleaning procedure B

An alternative cleaning procedure was the following (always under sonication):

- soapy water (soap/distilled water = 5/100 v:v), 15 min, T=30°C
- distilled water, 15 min, T=55°C
- ethanol, 15 min, T=40°C
- acetone, 15 min, T=40°C

Finally washed FTO glasses were air dried.

FILM deposition under solvothermal conditions

With the FTO glasses washed by procedure A, few attempts to deposit the active film by solvothermal procedure were carried out. The cleaned FTO glasses were dipped into a 1mM TATB solution in DMF (0.021 mmol of TATB dissolved in 20 mL of solvent) for 24 hours (the DMF solution was microfiltered prior soaking). After SAM procedure, the FTO glass was inserted in a 50 mL Schlenk tube containing a DMF solution (10 mL) of TATB (10 mg, 0.022 mmol) and $ZrOCl_2 \cdot 8H_2O$ (33 mg, 0.10 mmol) and TFA (0.1 mL) The tube was heated in an oil bath overnight at 120°C.

A second attempt was performed employing a fivefold higher concentration of the reagents and keeping the solvent volume constant: TATB (50 mg, 0.11 mmol), $ZrOCl_2 \cdot 8H_2O$ (166 mg, 0,93 mmol), TFA (0.5 mL).

EPD of pristine PCN-777

Activated PCN-777 (10 mg) was ground in an agate mortar under inert conditions (glove box), then the powder was added to a 20 mL capacity vial together with dry toluene (10 mL). The vial was capped with a septum and the resulting mixture was sonicated for 30 minutes, obtaining a homogenous suspension. The suspension was transferred by syringe into an EPD apparatus (previously degassed with Ar). Two identical FTO glasses (washed following the procedure B) were dipped in the suspension, with a separation distance of 0.7 cm. A constant voltage of 120 V was applied to the electrodes for 90 minutes.

EPD of PCN-777@NiFeL

A weighted amount of PCN-777@NiFeL (see Table 3.1) was transferred to a 20 mL glass vial and toluene was added. The resulting mixture was sonicated for 30 minutes, obtaining a homogenous suspension. The suspension was transferred by syringe into an EPD apparatus (previously degassed with Ar). Two identical FTO glasses (washed following the procedure A) were dipped in the suspension. A constant voltage of 120 V was applied to the electrodes for 90 minutes.

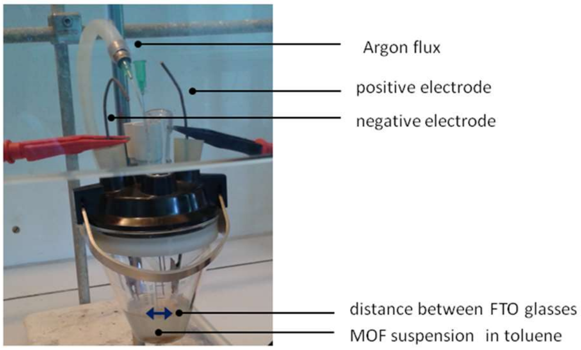

Figure 3.27 Apparatus for EPD experiments

The optimization of the deposition procedure was based on the variation of several parameters (see Table 3.1) and on the following experimental observations: Films obtained from the first EPD cycles were practically inactive. However, repeated EPD cycles on the same PCN-777@NiFeL suspension gave better results. A possible explanation could arise for the irregularity of the MOF granulometry, which is, in turn, affected by sonication time. However, a previous grinding of PCN-777@NiFeL did not lead to substantial improvements. Another issue derived from the limited stability of the suspension: within a few minutes the solid particles precipitated thus blocking the deposition process.

Entry	Cycle	Time	Distance	Other comments
1	1st [a]	3h 05min	0.7-0.8cm	toluene 20 mL / 10.1 mg MOF
2	2nd	3h 13min	0.7-0.8cm	Same suspension employed in entry 2
3	1st	3h 30min	0.7 cm	10 mL of toluene, 5.04 mg of MOF
4	2nd	3h 10min	0.7 cm	Same suspension of entry 3 No further sonication
5	1st	2h 5min	0.7 cm	10 mL of toluene, 5.04 mg of MOF
6	2nd	3h	0.7 cm	Same suspension of entry 5 No further sonication
7	3rd	2h	0.65 cm	Same suspension of entry 6 No further sonication,
8	1st	4h	0.65 cm	5 mL of toluene, 2.2 mg of MOF griound before sonication
9	1st	4h	0.7 cm	5.18 mg of MOF ground. 1h of sonication
10	2nd	3h	0.7 cm	Same suspension of entry 9
11	1st	2h	0.65-0.7 cm	5.1 mg MOF, sonicated for30 min
12	2nd	3h 30 min	0.65-0.7 cm	Same suspension of entry 11 (degassed for 10 minutes)
13	3rd	3h 45 min	0.7 cm	Same negative electrode and same suspension of entry 12

a) Suspension already used the for 2 unsuccessful EPD tests with ITO glasses.

b) EPD conditions that provided a good film deposition are highlighted in light blue

Table 3.1 Summary of EPD tests on PCN-777@NiFeL

3.6 Supplementary Materials

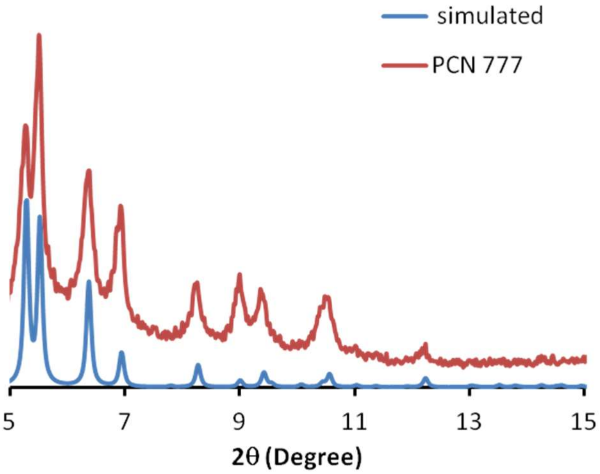

Figure 3.28 Overimposition of calculated and experimental PCN-777 xrpd patterns. PCN-777.

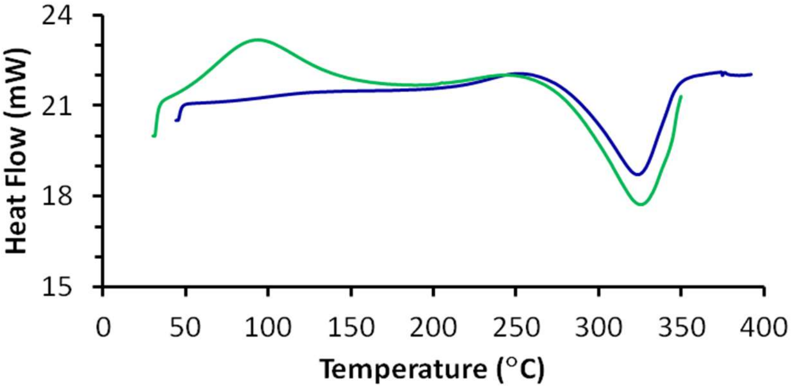

Figure 3.29 Comparison between DSC traces of PCN-777 (endo up): sample filtered and dried at 10^{-3} Torr at r.t (green curve) and after the heating at 140°C 10^{-5} atm (blue curve): the thermal activation leads to a complete removal of solvent.

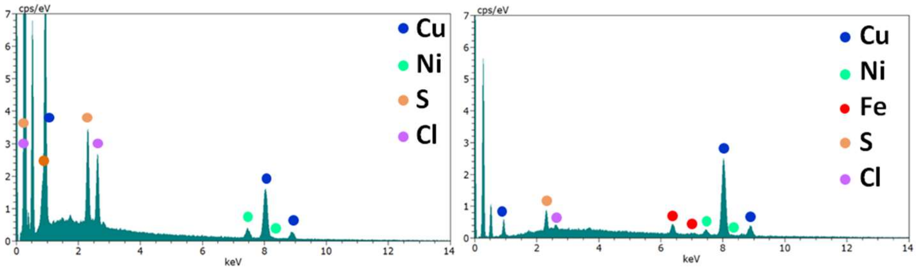

Figure 3.30 Left: EDS mapping of PCN-6’@NiL; Right: EDS mapping of PCN-6’@NiFeL

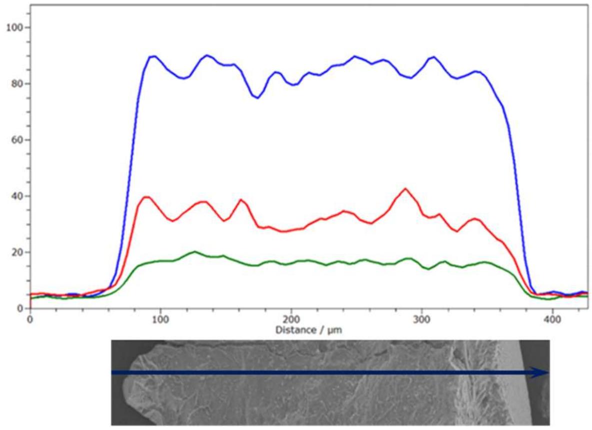

Figure 3.31 EDS line scan performed on the internal section of a PCN-6’@NiFeL crystal

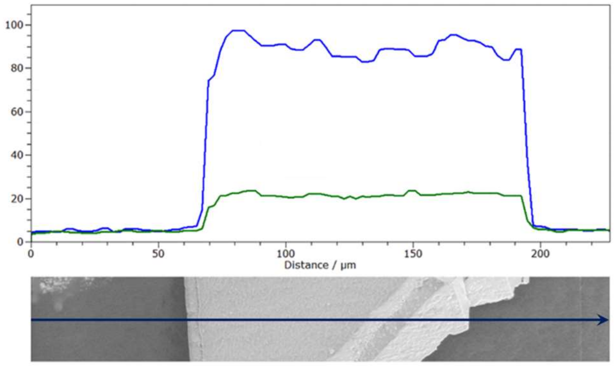

Figure 3.32 EDS line scan performed on the external surface of a PCN-6’@NiL crystal

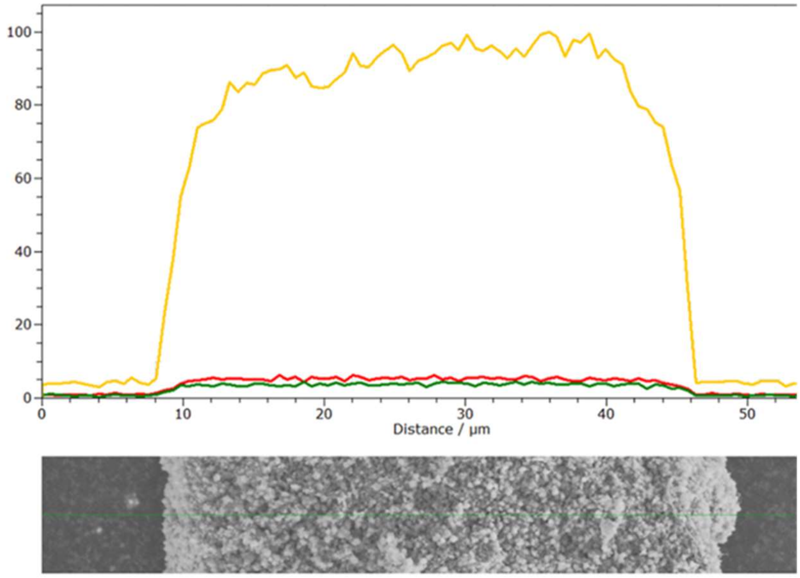

Figure 3.33 EDS line scan performed on a microcrystalline cluster of PCN-777@NiFeL

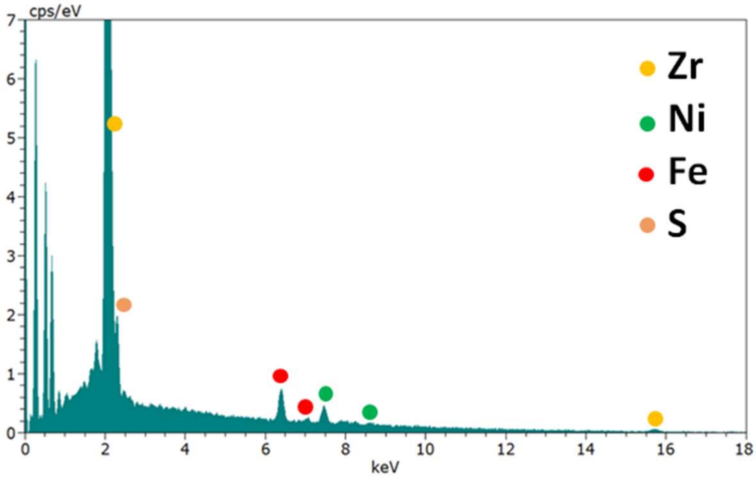

Figure 3.34: EDS mapping of PCN-777@NiFeL

4 Synthesis and Applications of New MOFs

"When I started out in chemistry, I always thought it should be possible to take two well defined molecules as building blocks and stitch them together into a predetermined chemical structure almost like you produce a blueprint of the structure ahead of time and then find the right building blocks necessary to build it. In this way, one can control the structure and the composition. This approach was difficult to implement at the beginning, but is not so difficult at this stage."

- Omar M. Yaghi-

4.1 Synthesis of the Ligands

Over the past few decades, the Buchwald-Hartwig coupling reaction, also known as aryl-amination reaction, has represented a very powerful tool for the construction of C-N bonds.[145] The reaction involves the formation of the carbon-heteroatom bond *via* a Pd(0) catalyzed reaction between amines (but also alcohols and amides can be used) and aryl halides (or other pseudo-halides). The general reaction mechanism is outlined in Scheme 4.1.

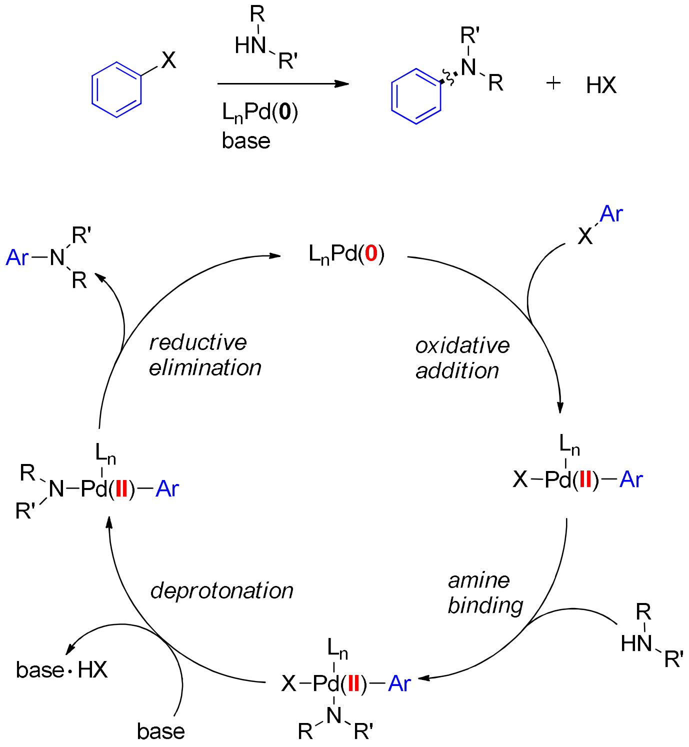

Scheme 4.1 Mechanism of the Buchwlad-Hartwig coupling reaction

The most appealing features of this reaction are the broad substrate scope and generality of reaction conditions, which make the Buchwald-Hartwig coupling more attractive with respect to traditional nucleophilic aromatic substitution (SN_{Ar}) and Cu-catalyzed Ullmann and Golberg couplings.[146]

Not only this process has gained a wide interest in Academia, but it has also attracted a broad attention from industry: in some cases the processes were performed on pilot plants on multi kg scales.[147, 148]

N-arylated aromatic substituents characterize the backbone of many biological active compounds and the palladium mediated SN_{Ar} reaction is described as one of the most frequent protocols in medicinal chemistry.[149, 150] In literature, the use of NH decorated ligands for the synthesis of Metal Organic Frameworks is very popular, because of the promising gas storage proprieties which feature these systems. For example, amino decorated pores are often related with high carbon dioxide uptakes.[151] It is also worth noting that the large majority of the MOFs described in literature are assembled from rigid linkers, often synthesized by Suzuki, Sonogashira or Ullman coupling protocols; indeed not-rigid MOFs are much less investigated. The introduction of amine functions in the ligand backbone means to lend them a higher degree of flexibility, aspect which can be transferred to the resulting MOFs.[152,153] This can lead to breathing MOFs, which adapt their crystalline framework to the entering/exiting of the guest.[154] Hence, we directed our efforts towards this goal exploiting a Buchwald coupling procedure. A series of amino decorated linkers, associated with different degrees of linearity and denticity was isolated and fully characterized, as summarized in Scheme 4.2. In particular, we started from two electrophiles: a 4,4’ biphenyl dihalide and 1,3,5 benzene trihalyde to provide, respectively, a di-substituted or a tri-substituted final scaffolds. Particularly important, for the scope of the reaction, has been the extension of the protocol to the use isonicotinamide coupling. This led to the isolation of pyridine containing ligand **L6** (Scheme 4.2), which was exploited as rigid linker for the fabrication of pillared MOFs (*vide infra*). In addition, the presence of an amide group in the MOF framework can be appealing for CO_2 trapping.[155]

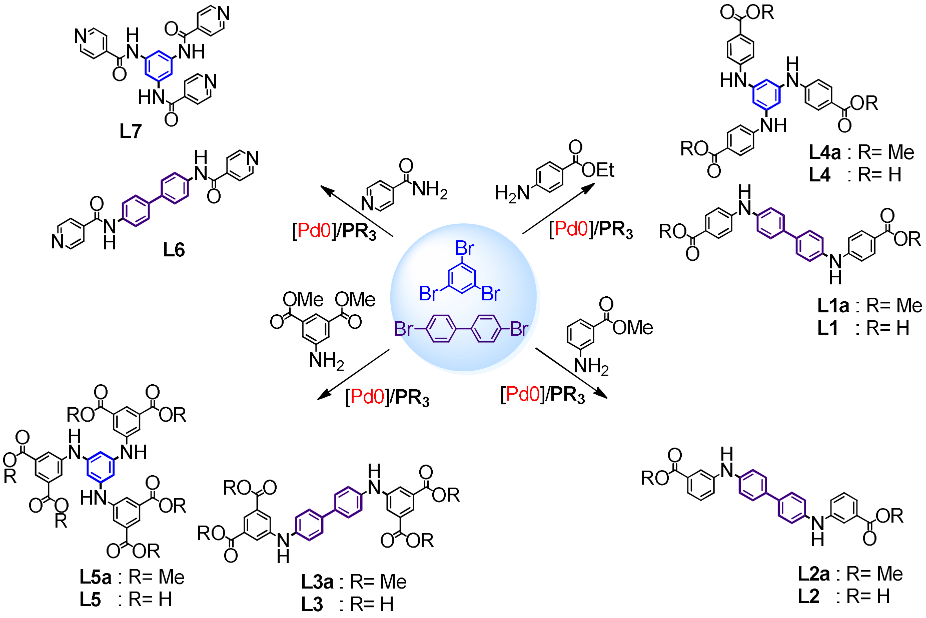

Scheme 4.2 General overview of the use of Buchwald-Hartwig protocol followed in this thesis

In order to exploit the N-H function as receptor site for the incoming guest species, we directed our efforts to the synthesis of secondary amines. Only very few examples of aminic linkers containing the biphenyl core are described in literature, especially for what concerns secondary amines.[156] Kaskel *et al.* described the synthesis of a tetratopic linker containing the tertiary amino-carboxylic ligand *N,N,N′,N′*-benzidine-tetrabenzoic acid, and its use in the synthesis of several MOFs with Zn.[157] In this case, flexible and porous materials were isolated. Cross coupling procedure started from benzidine as nucleophile using Cs_2CO_3 as base. An alternative way described to obtain *N,N,N′,N′*-benzidinetetrabenzoate considers the bromination of *N,N′*-diphenylbenzidine, followed by lithyation at -78°C and addition of $CO_{2(s)}$.[158] In our laboratory, the synthesis of the ligands **L1a**-**L5a** were carried out by cross coupling reactions starting from aryl halides, anilines and $Pd(OAc)_2$ as pre-catalyst. In order to generate the catalytically active species, the water activation protocol, reported by Buchwald, was adopted.[159] We consider this pathway more advantageous with respect to the previously reported procedures: the use of dry solvents was not strictly required and the use of benzidine, a carcinogenic compound, was also avoided.[160] A mixture of $Pd(OAc)_2$, a tertiary phospine and H_2O was heated at 110°C for 1 minute to obtain the catalytically active species. The main advantage of the procedure is the exclusion of exogenous additives for the reduction of Pd(II): the process only exploits an excess of phosphine and water to obtain the $(R_3P)_nPd(0)$ complex directly *in situ*. Two alkyl bis-aryl phosphines, BrettPhos® and tBuXPhos®, were used successfully to provide the amination products **L1a**-**5a** in excellent yields, as outlined in Table 4.1.

$$\text{Ar-X} + \text{R-NH}_2 \xrightarrow[\text{K}_2\text{CO}_3\text{, t-BuOH, 110°C, overnight}]{\text{0.5-2\% Pd(OAc)}_2\text{, 1.5-6\% phospine, 2\%-8\% H}_2\text{O}} \text{Ar-NH-R} + \text{HX}$$

Entry	Aryl Halide	Amine	Coupling Product	Yield[a]
1	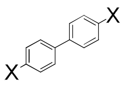 a) X=I b) X=Br	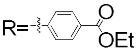	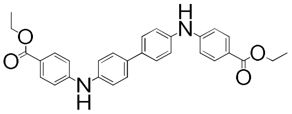	1a: 92% 1b: 98%[b]
2	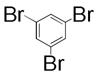		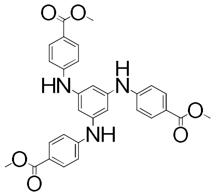	78%
3	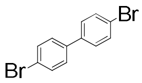	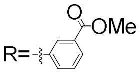	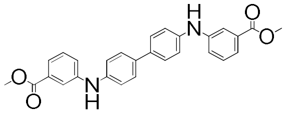	96%[b]
4	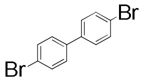	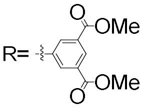	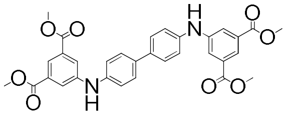	92%[b]
5	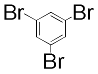		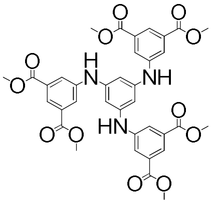	94%

a) calculated on isolated products, b) 0.5% $Pd(OAc)_2$, 1.5% tBuXPhos , 4%H_2O , b) $Pd(OAc)_2$ 3%, BrettPhos 9% , c) $Pd(OAc)_2$ 3%, tBuXPhos 9%

Table 4.1: Summary of the amination reaction

At first, 4,4’-diiodobyphenyl was chosen as suitable electrophile for the cross coupling with methyl 4-aminobenzoate, employing a 2 mol% of Pd and a 6% of BrettPhos®. After 16 hours, the reaction mixture was quenched with water and **L1a** was easily isolated by centrifugation, with no need of further purification. ^{1}H-NMR spectroscopy excluded the formation of the monoarylation product as well as the formation of the tertiary amine deriving from the coupling between the produced secondary amine with a second equivalent of electrophile. Hence, we decided to apply the same reaction conditions to 4,4’-dibromobiphenyl using tBuXPhos® and also in this case the complete conversion of the starting materials to the target compound was observed. Catalyst loading was lowered to 0.5 molar % without affecting the reaction rate. Synthetic attempts conducted with PPh_3, dppe and BINAP gave much less satisfactory results: only low reaction conversions or isolation of byproducts were observed. Encouraged by these results, we extended the scope of the amination protocol using methyl 3-aminobenzoate and dimethyl 5-aminoisophthalate, (Scheme 4.2 and Table 4.1, entries 3 and 4) to obtain **L2a** and **L3a**, respectively. Again, both compounds were isolated in high yields and purity. The analogous reactions performed on 1,3,5-tribromobenzene gave the desired products **L4a** and **L5a**, respectively (Scheme 4.2 and Table 4.1, entries 2 and 5). Also in these cases the compounds were isolated in high yields and purity. Similarly to the reaction involving aryl dihalides, no product deriving from partial substitutions were observed by NMR analysis. Zhou published an alternative procedure for the synthesis of the triester **L4a**. This procedure, compared to the Buchwald protocol, is certainly more demanding in terms of atom economy and wastes production. In fact, less solvent, milder conditions and a minor amount of ethyl 4-aminobenzoate were required by the Buchwald cross-coupling protocol.[161] Ligand **L4** was employed for the assembly of zinc and lanthanide based MOFs. [12,162] All the described esters were converted to the corresponding acids derivates via basic hydrolysis, performed with an aqueous solution of LiOH. Subsequent treatment with HCl gave compounds **L1-L3** and **L5** in good to quantitative yields.

For **L1a** and **L3a**, the scale up to gram scale was performed successfully: employing 1% molar $Pd(OAc)_2$ the reaction performed smoothly to the target esters (Table 4.2).

Compound	Coupling yield	Hydrolysis yield	Final product
L1a	98%	90%	1.53 g, 3.62 mmol
L3a	99%	99%	2.04 g, 3.98 mmol

Table 4.2: scale up of amination protocols

Subsequently, we focused our efforts on the application of the same protocol to obtain secondary amides. Previously described procedures reported the synthesis of *N,N'*-(biphenyl-4,4'-diyl)diisonicotinamide by nucleophylic acyl substitution (Scheme 4.3, pathway a), using phenyl phosphate for the activation of isonicotinic acid. [163]

Diamide **L6** was employed in the construction of molecular Borromean rings by Jin and coworkers, [164] and for the preparation of platinum(II) pyridine complexes with photoelectrical properties as reported in a patent.[165]

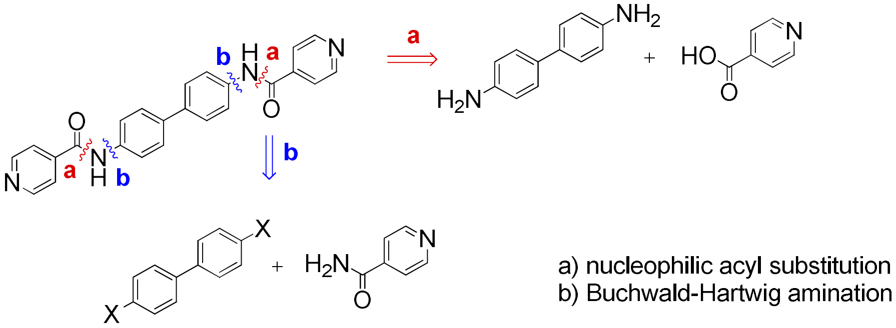

Scheme 4.3 Retrosynthetic routes to obtain the bisamidic ligand L6

We evaluated the amide coupling as an alternative route to obtain ligand **L6** (Scheme 4.3, pathway b), subsequently extending the scope of the reaction to the trisubstitution of 1,3,5-tribromobenzene as furnished in Table 4.3.

It is worth commenting that BrettPhos® is needed to achieve good yields, while tBuXPhos® provided only low yields.

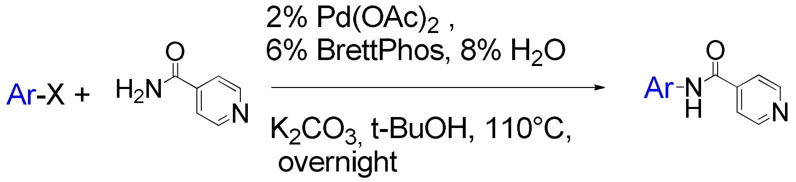

Entry	Aryl Halide	Coupling Product	Yield[a]
1	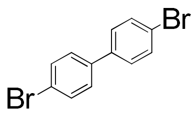	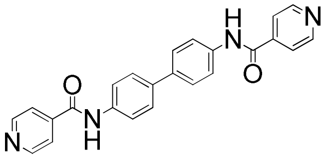	92%
2	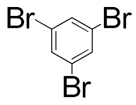	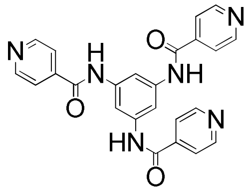	60%

a) calculated on isolated products

Table 4.3 Isonicotinamide coupling with different electrophyles

Notably, triamide **L7**, obtained in moderate yield**,** cannot be synthesized easily under nucleophilic acyl substitution, because reduction of 1,3,5 trinitrobenzene, a highly explosive compound, would be required. To the best of our knowledge, there is not any report dealing with the synthesis of ligand **L7** in literature, although the tri-ester analogue has been synthesized and used as building block both for coordination polymers and MOFs.[166,167]

4.2 Experimental part

General Methods

^1H NMR and $^{13}C\{^1H\}$ NMR spectra were recorded on 400MHz and 300 MHz Bruker instruments. Chemical shifts are reported in ppm relative to the solvent residual peak of $CDCl_3$ (δH 7.26, δC 77.0) or $(CD_3)_2SO$ (δH 2.50, δC 39.5). *J*-values are given in Hz and in the assignments s = singlet, d = doublet, t = triplet, q = quartet, m = multiplet, br = broad, dd = doublet of doublets, bb = broad band. EI(+)-MS spectra were collected with an ionising voltage of 70 eV by means of a Thermo DSQ II spectrometer equipped with a single quadrupole analyser. The analyses were conducted on pure solid samples by means of a DIP probe (direct insertion probe, flash thermolysis at 350 °C), or on diluted solutions of the samples by means of DEP probe (direct exposure probe, Re-filament, flash thermolysis at about 1000 °C). Methane was used as ionization gas for CI-MS analysis. IR spectra were obtained with a Thermo Scientific Nicolet 5PCFT-IR-ATR spectrometer (diamond crystal) in the 4000-400cm^{-1} interval. TLC was performed on silica gel plates visualized with a UV lamp (254 nm). All the organic and inorganic reagents as well as the solvents were purchased from Aldrich. The solvents used for the cross-coupling reactions were dried prior to use and stored over activated molecular sieves under an atmosphere of dry nitrogen. Schlenk techniques were employed for the cross-coupling reactions in order to assure that all the steps were conducted under strictly inert conditions.

General procedure A

Catalyst was generated *in situ* following the water activation procedure: An oven-dried Schlenk tube was charged with $Pd(OAc)_2$ (0.5 mol%), phosphine (1.5 mol%) and *tert*-butanol. The vessel was evacuated and backfilled with nitrogen 3 times. Water (4.0 mol%) was added with hamilton syringe then the mixture was heated at 110 °C for 1 min. Aryl halide, K_2CO_3 (2.6 equivalents) and amine (2.4 equivalents) were added to a second oven-dried Schlenk tube. The catalyst solution was cannulated into the second Schlenk and the reaction mixture was stirred at 110 °C overnight. Product was isolated by simple addition of water and centrifugation.

General procedure B

Same experimental protocol of general procedure A, with the following variations: a higher catalyst loading is required for amide couplings. BrettPhos® (6.0 mol%), $Pd(OAc)_2$ (2.0 mol%) and H_2O (8.0 mol%) were employed to generate the Pd(0) catalyst.

diethyl-4,4'-(biphenyl-4,4'-diylbis(azanediyl))dibenzoate (L1a)

Following the general procedure A: a mixture of 4,4’-dibromobiphenyl (280 mg, 0.9 mmol), ethyl 4-aminobenzoate (365 mg, 2.16 mmol, 2.4 equivalents), K_2CO_3 (348 mg, 2.52 mmol, 2.8 equivalents), $Pd(OAc)_2$ (1.0 mg, 0.5 mol %), tBuxPhos (5.7 mg, 1.5 mol%), H_2O (0.65 mg, 4 mol%), *tert*-butanol (5+10 mL). After 24 hours water (15 mL) was added to the reaction mixture and **L1a** was obtained as yellowish solid with good purity (422 mg, 0.88 mmol, 98%)

^{1}H-NMR (400 MHz, DMSO-d, 25 °C): δ 8.91 (bs, N*H* 2H), 7.83 (d, CH_{Ar}, *J*=8.8 Hz, 4H), 7.62 (d, CH_{Ar}, *J*=8.8 Hz, 4H), 7.26 (d, CH_{Ar} , *J*=8.8 Hz, 4H), 7.11 (d, CH_{Ar}, *J*=8.8 Hz, 4H), 4.25 (q, CH_2, *J*=7.2 Hz, 4H), 1.30 (t, CH_3, *J*=7.2 Hz, 6H) ppm ; ^{13}C-NMR (100.77 MHz, DMSO-d, 25 °C): δ 166.0, 148.7, 140.7, 133.6, 131.5, 127.3, 120.0, 119.9, 114.7, 60.4, 14.8 ppm; IR (ATR): cm^{-1} 3348, 3321, 2988, 2960, 2927, 1682, 1592), 1526,1505, 1495, 1337 , 1266, 1101 , 831, 804, 766, 586; MS (DEP/EI): m/z 480

dimethyl-3,3'-(biphenyl-4,4'-diylbis(azanediyl))dibenzoate (L 2a)

Following the general procedure A: a mixture of 4,4’-dibromobiphenyl (281 mg, 0.9 mmol), methyl 3-aminobenzoate (326 mg, 2.4 mmol), K_2CO_3 (348 mg, 2.8 mmol), $Pd(OAc)_2$ (1.7 mg, 0.5 mol %), BrettPhos (12.2 mg, 1.5 mol%), H_2O (0.65 mg, 4 mol%), *tert*-butanol (5 + 10 mL). After 24 hours water (15 mL) was added to the reaction mixture and **L2a** was obtained as beige solid with good purity (388 mg, 0.86 mmol, 96%)

^{1}H-NMR (400 MHz, $CDCl_3$, 25 °C): δ 7.77 (s, CH_{Ar}, 2H), 7.61 (d, CH_{Ar}, *J*=8.0 Hz, 2H), 7.54 (d, CH_{Ar}, *J*= 8.4 Hz, 4H), 7.36 (t, CH_{Ar}, *J*=8.0 Hz, 2H), 7.30 (d overlapped, CH_{Ar}, *J*=8.0 Hz, 2H), 7.18 (d, CH_{Ar}, *J*=8.4 Hz, 4H), 5.87 (s, N*H*, 2H), 3.93 (s, OCH_3, 6H) ppm; ^{13}C-NMR (100.77 MHz, $CDCl_3$, 25 °C): 167.1, 143.5, 141.2, 134.2, 129.4, 127.6, 121.9, 121.6, 118.7, 118.2, 52.2 ppm

Tetramethyl-5,5'-(biphenyl-4,4'-diylbis(azanediyl))diisophthalate (L3a)

Following the general procedure A: a mixture of 4,4’-dibromobiphenyl (280 mg, 0.9 mmol), dimethyl 5-aminoisophthalate (452 mg, 2.16

mmol, 2.4 equivalents), K_2CO_3 (348 mg, 2.52 mmol, 2.8 equivalents), $Pd(OAc)_2$ (1.0 mg, 0.5 mol %), tBuxPhos (5.7 mg, 1.5 mol%), H_2O (0.65 mg, 4 mol%), *tert*-butanol (5 + 10 mL). After 24 hours water (15 mL) was added to the reaction mixture and **L3a** was obtained as yellow solid with good purity (471 mg, 0.83 mg, 92%)

^{1}H-NMR (400 MHz, DMSO-d, 25 °C): δ 8.80 (bs, *NH*, 2H), 7.90 (pt, C*H*$_{Ar}$, *J* = 1,4 Hz, 2H), 7.87 (pd, C*H*$_{Ar}$, *J*=1,4Hz, 4H), 7.65 (d, C*H*$_{Ar}$, *J*=8.8 Hz, 4H), 7.21 (d, C*H*$_{Ar}$, *J*=8.8Hz, 4H), 3.88 (s, OC*H*$_3$, 12H) ppm ; ^{13}C-NMR (75 MHz, DMSO-d, 25 °C): δ 165.5, 144.8, 140.6, 132.9, 131.1, 126.9, 119.6, 118.7 ppm; IR (ATR): cm^{-1} 3383, 2952, 1711, 1595, 1529, 1498, 1462, 1433, 1357, 1237, 1218, 1118, 1013, 831, 751, 722; MS (DEP/CI): m/z 569 $[M+H]^+$, $[M+C_2H_5]^+$

Triethyl-4,4',4''-(benzene-1,3,5-triyltris(azanediyl))tribenzoate (L4a)

Following the general procedure A: a mixture of 1,3,5-tribromobenzene (120 mg, 0.38 mmol), ethyl 4-aminobenzoate (226 mg, 1.37 mmol, 3.6 equivalents), K_2CO_3 (220 mg, 1.59 mmol, 3.6 equivalents), $Pd(OAc)_2$ (2.5 mg, 3.0 mol %), BrettPhos (18.4 mg, 9.0 mol%), H_2O (0.8 mg, 12 mol%), *tert*-butanol (3 + 5 mL). After 24 hours water (10 mL) was added to the reaction mixture and **L4a** was obtained as brownish solid with good purity (170 mg, 0.30 mmol, 79%)

^{1}H-NMR (400 MHz, DMSO-d, 25 °C): δ 8.78 (bs, N*H*, 3H), 7.84 (d, C*H*$_{Ar}$, *J*= 8.8Hz, 6H), 7.13 (d, C*H*$_{Ar}$, *J*= 8.8Hz, 6H), 6.62 (s, C*H*$_{Ar}$, 3H), 4.26 (q, C*H*$_2$, *J*= 6.4Hz, 6H), 1.30 (t, C*H*$_3$, *J*= 6.4Hz, 9H) ppm.

hexamethyl 5,5',5''-(benzene-1,3,5-triyltris(azanediyl))triisophthalate (L5a)

Following the general procedure A: a mixture of 1,3,5-tribromobenzene (120 mg, 0.38 mmol), dimethyl 5-aminoisophthalate (286 mg, 1.37 mmol, 3.6 equivalents), K_2CO_3 (220 mg, 1.59 mmol, 3.6 equivalents), $Pd(OAc)_2$ (2.5 mg, 3.0 mol %), tBuxPhos (14.5 mg, 9.0 mol%), H_2O (0.8 mg, 12 mol%), *tert*-butanol (3+5 mL). After 24 hours water (10 mL) was added to the reaction mixture and **L5a** was obtained as brownish solid with good purity (250 mg, 0.36 mmol, 94%)

^{1}H-NMR (400 MHz, DMSO-d, 25 °C): δ 8.71 (bs, N*H*, 3H), 7.92 (pt, CH_{Ar}, *J* = 1,4 Hz, 3H), 7.89 (pd, CH_{Ar}, *J*=1,4Hz, 6H), 6.53 (s, CH_{Ar}, 3H), 3.85 (s, OCH_3, 18H) ppm.

***N,N'*-(biphenyl-4,4'-diyl)diisonicotinamide (L6)**

Following the general procedure B: a mixture of 4,4'-dibromobiphenyl (118 mg, 0.38 mmol), isonicotinamide (111 mg, 0.91 mmol, 2.4 equivalents), K_2CO_3 (147 mg, 1.06 mmol, 2.8 equivalents), $Pd(OAc)_2$ (1.7 mg, 2.0 mol %), BrettPhos® (12.2 mg, 6.0 mol%), H_2O (0.5 mg, 8 mol%), *tert*-butanol (3 + 5 mL). After 24 hours water (10 mL) was added to the reaction mixture and **L6** was obtained as off-white solid with good purity (142 mg, 0.36 mmol, 94%)

^{1}H-NMR (400 MHz, DMSO-d, 25 °C): δ 10.60 (bs, N*H*, 2H), 8.80 (d, CH_{Pyr}, *J*=5.8 Hz, 4H), 7.90-7.86 (m, CH_{Pyr} + CH_{Ar}, 8H), 7.72 (d, CH_{Ar}, *J*= 8.7 Hz, 4H) ppm; ^{13}C-NMR (100.77 MHz, DMSO-d, 25 °C): δ 164.4, 150.7, 142.4, 138.3, 135.7, 127.1, 122.1, 121.3 ppm; IR (ATR): 3334, 1647, 1611, 1587, 1552, 1507, 1409, 1397, 1337, 1318, 1286, 1258, 1218, 1065, 1004, 991, 904, 814, 754, 710, 665, 650, 581; MS (DEP/EI): m/z 394

N*,*N'*,*N''-(benzene-1,3,5-triyl)triisonicotinamide (L7)

Following the general procedure B: a mixture of 1,3,5-tribromobenzene (120 mg, 0.38 mmol), isonicotinamide (167 mg, 1.37 mmol, 3.6 equivalents), K_2CO_3 (220 mg, 1.59 mmol, 4.2 equivalents), $Pd(OAc)_2$ (2.5 mg, 3.0 mol %), BrettPhos (18.4 mg, 9.0 mol%), H_2O (0.8 mg, 12 mol%), *tert*-butanol (3 +5 mL). After 24 hours water (10 mL) was added to the reaction mixture and **L7** was obtained as beige solid with good purity (99 mg, 0,23 mmol, 60%);

^{1}H-NMR (400 MHz, DMSO-d, 25 °C): δ 10.68 (bs, NH, 3H) 8.80 (d, CH_{Pyr}, *J*=4,4Hz, 6H), 8.12 (s, CH_{Ar}, 3H), 7.90 (d, CH_{Pyr}, *J*=4.4Hz, 6H) ppm; ^{13}C-NMR (100.77 MHz, DMSO-d, 25 °C): δ 164.7, 150.8, 150.7, 142.4, 139.4, 122.1, 122.0, 109.0, 119.7 ppm; IR (ATR): cm^{-1} 3257, 3157, 3070, 2958, 1667, 1622, 1553, 1426, 1285, 1179, 1085, 996, 838, 746, 689.

General Hydrolysis protocol

Ester was dissolved in a mixture of tetrahydrofuran and methanol then an aqueous solution of LiOH was added (2.5 base equivalent for each carboxylic group). The resulting solution was stirred at 65°C for 48 hours. The reaction mixture was concentrated and neutralized with HCl 1M solution. Hydrolyzed derivative was isolated in good yield by centrifugation and washed with water.

4,4'-(biphenyl-4,4'-diylbis(azanediyl))dibenzoic acid (L1)

L1a (518 mg, 1.08 mmol) was placed in a 500 mL one neck round-bottom flask and solubilized in a mixture of tetrahydrofuran and methanol (240 mL: 15 mL). Then $LiOH\cdot H_2O$ (226 mg, 5.4 mmol, 5.0 equivalents) previously dissolved in H_2O (45 mL) was added. The resulting solution was stirred at 65°C for 48 hours. The crude mixture was acidified with HCl 1M and the concentrated at reduced pressure. **L1** was isolated by centrifugation as a pale yellow solid (443 mg, 1.05 mmol, 91%)

^{1}H-NMR (400 MHz, DMSO-d, 25 °C): δ 12.37 (bs, COO*H*, 2H,), 8.83 (s, N*H*, 2H), 7.81 (d, CH_{Ar}, 4H, *J*= 8.4 Hz, CH), 7.61 (d, CH_{Ar}, 4H, *J*= 8.4 Hz), 7.25 (d, CH_{Ar}, 4H, *J*= 8.6 Hz), 7.10 (d, CH_{Ar}, 4H, *J*=8.6 Hz) ppm; ^{13}C-NMR (100.77 MHz, DMSO-d, 25 °C): δ 167.1, 147.9, 140.4, 133.0, 131.2, 126.8, 120.4, 119.3, 114.2 ppm; IR (ATR): cm^{-1} 3416, 1675, 1599, 1521, 1502, 1422, 1317, 1292, 1276, 1234, 1175, 1108, 809, 764, 695; MS (DEP/EI): m/z 424

3,3'-(biphenyl-4,4'-diylbis(azanediyl))dibenzoic acid (L2)

Following the general procedure: **L2a** (388 mg, 0.86 mmol), was dissolved in a mixture of tetrahydrofuran (180 mL) and methanol (10 mL). A solution of LiOH (180 mg, 4.3 mmol, 5 equivalents) in 30 mL of H_2O was added and the reaction mixture was stirred at 65°C for 48 hours. The crude mixture was neutralized with HCl 1M and concentrated. **L2** was isolated by centrifugation as a pale beige solid (245 mg, 0.58 mmol, 72%)

^{1}H-NMR (400 MHz, DMSO-d, 25 °C): 12.85 (bb, COO*H*, 2H), 1.95 (s, N*H*, 2H), 7.68 (s, C*H*$_{\text{Ar}}$, 2H), 7.57 (d, C*H*$_{\text{Ar}}$, *J*= 11.0 Hz, 4Hz), 7.38-7.22 (m, C*H*$_{\text{Ar}}$, 6H), 7.16 (d, C*H*$_{\text{Ar}}$, *J*=11.0 Hz, 4H) ppm; ^{13}C-NMR (75 MHz, DMSO-d, 25 °C): δ 167.4, 143.8, 141.4, 132.0, 131.7, 129.4, 126.7, 120.3, 120.2, 117.7, 116.5 ppm; IR (ATR): cm^{-1} 4316, 2954, 1669, 1653, 1598, 1558, 1522, 1501, 1458, 1327, 1291, 1277, 1239, 1175, 811, 766.

5,5'-(biphenyl-4,4'-diylbis(azanediyl))diisophthalic acid (L3)

In a 1 L one neck round-bottom flask were placed **L3a** (2.27 g, 4 mmol), methanol (70 mL) and THF (500 mL). LiOH (1.68 g, 40 mmol, 10 equivalents) previously dissolved in 100 mL of H_2O was added to the reaction flask and the resulting solution was stirred at 65°C. After 48 hours the crude mixture was concentrated and acidified with HCl 1M. **L3** was isolated by centrifugation and washed with dichloromethane (10 mL) to give a orangish solid (2.040 g, 3.98 mmol, 99%)

^{1}H-NMR (400 MHz, DMSO-d, 25 °C): δ 13.14 (bb, COO*H,* 4H), 8.72 (bs, N*H,* 2H) 7.91 (pt, C*H*$_{\text{Ar}}$, *J*=1.6 Hz, 2H), 7.86 (pd, C*H*$_{\text{Ar}}$, *J*=1.6 Hz, 4H), 7.64 (d, C*H*$_{\text{Ar}}$, *J*=8.8 Hz, 4H), 7.21 (d, C*H*$_{\text{Ar}}$, *J*=8.8 Hz, 4H) ppm; ^{13}C-NMR (75 MHz, DMSO-d, 25 °C): δ 166.8, 144.5, 140.9, 132.6, 132.1 ppm; IR (ATR): cm^{-1} 2947, 1699, 1688, 1677, 1589, 1516, 1497, 1407, 1265, 1226, 1120, 1001, 988, 807, 752.

5,5',5''-(benzene-1,3,5-triyltris(azanediyl))triisophthalic acid (L5)

In a 500 mL one neck round-bottom flask were placed **5a** (250 mg, 0.36 mmol), methanol (17 mL) and THF (170 mL). LiOH (300 mg, 7.15 mmol , 20 equivalents) previously dissolved in 20 mL of H_2O was added to the reaction flask and the resulting solution was stirred at 65°C. After 48 hours the crude mixture was concentrated and acidified with HCl 1M **5b** was isolated by centrifugation and washed with dichloromethane (10 mL) to give a brownish solid (201 mg, 0.33 mmol, 92%)

^{1}H-NMR (400 MHz, DMSO-d, 25 °C): δ 13.12 (bb, COO*H*, 6H) 8.59 (bb, N*H*, 3H), 7.90 (bs, CH_{Ar}, 3H), 7.84 (bs, C$H_{Ar,}$ 6H), 6.51 (s, CH_{Ar}, 3H); ^{13}C-NMR (75 MHz, DMSO-d, 25 °C): δ 166.7, 144.2, 144.1, 132.1, 120.7, 100.0 ppm; IR (ATR): cm^{-1} 1704, 1683, 1634, 1595, 1558, 1423, 1349, 1271, 1185, 896, 756, 691, 659.

4.3 Pillar strategy: a brief introduction

As previously mentioned, linker **L6** brings amidic moieties that could play a double role regarding the final material properties: imparting a conformational freedom to the MOF assembly and, at the same time, acting as anchoring sites for the incoming guest. In fact, the NH group can behave as hydrogen bond donor towards hydrogen bond acceptor guests, while the amide C=O group can function as hydrogen bond acceptor towards hydrogen bond donor guests, as depicted in Figure 4.1.

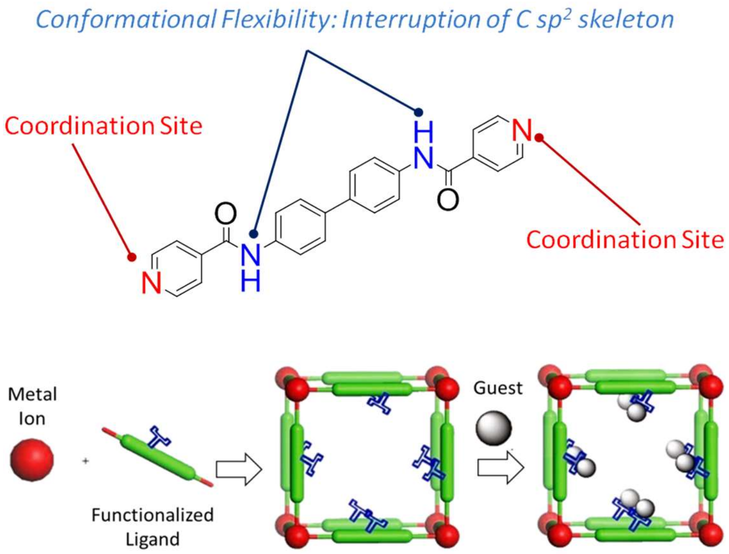

Figure 4.1: Ligand design and guest-uptake strategy for the materials containing L6

Until 2006, more than 2400 bis-pyridyl containing coordination polymers have been described: it is noteworthy that 30% of these structures derive by the self-assembly of 4,4'-bipy as linker.[168] However, the synthesis of homoleptic MOFs based on the unique metal-bipy assembly presents several drawbacks. The SBU structure depends largely upon the coordination geometry of the metal and the number of sites occupied by terminal linkers: the overall result is a common unpredictability of the final MOF structure. Furthermore, homoleptic metal-bipy MOFs are generally related to the inclusion of the metal counterions, reducing the internal voids. Moreover, they are usually characterized by a low thermal stability, with a $T_{dec} < 250°C$, owing to a low strength of the metal-nitrogen coordination bond.[169,170] For this reasons, we decided to focus our synthetic efforts towards the design of heteroleptic MOFs, combining **L6** with bimetallic paddle-wheel SBU, following a pillar strategy as shown in Figure 4.2.

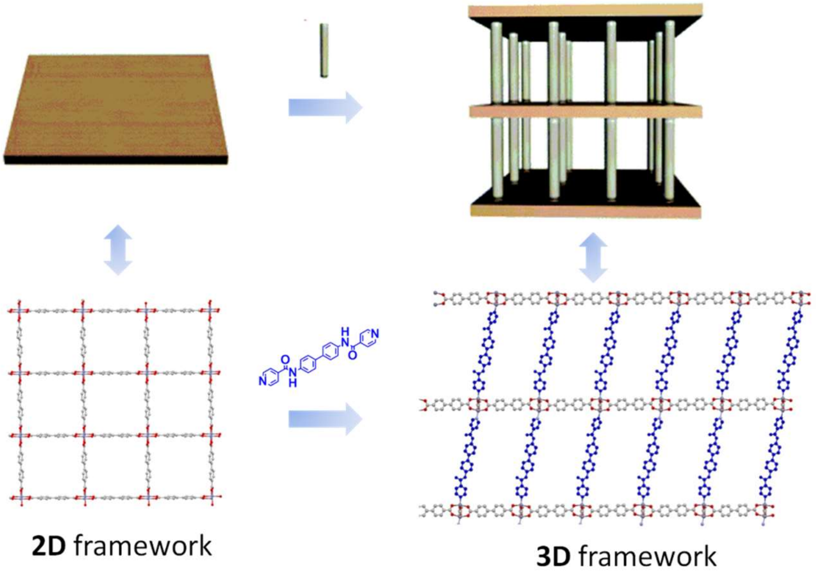

Figure 4.2 General overview on the pillar strategy, from 2D to 3D structures

2D planes formed by the combination of the $Zn_2(COO)_4$ SBUs with ditopic carboxylic ligands are bridged by **L6** to provide 3D architectures. Herein, we present a strategy for the design of a small family of heteroleptic MOFs, based on the combination of **L6** with three different dicarboxylic linkers, such as terephtalic acid, 2,6-naphthalene-di-carboxylic acid and 4,4´-biphenylene-di-carboxylic acid, as reported in Figure 4.3.

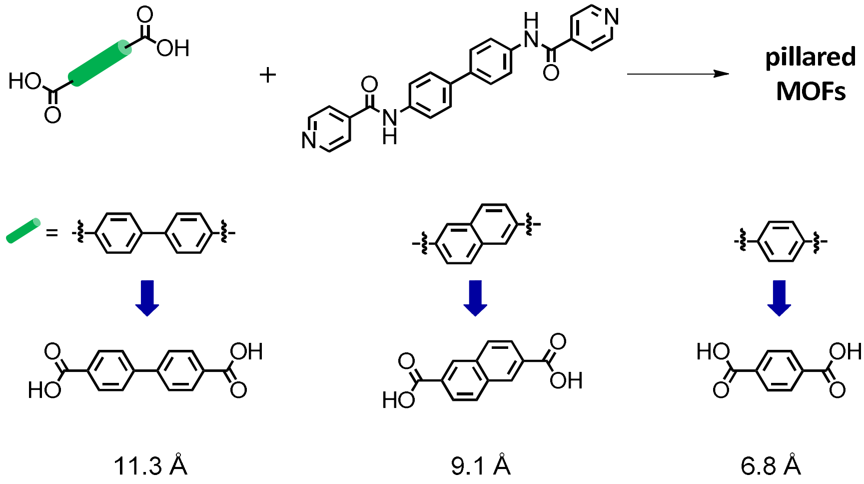

Figure 4.3 A brief summary of the pillar approach adopted in this work: building up of a small MOF family changing the length of the carboxylic linker.

The three dicarboxylic acids are featured by an increasing length of the aromatic spacer which separates the two COOH groups, from 6.8Å for terephtalic acid, to 9.1Å for the naphthalenic acid and 11.3Å for the biphenylene spacer. In principle, this can allow a modulation of the dimensions of the MOFs cavities, keeping constant the structural framework which should be governed by the pillar strategy. The shorter version of **L6**, *N,N′*-bis(4-pyridinecarboxamide)-1,4-benzene (named as **4-bpcb**), containing only one phenyl ring as spacer between the amide functions counts 26 structural characterized examples reported in the literature. [171,172] To the best of our knowledge, ligand **L6** has been rarely used for the construction of metal-containing assemblies.[164,165]

4.4 New Pillared MOFs

4.4.1 PUM168

Solvothermal reaction of a DMF solution containing $Zn(NO_3)_2{\cdot}6H_2O$, biphenyl-4,4′-dicarboxylic acid and bis-amidic ligand **L6** in a sealed tube provided the corresponding heteroleptic MOF, named PUM168 (PUM = Parma-University-Materials), as yellow crystals.

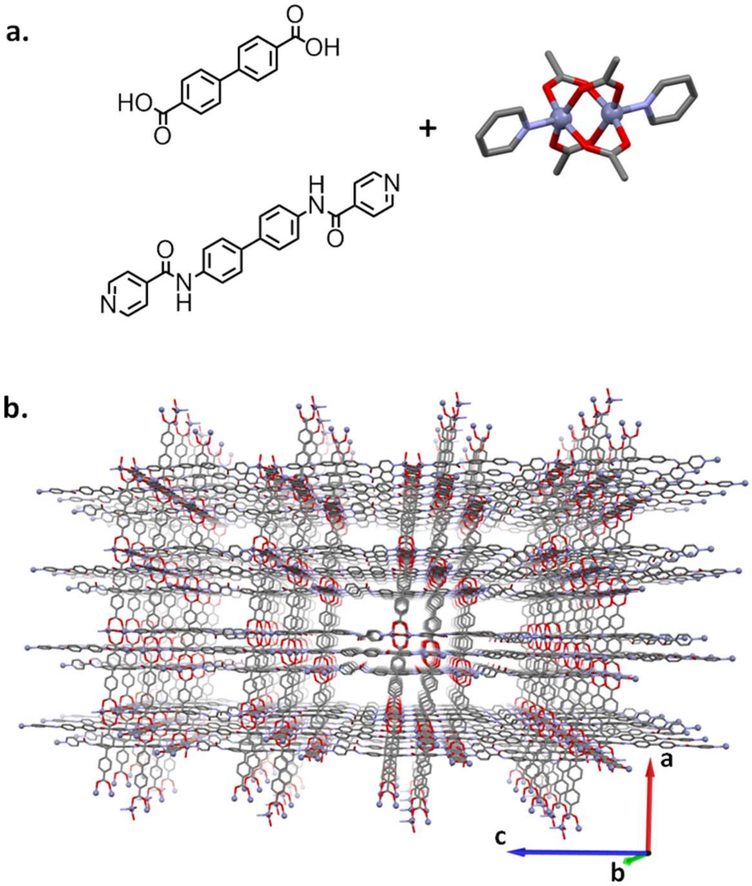

Figure 4.4: a) ligands and Zn paddle wheel SBU; b) PUM168 framework channels along crystallographic axis b

It should be noted that free bis-amide **L6** is a pale grey solid, whereas final PUM168 crystals are clearly yellow: a similar chromatic behaviour of Zn-pillared MOF was described by Hupp.[173]

The framework of PUM168 is based on paddle-wheel nodes of the type [$Zn_2(COO)_4$] combined with the ditopic carboxylic ligand and the bispyridine linker **L6** to give [$Zn_2(COO)_4(py)_2$] (Figure 4.4.a).

Taking into account the SBU, the Zn···O distances span the range 2.013-2.071Å, while Zn···N_{py} are in the range 2.025-2.053Å.

The resulting pillared structure is triply interpenetrated and it shows two different types of channels: 14x16 Å and 7x15 Å, respectively along crystallographic axes *b* and *c*, as shown in Figure 4.4.b and **Figure 4.5**:.a-b. Pores are filled by molecules of DMF which was the solvent of synthesis: removing solvent electron density and considering only MOF chains it is possible to calculate a 49% of empty volume for unit cell (Solvent Contact Surface Mercury) equal to 2914 Å^3 (**Figure 4.5**:).

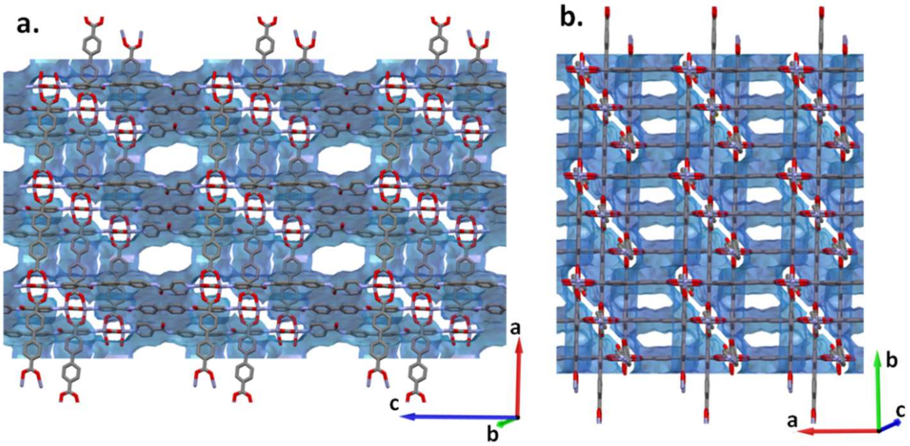

Figure 4.5: PUM168 channels and calculated void surface: a) along the crystallographic axis *b*; b) along the crystallographic axis *c*

PUM168 nets show different conformations of the amidic linker: in fact, two nets exhibit a *cis* orientation of the C=O moieties (plotted in light and deep green in Figure 4.6-a) which are inversion related, while in the third one the ligand stands on an inversion centre and it is characterized by a *trans* orientation of the C=O groups (plotted in blue, see Figure 4.6.b for details).

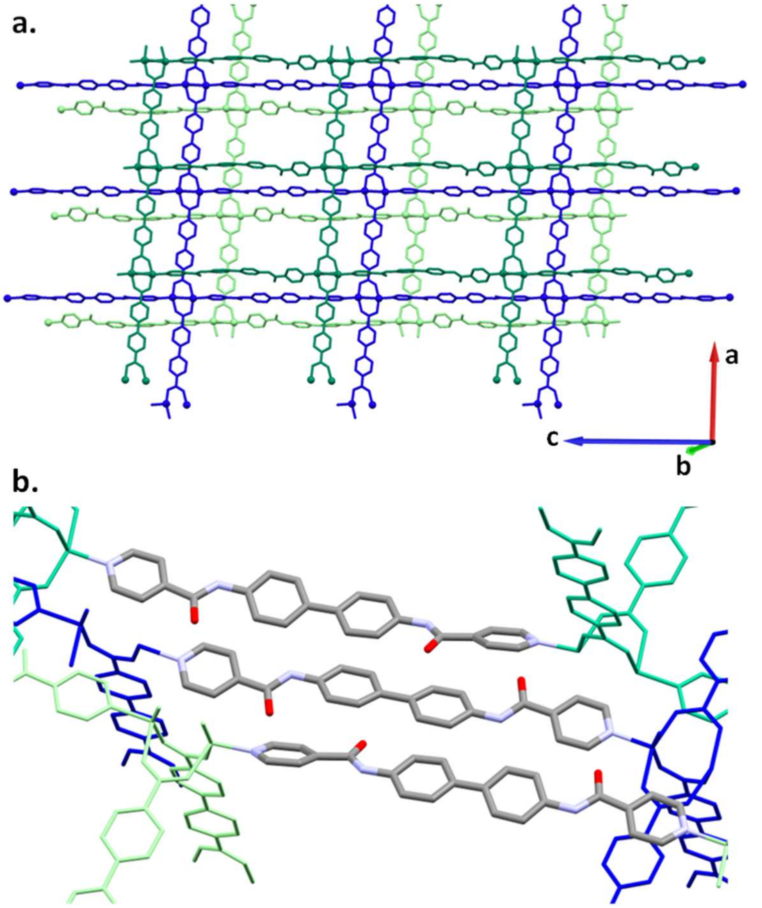

Figure 4.6 a) PUM 168 nets: blue color for the trans net, green colours for the two cis nets; b) zoom displaying the different amide orientations in each MOF net

X-ray structural analysis allowed the modelling of various solvent molecules: several DMF molecules are stabilized by hydrogen bonds to NH groups of **L6**. The number of DMF molecules involved in hydrogen bond contacts is different for each net: in the *trans* net both NH moieties act as H-bond donors, while in the *cis* net only an amidic NH group interacts with one DMF (Figure 4.7.b).

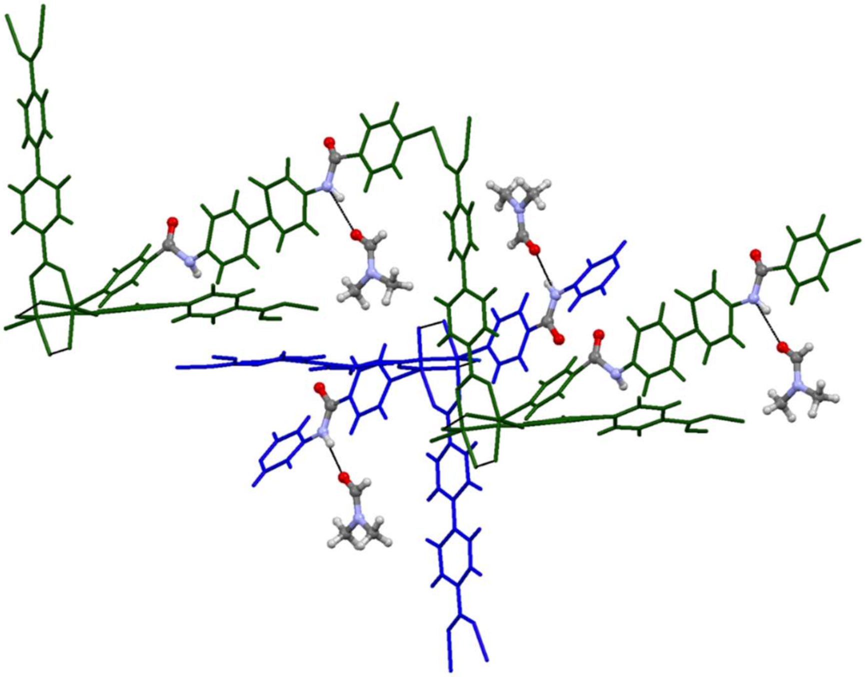

Figure 4.7 H-bond interactions between amidic NH moieties and DMF molecules: blue colour for *trans* net, green colour for *cis* nets.

4.4.2 PUM 210

PUM210 was synthesized applying the same reaction conditions used for PUM168. Surprisingly, the shortening of carboxylic ligand is related to a variation of the final MOF structural motif, as shown in Figure 4.9.

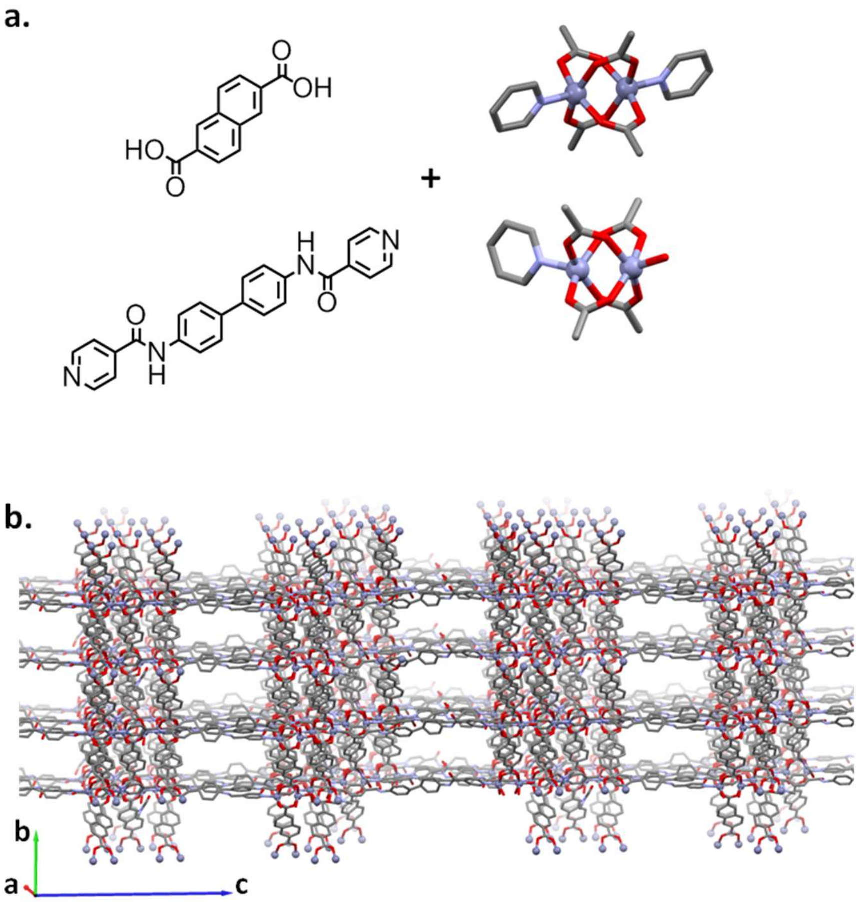

Figure 4.8 a) linkers and the two different Zn paddle wheel SBUs of PUM210; b) MOF channels along crystallographic axis a.

PUM210 shows in fact two different Zn paddle-wheel SBUs. One is the classical $[Zn(COO)_4(\mathbf{L6})_2]$, equivalent to the one seen in PUM168, while the other is a uncommon paddle-wheel of the type [$Zn_2(COO)_4$(**L6**)(H_2O)]. Water coordination to Zn ion is associated with a truncation of the polymeric net, producing 2D slabs, as displayed in Figure 4.9.

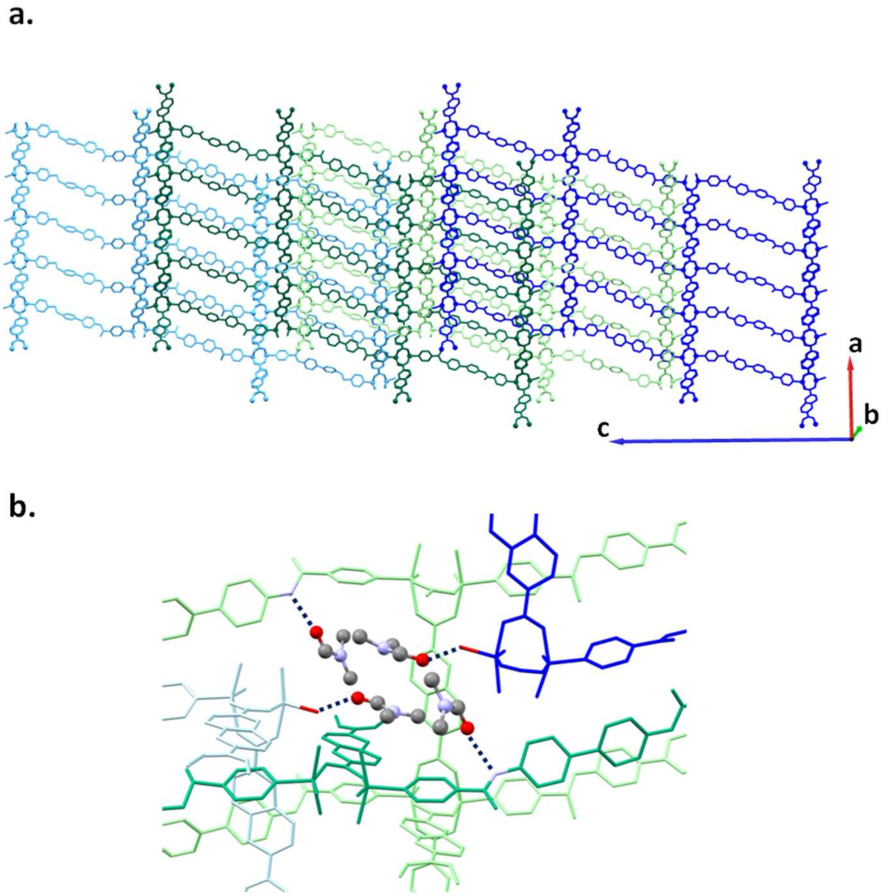

Figure 4.9 a) view of PUM 210 nets along crystallographic axis b ; b) hydrogen bond interaction between terminal water of Zn paddle-wheel units belonging to different MOF nets and DMF molecules

These slabs are characterized by an infinite polymeric expansion along the directions of crystallographic axes *a* and *b.* On the other hand, a finite dimension, corresponding to a step of three **L6**-units, is observed along *c* direction.

As illustrated in Figure 4.9.a, the parallel blue and light blue 3D nets are catenated by two other slabs, represented in green colours; both green layers result interlinked with blue ones.[174]

A cluster of four DMF molecules is trapped in the space between the blue and the light blue nets, as shown in Figure 4.9-b: two DMF interact with the coordinated water molecule of the truncated paddle-wheel [$Zn_2(COO)_4$(**L6**)(H_2O)], while the remaining two DMFs are involved in hydrogen bond interactions with amidic NH moieties of the green sheets. Then the DMF cluster ensures structural continuity between the different slabs.

It should be noted that only very few examples of truncated Zn-paddle-wheels are reported in literature [175,176] and none concerns pyridinic ligand.

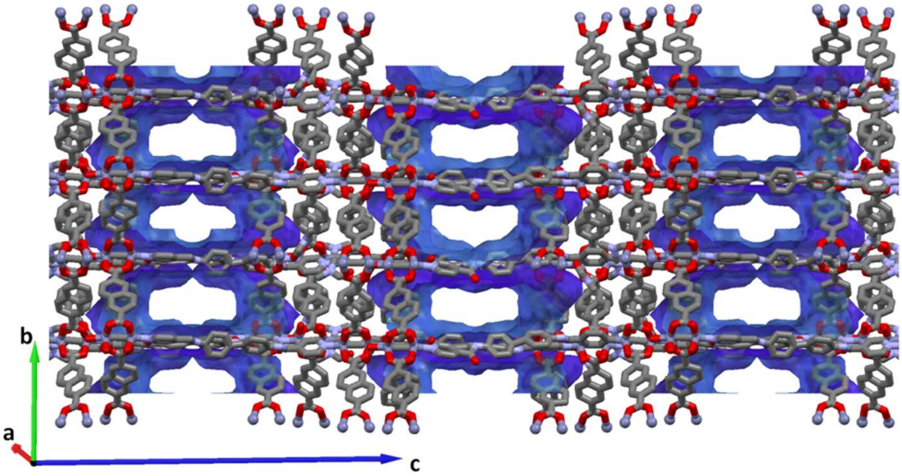

Figure 4.10: A view of dbd210 channels along crystallographic axis *a*, void contact surface plotted in blue colour.

For what concerns porosity, PUM210 exhibits 1D open channels (Figure 4.10), 12x8 Å wide, along crystallographic axis *a,* which presents a parallel orientation with respect to the plane containing **L6** pillars. The resulted calculated void volume reaches the 32% of unit cell, equal to 6724 Å^3 (Contact Surface function by Mercury), as illustrated in Figure 4.10.

4.4.3 PUM198

An even more remarkable framework variation is obtained employing 1,4-bezendicarboxylic acid (named BDC) as carboxylic ligand: Zn_2 paddle-wheel observed in PUM168 and in PUM210 is now substituted with a different SBU, as illustrated in Figure 4.11-a.

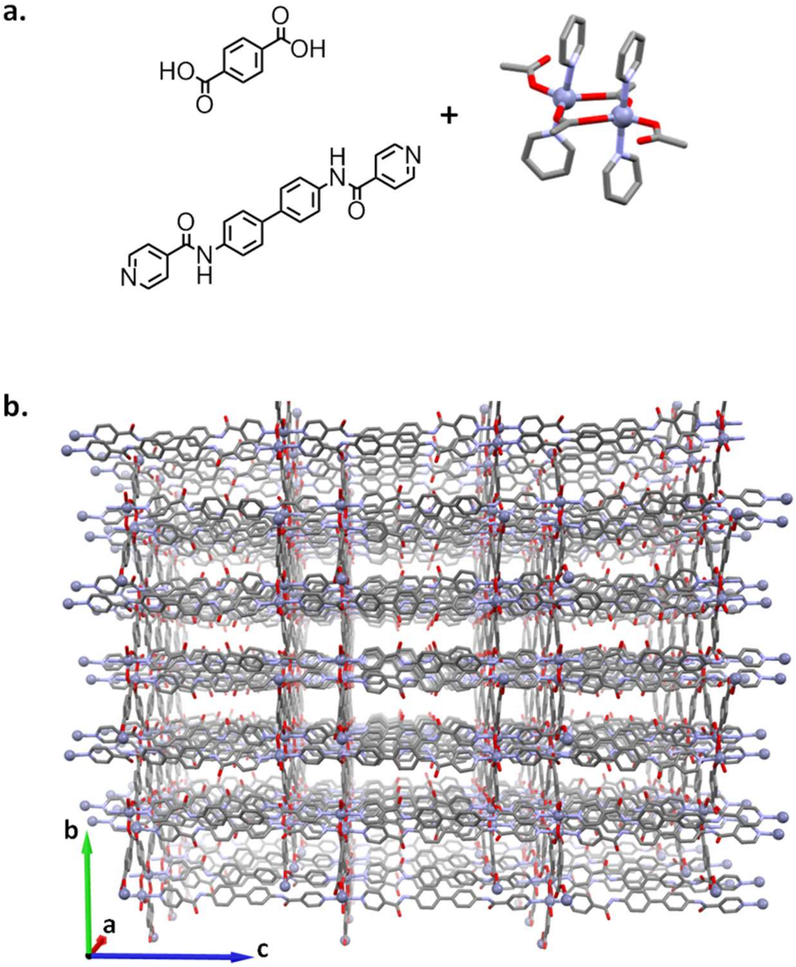

Figure 4.11: a) linkers used for the synthesis of PUM198 and SBU found in the relative structure; b) view of PUM198 pores along crystallographic axis *a*.

As shown in Figure 4.11-a, metal SBU is formed by Zn nodes of the type $[Zn_2(\eta_1\text{-BDC})_2(\eta_2\text{-BDC})_2(\mathbf{L6})_4]$. In this case the two carboxylic functions of a BDC anion behave differently: one COO group bridges two Zn ions belonging to the aforementioned SBU, while the other COO group is η^1-coordinated to a second Zn ion and forms a C=O···H-N contact with a neighbouring amide function, with a D···A distance equal to 2.835Å. (Figure 4.12-b).

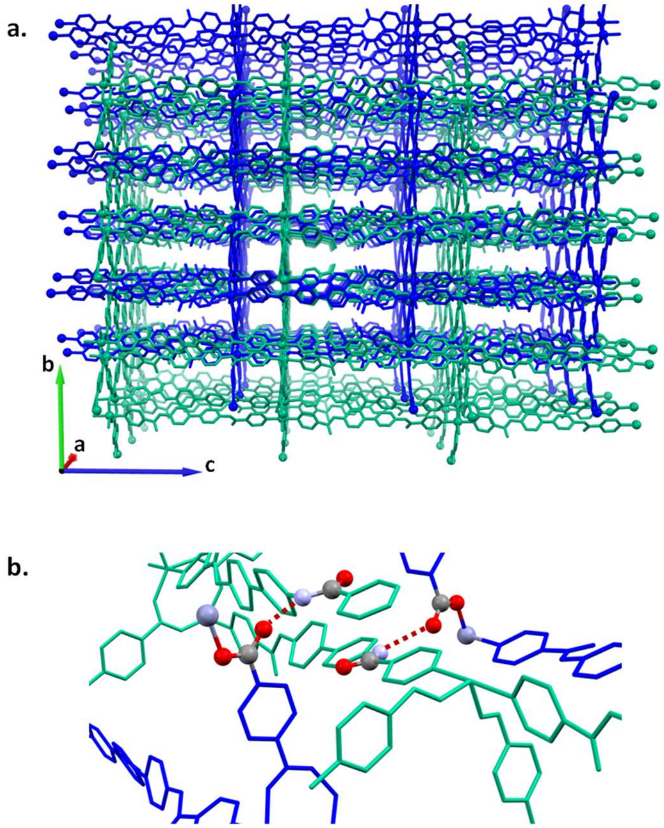

Figure 4.12 a) interpenetrated structure of PUM198: the two nets are plotted in blue and green colours, respectively; b) hydrogen bond interactions (dotted red lines) between monodentate carboxylic moieties and NH sites of the neighbouring MOF net are highlighted

Taking a closer insight to the metal SBU, the Zn···O distances span the range 1.93-1.94, for η_1-BDC, while for η_2-BDC Zn···O are in the range 1.94-1.97 Å. **L6** is bonded to Zn(II) ions with a related Zn···N_{py} distance ranging from 2.19 to 2.25 Å.

The overall structural motif is a doubly interpenetrated framework with pores of 5.6 x 17.4 Å dimensions, filled by several DMF molecules, as shown in Figure 4.13. After removal of solvent electron density, the calculated void volume corresponds to 28% of unit cell, equal to 2125 Å^3 (Contact Surface function by Mercury).

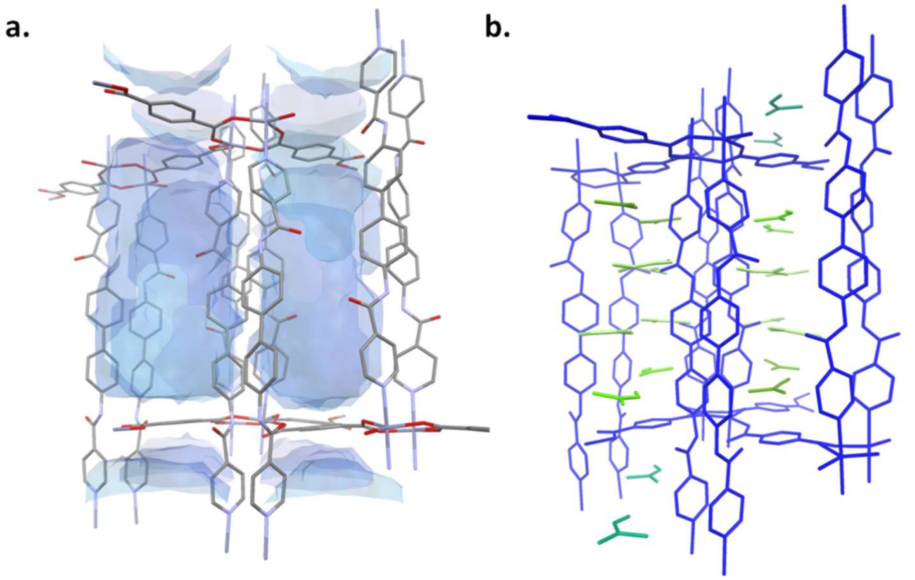

Figure 4.13 a) view of the void surface calculated with Mercury for PUM168; b) DMF molecules filling the pores of PUM168 (view along crystallographic axis a)

Hence, we examined the thermal behaviour of this novel pillared MOF family. Thermogravimetric traces were collected using crystals evacuated by a prior vacuum drying (Figure 4.14). All three frameworks show a good thermal stability, as they decompose at T> 360°C. As expected, the highest temperature of decomposition was observed for the less porous PUM198, which decomposes at around 400°C.

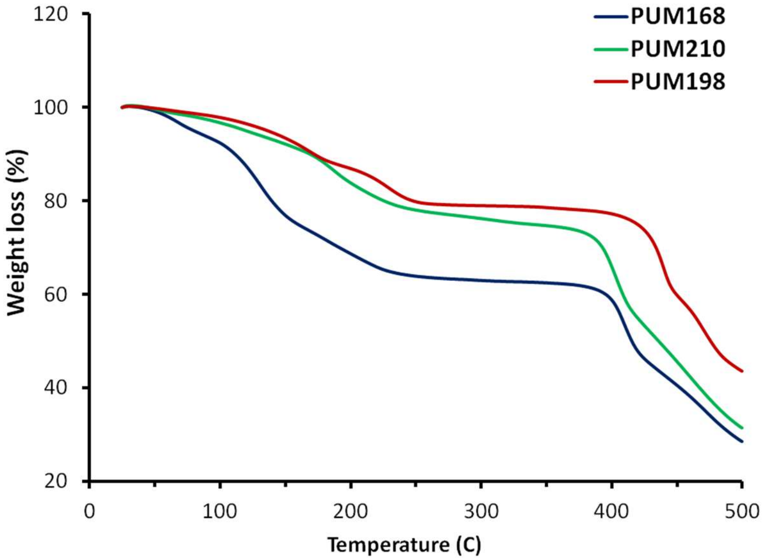

Figure 4.14 Comparison between the thermal traces of the reported pillared MOFs PUM198, PUM168 and PUM210.

All the three traces display an initial slope from room temperature to 250°C, due to the solvent extrusion. As expected, the greatest weight loss was found for PUM168, with an average 36% weight loss. The two slopes observed in the range 160-250°C are reasonably caused by the desorption, the first, of DMF molecules trapped into the channels but not interacting with the MOF walls, while the second derives from the desorption of H-bonded DMF molecules. The progressive drop of the pore volumes associated to the shortening of the carboxylic ligand which is found moving from PUM168 to PUM210 and PUM198, corresponds to a reduction of the amount of extruded solvent: 23% for PUM210 and 19% for PUM198, respectively.

4.5 APIs confinement: a brief introduction

“Are you going to Scarborough Fair?
Parsley, sage, rosemary and thyme,
Remember me to one who lives there,
For she/he once was a true love of mine”.

-Traditional English ballad-

“Nose, nose, jolly red nose,
And who gave thee that jolly red nose?
Nutmegs and ginger, cinammon and cloves;
And they gave me this jolly red nose.”

-Francis Beaumont-

“He that sleeps feels not the tooth-ache.”

-William Sheakspeare, Cymbeline, Act V-

“Take thou this vial, being then in bed,
And this distilled liquor drink thou off;
When presently through all thy veins shall run
A cold and drowsy humour, for no pulse
Shall keep his native progress, but surcease:
No warmth, no breath, shall testify thou livest”

-William Sheakspeare, Romeo and Juliet, Act IV-

Phenol derivatives such as carvacrol, thymol, eugenol and propofol (Scheme 4.4) have been associated to nutraceutical and pharmacological activity.

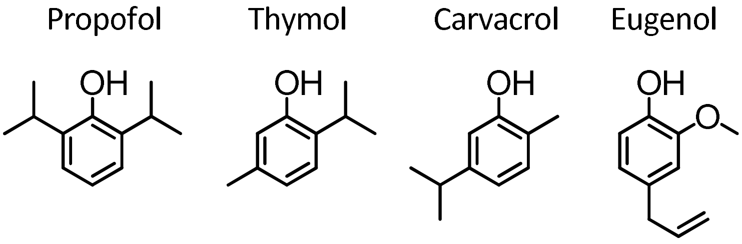

Scheme 4.4 Comparison between structures of the APIs employed in this study.

All these compounds are characterized by a high lipofilicity and a consequent low solubility in water; recent studies suggest that they act as positive allosteric modulators of $GABA_A$ receptor [177,178].

For what concerns propofol, the most famous application is certainly the induction and maintenance of sedation: [179] for this features propofol has been inserted in the World Health Organization's List of Essential Medicines[180]. For the intravenous administration it has been commercialized as DIPRIVAN®, which is a water emulsion: for its chromatic appearance it has also been referred as “milk of anhestesia”.[181] Despite its broad pharmacological application, several issues remain unanswered: among them, the target role of the hydroxyl group [182] and both the action sites in the human brain[183] have been debated.

Carvacrol, thymol and eugenol are plant-derived terpenoids, and belong to the broader family of essential oils, which present the appealing feature to be potential food-preservative.[184] In fact, their anti-oxidative action is coupled with an anti-bacterial activity.[185,186,187] For carvacrol and thymol the inhibitory effect against the growth of *Escherichia coli* bacteria is ascribed to their ability to permeabilize the cytoplasmic membrane. [188] It is noteworthy reporting also their fungicide[189] and anticancer[190] activities.

All this compounds are liquid at room temperature with the exception of tyhmol, that is a low melting solid ($T_{melting}$ =51°C). The crystalline structures of pure carvacrol and eugenol are still unknown.

Essential oils are subjected to several stability problems : oxidative and polymerization processes may lead to alteration of organoleptic properties, joined with the loss of pharmacological properties. [191]
Several attempts have been conducted in order to stabilize essential oils and to build a controlled-release device, with the final goal of obtaining a packaging device able to elongate the food shelf-life.[192] In particular, the activity of pure and mixture of carvacrol and thymol confined in polymer membranes have been examined. The extrusion of these compounds from plastic films was reported by Rupika *et al.* in 2007.[193] More recently, Valero reported the controlled release and the synergic effect of a 1:1 mixture carvacrol/thymol on the proliferation of a number of microorganisms.[194] Furthermore, the use of other combinations of essential oils has been described advantageous for the occurring synergic effects.[195]

In the past few years, our research group has been involved in the study of this series of essential oils: a stabilization has been achieved through the API cocrystallization tools, exploiting both hydrogen and halogen bond interactions with suitable coformers.[103]

Hence, we decided to investigate the trapping of these family of phenols inside our home-made MOFs. We selected PUM168 for several reasons: 1) it assures the formation of high quality X-ray single crystals of mm size; 2) the flexibility coupled with the low symmetry of the host matrix can be advantageous for the definition of the electron density maps of the guest molecules captured inside the host matrix. The low symmetry triclinic P_{-1} group avoids the occurring of static disorder, generated when guest molecules lay on the symmetry elements, which can be a severe issue for high symmetry groups.[77b]

The structural features of the guests should assure an efficient anchoring to the walls of the host species. The hydroxyl groups can in fact play the role of hydrogen bond donor and acceptor group, simultaneously, which renders them capable of interaction with the amidic groups of ligands **L6**. It should be also taken into account that the OH···N is a classical synthon in the field of crystal engineering for the design of molecular architectures.[196]

Owing to the presence of large cavities (14 x 16 Å), with respect to the crystalline sponge used by Fujita, PUM168 can host more than one molecule for pore. The affinity the guest has towards the amide group can pave the way for the creation of guest···guest interactions, which can be responsible of a starting clustering of guest molecules induced by their nanoconfinement into a crystalline matrix.

4.6 Encapsulation of APIs

Propofol and essential oils were loaded into PUM168 by a simple soaking procedure, similarly to PCN-6′@nicotine (page 26). With respect to the protocol employed for PCN-6′, the major difference is the possibility of avoiding the MOF activation protocol. Owing to the high flexibility of PUM168 (see paragraph on gas adsorption, page 178), the removal of solvent from synthesis led to a framework variation associated to a reduction of porosity and a loss of crystallinity. Hence, we decided to perform the soaking experiments directly on as-synthesized MOF: crystals of PUM168 were removed from mother-liquor (usually from 2 to 10 mg) and dipped in neat guest (0.5-2.0 mL). The vial was transferred into a rocking shaker and shacked at room temperature for at least 4 days.

Then, loaded crystals were carefully filtered and dried on a paper prior to be subjected to analytical measurements. The accomplishment of the guest loading was confirmed by DIP/EI-MS analysis: the MS spectra of the extruded gases clearly pointed out the typical m/z fragmentation pattern of the included APIs. A more accurate quantification of the guest was furnished by ^{1}H-NMR spectroscopy, as shown in Figures 4.15-4.18. The crystals were digested in a mixture of deuterated trifluoroacetic acid and dmso getting a clear solution. Taking into account the elemental cell of the native MOF, the asymmetric unit of PUM168 contains three molecules of **L6**: for this reason, a normalized value of 12 protons was attributed to each **L6** doublet (aromatic CH). The integral ratio between these areas and the ones of the diagnostic guest signals (singlet of the CH_3 group for carvacrol and thymol, the doublet belonging to the CH_3 groups of the isopropyl for propofol and singlet belonging to the OCH_3 group for eugenol) can give an estimation of the amount of loaded compound.

Several elements are noteworthy: the presence of a significant residual amount of DMF was confirmed (singlets at ~ 2.8 and 2.7 ppm) for all the soaking experiments, which was estimated to correspond to ~5 DMF molecules for each asymmetric unit. This finds a good agreement with the number of DMF pinpointed in the X-ray structure of native PUM168, molecules which are involved in H-bond interactions with the amidic groups of ligand **L6** as displayed in Figure 4.7. A higher DMF amount was detected with thymol, calculating 12 solvent molecule for native asymmetric unit. Disappointingly, in the case of thymol, the loading performed at 75°C (molten thymol) led to a severe crystal cracking hampering any possible structural investigation.

Sample	Guests molecules	DMF molecules
PUM168@eugenol	~8-9	~5
PUM168@propofol	~11	~5
PUM168@carvacrol	~10	~5
PUM168@thymol	~7	~12

Table 4.4 Summary of ^{1}H-NMR results for PUM168@phenols

Table 4.4 outlines that in all the cases, a considerable loading is reached. In order to exclude the possible effect of a simple guest physisorption, loaded crystals were quickly washed with acetone, subsequently repeating the NMR quantification. Collected NMR proton spectra pointed out again the guest presence, ranging from 2 to 5 molecules, and confirmed unambiguously the successful encapsulation.

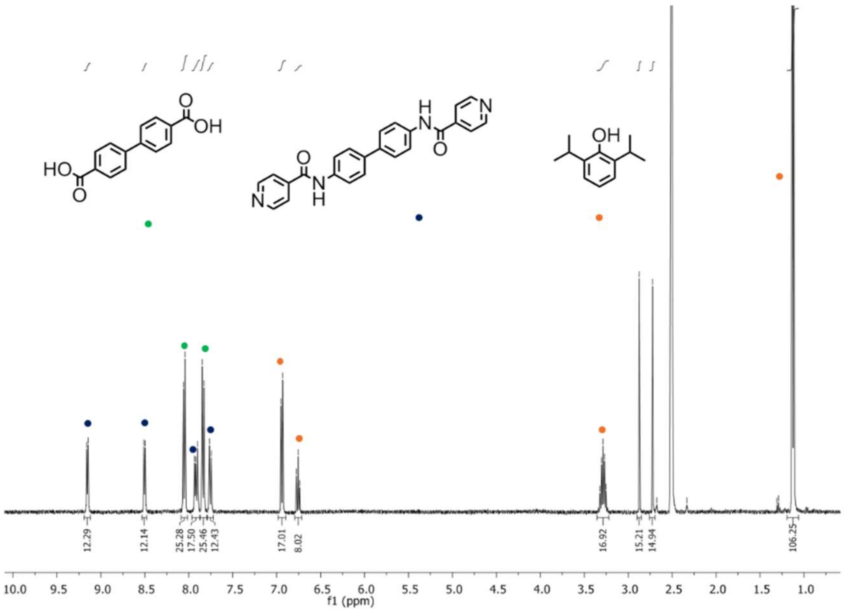

Figure 4.15: ^{1}H-NMR (300 MHz, DMSO-d/TFA-d) digestion of PUM168@propofol

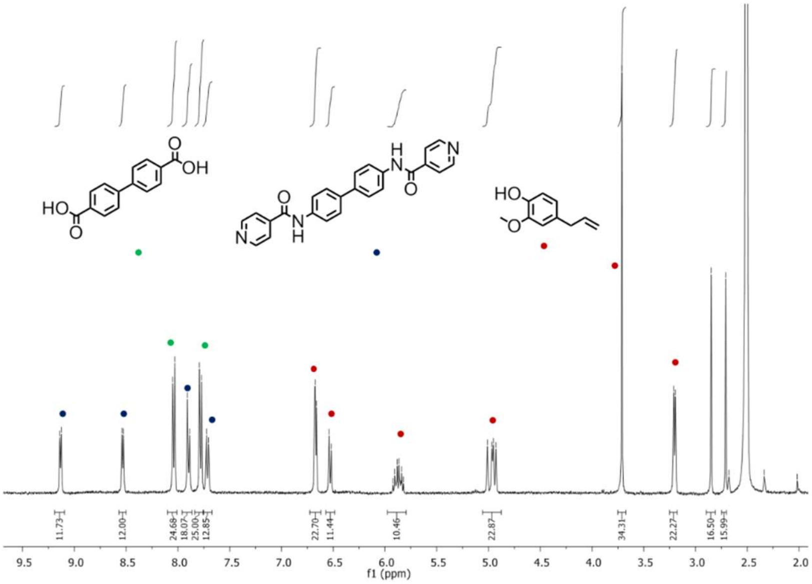

Figure 4.16: ^{1}H-NMR spectrum (300 MHz, DMSO-d/TFA-d) of PUM168@eugenol

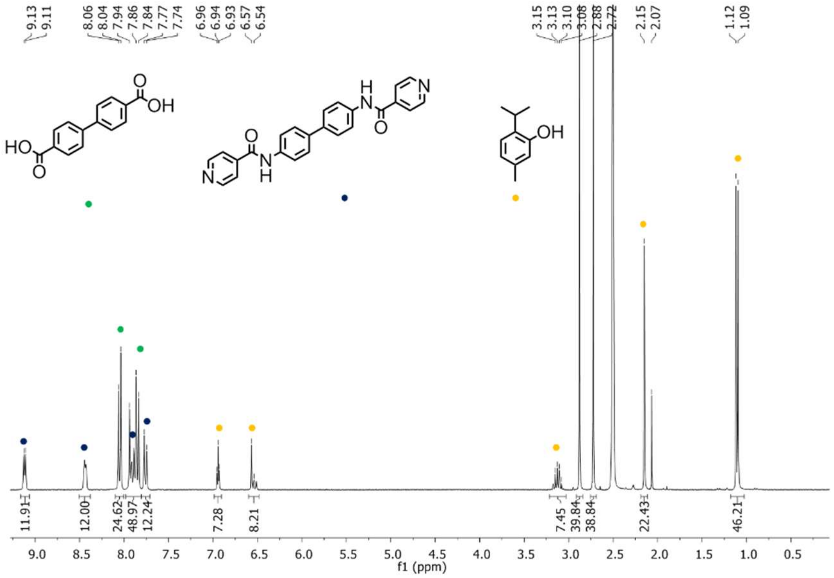

Figure 4.17: ^{1}H-NMR spectrum (300 MHz, DMSO-d/TFA-d) of PUM168@thymol

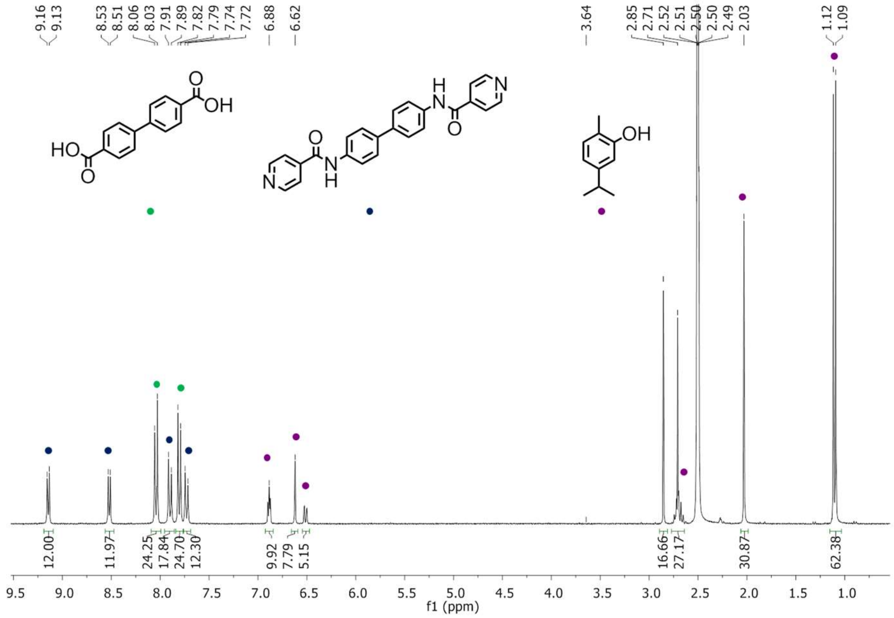

Figure 4.18 ^{1}H-NMR spectrum (300 MHz, DMSO-d/TFA-d) of PUM168@carvacrol

4.6.1 Structural analysis

To gain optimal structural data, SC-XRD experiments were carried out with synchrotron light radiation. Good results were obtained with carvacrol, eugenol and propofol. Fresh crystals from the soaking vials were flash frozen in liquid nitrogen and analysed at 100K.

The crystals of all three host-guest systems, i.e. PUM168@carvacrol, PUM168@eugenol and PUM168@propofol showed high resolution data. These allowed an accurate structural investigation not limited to the host but suitable also for several included guest molecules. These results can be considered highly significant owing to the difficulty usually experienced in modelling guest molecules accommodated in large cavities, due to the high molecular disorder. This allowed for an analysis of the host-guest interactions responsible of the embedding of the guest molecules into the cavities featuring the crystal framework of PUM168, making also possible the definition of some intermolecular interactions between different guest molecules. The knowledge of such interactions is of paramount importance to gain information about the mechanism governing the uptake process and to study some possible aggregation phenomena involving nanoconfined molecular guests.

A view of the filling of the cavities present in PUM168 with molecules of eugenol is given in Figure 4.19.

Figure 4.20 shows instead a detail about the intermolecular interactions occurring between eugenol and the walls of PUM168.

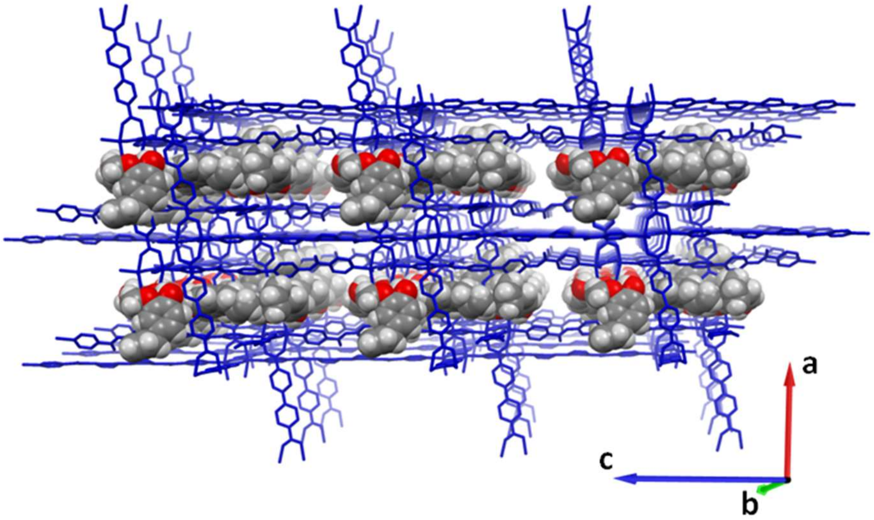

Figure 4.19 Overview of PUM168@eugenol channels filled by guest molecules.

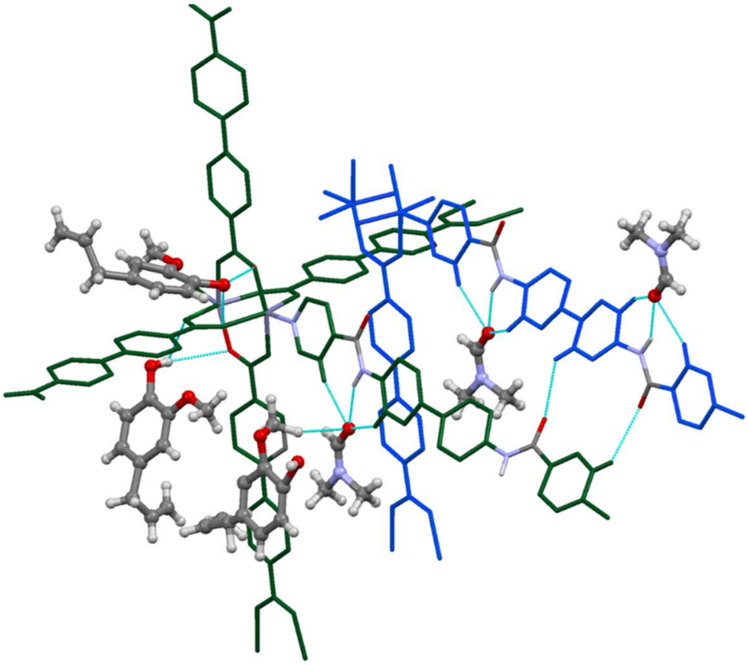

Figure 4.20 Hydrogen bond contacts found in the structure of PUM168@eugenol. The two different nets of the MOF are coloured in blue (*trans* net) and green (*cis* nets). It can be noted that eugenol interacts with an oxygen of the paddle-wheel, while DMF molecules interact with the amide groups.

The structural result evidences that eugenol is able to insert into the crystalline framework and finding good interaction sites for its stabilization. The uptake of eugenol, however, does not lead to the replacement of the DMF molecules H-bonded to the amide groups, which maintain the same positions occupied in native PUM168. The stabilization of eugenol occurs in fact through hydrogen bond interactions involving the OH group of the guest with a carboxylic oxygen of the Zn paddle-wheel, with a OH•••O distance of 2.81Å. Taking disorder and partial occupancy into consideration, PUM168@eugenol counts 4 molecules of eugenol and 4 molecules of DMF for three paddle-wheels. As previously mentioned, the flexibility of the host framework might play an important role for the encapsulation process. In fact, the partial replacement of DMF with eugenol leads to a deformation, with respect to native PUM168, of both the centric and acentric nets along the b axis, as shown in Figure 4.21.

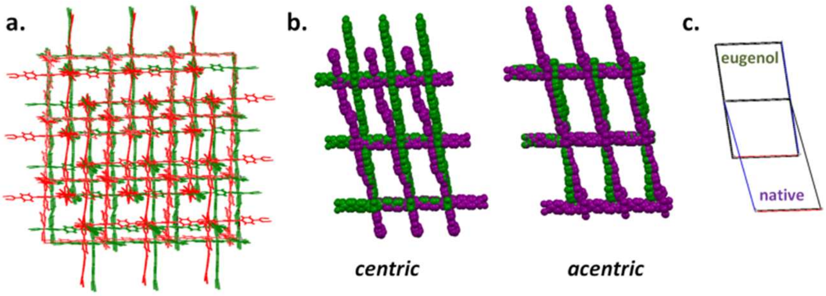

Figure 4.21 a) Deformation of the framework caused by eugenol trapping (red colour for native nets, green colour for PUM168@eugenol; b) Comparison between centric and acentric nets of PUM168 (left) and PUM168@eugenol (right); c) Variation of the beta angle of the unit cell after eugenol encapsulation.

This deformation is more pronounced for the centric net and is reflected on the difference in the beta angle between the two structures.

Differently from eugenol, trapped propofol is involved in interactions with the amidic groups of **L6**, as displayed in Figure 4.22.

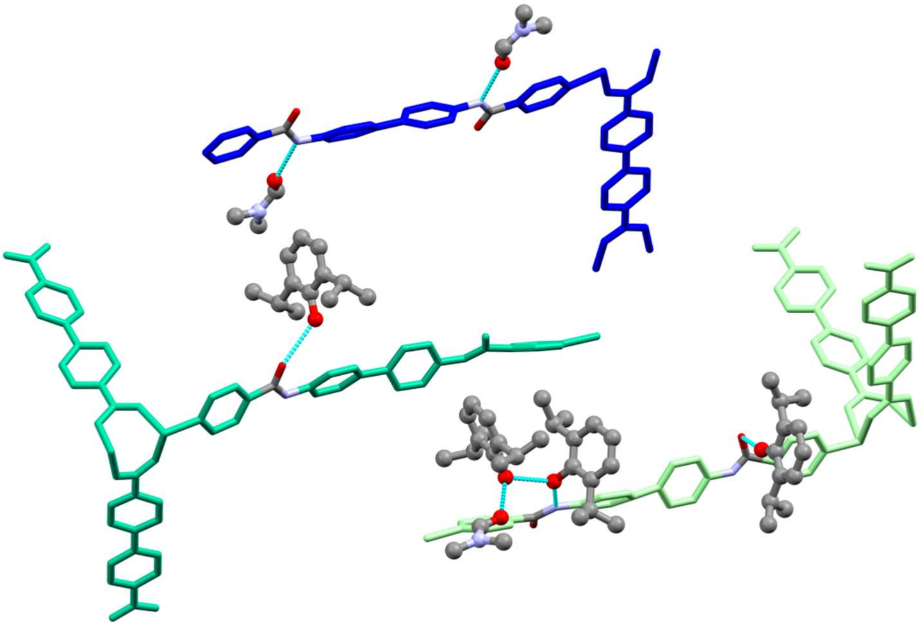

Figure 4.22: Hydrogen bond interactions between propofol and the amide groups of L6 in PUM168@propofol (hydrogen atoms are omitted for clarity)

One interaction is a OH···O=C hydrogen bond involving propofol as HB donor and the amidic oxygen as HB acceptor, with a O-H···O distance of 2.84Å. The second H-bond motif regards propofol acting as a mutual H-bond donor-acceptor: one propofol molecule receives H-bond from amidic nitrogen and at the same time acts as a H-bond donor towards a second guest molecule. The N-H···O and O-H···OH contact distances are 3.01Å and 2.62Å, respectively.

It should be also recalled that pure propofol crystallizes as a tetramer, displaying a square planar arrangement of four hydroxyl groups sustained by OH···OH contacts: the averaged O···O distance of 2.73 Å, value very similar to the one observed above between nanoconfined guest molecules into PUM168. [197]

Similarly to propofol, carvacrol acts both as an hydrogen bond donor and acceptor, as highlighted in Figure 4.23. This trait allows the formation of carvocrol homodimers embedded in PUM168.

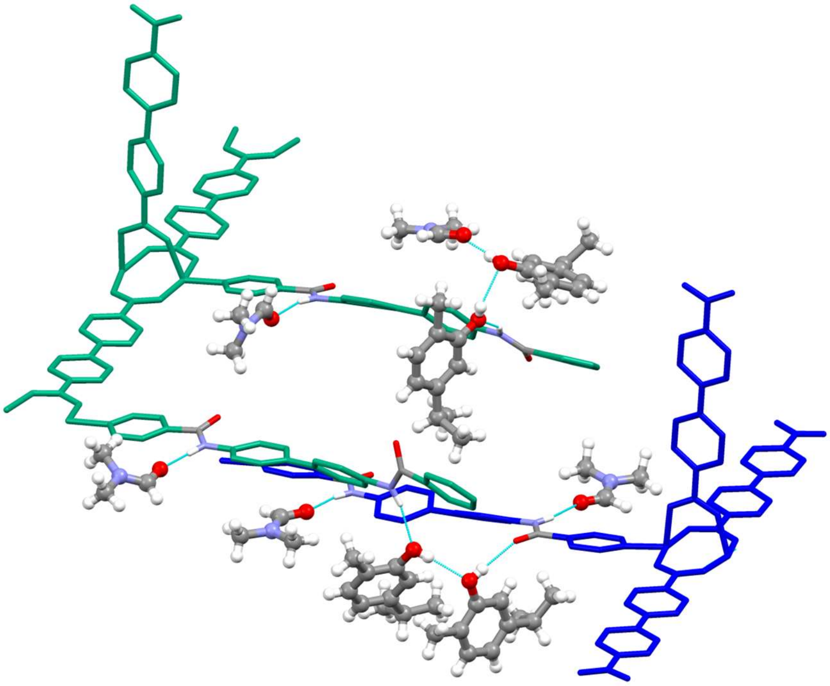

Figure 4.23: Carvacrol interactions with MOF net: *trans* net plotted in blu, *ci*s net plotted in deep green. Two distinct hydrogen bond motifs are clearly visible.

Likewise PUM168@propofol, one NH moiety of the *cis*-net is H-bonded to a carvacrol OH group which, in turn, interacts with a second carvacrol guest. The latter acts as HB donor towards a DMF molecule. The D•••A distances are very similar to the ones previously commented for propofol, with a O•••O contact of 2.76 Å. A comprehensive overview of the HB motifs, as can be inferred from Table 4.5.

MOF	***N*H···*O*H (Å)**	***O*H···*O* (Å)**	***O*H···*O*=C_{DMF} (Å)**
PUM168@prop	3.01	2.68	2.62
PUM168@carv	3.01	2.76	2.69

Table 4.5 HB motifs found in PUM168@propofol and PUM168@carvacrol

Interestingly, in all the host-guest systems described, the *trans*-net maintains the H-bonded DMFs. In PUM168@carvacrol the trans net is engaged in host-guest interactions involving the amidic C=O group (see Figure 4.23).

Figure 4.24 highlights the hydrogen bond network involving two molecules of carvacrol, the CO group of the trans net and the NH group of the cis(oid) net (green frameworks and guest molecules).

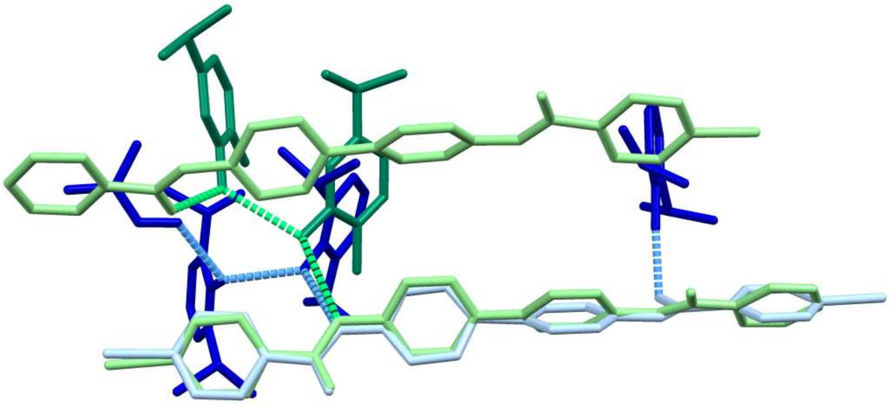

Figure 4.24 Superimposition of bis-amidic **L6** linkers and H-bonded guests for PUM168@carvacrol (light green, trans-net and cisoid-net) and PUM168@propofol (light blue, transoid-net). Propofol is plotted in blue, carvacrol is plotted in deep green. Hydrogen bond interactions are depicted in light blue for PUM168@propofol, and in light green for PUM168@carvacrol.

A similar pattern is found in PUM168@propofol, where the C=O group now belongs to DMF instead of L6 (blue frameworks and guests in Figure 4.24). A summary of the D···A distances is provided in Table 4.6.

MOF	***N***H···***O***H (Å)	***O***H···***O***H (Å)	***O***H···C=***O*** (Å)	***N***H-***O***H-***O***H (°)
PUM168@prop	3.01	2.68	2.62	116.8
PUM168@carv	3.06	2.88	2.78	136.5

Table 4.6 A comparison between the HB contacts in PUM168@carvacrol and in PUM168@propofol

One possible explanation of the two different geometries of these two H-bond arrangements might rise from the different substituents occupying the orto position in the aromatic ring of the phenol derivatives. Owing to the larger steric hindrance of isopropyl groups, propofol molecules are not able to bridge two neighbouring MOF nets, preferring the HB contact with a DMF molecule.

The inclusion of the guests leads to different structural rearrangements of the crystalline host framework. In Figure 4.25 the networks of native PUM168 (Figure 4.25-a) and of the three host-guest species PUM168@eugenol (Figure 4.25-b), PUM168@propofol (Figure 4.25-c) and PUM168@carvacrol (Figure 4.25-d) are reported.

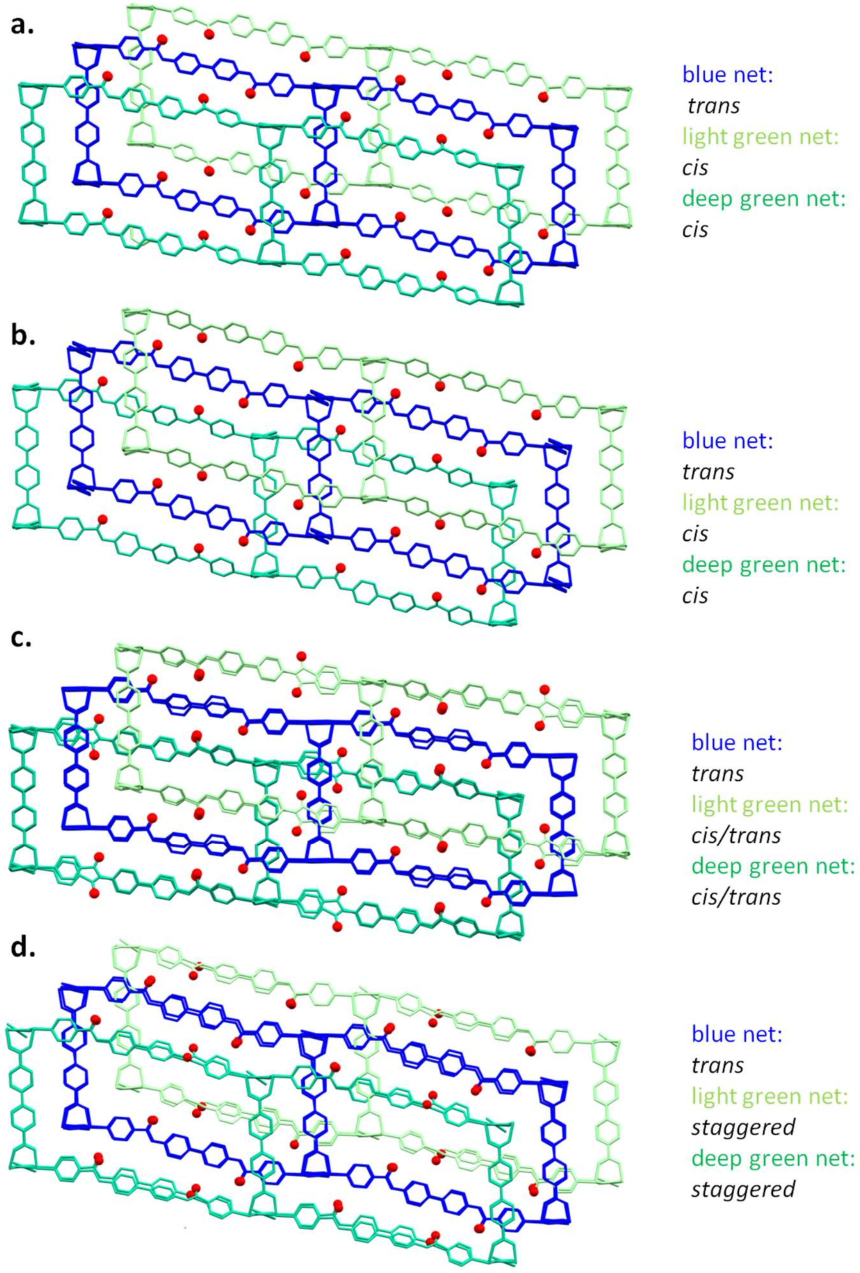

.

Figure 4.25 Comparison between the amide conformation for: a) native PUM168, b) PUM168@eugenol, c) PUM168@propofol, d) PUM168@carvacrol. The amidic oxygens are plotted in red, hydrogen atoms and disordered positions are omitted for clarity.

The conformational rearrangements involve only the cis frameworks, which see the replacement of the DMF molecules with the guest ones. The trans framework remains unaltered and retains the H-bonded DMF molecules (compare Figure 4.25.a-d).

In the case of eugenol, only a very slight change is observed and the acentric nets retain a *syn* conformation (compare Figure 4.25a-b).

An intermediate situation is observed for carvacrol, where the guest inclusion is related to a the rotation of an amide C=O group of **L6** of about 90° with respect to the pristine PUM168, (compare Figure 4.25.a and d) which leads to a final staggered conformation of the amidic nets. This rotation allows the formation of the carvacrol dimers depicted in Figure 4.24.

Finally, as reported in Figure 4.25.c, the propofol encapsulation is associated to an even more significant rearrangement of the *cis* nets with respect to native PUM168 Figure 4.25-a.

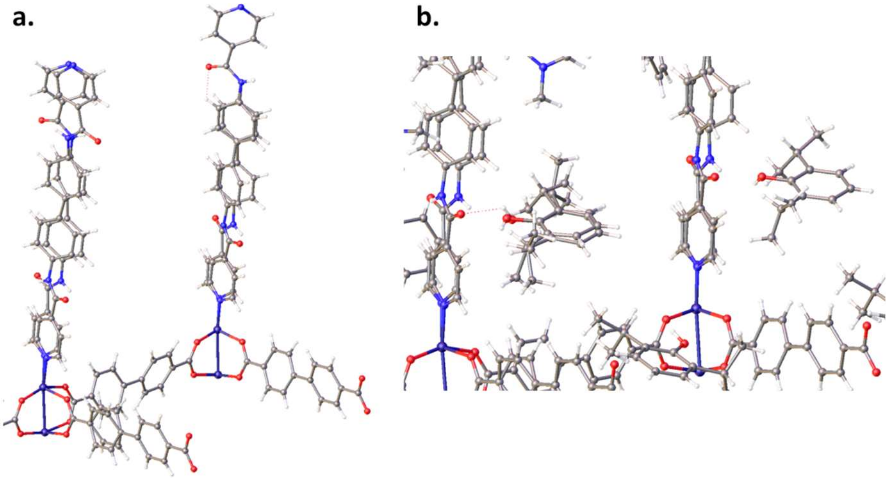

Figure 4.26: a) Former *cis* net after propofol inclusion: disorder of amidic ligands; b) propofol interaction with disordered net

In fact, propofol inclusion is also associated with an extended conformational disorder of the amidic linker, indicating the partial cis-to-trans conformational isomerization of the amide groups. It has been possible to structurally model the two different isomers, as illustrated in Figure 4.26-a.

Interestingly, both conformers are engaged in H-bond contacts with propofol molecules. Figure 4.26-b shows the overlap of two modelled propofols, each with a 50% occupancy: one interacting with a C=O group of the cis net, the latter displaying an interaction with a NH group belonging to the trans isomerised conformer

The network behaviour upon the guest inclusion is deeply reflected also in the unit cell parameters, as shown in Figure 4.27. This allows to obtain a more rigorous rationalization of the guest driven rearrangement. Crystallographic axis *c* represents the pillar dimension with an average length of 26.9 Å, and for this reason it remains unaltered for all the unit cells of PUM-168@phenols.

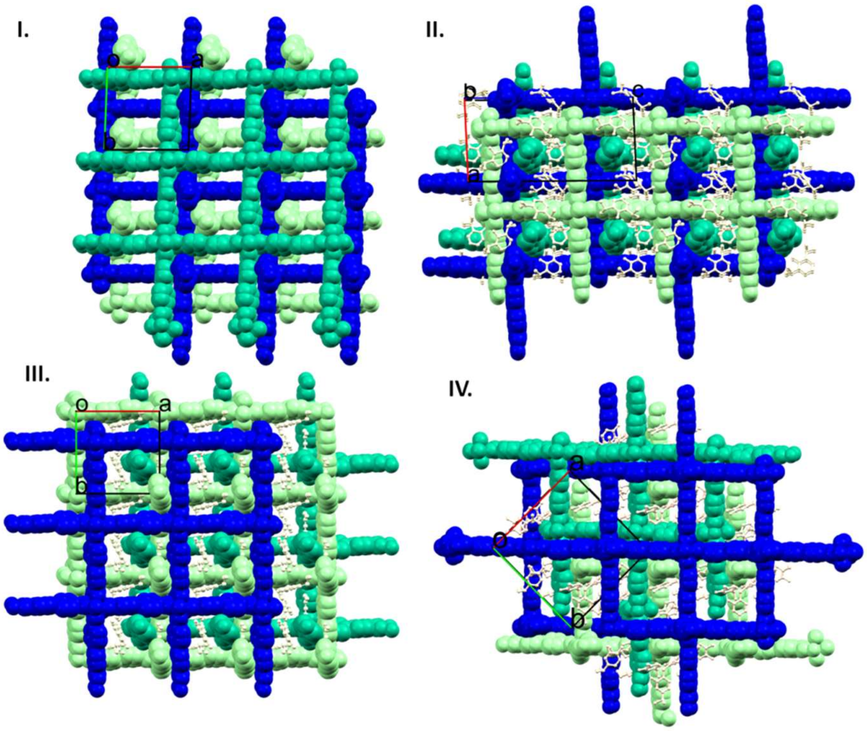

PUM168 native	PUM168@eug	PUM168@prop	PUM168@carva
a= 15.116 Å	a= 15.178 Å	a= 15.266 Å	a= 21.478 Å
b= 15.204 Å	b= 15.218Å	b= 30.503 Å	b= 21.554 Å
c= 26.896 Å	c= 26.910 Å	c= 26.955 Å	c= 26.888 Å
α= 101.52 °	α= 78.44 °	α= 89.23 °	α= 94.90 °
β= 103.54 °	β= 83.16 °	β= 97.84 °	β= 102.41 °
γ= 90.375 °	γ= 88.50 °	γ= 92.20 °	γ= 89.99 °
V= 6133 Å^3	V= 6042 Å^3	V= 12421Å^3	V= 12109 Å^3

Figure 4.27 Comparison between unit cells of native PUM168 and PUM168@phenol series: I) native PUM168; II) PUM168@propofol; III) PUM168@eugenol; PUM168@carvacrol.

On the other hand, crystallographic axes *a* and *b* correspond to carboxylate square grids: their lengths change depending on the network rearrangement. As previously commented, PUM168@eugenol is characterized only by marginal framework variations due to MOF flexibility, while no conformational change of **L6** is detected. Consequently, the crystallographic axes *a* and *b* do not change appreciably.

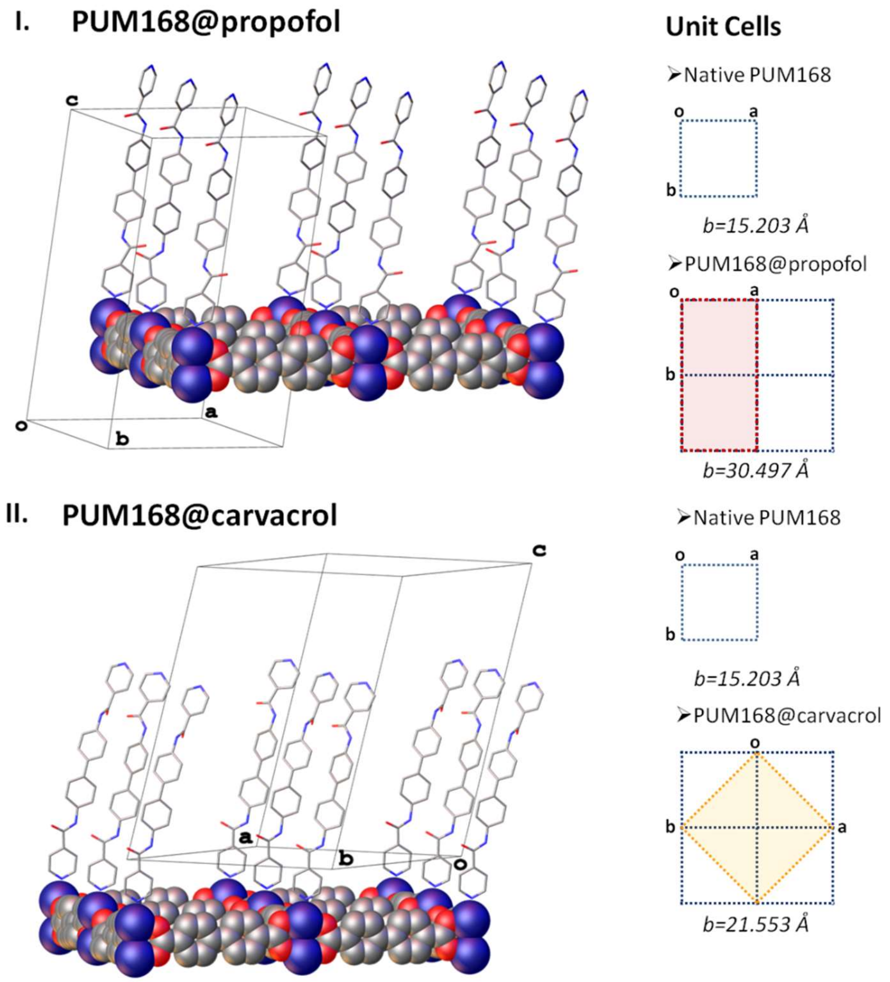

I. PUM168@propofol

Unit Cells

II. PUM168@carvacrol

Figure 4.28 Rationalization of the conformational changes on *b* parameter of unit cells of PUM168@propofol (I) , and PUM168@carvacrol (II).

The occurring conformational changes of the acentric net for PUM168@propofol and PUM168@carvacrol are associated to a nonequivalence of the amidic functions, as illustrated in Figure 4.28. This leads to a remarkable variation of *b* axis which differs from the original one, being elongated by the reduced translational symmetry.

As shown in Figure 4.28-I, PUM168@propofol shows an alternate trans/cis conformation of the amidic moieties: *b* axis is doubled in order to consider one cis and one trans **L6** conformation at the same time, with a final value of 30.497Å.

PUM168@carvacrol is related to a slight different transformation of the unit cell: the staggered conformation leads to a loss of translational order within the same row, as displayed in Figure 4.28-II. The central **L6** of the second row exhibit a dissimilar staggered conformation with respect to neighbouring nodes. The result is a difference both in the cell orientation and dimension, with crystallographic axes *a* and *b* equal to ~21.5 Å. The point of diagonals intersection of the resulting square corresponds to the position of the staggered amide with unrepeated conformation in Figure 4.28-II.

4.6.2 APIs mixture

Encouraged by the excellent results obtained with the loading of pure APIs, we decided to move our attention onto the loading of guests mixtures. In this case, our final aim was the investigation of a possible selectivity of PUM168 towards a specific guest inclusion. Moreover, it has been reported that the inclusion of a mixture of essential oils inside a polymeric film led to higher antibacterial proprieties with respect to the single components.[194]

For the loading tests, we applied the same protocol previously described for the pure guests (page 139) employing an equimolar ratio of each essential oil. In the case of mixtures containing thymol, the only solid guest employed, this was dissolved easily in the other liquid component (carvacrol or eugenol). To gain a first quantification of the ratios of each component included, after soaking the filtered crystals were digested in deuterated TFA and subjected to ^{1}H-NMR analysis. The results for 1:1 mixtures of eugenol/carvacrol (named PUM168@ec-mix), eugenol/thymol (named PUM168@et-mix) and carvacrol/thymol (named PUM168@ct-mix) are collected in

Table 4.7; the spectra are collected in Figure 4.29-4.31.

Sample	Guests Ratios	DMF molecules
PUM168@ec-mix	Eu/Car 2.38: 1	~0,45
PUM168@et-mix	Eu/Thy 1.81:1	~3,18
PUM168@ct-mix	Car/Thy 1.79:1	~0,59

Table 4.7 Summary of the NMR results for PUM168@mix series.

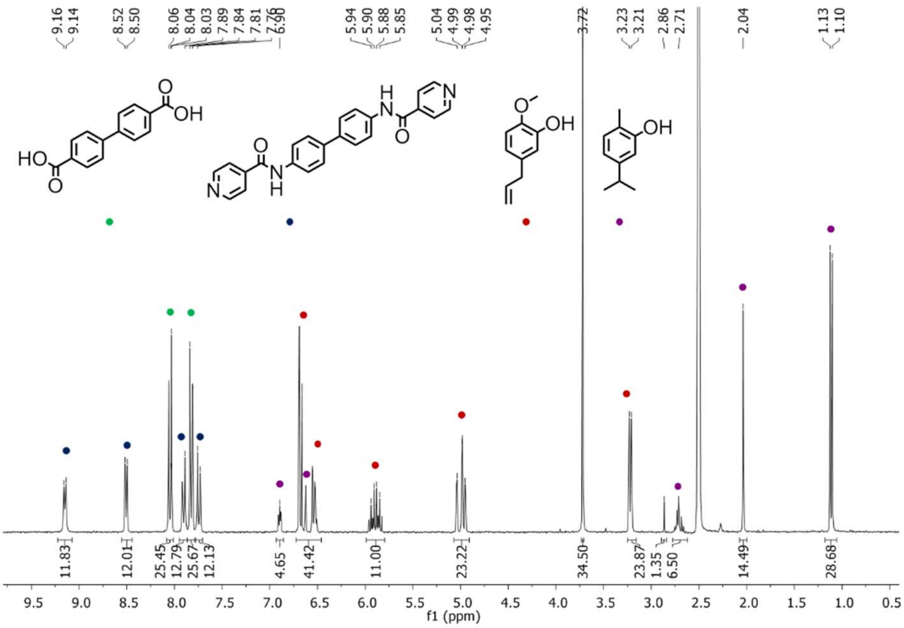

Figure 4.29: ^{1}H-NMR spectrum (300 MHz, DMSO-d/TFA-d)of PUM168@ec-mix

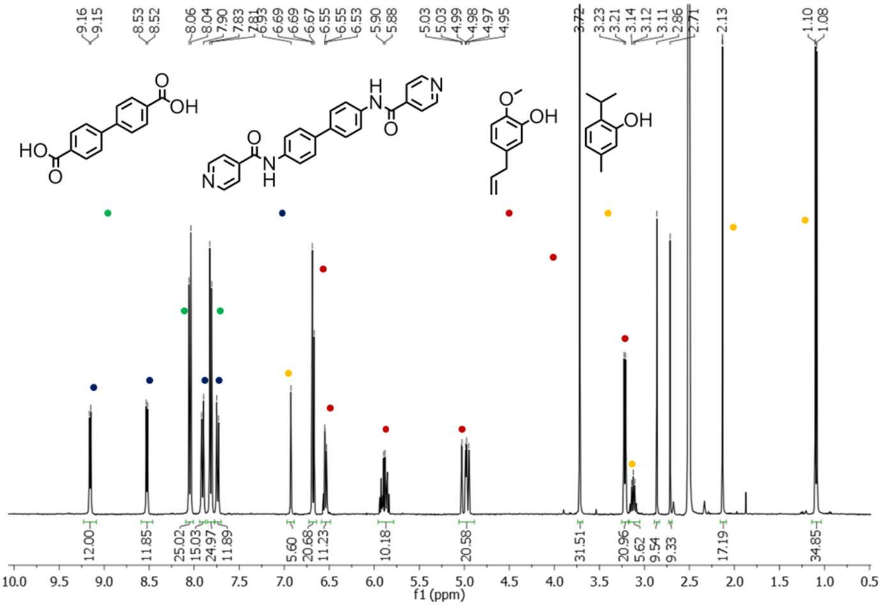

Figure 4.30 ^{1}H-NMR (300 MHz, DMSO-d/TFA-d) spectrum of PUM168@et-mix

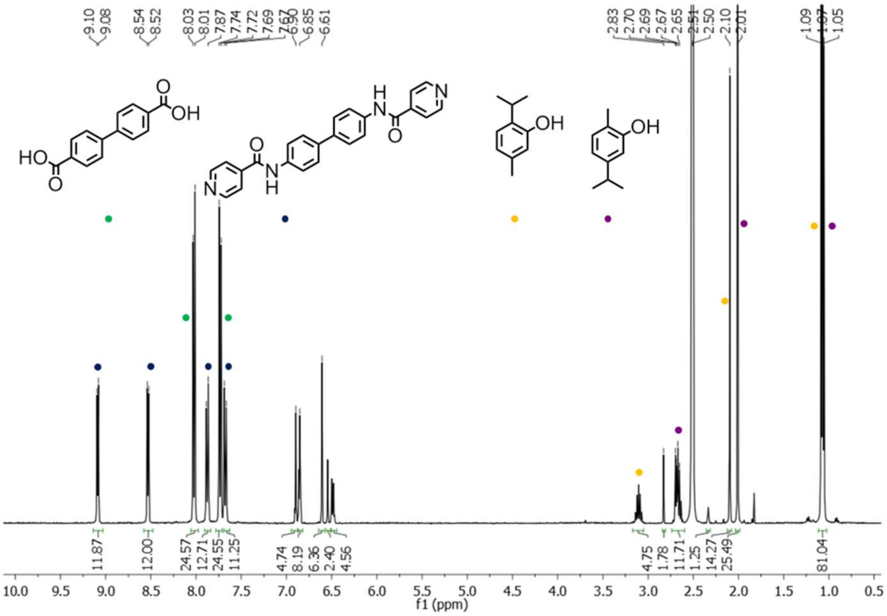

Figure 4.31 ^{1}H-NMR (400 MHz, DMSO-d/TFA-d) digestion of PUM168@ct-mix

As previously commented for the soaking of pure phenol derivatives, a normalized area of 12 protons was attributed to each aromatic doublet of **L6**, taking into account the number of **L6** in the asymmetric unit of native PUM168. Hence, the normalized areas of each guest are related to three **L6** units.

All collected spectra point out a remarkable lower residual amount of DMF (signals at 2.83-2.70 ppm) compared with the ones observed for the soakings of the single guest: the number of the residual DMF molecules range from 0.45 (PUM168@ec-mix) to 3.18 (PUM168@et-mix) molecules. The presence of carvacrol seems to be beneficial for the almost complete DMF removal. This might hint the presence of a cooperative effect played by the two different guests in the guest-DMF exchange process.

In all samples, both guest species were detected at the same time, indicating the success of nanoconfinement of the essential oil mixture into PUM168 pores.

In addition, a moderate selectivity among the single component encapsulation was detected: the analyses suggest a superior affinity for eugenol over carvacrol and thymol. On the other hand, the preferential loading of carvacrol is observed with respect to its positional isomer (Table 4.7).

4.6.3 Structural Analysis

SC-XRD experiments were carried out with synchrotron light radiation, by flash freezing at 100K of fresh crystals taken directly from the soaking mixtures after 4 days.

In all cases the crystals of PUM168@ec-mix, PUM168@et-mix and PUM168@ct-mix showed high resolution data, suitable for a very fine modelling of the guest electron density located in the pores of PUM168. For each sample, both guests were detected at the same time, indicating the success of nanoconfinement of the essential oil mixture into PUM-168 pores.

For PUM168@ec-mix, two DMF molecules are still hydrogen bonded to NH moieties of the *trans*-net, which then do not participate to host-guest interactions.

The modelling of the electron density map allows to detect several disordered molecules of eugenol and carvacrol inside the cavities of the MOF. As seen with PUM168@eugenol and PUM168@carvacrol, the pinpointing of the guest molecules was possible only for those interacting with the host-walls through hydrogen bonds. Interestingly, the two guests occupy the same positions they have in the corresponding single-guest systems, i.e. PUM168@eugenol and PUM168@carvacrol. Then, two molecules of eugenol contact a paddle-wheel unit through O-H···O hydrogen bond interactions, while carvacrol contacts the NH moiety of one amide group of the cis net. The intermolecular contacts are displayed in Figure 4.32.

For eugenol, the two OH···O distances are 2.84 Å and 3.08 Å, while for carvacrol the contact distance is 2.96 Å.

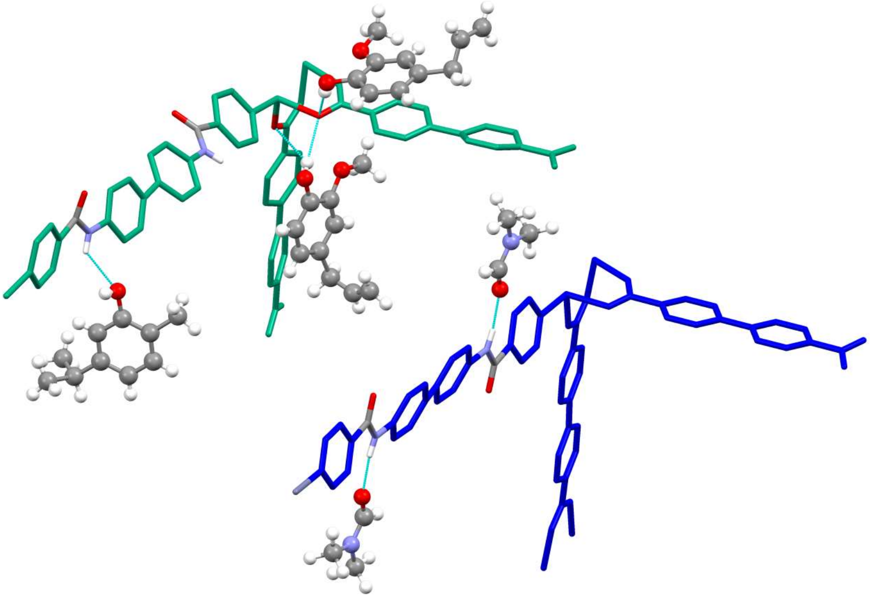

Figure 4.32 H-bond interactions found in PUM168@ec-mix involving the two guests carvacrol and eugenol.

The higher trapping of eugenol is reflected also on the guest modelling: a series of disordered eugenol molecules can be defined in the asymmetric unit. Figure 4.33.a-b illustrates some examples of disordered eugenol molecules. It is worth commenting that, also in the proximity of the amidic NH involved in H-bond with one molecule of carvacrol, a disordered eugenol molecule is located (Figure 4.33.a).

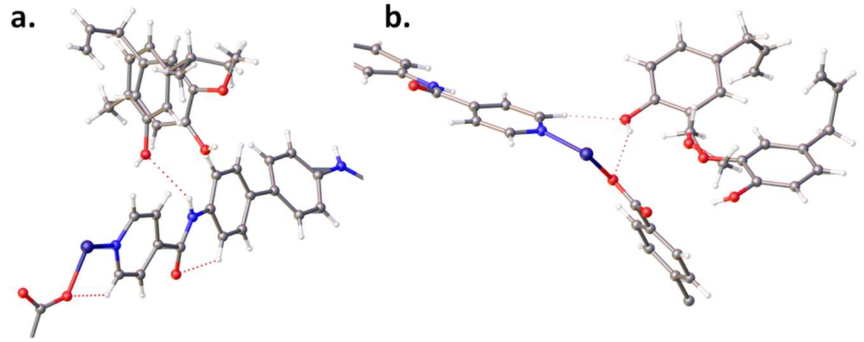

Figure 4.33 a) overlap of disordered carvacrol and eugenol interacting with the amide function in PUM168@ec-mix; b) disordered eugenol molecules interacting with the COO group in PUM168@ec-mix; a second weak interaction involving a pyridine hydrogen is also highlighted

In this case, eugenol is capable of interacting with the amidic NH group of the cis net. Similarly to the neighbouring disordered carvacrol, the observed contact is a NH···O where eugenol acts as HB acceptor, with a N-H···O distance of 3.08Å.

The switch of carvacrol with its substitution isomer, thymol, led to a substantial different structural arrangement corresponding to PUM168@et-mix, as illustrated in Figure 4.34. Here, the amidic linkers belonging to the trans net are not innocent towards the host-guest interactions. Although both N-H donors remain engaged in H-bonds with DMF molecules, the C=O functions are contacted by thymol molecules which behave as HB donors. The resulting motif is of the type OH···O=C, with a $O_{thymol}\cdots O_{DMF}$ separation of 2.74 Å. As regard eugenol, it behaves similarly to what seen in PMU168@ec-mix, forming NH···OH contacts with the amide groups of the cis-net (NH···O distance of 3.05Å) and forming OH···O contacts with the paddle-wheel unit (distance of 2.74 Å).

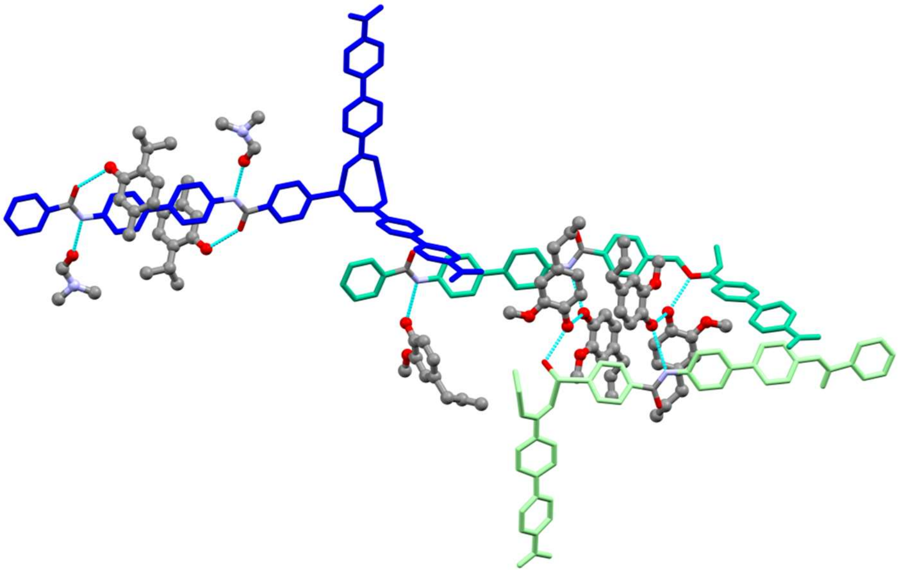

Figure 4.34 Overview of PUM168@et-mix: trans net plotted in blue colour, cis nets depicted in green colours. A representation of the different HB motifs is provided.

However, the most remarkable structural motif is the formation of two eugenol···eugenol homodimers, which bridge together two adjacent cis framework, as depicted in Figure 4.34). Starting from the NH donor sites, two eugenol molecules act both as HB donor and acceptor linking the final COO carboxylate oxygen belonging to the Zn paddle-wheel, with a zig-zag arrangement. Shortest distances are the OH···OOC and the homodimer OH···OH, both featured by a corresponding donor···acceptor distance of 2.75Å. Interestingly, this intra-dimer distance is intermediate between the value of 2.68 Å found with propofol and the of 2.88Å found with carvacrol. Finally, a weaker contact is related to the synthon NH···OH, with a H···O and N···O distances of 2.38Å and 3.19Å, respectively.

The structural analysis of PUM168@ct-mix, conveys a series of fascinating elements.

In this case the DMF molecules are not yet retained in the structure, structure which has undergone a significant variation also at the expense of the trans net. The absence of the solvent molecules found a nice agreement with the NMR spectroscopic data, which showed a very low residual amount of DMF. Considering the number of molecules pinpointed in the structure, a prevalence of carvacrol over thymol could be hypothesized (in agreement with the ^{1}H-NMR data).

The host guest interactions involving initially trans net are depicted in Figure 4.35.

The amidic C=O acts as HB acceptors towards the contact hydroxyl groups, with a O_{carv}···O distance ranging from 2.70 Å to 2.75Å. The hydrogen bonded carvacrol molecules lay on the same plane of the engaged carbonyl moiety.

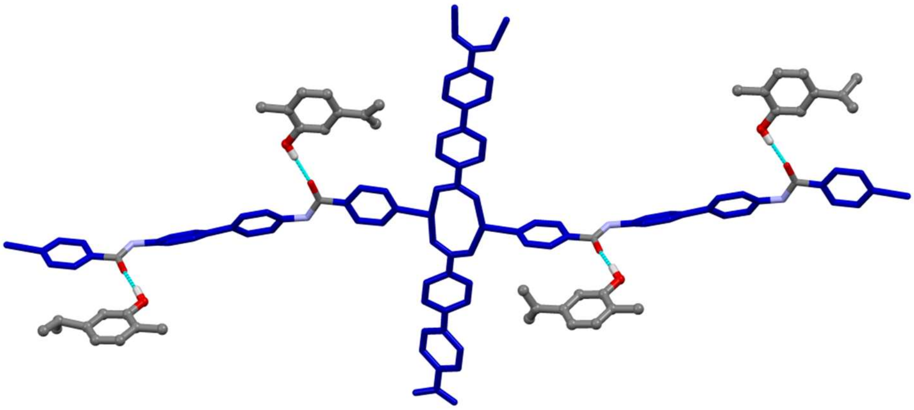

Figure 4.35 Carvacrol interactions with the net of PUM168@ct-mix

Moving our attention to a neighbouring net, an additional type of carvacrol interaction is observed, now involving the carboxylate oxygen of the Zn paddle-wheel (Figure 4.36). The $O_{carv}\cdots O$ distance is now 2.75Å.

In Figure 4.36, the very first examples of OH···OH hetero-dimer aggregations in a nanoconfined space can be evidence, indicated as **a**, **b** and **c**. In a and b the hetero-dimer are anchored to the MOF nets, whereas in **c** the hetero-dimer does not interact with the MOF walls.

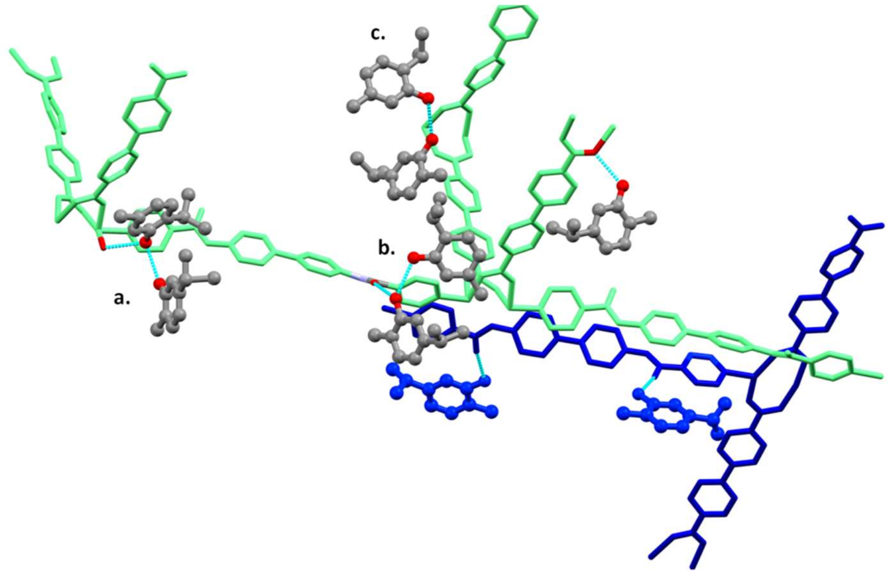

Figure 4.36 Heterodimers carvacrol-thymol observed in PUM168@ct-mix

The **a** and **b** nano-aggregates engage two different anchoring sites of the host: a carboxylic oxygen belonging to Zn paddle-wheel and the amidic C=O moiety, respectively. For the heterodimer **a** thymol acts as HB-donor towards the acceptor anchoring site, while for **b** this role is played by carvacrol. The resulting OH···O interactions display a D···A distance of 2.67Å for **a**, and of 2.72Å for **b**, respectively. In the two hetero-dimers a and b the OH•••O distances are 2.76Å and 2.81Å, respectively. Finally, the heterodimer **c** is based on a OH···O contact of 2.79Å.

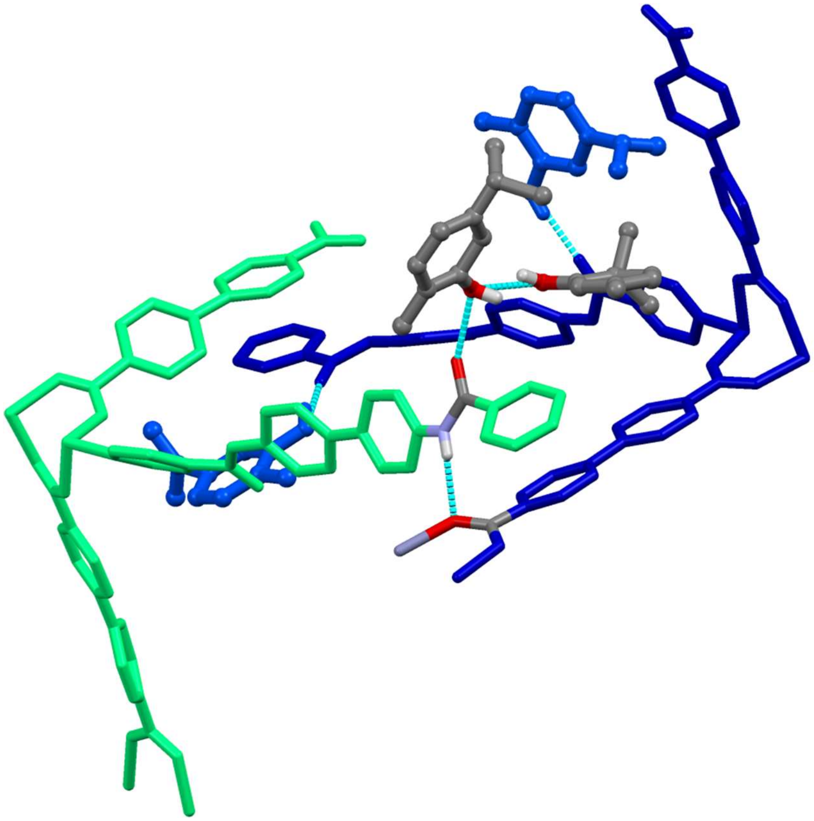

Figure 4.37 H-bond interactions between MOF nets in PUM168@ct-mix: NH moiety acts as HB-donors towards carboxylate paddlewheel.

Figure 4.37 provides a closer look of the environment of the heterodimer **b**: the guest-induced structural rearrangement leads to the occurring of a N-H···OOC H-bond involving the amide and the carboxylate groups of neighbouring nets. The NH···OOC distance is of 3.03Å.

Significative structural deformations of the host frameworks deriving from trapping of the guests mixtures were evident only in the case of PUM168@mix-ct (Figure 4.38).

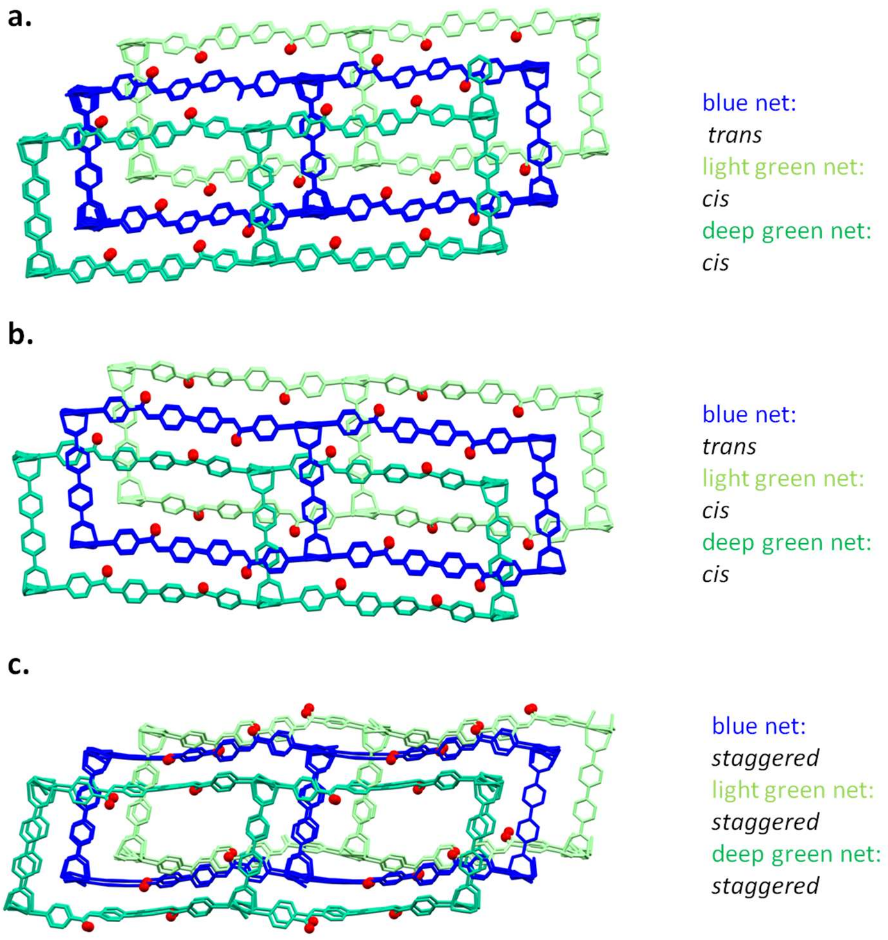

Figure 4.38 Comparison between the amide conformations found in: a) PUM168@ec-mix , b) PUM168@et-mix, c) PUM168@ct-mix. The amidic oxygens are plotted in red, hydrogen atoms are omitted for clarity.

In fact, PUM168@ct-mix displays all the nets in the staggered conformation, included the trans one (Figure 4.38-c). A different behaviour is instead found in the other two mix-guests compounds, PUM168@ce-mix and PUM168@et-mix, which show only minor variations of the amidic conformations, as shown in Figure 4.38a-b.

In Figure 4.39 a comparison of the unit cells of the mixed-guests compounds is reported. As previously seen in PUM168@eugenol, the use of mixtures containing eugenol lead to a moderate variation of the cell axes *a* and *b* (Figure 4.39-I and II). This behaviour is attributed to the absence of significant conformational variation of the acentric nets.

On the other hand, PUM168@ct-mix displays broad conformational changes of all nets upon the inclusion of carvacrol/thymol mixture, which are reflected in the unit cell parameters displayed in Figure 4.39-III. The orientation and dimension of the unit cell are similar to the one observed for PUM168@carvacrol, with crystallographic axes *a* and *b* equal to 20.51Å and 22.41Å , respectively: this evidence can be associated to the trans-to-staggered rearrangement undergone by the amide functions during the uptake process, which leads to a loss of translational symmetry.

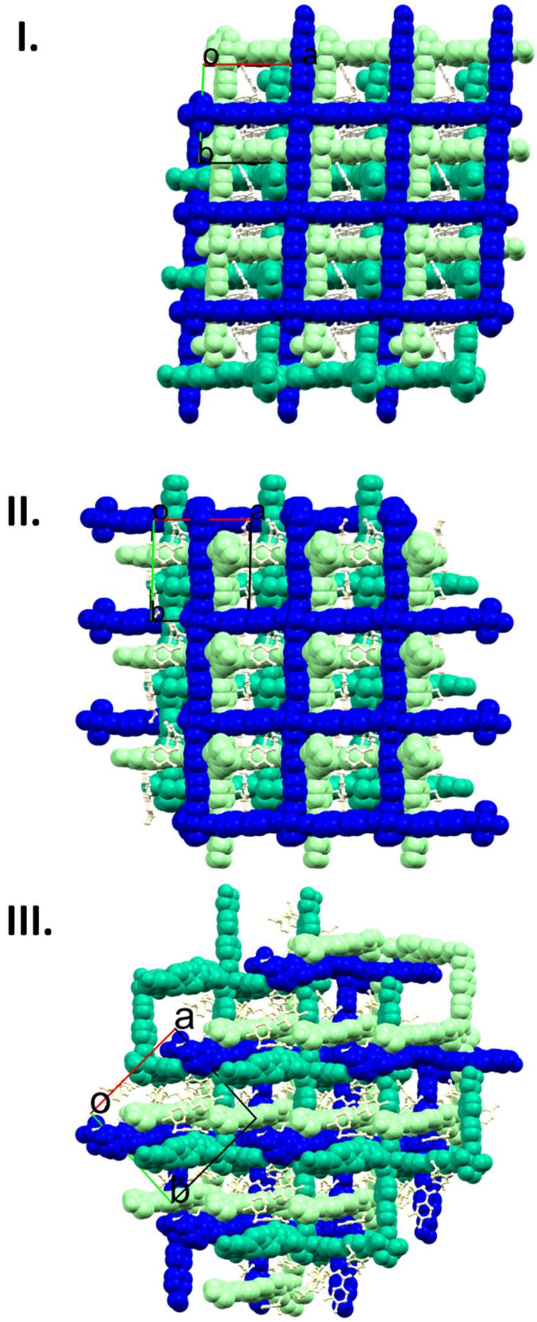

PUM168@ec-mix

a= 15.195 Å

b= 15.214 Å

c= 26.935 Å

α= 97.292 °

β= 95.661 °

γ= 91.782 °

V= 6133 Å^3

PUM168@et-mix

a= 15.119 Å

b= 15.152 Å

c= 26.786 Å

α= 90.15 °

β= 106.21 °

γ= 91.17 °

V= 5888 Å^3

PUM168@ct-mix

a= 20.519 Å

b= 22.415 Å

c= 28.365 Å

α= 113.19 °

β= 96.99 °

γ= 90.04 °

V= 11887 Å^3

Figure 4.39 Unit cells comparison between PUM168@mix-phenols series

4.7 Release Tests

The application of MOFs@guest as systems for a controlled release of food preservatives and fragrances has been the subject of studies in the past few years. In 2013, Li and Pan[198] reported the desorption of fragrances from the pillared MOFs, named as RPM1-Zn and RPM3-Zn. The host frameworks were based on $Zn_3(COO)_6$ trimers and $Zn_2(COO)_2$ dimers, respectively, employing biphenyl-4,4’-dicarboxylate as linker. The 3D architecture was generated by the insertion of 4,4’-bipyridine or 1,2-bipyridylethene as pillar ligands. Both lipophilic and hydrophilic guests were chosen: sorption ad desorption of ethyl-butirate and D-limonene were recorded. Authors outlined the key role of moisture for a prolonged guest release.

More recently, in 2016 Li [199] described the release of allyl isothiocyanate (AITC), a common food preservative. The study illustrated that included AITC could be released in controlled atmospheres with well-defined relative humidity: the moisture exposure dramatically influenced the MOF structure, which varies from a porous to a nonporous structure and consequently triggered the fragrance desorption.

Hence, we decided to study the guest release on the structurally characterized PUM168@phenols series. Preliminary studies on the guest desorption will be the subject of the following paragraph.

We first monitored the behaviour of PUM168@phenols towards the guest release in DMF, in order to investigate the reversibility of the solvent-guest exchange process. For this purpose, a weighted amount of PUM168@phenol (~1 mg) was introduced in a quartz cuvette, then DMF (3 ml) was added and the sample was subjected to UV-VIS measurements at room temperature. For all the three host-guest systems, a progressive increasing of the absorbance peak related to the guest was monitored. This witnessed a quick guest desorption, which reached a plateau within 2 hours (see supplementary information for UV-VIS spectra).

Then we moved our attention on the investigation of the thermal guest extrusion by TGA and headspace GC-MS analysis. The analyses were conducted on crystals removed from the soaking vials and carefully dried over a clean paper sheet.

Both techniques showed the extrusion of DMF and of the guest. For what concerns GC-MS, consecutive desorptions were performed at increasing temperatures, from 30°C to 200°C, with increments of 30°C. A general summary on the release results is furnished in Figure 4.40, where the GC-answers with temperature are reported for the three PUM168@phenols compounds.

A massive guest release was detected for PUM168@eugenol, PUM168@propofol and PUM168@carvacrol: all samples showed a progressive enhancement in the guest release with increasing temperature.

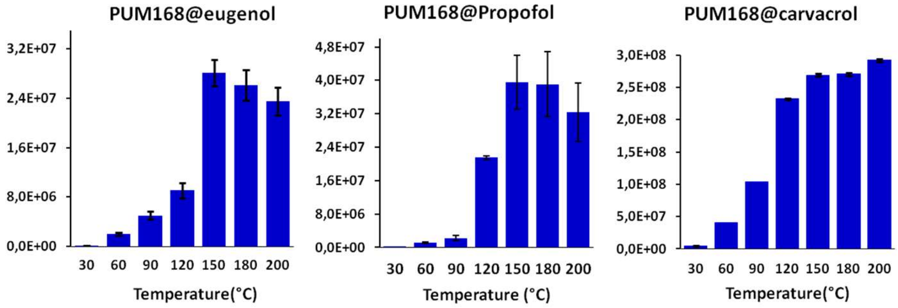

Figure 4.40 Head space GC-MS analysis responses on filtered crystals of PUM168@eugenol, PUM168@propofol and PUM168@carvacrol.

There are no significant differences in the guest extrusion in the range from 150 to 200°C and at 200°C the guest release is still well visible. Finally, it should be underlined that the occurrence of a moderate guest release at 30°C could be appealing in the field of food packaging.

Then, we examined also the headspace GC-MS response of PUM168@phenol after a prior washing with acetone. This second protocol was performed to discharge any influence of a possible fraction of physisorbed guest on the crystals surface. The results are furnished in Figure 4.41.

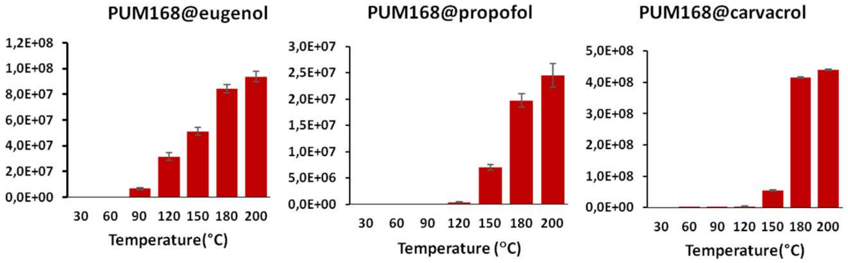

Figure 4.41 Head space GC-MS analysis response on crystals of PUM168@eugenol, PUM168@propofol and PUM168@carvacrol washed with acetone.

In this case, the guest desorption at low temperatures is not observed, hinting a partial guest substitution by acetone, as previously commented for the NMR characterization (pag. 139). The extrusion process starts at 90°C with eugenol, while for propofol and cravacrol the desorption starts at 120°C and 150°C, respectively.

Finally, we evaluated the PUM168@phenols response to consecutive desorption, at a constant temperature of 30°C over a period of 5 hours. The analysis was performed on filtered crystals of PUM168@eugenol, PUM168@propofol and PUM168@carvacrol, not washed with acetone. A different behaviour characterizes the three host-guest species, as displayed Figure 4.42.

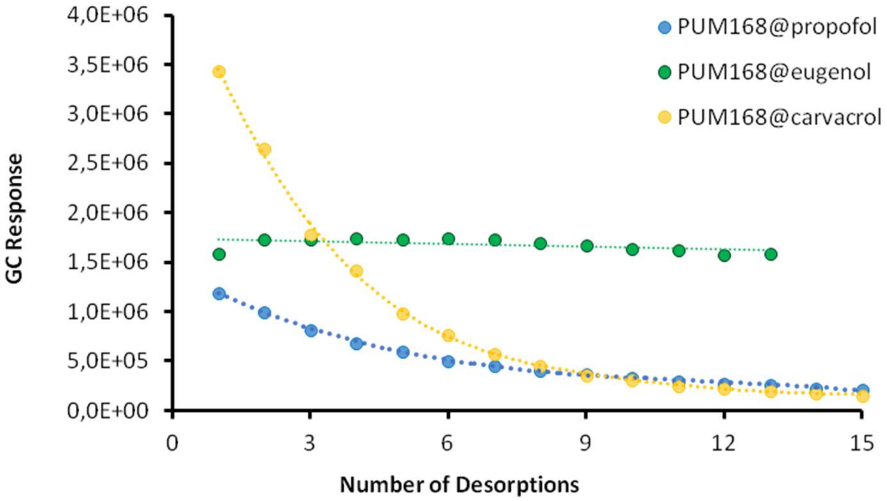

Figure 4.42 Head space GC-MS analysis: repeated desorption tests at constant temperature of 30°C

PUM168@carvacrol and PUM168@propofol evidence an unstable guest release, with a gradual lowering, with time, of the amount of guest detected: i.e. the consistent drop in the response from the first to the 15th analysis reaches ~82% in the case of propofol.

On the other hand, PUM168@carvacrol furnished a good stability in the response, hinting a controlled release for the entire time interval scanned.

4.8 Activation and Gas adsorption measurements

One of the most typical applications of MOFs as functional materials is certainly their use as gas-storage devices. The attention of many researchers has been then devoted to the storage of energetic or environmentally related gases, such as methane, hydrogen and carbon dioxide. Due to the porous character combined with the presence of amidic groups, the gas storage capacity of the two MOFs PUM168 and PUM210 were evaluated. Our interest was mainly focused on the carbon dioxide adsorption, as a preliminary test in order to evaluate a possible future development of these materials as CO_2 adsorbents. A convenient activation protocol necessary to remove the molecules of DMF filling the pores of the as-synthesized MOFs was then required. Thermal activation, performed by heating the crystals at 130°C overnight under high *vacuum*, was associated with an obstruction of the pores, as evidenced by BET (Brauner-Emmet-Teller) measurements: N_2 adsorption measurements revealed very low surface area values: 11 m^2/g and 112 m^2/g for PUM168 and PUM210, respectively.

To preserve integrity of the cavities we then considered a milder activation procedure, such as the one based on the solvent exchange protocol. As-synthesized crystals were soaked first in acetone for 48 hours, then in dichloromethane for 48 hours and finally dried at 10^{-3} torr. The complete removal of the solvent molecules was confirmed by

DSC analysis. Disappointingly, this protocol gave only a minor improvement of the gas adsorption capacity for PUM168 towards N_2 at 77K, as reported in Figure 4.43 (green trace). The corresponding BET surface areas was 68,19 m^2/g for N_2. A slightly better, but still insufficient, result was obtained with CO_2 at 195K, with a BET surface area of 200,99 m^2/g (red trace in Figure 4.43).

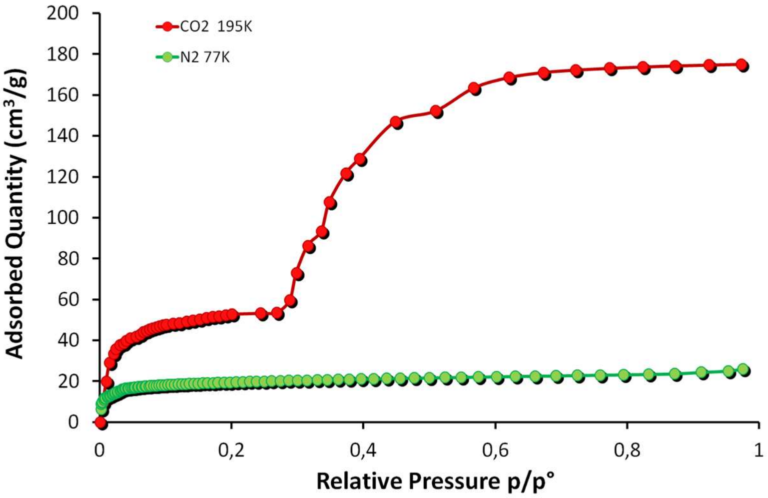

Figure 4.43 N_2 adsorption isotherm at 77K (green markers) and CO_2 adsorption isotherm (red markers) performed at 195 K for PUM168.

In the case of PUM-210, a different behaviour was instead found. N_2 sorption isotherm assessed maintenance of a porous structure, as outlined in Figure 4.44. The experimental BET surface area obtained with N_2 was ~710 m^2/g, while BET surface area obtained with CO_2 was ~491 m^2/g. Interestingly, the shape of the N_2 sorption curve points out a low affinity towards this gas, while the CO_2 sorption isotherm exhibits a typical type I Langmuir behaviour,[137] indicating a better interaction between the walls of PUM210 and carbon dioxide molecules during the adsorption process.

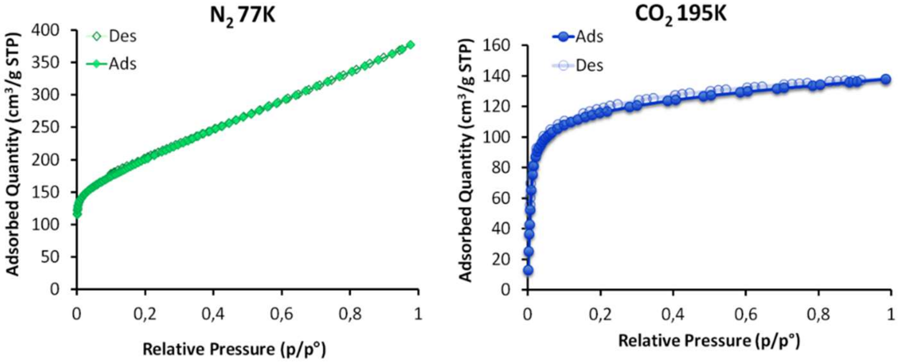

Figure 4.44 Left: N_2 adsorption isotherm at 77K; right: CO_2 adsorption isotherm performed at 195 K

A confirmation of such a selectivity was provided by sorption analyses conducted at 298 and 273K, as outlined in Figure 4.45.

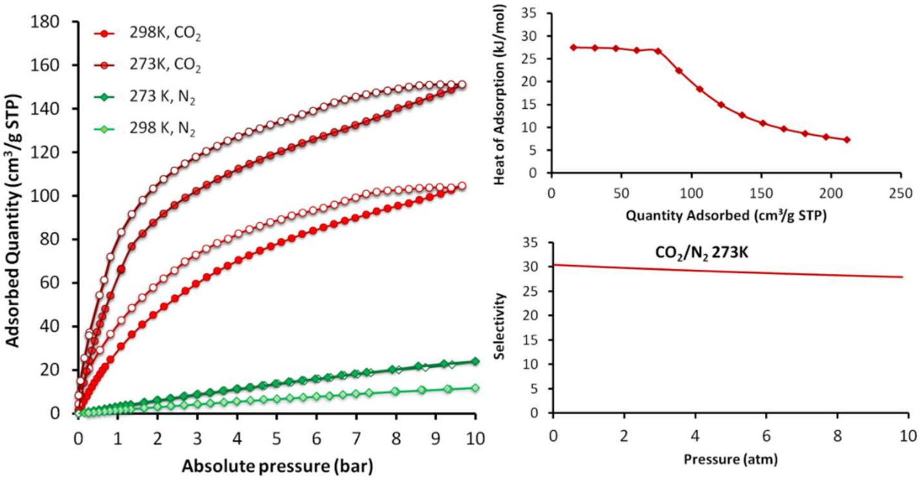

Figure 4.45 Left: comparison between adsorption (plain markers) and desorption curves (empty cycles) of N_2 and CO_2 performed at 273K and 298K; top right: heat of adsorption curve for carbon dioxide; bottom right, : MOF selectivity towards CO_2.

At 273 K and 10 bar of pressure, PUM210 showed a CO_2 uptake of ~150 cm^3 g^{-1}, whereas at the same temperature and pressure only 24 cm^3 g^{-1} of N_2 were adsorbed. A similar trend occurred at 298K and 10 bar of pressure: the amount of sorbed carbon dioxide was ~105 cm^3 g^{-1}, a value significantly higher than the one found with nitrogen under the same conditions, corresponding to ~12 cm^3 g^{-1}.

The selectivity of CO_2 vs N_2 binary mixtures was predicted by the single-component isotherms using the IAST theory (acronym for ideal adsorbed solution theory), which has been commonly employed to determine the gas mixture separation by porous materials.[200] Under a temperature of 273K, PUM-210 displays a CO_2/N_2 selectivity of 30, starting from a 15:85 mixture. The selectivity is related to a calculated heat of adsorption[201] of 27,4 kJ mol^{-1}. These two values point out a superior CO_2 trapping over N_2.

4.9 Experimental

4.9.1 General methods

^{1}H NMR and spectra were recorded on 400MHz and 300MHz Bruker instruments. Chemical shifts are reported in ppm relative to the solvent residual peak of $(CD_3)_2SO$ (δH 2.50, δC 39.5). *J*-values are given in Hz and in the assignments s = singlet, d = doublet, t = triplet, q = quartet, m = multiplet, bs = broad signal, dd = doublet of doublets, bb = broad band.

EI(+)-MS spectra were collected with an ionising voltage of 70 eV by means of a Thermo DSQ II spectrometer equipped with a single quadrupole analyser. The analyses were conducted on loaded MOF crystal samples by means of a DIP probe (direct insertion probe, flash thermolysis at 350 °C).

Thermogravimetric analyses were performed on a PerkinElmer instrument (sample mass approx. 5-10 mg) at a heating rate of 10 °C min^{-1} in a temperature range from 25-500 °C. The measurement was performed at atmospheric pressure under flowing nitrogen (80 mL min^{-1}). Differential scanning calorimetry analyses on MOF powder samples were performed with a PerkinElmer Diamond equipped with a model ULSP 90 ultra-cooler. All analyses were carried out by heating, under nitrogen atmosphere from r.t. to 445°C. Analyses were then performed in perforated 50μl Al-pans at 5°C/min.

X-ray single crystal measurements were performed at *Elettra Sincrotrone* (Trieste, Italy) on beamline XRD1 at 100K under cold nitrogen flux. The source used for the analysis was a NdBFe Multipole Wiggler (Hybrid linear), 4.27 KeV with a power of 8.6 kW, a source size FWHM of 2.0 x 0.37 mm (0.7 x 0.2 mm FWHM beam size at sample) and photon flux 10^{12}-10^{13} ph/sec.

Both native and loaded MOFs crystals were taken respectively from synthesis solution and soaking liquid and mounted with cryoloops (0.05-0.3 mm), prior a flash freezing at 100K.

Diffraction data were indexed, integrated, and scaled using CrysAlis software.[114] Structures were solved by direct methods using SHELXS and refined by full-matrix least-squares on all F2 using SHELXL[115] implemented in Olex2[116]. For all the structures, anisotropic displacement parameters were refined except for hydrogen atoms.

Adsorption measurements. Nitrogen adsorption-desorption isotherms at 77 K and CO_2 at 195 K were performed using a Micromeritics analyzer ASAP 2020 HD up to 1 bar, while N_2 and CO_2 isotherms at 273 K and 298 K up to 10 bar were collected using a Micromeritics analyzer ASAP 2050. The samples were previously evacuated under vacuum at 100°C overnight. The isosteric heat of adsorption Q_{st} value was determined by applying the Clausius-Clapeyron equation while the selectivities of CO_2/N_2 binary mixture were determined from the single-component isotherms using the ideal adsorbed solution theory (IAST) and a CO_2/N_2 ratio of 15:85 (mol:mol).

UV spectra were collected with quartz cuvette on a UV-visibel Bio Evolution Thermo scientific 260 spectrophotometer. The maximum value of absorbance characteristic for each species was monitored:

eugenol λ_{max}=285 nm, propofol λ_{max}=280 nm, carvacrol λ_{max}=279 nm in dimethylformamide as solvent.

GC-MS analysis

All the analyses were performed on a HP 6890 Series Plus gas chromatograph (Agilent Technologies, Palo Alto, CA) equipped with a MSD 5973 mass spectrometer (Agilent Technologies). Helium was used as the carrier gas at a constant flow rate of 1.3 mL min^{-1}; the gas chromatograph was operated in split mode (split ratio: 100) for 1 min with the PTV injector (Agilent Technologies) maintained at the temperature of 270 °C and equipped with a 1.5 mm i.d. multibaffled liner (Agilent Technologies). Chromatographic separation was performed on a MDN-5S (30 m, i.d.=250 µm, d.f.=0,25 µm) capillary column (Supelco, Milan, Italy), using the following temperature program: 70°C, 10 °C min^{-1} until 140°C, 5°C min^{-1} until 170°C.

The transfer line and source were maintained at the temperatures of 220 and 150°C, respectively. Full scan EI data were acquired for all the samples by operating under the following conditions: ionization energy: 70 eV; mass range: 40-200 amu; scan time: 3 scan s^{-1}; electron multiplier voltage: 2000 V.

The extracted ion chromatogram mode was then used to calculate the GC response for each analyte by recording the current of the following ions: *m/z* 135 and 150 for carvacrol, *m/z* 149 and 164 for eugenol and *m/z* 163 and 178 for propofol.

Signal acquisition and data handling were performed using the HP Chemstation (Agilent Technologies).

Statistical analysis was performed by using the SPSS v.23.0 software (IBM, Milan, Italy).

New MOF synthesis

PUM168

In a 70 mL pyrex glass tube, L6 (0.2 mmol, 80 mg) and biphenyl-4,4′-dicarboxylic acid (0.4 mmol, 96 mg) and $Zn(NO_3)_2{\cdot}6H_2O$ (0.4 mmol, 120 mg) were added to 41 mL of dimethylformamide (DMF). The resulting mixture was sonicated and heated at 80°C. After 1 week the reaction vessel was slowly cooled to room temperature. The resulting large yellow crystals were washed with DMF (2 x 10mL).

PUM210

In a 70 mL pyrex glass tube, L6 (0.2 mmol, 80 mg) and 2,6-naphtalendicarboxylic acid (0.4 mmol, 80 mg) and $Zn(NO_3)_2{\cdot}6H_2O$ (0.4 mmol, 120 mg) were added to 41 mL of dimethylformamide (DMF). The resulting mixture was sonicated and heated at 80°C. After 5 days the reaction vessel was slowly cooled to room temperature. The resulting yellow small crystals were washed with DMF (2 x 10mL).

PUM198

In a 70 mL pyrex glass tube, L6 (0.2 mmol, 80 mg) and terephtalic acid (0.4 mmol, 66 mg) and $Zn(NO_3)_2{\cdot}6H_2O$ (0.4 mmol, 120 mg) were added to 41 mL of dimethylformamide (DMF). The resulting mixture was sonicated to provide a clear solution and heated at 80°C. After 4 days the reaction vessel was slowly cooled to room temperature. The resulting small yellow crystals were washed with DMF (2x 10mL).

Pure API Soaking

As synthesized PUM168 (5 to 10 mg) was transferred into a 5 mL glass vial and dipped into neat guest (0.5 to 1.5 mL). The vial was capped and crystals were allowed to soak at room temperature for at least 4 days, under basculating conditions by means of a rocking shaker.

API Mixture Soaking

In the case of thymol containing mixture: a weighted amount of thymol (1.0 mmol, 150.2 mg) was transferred into a 5 mL glass vial and dissolved into a equimolar amount corresponding liquid component (carvacrol or eugenol, 1.0 mmol ~150 μL) obtaining an homogeneous colourless mixture. Then, as synthesized PUM168 (5 to 10 mg) was soaked into the mixture. The vial was tightly capped and allowed to basculate for at least 4 days.

In the case of eugenol-carvacrol mixture: equimolar mixture of the two liquid guests. Same soaking conditions employed above for thymol-mix.

PUM168@phenol UV measurements

After 4 days' time of soaking, MOF crystals were separated employing a hirsch funnel and filter paper disk. After the removal of neat guest by filtration, crystals were dried quickly under vacuum.

UV meseaurement:

2.24 mg of loaded MOF were placed inside a quartz cuvette, then DMF was added (3 mL). UV-Vis spectrum was recorded, then the solution was discarded and fresh DMF (3 mL) was added. The kinetic of propofol desorption was analyzed collecting a UV-VIS spectrum each 5 minutes.

HS-GC analysis

Headspace analyses were performed by using a PAL Combi-xt autosampler (CTC Analytics AG Zwingen, Switzerland).

0.5 mg of MOF@analyte were weighted into a 10 mL vial and heated at the proper temperature (from 30 to 200°C) for 20 min. One mL of the headspace was injected into the GC inlet by using a 2.5 mL gas tight syringe.

4.10 Supplementary Materials

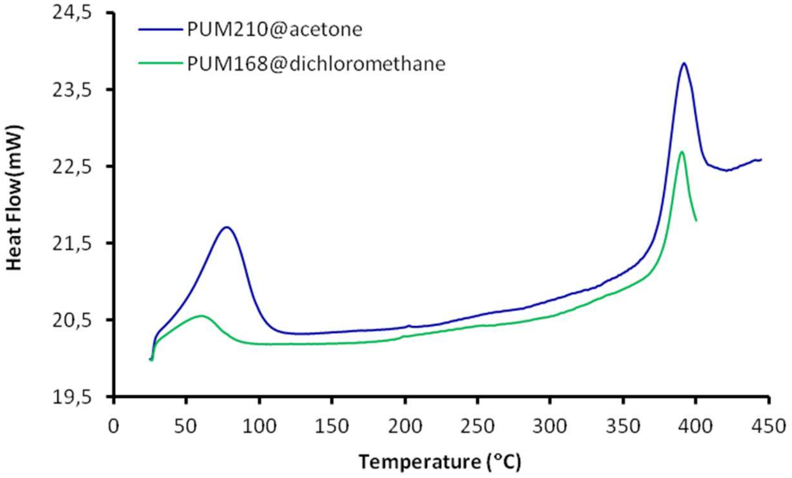

Figure 4.46 DSC traces of PUM210 samples after the various steps of the solvent activation protocol: PUM210@acetone (plotted in blue) and PUM210@dichloromethane (plotted in green)

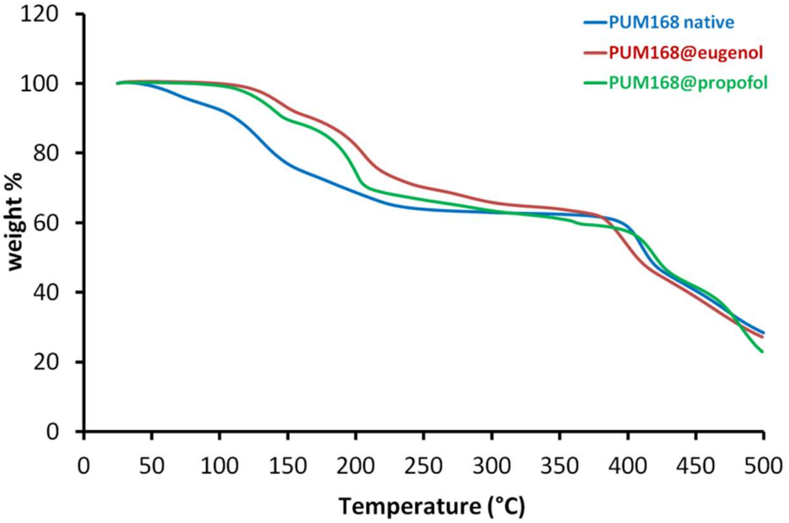

Figure 4.47: TGA traces of pristine PUM168 (blue curve) and after soaking in eugenol (red curve), and propofol (green curve)

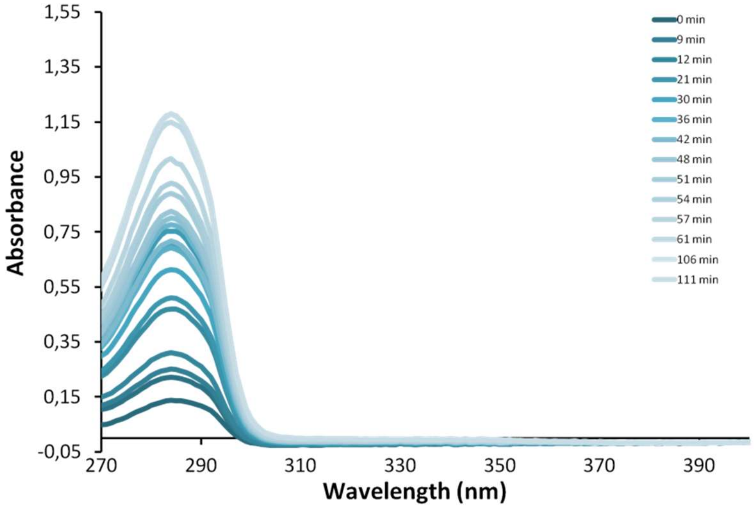

Figure 4.48 UV-VIS desorption of eugenol from PUM168@eugenol: a plateu concentration is reached in ~2 hours

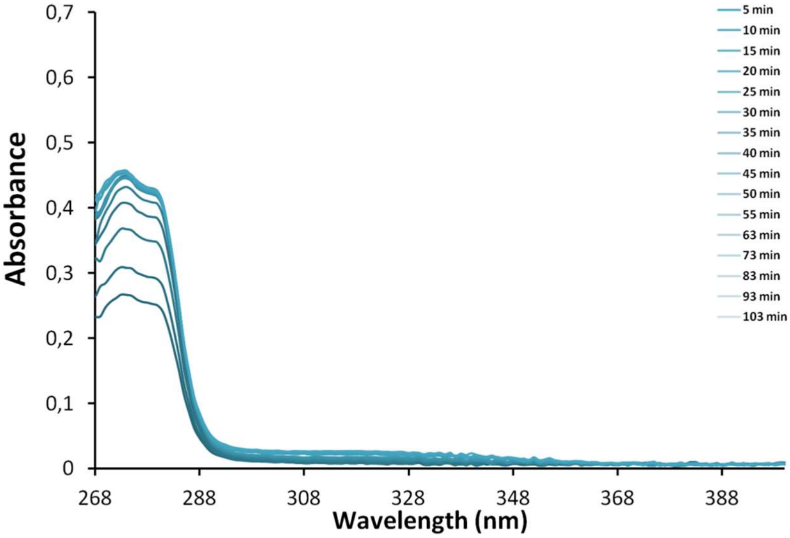

Figure 4.49 UV-VIS desorption of propofol from PUM168@propofol: a plateu concentration is reached in ~ 40 minutes.

5 Synthesis of new MOFs containing aminocarboxylic linkers

5.1 Structural Analysis

In addition to the aforementioned bis-amide ligand **L6**, also the remaining ligands obtained by Buchwald protocol were tested with a large series of metal salts for the synthesis of novel MOFs. Owing the superior flexibility of amino-carboxylic linkers, the rationalization *a priori* of the final architectures as well as the optimization of the synthetic protocols resulted quite difficult to be accomplished. However, **L1** and **L3** (Scheme 4.2) were successfully employed in the synthesis of high quality crystalline materials, suitable for SC-XRD analysis. In this chapter the syntheses, the structural characterizations and some preliminary studies on the stability of the isolated materials will be presented.

The solvothermal reaction of **L1** and $Zn(NO_3)_2$ $6H_2O$ provided colorless platelets crystals of PUM-FLEX-Zn, which framework is generated by the assembly of the ligand with the Zn_4O SBU, shown in Figure 5.1-a.

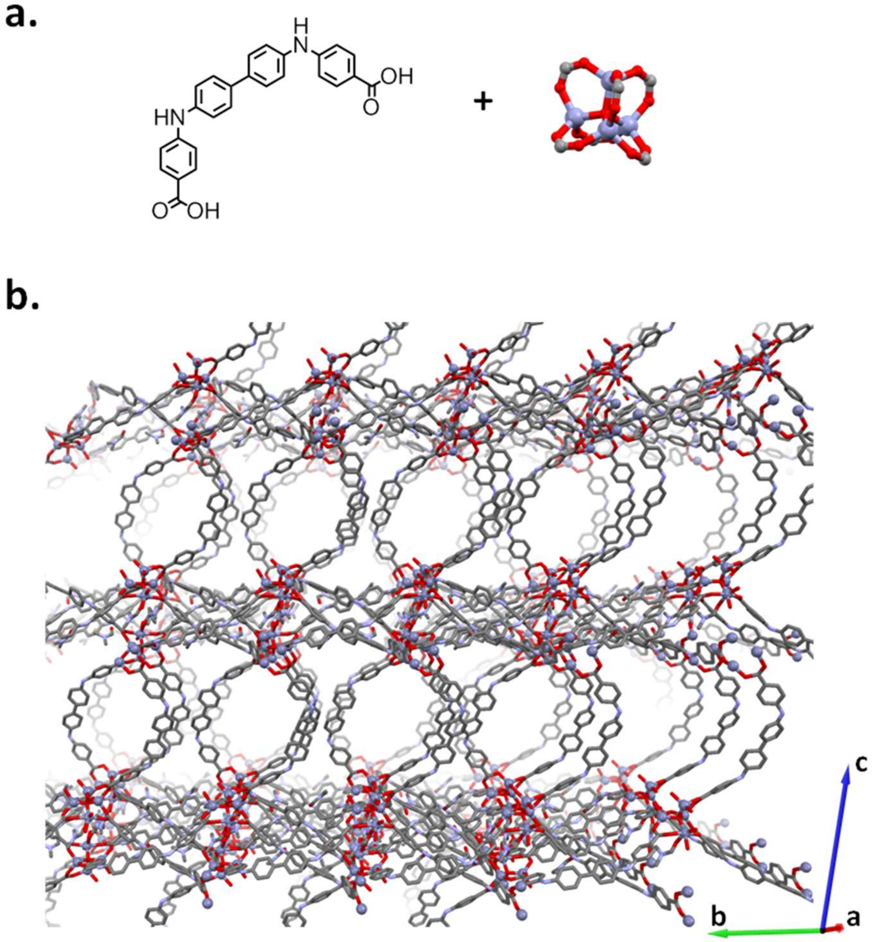

Figure 5.1: a a) ligand and SBU found in PUM-FLEX-Zn b) view of channels along crystallographic axis a.

The resulting architecture (Figure 5.1b) reveals a considerable fraction of voids: removing the solvent electron density, a 54% of void cell volume was calculated, corresponding to 4238Å^3.

The MOF porosity develops through two different types of channels, with a distinct shape and diameter. Cylindrical channels, running along crystallographic axis a, exhibit maximum dimensions of 17×14 Å (Figure 5.1-b). Rectangular channels along crystallographic axis b display a slightly larger width, with maximum dimensions of 21×15Å (Figure 5.2).

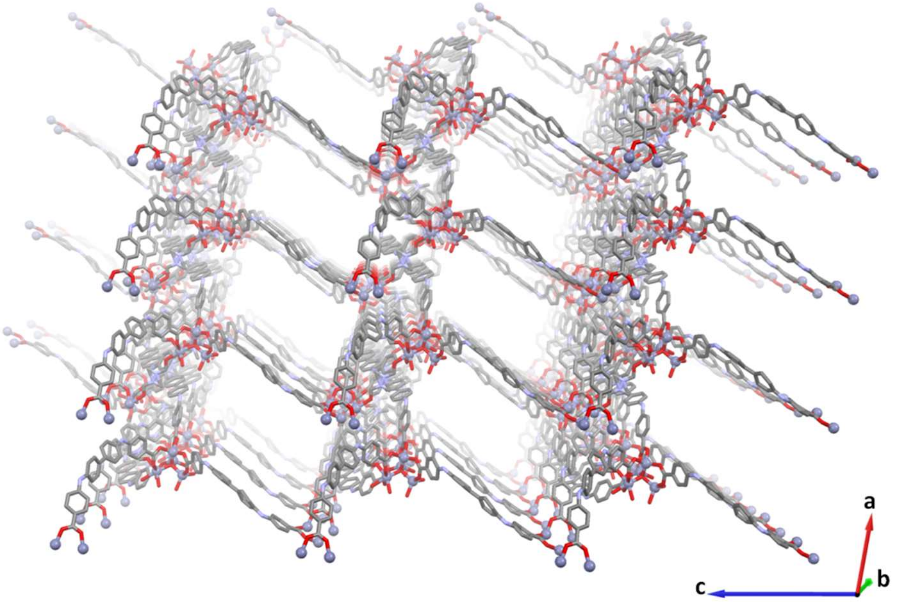

Figure 5.2 View of rectangular channels in PUM-FLEX-Zn along the crystallographic axis b.

The SBU is composed by four Zn^{2+} ions bridged by a μ_4-O atom, while each **L1** carboxylate bridges two Zn^{2+} ions. The overall cluster geometry can be described as a distorted tetrahedron, as shown in Figure 5.3-a: for three Zn^{2+} ions, named Zn1, Zn2 and Zn3, the tetrahedral coordination environments involves three carboxylates each bridging two Zn ions (κ_1:κ_1:μ_2) and the μ_4-oxo group. The fourth

Zn^{2+} ion, named Zn4, is characterized by an octahedral coordination generated by three bridging carboxylates ($\kappa_1:\kappa_1:\mu_2$), one μ_4-oxo group and two C=O belonging to two DMF molecules. Similar SBUs have already been described in literature.

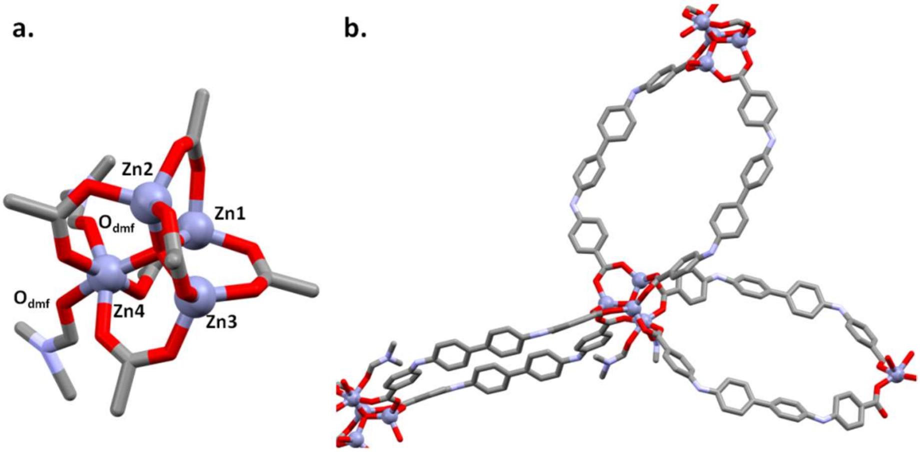

Figure 5.3 a) Detailed view on Zn coordinations found in PUM-FLEX-Zn b) L1 bridging Zn_4O SBUs in PUM-FLEX-Zn.

The Zn–$O_{carboxylate}$ bond lengths are in the range 1.85–2.04 Å and the two Zn-O_{DMF} bond lengths are 2.03 and 2.11 Å. The Zn···Zn distances range from 3.10 to 3.23Å, while the bond lengths between each Zn and the central oxygen atom vary from 1.90 to 1.98 Å.

Each Zn_4O unit is connected to three other clusters by six bridging linkers **L1**, as displayed in Figure 5.3-b. Taking into account two **L1** ligands and the related Zn_4O clusters, a 22.5×13.3 Å metallamacrocycle ring is generated (measured by taking into account the O···O intercluster distance and the C···C distance between two opposite biphenylene units). The combination of this metallamacrocyclic motif generates 2D planes, Figure 5.4a-b.

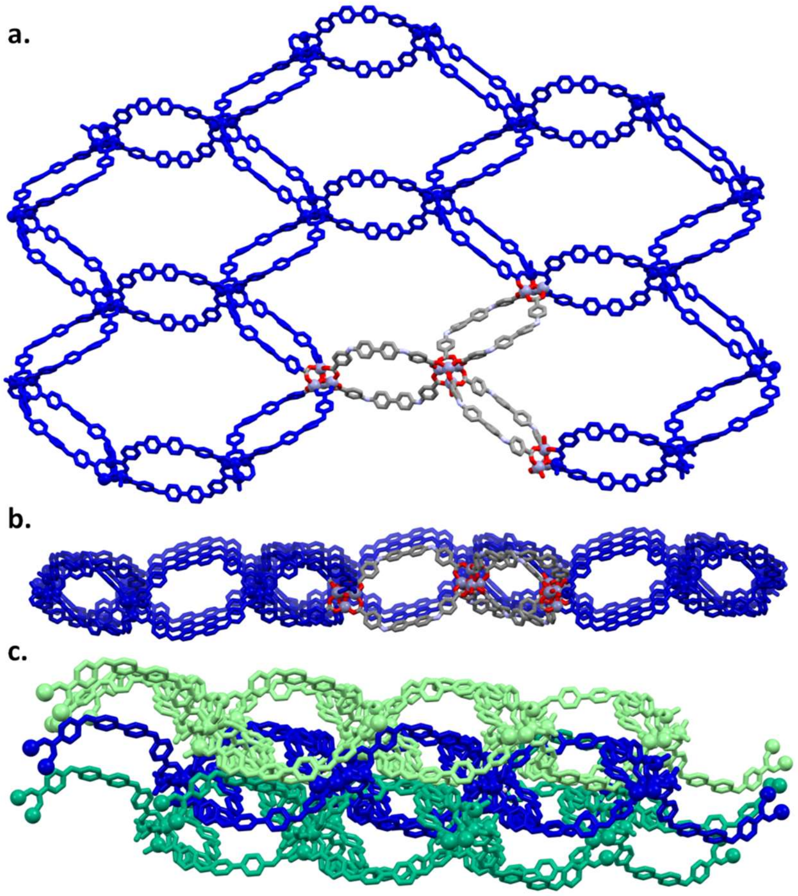

Figure 5.4 Framework of PUM-FLEX-Zn. a) Top view of the 2D plane, the repeating structural unit is in colour; b) Side view of the 2D plane c) 3D structure resulting from polycatenation of three different (blue, light green and dark green) 2D planes

Furthermore, the large voids volume allows the occurring of polycatenation: two additional sheets are interwoven to the first lane, generating a 3D infinite chain-mail architecture, as shown in Figure 5.4-c.

The solvothermal combination of a DMF solution of $ZrCl_4$ and **L1** provided the Zr-based MOF PUM-FLEX-Zr, as shown in Figure 5.5.

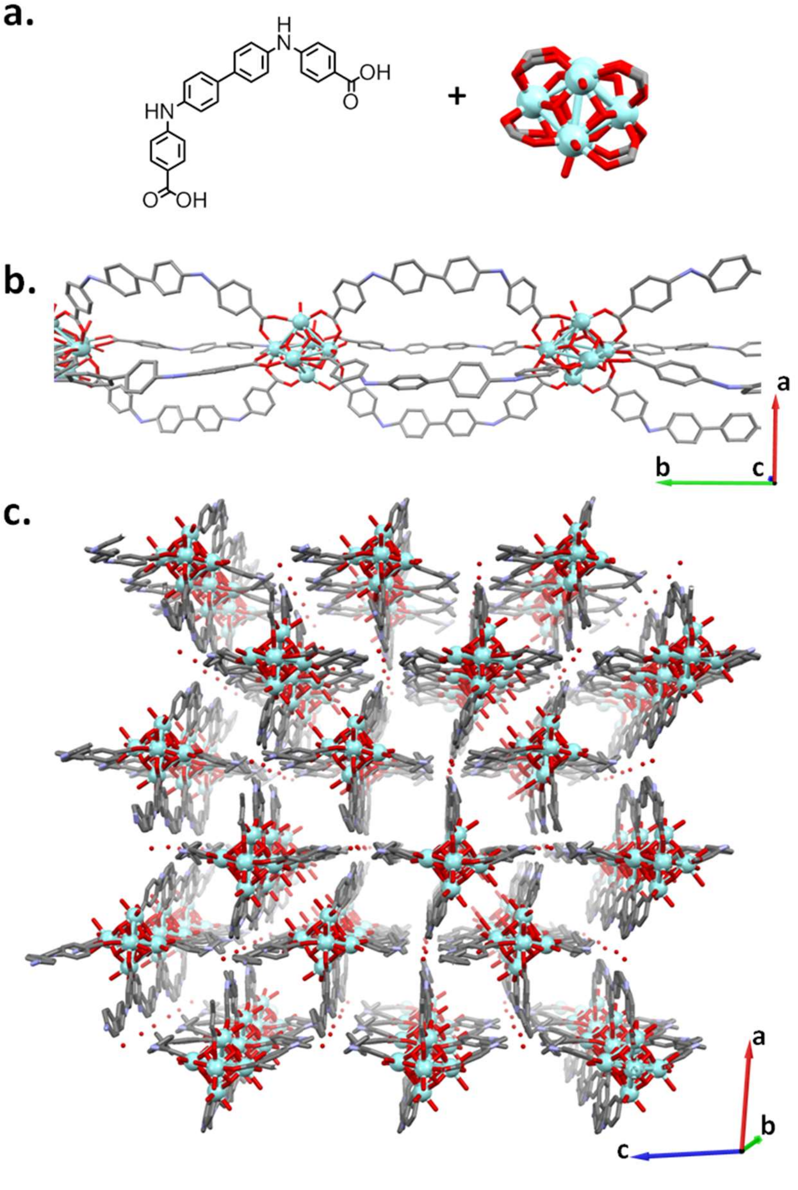

Figure 5.5 a) ligand and SBU found in PUM-FLEX-Zr; b) 1D infinite chains; c) 3D structure generated by hydrogen bonds between 1D chains and water molecules.

Synthesis of large single crystals of Zr-based MOFs is described as challenging,[202] owing to the strong nature of metal-ligand bonding: this feature hampers the crystallization process and leads to a precipitation of a microcrystalline powder. In fact, the formation of high quality single crystals is associated with labile metal-to-linker interactions, which allow a slow equilibration in solution with formation of extended polymeric frameworks. A synthetic pathway generally proposed to enhance crystallinity is the addition of an acidic modulator, which acts as a competitor ligand slowing the crystallization course.[203] After an experimental screening with different acids, TFA has been chosen as valid modulator providing crystals suitable for SCXRD-analysis. The metal SBU is a hexanuclear cluster of Zr^{4+} of formula $Zr_6(\mu_3\text{-}O_4)(\mu_3\text{-}OH)_4(OH)_4(COO)_8$: each Zr^{4+} ions is eight-coordinated. Since the hydrogen atoms linked to the oxygens of the cluster cannot be located during the structural resolution, the overall cluster formula is proposed to assure electroneutrality. **L1** acts as μ_4-bridge, linking four Zr^{4+} ions belonging to two different clusters in a μ_4-η_2:η_2 mode. The $Zr–O_{carboxylate}$ bond lengths are in the range 1.74–2.50 Å, the Zr-OH bond lengths are in the range 2.06-2.44 Å and the Zr–μ_3-O or Zr–μ_3-OH bond lengths are in the range 1.90-2.45 Å. The Zr···Zr distances vary from 3.52 to 3.61 Å. Each SBU is connected to two adjacent clusters by eight **L1**, developing a 1D independent chain, as displayed in Figure 5.5a-b. The chain is involved in H-bond interactions with water molecules contacting the aminic moieties: O_w···H-N distances are in range 2.04-2.25Å. This H-bond motif links the various chains together building a 3D network, which exhibits open square channels of size 14x14 Å, along crystallographic axis b. The channels are partially occluded by water molecules coordinated to Zr ions. PUM-FLEX-Zr presents a notable void volume of ~ 53% of the unit cell (calculated by Mercury), which corresponds to 4893Å^3.

The solvothermal reaction of $Cd(NO_3)_2$ salts and **L3** produced the supramolecular architecture reported in Figure 5.6.

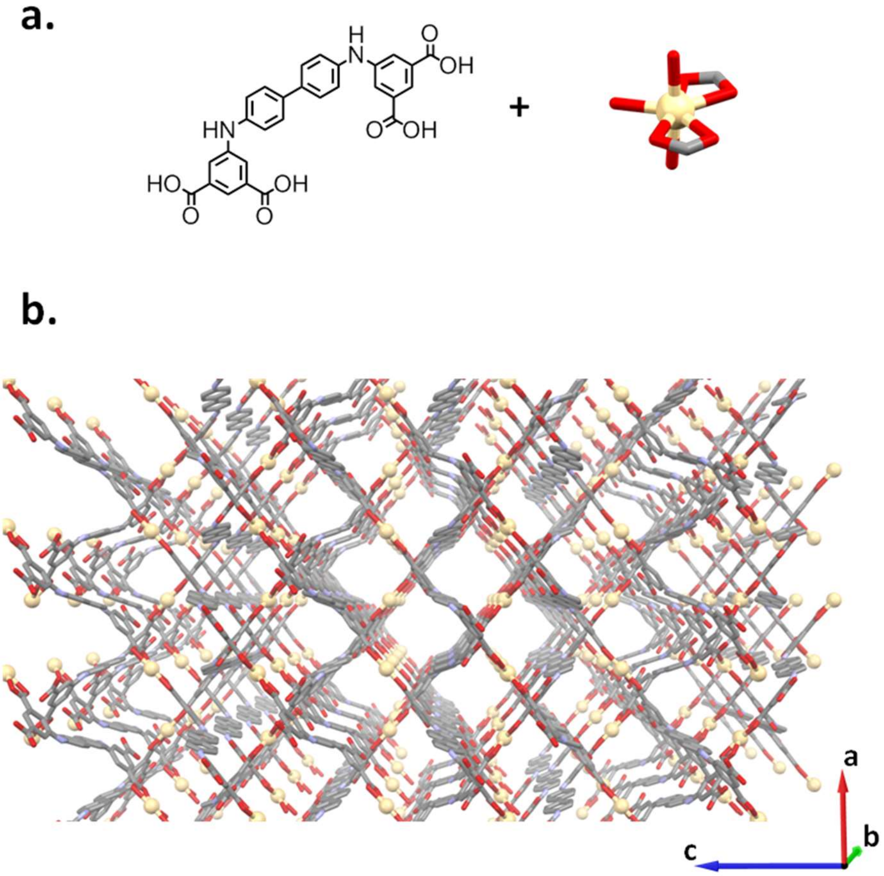

Figure 5.6 a) ligand L3 and SBU found in PUM-FLE-Cd; b) 3D structure exhibiting channels along crystallographic axis b, DMF molecules are omitted for clarity

The metal SBU is formed by a heptacoordinated Cd^{2+} ion, characterized by a distorted pentagonal bipyramidal coordination.

The apical positions are occupied by two DMF molecules, while the five remaining coordination sites are filled by four oxygen atoms of two chelating carboxylates from two different **L3** linkers and from one water molecule, as displayed in Figure 5.7-a. The Cd-$O_{carboxylate}$ bond lengths are in the range of 2.360-2.370 Å, the Cd-O_{DMF} distance is 2.276 Å and the Cd-O_w bond length is 2.287 Å. **L3** adopts a transoid-conformation, as shown in Figure 5.7-a.

Despite the tetratopic character, **L3** acts as bidentate ligand, using only two carboxylate moieties to bind Cd, forming infinite 1D zig-zag chains where the Cd···Cd distances are 18.665 Å.

The presence of two non-coordinating carboxylates for each linker allows the interaction between adjacent 1D chains through hydrogen bonds: a comprehensive overview of the resulting architecture is provided in Figure 5.7-b. Each 1D chain displays two different type of interactions: the first one involves neighbouring chains laying on the same plane (plotted in green in Figure 5.7-b), and being based on NH…O=$C_{carboxylic}$ interactions, thus allowing the formation of infinite 2D supramolecular planes. The N-H···O distance is 2.92Å while the N-H···O angle is equal to 163.5° degree. A second type of interaction regards the uncoordinated COOH moiety that in this case acts as hydrogen bond donor towards a coordinated COO group. The resulting COO-H···OOC distance is 2.55Å with an angle of 163.0°; these values confirm the strength of these H-bonds. This allows the growth of the framework outside the plane (blue framework in Figure 5.7-c), generating a 3D grid-like structure.

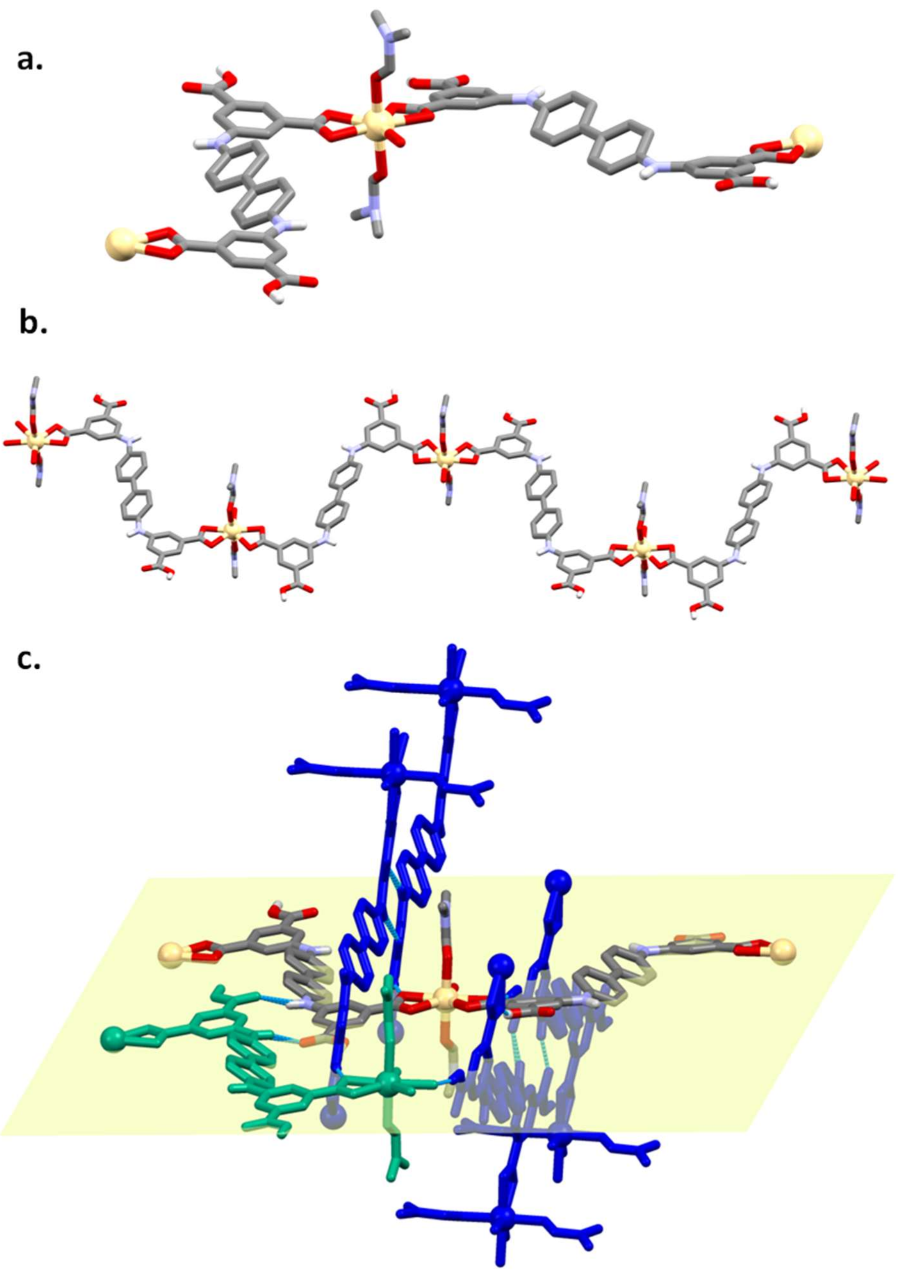

Figure 5.7 a) Cd^{2+} coordination environment in PUM-FLEX-Cd; b)1D zig-zag chain; c) H-bond interactions between independent chains: expansion along the plane (plotted in green) and outside the plane (plotted in blue)

The resulting supramolecular architecture shows square microporous channels, with an average diameter of 9Å, running along crystallographic axis b.

A 21% void volume has been calculated using MERCURY software, however this empty space in not accessible without a prior MOF activation: the presence of DMF molecules coordinated to Cd ions hinders completely the MOF windows, as depicted in Figure 5.8.

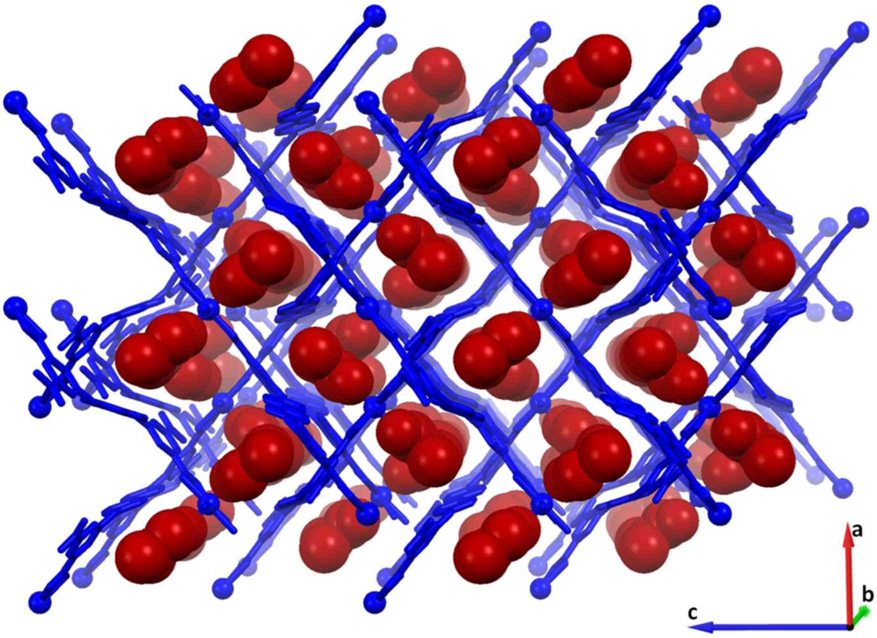

Figure 5.8 View along crystallographic axis b in PUM102: DMF molecules plotted in red occlude the square channels along crystallographic axis b.

5.2 Thermal characterization

After having determined the solid state structures of the three new frameworks PUM-FLEX-Zn, PUM-FLEX-Zr and PUM-FLEX-Cd, we investigated their thermal stability. All samples were quickly washed with acetone and then dried under vacuum before being subjected to thermal analysis.

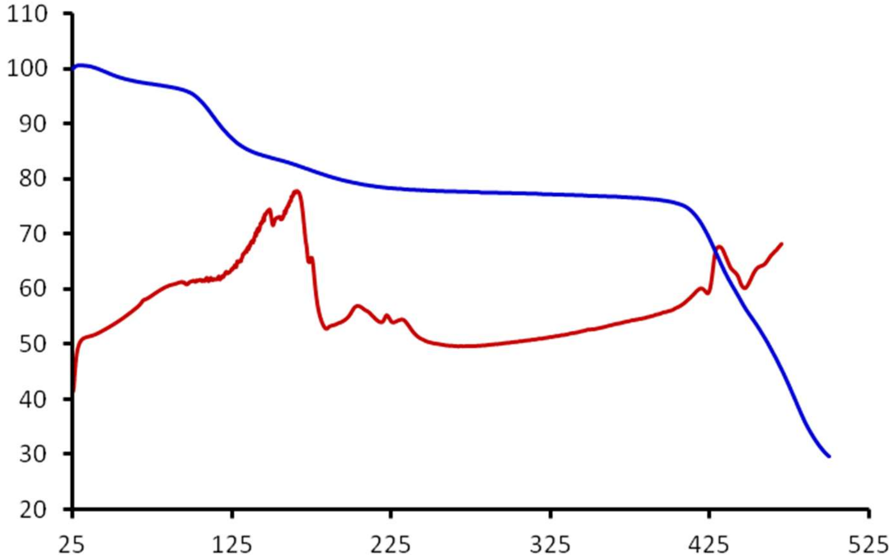

Figure 5.9 TGA trace (plotted in blue) and DSC trace (plotted in red) of PUM-FLEX-Zn

As shown in Figure 5.9, PUM-FLEX-Zn demonstrates an excellent thermal stability, since the decarboxylative step occurs at T> 380°C.

The TGA trace reveals a mass loss of about 19 % in two endothermic steps at low temperature: a first slope takes place in the range 80°C to 153°C, equivalent to a 13,6% of weight. A second loss corresponding to a 5,3% is observed in the interval 153°C-232°C. These two steps can then be attributed to the loss of the uncoordinated and coordinated DMF molecules, respectively.

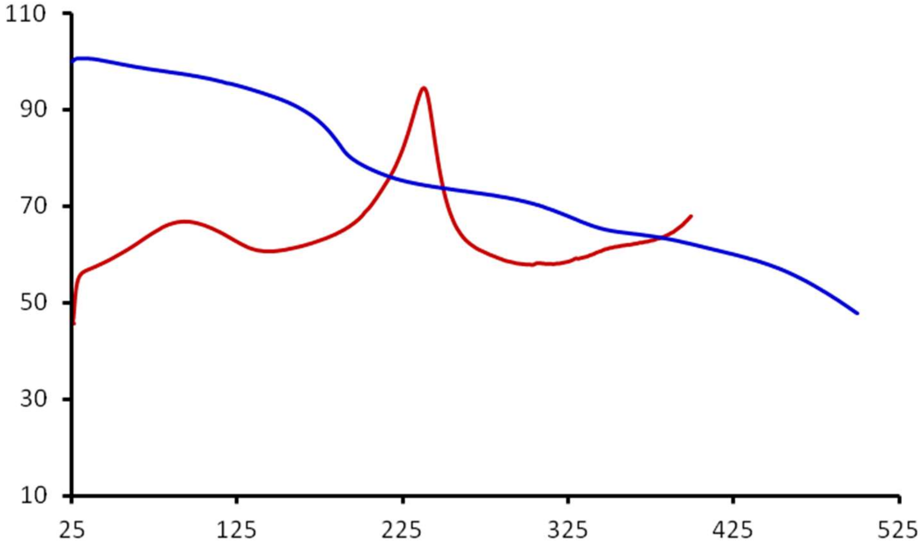

Figure 5.10 TGA trace (plotted in blue) and DSC trace (plotted in red) of PUM-FLEX-Zr.

A lower thermal stability features the H-bond based supramolecular architecture of PUM-FLEX-Zr. In this case no flat part of the TGA trace is observed and the thermogram displays a multispep slope behaviour (Figure 5.10).

A first mass loss of about 22 %, is detected in the range from 117°C to 248°C, by means of an endothermic process ((Figure 5.10). This phenomenon can be attributed to desorption of the solvent which filled the pores. Then, a smaller weight loss (8.25%) is observed in the temperature range of 275–365 °C.

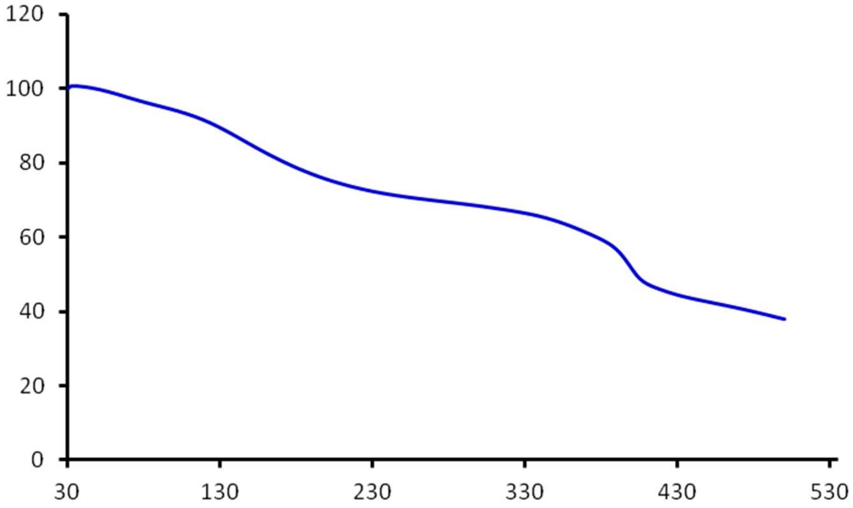

Figure 5.11 TGA trace of PUM-FLEX-Cd

Thermal analysis relative to the crystalline sample of PUM-FLEX-Cd shows a mass loss of about 22 % in the range 95°C-225°C (Figure 5.11). This mass loss is compatible with the removal of coordinated water and DMF molecules. At temperatures higher than 330°C the thermogram shows a mass loss of about 23% imputable to the decarboxylation of the linkers.

5.3 Experimental Part

General materials and methods

All chemicals and solvents were purchased from commercial suppliers (Sigma-Aldrich, Carlo Erba) and used without further purifications. All MOFs were synthesised using solvothermal reactions. If not diversely stated, the characterization of the *as-synthesised* crystals was performed on crystals that were just washed with a small amount of fresh DMF. Otherwise, the crystals were washed with different solvents (reported for each procedures).

IR spectra were obtained with a Thermo Scientific Nicolet 5PCFT-IR-ATR spectrometer (diamond crystal) in the 4000-400cm^{-1} interval.

Differential scanning calorimetry was performed on a PerkinElmer DSC 6000 with a heating rate of 5 °C min^{-1} in a temperature range from 25 °C to 400 °C. The samples (mass approx. 5 mg) were sealed in a 50 µL perforated aluminium crucible. The measurement was performed at atmospheric pressure under flowing nitrogen (20 mL min^{-1}). TGA analyses were performed on a PerkinElmer instrument (sample mass approx. 5-10 mg) at a heating rate of 10 °C min^{-1} in a temperature range from 25-500 °C. The measurement was performed at atmospheric pressure under flowing nitrogen (80 mL min^{-1})

X-ray single crystal measurements were performed at *Elettra Sincrotrone* (Trieste, Italy) on beamline XRD1 at 100K. The source used for the analysis was a NdBFe Multipole Wiggler (Hybrid linear), 4.27 KeV with a power of 8.6 kW, a source size FWHM of 2.0 x 0.37 mm (0.7

x 0.2 mm FWHM beam size at sample) and photon flux 10^{12}-10^{13} ph/sec.

Synthesis of PUM-FLEX-Zn

L1 (212 mg, 0.5 mmol) and $Zn(NO_3)_2 \cdot 6H_2O$ (223 mg, 0.75 mmol) were dissolved in 25 mL of DMF at room temperature in a 40 mL Rotaflo. The solution was sonicated for 1 minute at room temperature prior to be heated. The reaction mixture was heated to 110°C for four days. After the reaction, the Rotaflo was slowly cooled to room temperature. The resulting colourless plates crystals were separated by filtration and then washed three times with fresh DMF (10mL).

Scaled up synthesis.

L1 (212 mg, 0.5 mmol) and $Zn(NO_3)_2 \cdot 6H_2O$ (223 mg, 0.75 mmol) were dissolved in 25 mL of DMF at room temperature in a 40 mL Rotaflo. The solution was sonicated for 1 minute at room temperature prior to be heated. The reaction mixture was sealed in the Rotaflo and it was heated to 110°C for four days. After the reaction, the Rotaflo was slowly cooled to room temperature. The resulting colourless plates crystals were separated by filtration and then washed three times with fresh DMF (10mL). After removal of the solvent the sample was dried under vacuum at room temperature overnight.

The solvothermal reaction yielded 100 mg of product (0.06 mmol, 12%, based on the ligand).

Synthesis of PUM-FLEX-Cd

L3 (15 mg, 0.029 mmol) and $Cd(NO_3)_2 \cdot 4H_2O$ (22.6 mg, 0.073 mmol) were dissolved in 6 mL of DMF at room temperature in a 10-mL screw-capped pyrex glass tube. The solution was sonicated for 1 minute at room temperature prior to be heated. The reaction mixture was heated at 80°C for four days. Then, the glass tube was slowly cooled to room temperature. The resulting purple plates crystals were separated by filtration and then washed three times with fresh DMF (10mL).

Synthesis of PUM-FLEX-Zr

$ZrCl_4$ (55 mg, 0.24mmol) was dissolved in 10 mL of DMF at room temperature in a 17-mL screw-capped pyrex glass tube. Then 0.27 mL of TFA were added and the mixture was sonicated for one minute. The sealed glass tube was heated at 80°C for one hour then it was slowly cooled at room temperature. Afterwards, the mixture was added of **L1** (50 mg, 0.12 mmol), then the glass tube was sealed and heated at 120°C for four days. The resulting white cubic crystals were washed three times with fresh DMF (10mL).

Scaled up synthesis

$ZrCl_4$ (226,6 mg, 0.98 mmol) was dissolved in 41.2 mL of DMF at room temperature in a 70-mL screw-capped pyrex glass tube. Then 1.12 mL of TFA were added and the mixture was sonicated for one minute. The sealed glass tube was heated at 80°C for one hour then was slowly cooled at room temperature. Afterwards, the mixture was added of **L1** (206 mg, 0.49 mmol), then the glass tube was sealed and heated at 120°C for four days. The resulting microcrystalline white cubic crystals were washed three times with fresh DMF (20mL). After the removal of the solvent by centrifugation the sample was dried under vacuum at room temperature overnight. The solvothermal reaction yielded 280 mg of product (0.115 mmol, 12%, based on the ligand).

6 Conclusions

MOFs proved to be versatile porous materials which can be engineered to obtain a fine tuning of both size and shape of the cavities.

In the first part of this thesis, we reported how liquid nicotine can be hosted in PCN-6'/PCN-6 pores. Both NMR spectroscopic and thermogravimetric studies outlined a very efficient guest uptake. From the combination of these two techniques, we were able to provide an estimation on the amount of nicotine trapped. The obtained result of a ~30-40 wt% nicotine loading is in line with other very high guest loading reported in literature (e.g 50 wt% caffeine loading into (Fe)MIL-100, described by Serre). Disappointingly, SC-XRD analysis was not able so far to reveal the structure of nicotine assemblies inside PCN-6 cavities. In fact, only the guest molecules close to Cu paddle-wheels showed a distribution of the electron density which could be modeled as coordinated nicotine to the copper centers.

In Chapter 3, we pointed out the successful inclusion of moderately large Ni complexes, active in the homogeneous proton reduction to

H_2, into mesoporous Zr-based PCN-777. Taking advantage of supramolecular interactions, we were able to encapsulate the Ni complexes, leading to a final catalyst heterogenization. Thus, it was possible avoiding the need of complicate post-synthetic-modification approaches, usually required for the trapping of organometallic species inside a MOF pores. The effectiveness of the complex loading, as well as the confirmation of its integrity, were outlined by ESEM-EDS, ICP, SS-NMR e BET analyses. Hence, we moved our attention on the optimization of PCN-777@complex thin film deposition on conductive glasses (FTO). Preliminary evidences for the catalytically activity of PCN-777@complex coatings were furnished and future studies will regard the possibility to gain a H_2 production.

In the third part of this thesis, we described the *ex-novo* design of a small library of ligands and their application for the building of novel flexible MOFs. This goal was achieved by a Buchwald-Hartwig coupling protocol: a new family of amino-carboxylate and amido-pyridinic linkers was successfully synthesized: desired products were isolated by simply precipitation, in high yields, without need of further purification steps.

Then, the solvothermal reaction of these linkers with a large series of metal ions, allowed us to build a small family of novel MOFs. In Chapters 4 and 5 the synthesis procedure, structural characterization and study of the new materials were provided.

Hence, some of the new MOFs were tested both in the storage of gas (CO_2 and N_2) as well as in the uptake of small organic molecules. In particular, a series of APIs (Active Pharmaceutical Ingredients) characterized by a substituted phenol core, was selected as for the encapsulation studies. The attention was mainly directed to carvacrol, thymol, eugenol and propofol. The mutual hydrogen bond donor/acceptor character of the chosen phenolic guests was believed to promote the host-guest interactions with the amine or amide moieties pending from the MOFs walls. The soaking protocol in neat guest provided satisfactory results: we succeeded to pinpoint with high precision the encapsulated API guests and the interactions responsible of the nanoconfined inclusion processes.

It should be underlined that only very few examples of structurally defined guest@MOF systems are reported in literature, and that the structural definition of the nanoconfined guest···guest interactions must be considered an absolute innovation.

Some preliminary tests aimed at revealing the possibility of having a controlled guest desorption by thermal treatment have then been carried out, results which are collected at the end of Chapter 4.

7 Appendix I

Table S1. Crystal data and structure refinement for PCN6@nicotine[a]

Empirical formula	$2[Cu_4(C_{24}H_{12}N_3O_6)_{2/3}]\ 4(C_{10}H_{14}N_2)$
Formula weight	3495.19
Temperature/K	100
Crystal system	trigonal
Space group	R32
a/Å	33.094
b/Å	33.093
c/Å	79.840
α/°	90
β/°	90
γ/°	120
Volume/Å^3	75727
Z	9
ρ_{calc}g/cm^3	0.690
μ/mm^{-1}	0.514
F(000)	16056.0
Radiation/Å	synchrotron λ = 0.700
Reflections collected	102014
Independent reflections	24158 [R_{int} = 0.0774, R_{sigma} = 0.0605]
Data/restraints/parameters	24158/598/710
Goodness-of-fit on F^2	1.148
Final R indexes [I>=2σ (I)]	R_1 = 0.0702, wR_2 = 0.1998
Final R indexes [all data]	R_1 = 0.0962, wR_2 = 0.2144
Largest diff. peak/hole / e Å^{-3}	1.41/-0.59
Flack parameter	0.440(16)

a. Under investigations, centricity has to be assessed.

Table S2. Crystal data and structure refinement for PUM168 native

Empirical formula	$[Zn_3(C_{24}H_{18}N_4O_2)_{1.5}\cdot(C_{14}H_8O_4)_3]\cdot 3(C_3H_7NO)$
Formula weight	1727.64
Temperature/K	100
Crystal system	triclinic
Space group	P-1
a/Å	15.153
b/Å	15.198
c/Å	26.876
α/°	102.95
β/°	96.99
γ/°	90.53
Volume/Å^3	5981
Z	2
ρ_{calc} g/cm^3	0.967
μ/mm^{-1}	0.625
F(000)	1795.0
Radiation/Å	synchrotron λ = 0.700
Reflections collected	133395
Independent reflections	22710 [R_{int} = 0.0588, R_{sigma} = 0.0549]
Data/restraints/parameters	22710/1800/1153
Goodness-of-fit on F^2	1.110
Final R indexes [I>=2σ (I)]	R_1 = 0.1173, wR_2 = 0.3174
Final R indexes [all data]	R_1 = 0.1223, wR_2 = 0.3212
Largest diff. peak/hole / e Å^{-3}	2.12/-1.68

Table S3. Crystal data and structure refinement for PUM210[a]

Empirical formula	$[Zn_8(C_{24}H_{18}N_4O_2)_3 \cdot (C_{12}H_6O_4)_8 \cdot (H_2O)_2] \cdot 6(C_3H_7NO)$
Formula weight	3961.77
Temperature/K	100
Crystal system	monoclinic
Space group	C2
a/Å	18.985
b/Å	18.002
c/Å	62.087
α/°	90
β/°	90.47
γ/°	90
Volume/Å^3	21223
Z	4
ρ_{calc}g/cm^3	1.240
μ/mm^{-1}	0.926
F(000)	8142.0
Radiation	Synchrotron λ = 0.700
Reflections collected	64186
Independent reflections	41693 [R_{int} = 0.0835, R_{sigma} = 0.0670]
Data/restraints/parameters	41693/793/2265
Goodness-of-fit on F^2	1.390
Final R indexes [I>=2σ (I)]	R_1 = 0.1227, wR_2 = 0.3312
Final R indexes [all data]	R_1 = 0.1519, wR_2 = 0.3608
Largest diff. peak/hole / e Å^{-3}	4.47/-3.00
Flack parameter	0.53(13)

[a] Preliminary Data, centricity has to be assessed.

Table S4. Crystal data and structure refinement for PUM198

Empirical formula	$[Zn_2(C_{24}H_{18}N_4O_2)_2(C_8H_4O_4)_2]\ 3(C_3H_7NO)$
Formula weight	1463.11
Temperature/K	100(2)
Crystal system	monoclinic
Space group	$P2_1/c$
a/Å	24.340
b/Å	17.380
c/Å	17.850
α/°	90
β/°	94.493
γ/°	90
Volume/Å^3	7529.2
Z	4
ρ_{calc}g/cm^3	1.291
μ/mm^{-1}	0.680
F(000)	3032.0
Radiation/Å	synchrotron λ = 0.700
Reflections collected	150133
Independent reflections	18575 [R_{int} = 0.0811, R_{sigma} = 0.0473]
Data/restraints/parameters	18575/84/796
Goodness-of-fit on F^2	1.035
Final R indexes [I>=2σ (I)]	R_1 = 0.1073, wR_2 = 0.2992

Table S5. Crystal data and structure refinement for PUM168@eugenol

Empirical formula	$[Zn_3(C_{24}H_{18}N_4O_2)_{1.5}\cdot(C_{14}H_8O_4)_3]\cdot2(C_3H_7NO)$ $2(C_{10}H_{12}O_2)$
Formula weight	1989.45
Temperature/K	100
Crystal system	triclinic
Space group	P-1
a/Å	15.178
b/Å	15.218
c/Å	26.910
α/°	78.44
β/°	83.16
γ/°	88.50
Volume/Å^3	6044
Z	2
ρ_{calc}g/cm^3	1.094
μ/mm^{-1}	0.627
F(000)	2061.0
Radiation/Å	synchrotron λ = 0.700
Reflections collected	226556
Independent reflections	38355 [R_{int} = 0.0244, R_{sigma} = 0.0183]
Data/restraints/parameters	38355/1867/1563
Goodness-of-fit on F^2	1.041
Final R indexes [I>=2σ (I)]	R_1 = 0.0806, wR_2 = 0.2434

Table S6. Crystal data and structure refinement for PUM168@propofol

Empirical formula	$2[Zn_3(C_{24}H_{18}N_4O_2)_{1.5}\cdot(C_{14}H_8O_4)_3]$ $3.5(C_3H_7NO)$ $8(C_{12}H_{18}O)$
Formula weight	4742.46
Temperature/K	100
Crystal system	triclinic
Space group	P-1
a/Å	15.266
b/Å	26.955
c/Å	30.503
α/°	89.23
β/°	87.83
γ/°	82.19
Volume/Å^3	12421
Z	2
ρ_{calc}g/cm^3	1.268
μ/mm^{-1}	0.621
F(000)	4980.0
Radiation/Å	synchrotron λ = 0.700
Reflections collected	471438
Independent reflections	79376 [R_{int} = 0.0335, R_{sigma} = 0.0242]
Data/restraints/parameters	79376/4896/3226
Goodness-of-fit on F^2	1.023
Final R indexes [I>=2σ (I)]	R_1 = 0.0793, wR_2 = 0.2452

Table S7. Crystal data and structure refinement for PUM168@carvacrol

Empirical formula	$2[Zn_3(C_{24}H_{18}N_4O_2)_{1.5}\cdot(C_{14}H_8O_4)_3]$ $5.5(C_3H_7NO)$ $9(C_{10}H_{14}O)$
Formula weight	4869.70
Temperature/K	100
Crystal system	triclinic
Space group	P-1
a/Å	21.478
b/Å	21.554
c/Å	26.888
α/°	94.90
β/°	102.41
γ/°	89.99
Volume/Å^3	12109
Z	2
ρ_{calc} g/cm^3	1.336
μ/mm^{-1}	0.665
F(000)	5098.0
Radiation	synchrotron λ = 0.7000
Reflections collected	437306
Independent reflections	59235 [R_{int} = 0.0288, R_{sigma} = 0.0234]
Data/restraints/parameters	59235/228/3187
Goodness-of-fit on F^2	0.999
Final R indexes [I>=2σ (I)]	R_1 = 0.0707, wR_2 = 0.2058

Table S8. Crystal data and structure refinement for PUM168@ce-mix

Empirical formula	$[Zn_3(C_{24}H_{18}N_4O_2)_{1.5}\cdot(C_{14}H_8O_4)_3]\cdot(C_3H_7NO)$ $2(C_{10}H_{12}O_2)0.5(C_{10}H_{14}O)$
Formula weight	1975.94
Temperature/K	293(2)
Crystal system	triclinic
Space group	P-1
a/Å	15.186
b/Å	15.214
c/Å	26.945
α/°	97.30
β/°	95.67
γ/°	91.78
Volume/Å^3	6146.2
Z	2
ρ_{calc}g/cm^3	1.070
μ/mm^{-1}	0.617
F(000)	2045.0
Radiation/Å	synchrotron λ = 0.700
Reflections collected	216011
Independent reflections	36214 [R_{int} = 0.0216, R_{sigma} = 0.0301]
Data/restraints/parameters	36214/36/1553
Goodness-of-fit on F^2	1.061
Final R indexes [I>=2σ (I)]	R_1 = 0.0743, wR_2 = 0.2385
Final R indexes [all data]	R_1 = 0.0772, wR_2 = 0.2417
Largest diff. peak/hole / e Å^{-3}	2.13/-1.37

Table S9. Crystal data and structure refinement for PUM168@et-mix

Empirical formula	$[Zn_3(C_{24}H_{18}N_4O_2)_{1.5}\cdot(C_{14}H_8O_4)_3]\cdot(C_3H_7NO)$ $3(C_{10}H_{12}O_2)$ $1.5(C_{10}H_{14}O)$
Formula weight	2301.37
Temperature/K	100
Crystal system	triclinic
Space group	P-1
a/Å	15.119
b/Å	15.152
c/Å	26.786
α/°	90.15
β/°	106.21
γ/°	91.17
Volume/Å^3	5890
Z	2
ρ_{calc}g/cm^3	1.298
μ/mm^{-1}	0.654
F(000)	2400.0
Radiation/Å	synchrotron λ = 0.700
Reflections collected	194171
Independent reflections	23759 [R_{int} = 0.1093, R_{sigma} = 0.0813]
Data/restraints/parameters	23759/222/1472
Goodness-of-fit on F^2	1.014
Final R indexes [I>=2σ (I)]	R_1 = 0.0863, wR_2 = 0.2265
Final R indexes [all data]	R_1 = 0.1045, wR_2 = 0.2417

Table S10. Crystal data and structure refinement for PUM 168@ct-mix [a]

Empirical formula	$4[Zn_3(C_{24}H_{18}N_4O_2)_{1.5}\cdot(C_{14}H_8O_4)_3]\ 15(C_{10}H_{14}O)$
Formula weight	8383.13
Temperature/K	100
Crystal system	triclinic
Space group	P1
a/Å	20.519
b/Å	22.415
c/Å	28.365
α/°	113.19
β/°	96.99
γ/°	90.04
Volume/Å^3	11887
Z	1
ρ_{calc}g/cm^3	1.179
μ/mm^{-1}	0.640
F(000)	4397.0
Radiation/Å	synchrotron λ = 0.700
Reflections collected	311283
Independent reflections	48186 [R_{int} = 0.0887, R_{sigma} = 0.0486]
Data/restraints/parameters	48186/381/5033
Goodness-of-fit on F^2	1.022
Final R indexes [I>=2σ (I)]	R_1 = 0.0972, wR_2 = 0.2782
Final R indexes [all data]	R_1 = 0.1393, wR_2 = 0.3196
Largest diff. peak/hole / e Å^{-3}	3.39/-1.83

a) Preliminary data, centricity has to be assessed.

Table S11. Crystal data and structure refinement for PUM-FLEX-Zn

Empirical formula	$[ZnO_4(C_{26}H_{18}N_2O_4)_3]\cdot 4(C_3H_7NO)$
Formula weight	1829.07
Temperature/K	100
Crystal system	triclinic
Space group	P-1
a/Å	15.273
b/Å	18.396
c/Å	29.288
α/°	101.24
β/°	98.56
γ/°	98.33
Volume/Å^3	7851
Z	2
ρ_{calc}g/cm^3	0.770
μ/mm^{-1}	0.619
F(000)	1872.0
Radiation/Å	synchrotron λ = 0.700
Reflections collected	57294
Independent reflections	19098 [R_{int} = 0.0819, R_{sigma} = 0.0972]
Data/restraints/parameters	19098/0/1093
Goodness-of-fit on F^2	1.092
Final R indexes [I>=2σ (I)]	R_1 = 0.0937, wR_2 = 0.2672

Table S12. Crystal data and structure refinement for PUM-Flex-Zr [a]

Empirical formula	$[Zr_6O_4OH_4(C_{26}H_{18}N_2O_4)]_4$ 6.5(H_2O)
Formula weight	2476.11
Temperature/K	100
Crystal system	monoclinic
Space group	$P2_1$
a/Å	19.551
b/Å	24.348
c/Å	19.579
α/°	90
β/°	98.16
γ/°	90
Volume/Å^3	9225.8
Z	2
ρ_{calc}g/cm^3	0.890
μ/mm^{-1}	0.357
F(000)	2488.0
Radiation/Å	synchrotron λ = 0.700
Reflections collected	45594
Independent reflections	24792 [R_{int} = 0.2666, R_{sigma} = 0.4495]
Data/restraints/parameters	24792/2666/1154
Goodness-of-fit on F^2	0.819
Final R indexes [I>=2σ (I)]	R_1 = 0.0961, wR_2 = 0.2228
Final R indexes [all data]	R_1 = 0.2877, wR_2 = 0.3326
Largest diff. peak/hole / e Å^{-3}	1.04/-0.88
Flack parameter	0.39(10)

a) Centricity has to be assessed.

Table S13. Crystal data and structure refinement for PUM-Flex-Cd

Empirical formula	$Cd(C_{28}H_{18}N_2O_8)\ (C_3H_7NO)_2{\cdot}H_2O$
Formula weight	787.05
Temperature/K	100
Crystal system	orthorhombic
Space group	Pbcn
a/Å	12.4671
b/Å	16.3497
c/Å	21.3495
α/°	90
β/°	90
γ/°	90
Volume/Å^3	4351.71
Z	4
ρ_{calc}g/cm^3	1.201
μ/mm^{-1}	0.534
F(000)	1608.0
Radiation/Å	synchrotron $\lambda = 0.70000$
Reflections collected	90766
Independent reflections	5408 [$R_{int} = 0.0417$, $R_{sigma} = 0.0141$]
Data/restraints/parameters	5408/186/241
Goodness-of-fit on F^2	1.036
Final R indexes [I>=2σ (I)]	$R_1 = 0.0706$, $wR_2 = 0.2048$
Final R indexes [all data]	$R_1 = 0.0723$, $wR_2 = 0.2071$
Largest diff. peak/hole / e Å^{-3}	2.47/-2.22

8 Appendix II

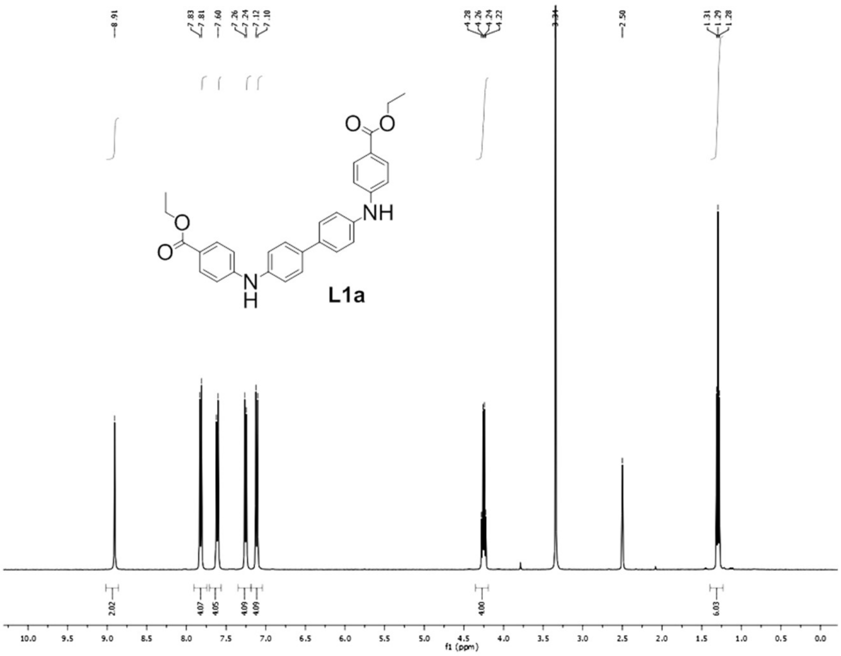

Figure S1 ^{1}H-NMR (400 MHz, dmso-d, 25°C) of **L1a**

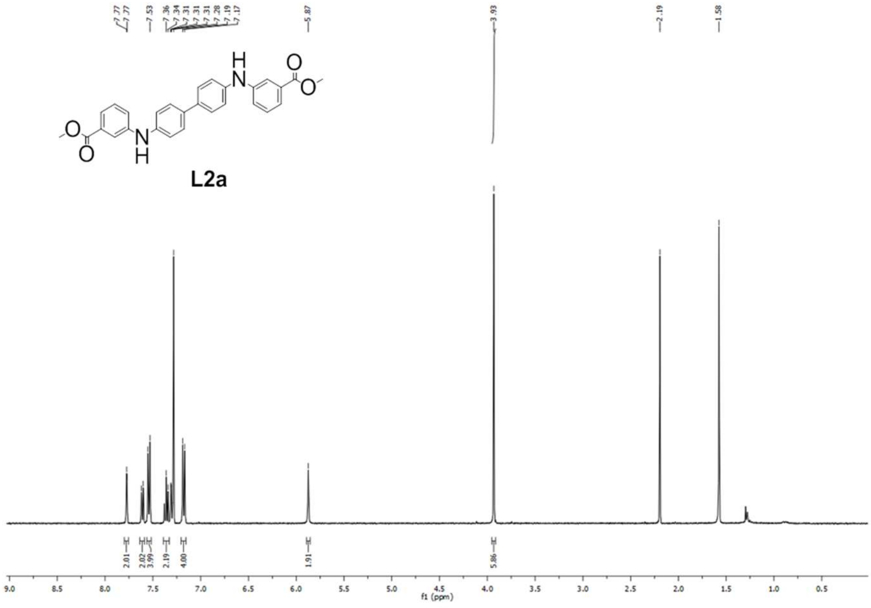

Figure S3 ^{1}H-NMR (400 MHz, CDCl$_3$, 25°C) of **L2a**

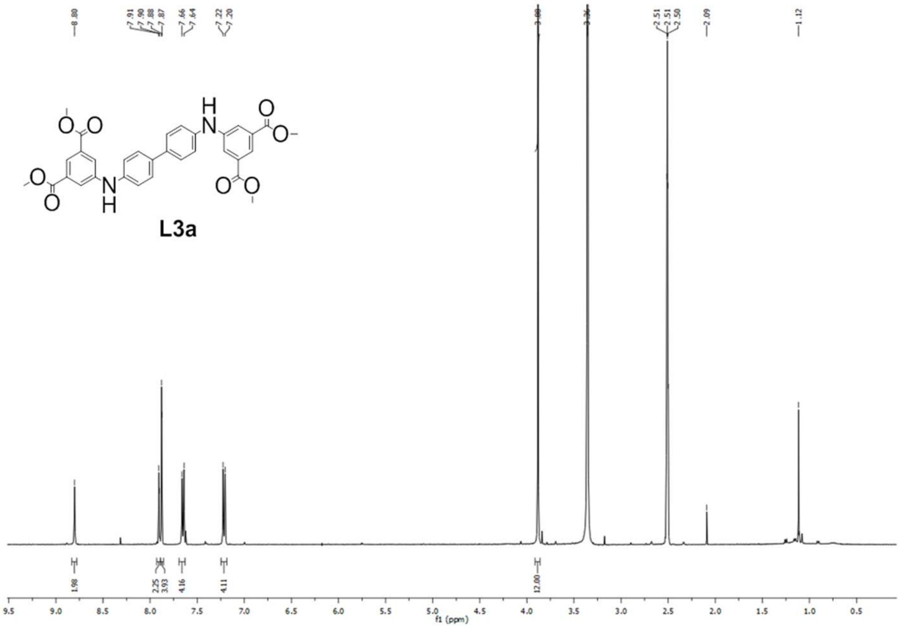

Figure S3 ^{1}H-NMR (400 MHz, dmso-d, 25°C) of **L3a**

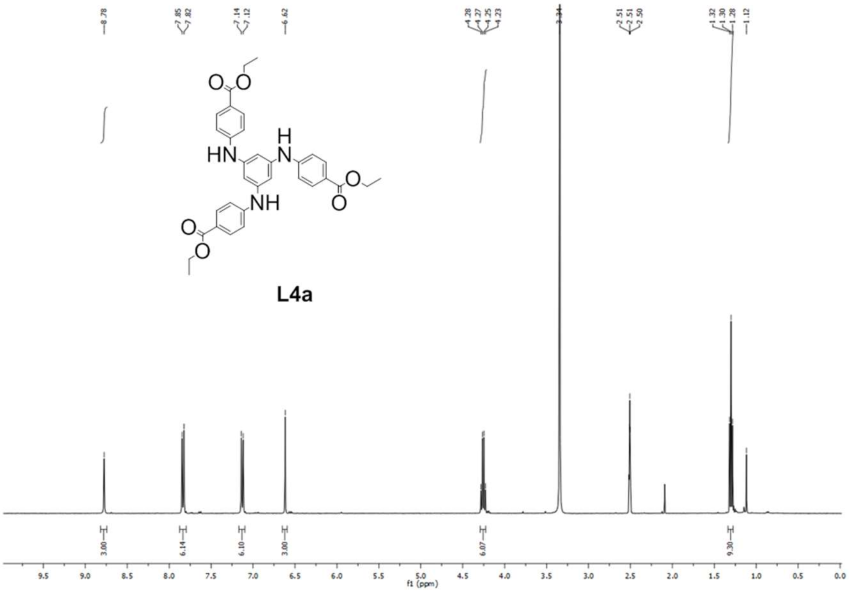

Figure S4 ^{1}H-NMR (400 MHz, dmso-d, 25°C) of **L4a**

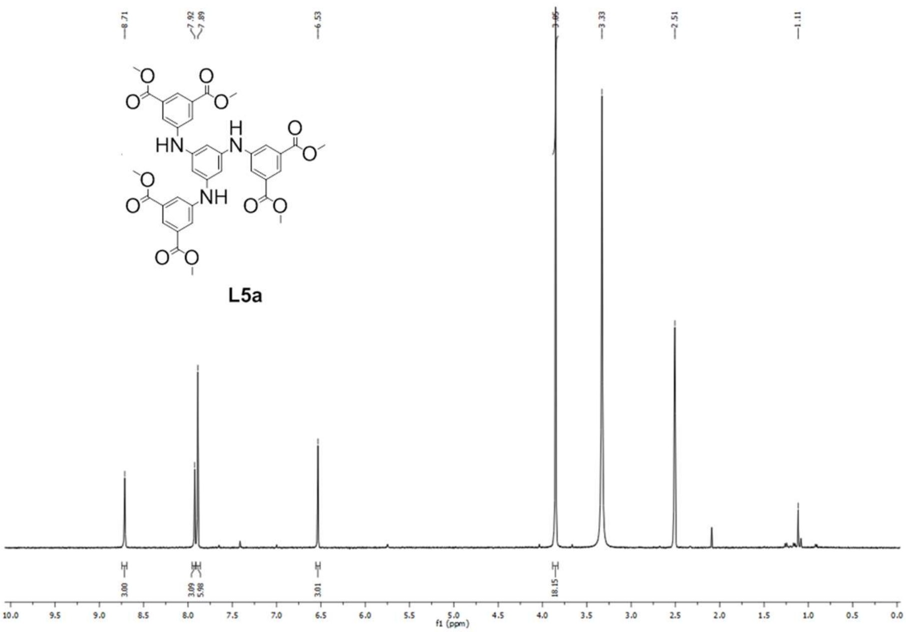

Figure S5 ^{1}H-NMR (400 MHz, dmso-d, 25°C) of **L5a**

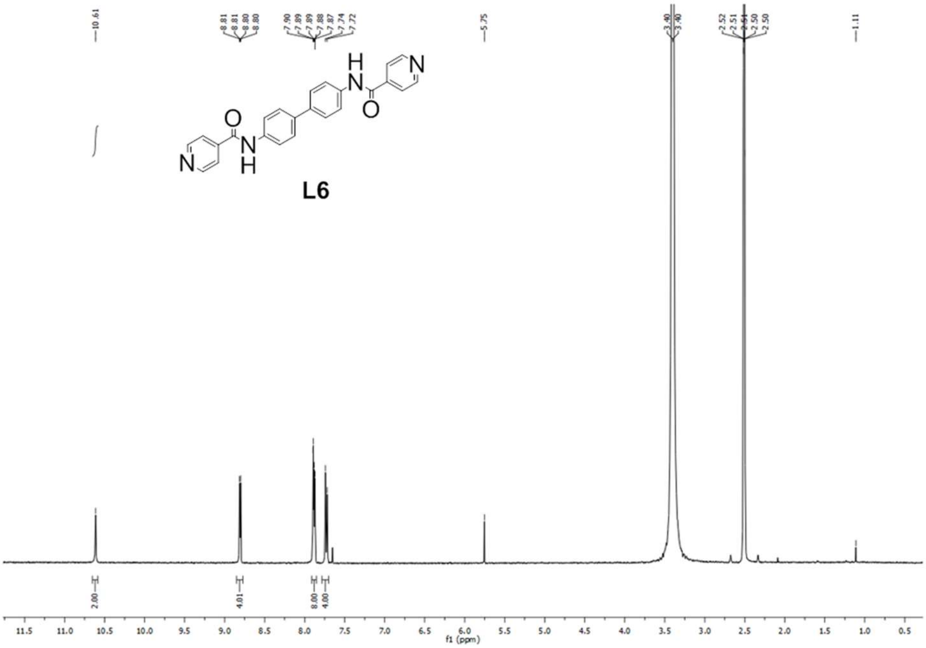

Figure S6 ^{1}H-NMR (400 MHz, dmso-d, 25°C) of **L6**

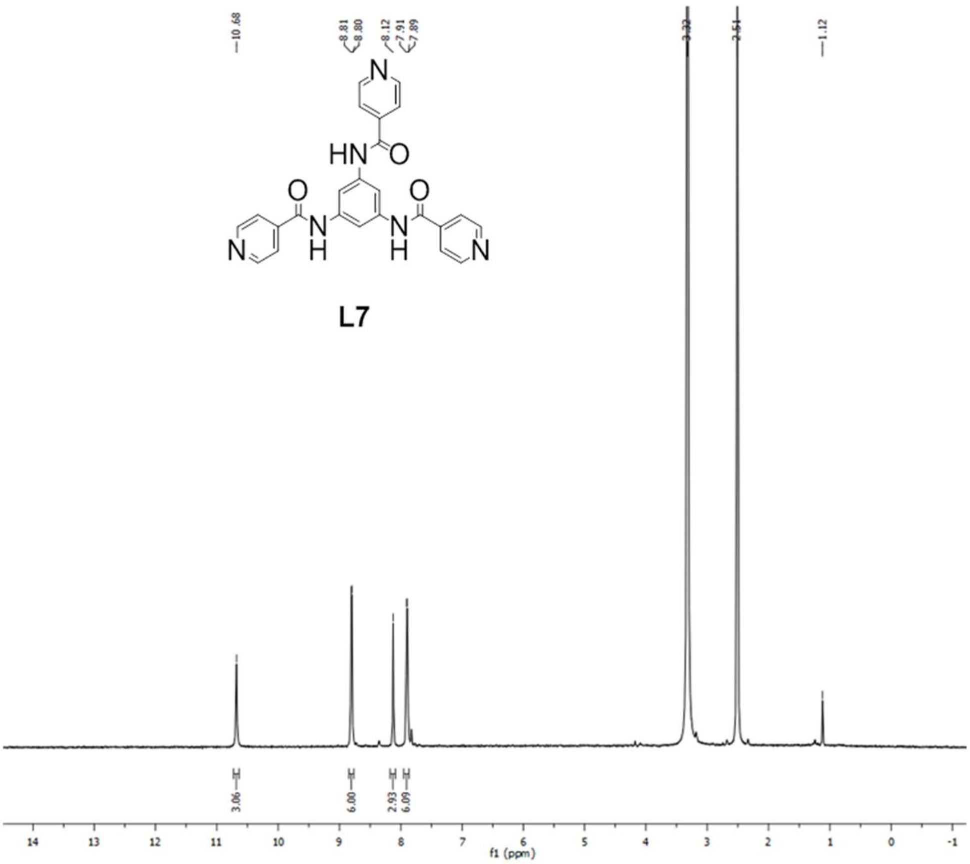

Figure S6 ^{1}H-NMR (400 MHz, dmso-d, 25°C) of **L7**

9 References

---

[1] M. Thommes, K. Kaneko, A. V. Neimark, J. P. Olivier, F. R. Reinoso, J. Rouquerol and K. S.W. Sing, *Pure Appl. Chem.* **2015**, DOI 10.1515/pac-2014-1117

[2] A. G. Slater and A. I. Cooper, *Science*, **2015**, 348, aaa8075; doi: 10.1126/science.aaa8075

[3] Handbook of porous solids, F. Schüth, K. S. W. Sing, J. Weitkamp (Editors). Wiley-VCH, 2002

[4] E. T. C. Vogt and B. M. Weckhuysen, *Chem. Soc. Rev.,* **2015***,* DOI: 10.1039/c5cs00376h.

[5] T. Blasco, A. Corma, M.T. Navarro, J.P. Pariente, *Journal of Catalysis*, **1995**, 156, 1, 65-74, doi:10.1006/jcat.1995.1232

[6] J. Iglesias, , J. A. Melero, J. S. Pardo, *Journal of Molecular Catalysis A: Chemical*, **2008**, 291 75–84

[7] Ordered Porous Solids, V. Valtchev, S. Mintova, M. Tsapatsis (Editors), Elsevier, **2009**, Amsterdam. 2013.

[8] P. M. Ajayan, Nanotubes from carbon. *Chemical Reviews* **1999,** *99* (7), 1787-1799.

[9] M. Trojanowicz, *Trends in Analytical Chemistry*, **2006**, Vol. 25, No. 5, 480-489; doi:10.1016/j.trac.2005.11.008

[10] A.N. Khlobystov, D. A. Britz, G. A. D. Briggs, Molecules in carbon nanotubes. *Accounts of Chemical Research,* **2005,** *38* (12), 901-909.

[11] L.J. Li, A.N. Khlobystov, J. G. Wiltshire, G. A. D. Briggs, R. J. Nicholas, Diameterselectiveencapsulation of metallocenes in single-walled carbon nanotubes, *Nature Materials* **2005,** *4* (6), 481-485.

[12] S.Y. Ding and W. Wang, *Chem. Soc. Rev*., **2013**, 42, 548; DOI: 10.1039/c2cs35072f

[13] A. P. Cŏté, A. I. Benin, N. W. Ockwig, M. O’Keeffe, A. J. Matzger and O. M. Yaghi, *Science*, **2005**, 310, 1166.

---

[14] F. J. Uribe-Romo, J. R. Hunt, H. Furukawa, C. Klock, M. O'Keeffe and O. M. Yaghi, *J. Am. Chem. Soc.*, **2009**, 131, 4570.

[15] F. J. Uribe-Romo, C. J. Doonan, H. Furukawa, K. Oisaki and O. M. Yaghi, *J. Am. Chem. Soc.*, **2011**, 133, 11478.

[16] P. Kuhn, M. Antonietti and A. Thomas, *Angew. Chem., Int.Ed.,* **2008**, 47, 3450.

[17] T. Ben and S. Qiu*, CrystEngComm*, **2013**, 15, 17-26; DOI: 10.1039/c2ce25409c

[18] T. Ben, H. Ren, S. Ma, D. Cao, J. Lan, X. Jing, W. Wang, J. Xu, F. Deng, J. M. Simmons, S. Qiu, and G. Zhu, *Angew. Chem. Int. Ed*. **2009**, 48, 9457 –9460, DOI: 10.1002/anie.200904637

[19] S. R. Batten, N. R. Champness, X. M. Chen, J. G. Martinez, S. Kitagawa, L. Öhrström, M. O'Keeffe, M. P. Suh and J. Reedijk, *Cryst. Eng. Comm.*, **2012**, 14, 3001, doi: 10.1039/c2ce06488j

[20] M. Eddaoudi, D. B. Moler, H. Li, B. Chen,T. M. Reineke, M. O'Keeffe and O. M. Yaghi, Acc. Chem. Res., **2001,** 34, 319-330, doi:10.1021/ar000034b

[21] H. Li, M. Eddaoudi, M. O'Keeffe and O. M. Yaghi, *Nature,* **1999***,* 402, 276-279; doi:10.1038/46248.

[22] L. J. Murray, M. Dincă and J. R. Long, *Chem. Soc. Rev.,* **2009**, 38, 1294–1314; doi: 10.1039/b802256a

[23] M. Eddaoudi, J. Kim, N. Rosi, D. Vodak, J. Wachter, M. O′Keeffe, O. M. Yaghi, *Science,* **2002***,* 295 (5554), 469-472; doi: 10.1126/science.1067208

[24] J. L. C. Rowsell and O. M. Yaghi*, J. Am. Chem. Soc.*, **2006**, 128, 1304-1315 10.1021/ja056639q

[25] H. Deng, S. Grunder, K. E. Cordova, C. Valente, H. Furukawa, M. Hmadeh, F. Gándara, A. C. Whalley, Z. Liu, S. Asahina, H. Kazumori, M. O′Keeffe, O. Terasaki, J. F. Stoddart, O. M. Yaghi, *Science,* **2012**, 336, Issue 6084, 1018-1023, DOI:10.1126/science.1220131

[26] H. Furukawa, K. E. Cordova, M. O'Keeffe, O. M. Yaghi, *Science,* **2013**, 341, 1230444; DOI: 10.1126/science.1230444

[27] Cambridge Structural Database System, Cambridge Crystallographic Data Centre, Cambridge, UK Version 5.32.

[28] R. M. Izatt, J. S. Bradshaw, S. R. Izatt and R. G. Harrison, *Macrocyclic and Supramolecular Chemistry: How Izatt–Christensen Award Winners Shaped the Field*, **2016**, ISBN: 978-1-119-05384-2

[29] H. L. Jiang, T. A. Makal, H. C. Zhou, *Coordination Chemistry Reviews* **2013**, 257,2232– 2249; doi: 10.1016/j.ccr.2013.03.017.

[30] A. Ferguson, L. Liu, S. Blackwood and S. G. Telfer, *Chemistry in New Zealand*,**2014**, 113-118.

[31] J. H. Park, W. R. Lee, Y. Kim, H. J. Lee, D. W. Ryu, W. Ju Phang, and C. S. Hong, *Cryst. Growth Des.*, **2014**, 14, 699−704, doi: 10.1021/cg401583v

[32] G.S. Yang, Z. L. Lang, H. Y. Zang, Y.Q.Lan, W. W. He, X.L Zhao, L. K. Yan, X.L. Wang, Z. M. Su, *Chem. Comm.*, **2013**, 49, 1088-1090.

[33] J. Zhang, L. Wojtas, R. W. Larsen, M. Eddaoudi, M. J. Zaworotko, J. *Am. Chem. Soc.,* **2009**, 131, 17040-17041.

[34] H. L Jiang, Y. Tatsu, Z. H. Lu, Q. J. Xu, *J. Am. Chem. Soc.*, **2010**, 132, 5586-5587

[35] O. K. Farha, C. D. Malliakas, M. G. Kanatzidis, and J. T. Hupp, *J. Am. Chem. Soc.*, **2010**, 132, 950–952.

[36] R. K. Deshpande, G. I. N. Waterhouse,G. B. Jameson and S. G. Telfer, *Chem. Commun.*, **2012**,48, 1574–1576; DOI: 10.1039/c1cc12884a

[37] O. Shekhah, H. Wang, M. Paradinas, C. Ocal, B. Schüpbach, A. Terfort, D. Zacher, R, A. Fischer and C. Wöll, *Nature Materials* , **2009**, 8, 481 – 484; doi:10.1038/nmat2445

[38] R. Haldar, N. Sikdar and T. K. Maji, *Materials Today*, **2015**, Vol. 18, 2, 97-116

[39] Y. Takashima, V. M. Martínez, S. Furukawa, M. Kondo, S. Shimomura, H. Uehara, M. Nakahama, K. Sugimoto and S. Kitagawa, *Nature Communications*, **2011**, 2, 168; doi:10.1038/ncomms1170

[40] Z. Wanga and S. M. Cohen, *Chem. Soc. Rev.,* **2009**, 38, 1315-1329 ; **DOI:** 10.1039/B802258P

[41] P. Deria, J. E. Mondloch, O. Karagiaridi, W. Bury,J. T. Hupp and O. K. Farha, *Chem. Soc. Rev.,* **2014**, 43, 5896

[42] A. D. Burrows, *Encyclopedia of Inorganic and Bioinorganic Chemistry,* **2014**, Metal–Organic Frameworks: Postsynthetic Modification; doi: 10.1002/9781119951438.eibc2207

[43] a) J. A. Mason, M. Veenstra and J. R. Long, *Chem. Sci*., **2014**, 5, 32-51; DOI: 10.1039/c3sc52633j; b) T. He, P. Pachfule, H. Wu, Q. Xu and P.Chen, *Nature Reviews Materials* **, 2016,** 1-17 doi:10.1038/natrevmats.2016.59

[44] a) D. M. D’Alessandro, B. Smit and J. R. Long, *Angew. Chem. Int. Ed.*, **2010**, 49, 6058; b) J.-R. Li, J. Sculley and H.-C. Zhou, *Chem. Rev*., **2012**, 112, 869

[45] J.-R. Li, J. Sculley and H.-C. Zhou, *Chem. Rev*., **2012**, 112, 869

[46] S. R. Venna, M. A. Carreon, *Chemical Engineering Science,* **2015**, 124, 3–19

[47] A. H. Chughtai, N. Ahmad, H. A. Younus, A. Laypkovc and F. Verpoort, *Chem. Soc. Rev.*, **2015**, 44, 6804-6849; DOI: 10.1039/c4cs00395k

[48] L. E. Kreno, K. Leong, O. K. Farha, M. Allendorf, R. P. V. Duyne, and J. T. Hupp, *Chem. Rev.*, **2012**, *112* (2), pp 1105–1125; DOI: 10.1021/cr200324t

---

[49] a) S. Achmann, G. Hagen, J. Kita , I. M. Malkowsky, C. Kiener and R. Moos, *Sensors,* **2009**, *9*, 1574-1589; doi:10.3390/s90301574; b) K. Müller-Buschbaum, F. Beuerle , C. Feldmann, *Microporous and Mesoporous Materials*, **2015**, 216 171-199.

[50] T. Yamada, K. Otsubo, R. Makiurac and H. Kitagawa*, Chem. Soc. Rev*., **2013**, 42, 6655-6669; DOI: 10.1039/c3cs60028a

[51] M. Kurmoo, *Chem. Soc. Rev*., **2009**,38, 1353-1379; DOI: 10.1039/B804757J

[52] a) for methane storage: Y. Peng, V. Krungleviciute, I. Eryazici, J. T. Hupp, O. K. Farha , T. Yildirim , *J. Am. Chem. Soc.* , **2013**, 135, 11887−11894, doi: 10.1021/ja4045289; b) for carbon dioxide: K. Sumida, D. L. Rogow, J. A. Mason, T. M. McDonald, E. D. Bloch, Z. R. Herm, T. H. Bae and J. R. Long, *Chem. Rev.*, **2012**, 112, 724–781, doi:10.1021 /cr2003272

[53] a) for methane storage: Y. Peng, V. Krungleviciute, I. Eryazici, J. T. Hupp, O. K. Farha , T. Yildirim , *J. Am. Chem. Soc.* , **2013**, 135, 11887−11894, doi: 10.1021/ja4045289; b) for carbon dioxide: K. Sumida, D. L. Rogow, J. A. Mason, T. M. McDonald, E. D. Bloch, Z. R. Herm, T. H. Bae and J. R. Long, *Chem. Rev.*, **2012**, 112, 724–781, doi:10.1021 /cr2003272

[54] a) D. Zhao, D. Yuan and H. C. Zhou, *Energy Environ. Sci*., **2008**, 1, 222–235, DOI: 10.1039/b808322n; b) DOE Office of Energy Efficiency and Renewable Energy Hydrogen, Fuel Cells & Infrastructure Technologies Program Multi-Year Research, Development and Demonstration Plan, available at: http://www.eere.energy.gov/ hydrogenandfuelcells/mypp.

[55] H. Furukawa et al*, Inorg. Chem*., **2011**, 50, 9147–9152.

[56] H. Deng et al., *Science*, **2010**,327,846–850.

[57] O. K. Farha et al., *J. Am. Chem. Soc*., **2012**, 134, 15016–15021

[58] H. Wu, J. Yang, Z.-M. Su, S. R. Batten, J.-F. Ma*, J. Am. Chem. Soc*., **2011**, 133, 11406–11409.

[59] O. K. Farha et al., *Nat. Chem.*, **2010**, 2, 944–948.

[60] S. Ma et al., *J. Am. Chem. Soc.*, **2008**, 130,1012–1016.

[61] H. Furukawa et al., *Science*, **2010**, 329, 5990.

[62] T. C. Narayan, T. Miyakai, S. Seki, M. Dincă, *J. Am. Chem. Soc*., **2012**, 134, 12932–12935.

[63] K. Saravanan, M. Nagarathinam, P. Balaya, J. J. Vittal, *J. Mater. Chem*., **2010**, 20, 8329.

[64] M. Fujita, Y. J. Kwon, S. Washizu, K. Ogura, *J. Am. Chem. Soc*., **1994**, 116, 1151–1152.

[65] J. S. Seo et al., *Nature*, **2000**, 404, 982–986.

[66] K. M. L. Taylor, W. J. Rieter, W. Lin, *J. Am. Chem. Soc*., **2008**, 130, 14358–14359.

---

[67] P. Horcajada, T. Chalati, C. Serre, B. Gillet, C. Sebrie, T. Baati, J. F. Eubank, D. Heurtaux, P. Clayette, C. Kreuz, J. S. Chang, Y. K. Hwang , V. Marsaud, P. N. Bories, L. Cynober, S. Gil , G. Férey , P. Couvreur and R. Gref, *Nature Materials,* **2010***,* 9, 172–178, doi:10.1038/nmat2608

[68] P. Horcajada, C. Serre, M. Vallet-Reg, M. Sebban, F. Taulelle, and G. Férey, *Angew. Chem. Int. Ed*. **2006**, 45, 5974 –5978; DOI: 10.1002/anie.200601878

[69] P. Horcajada, C. Serre, G. Maurin, N. A. Ramsahye, F. Balas, M. Vallet-Regí, M. Sebban, F. Taulelle and G. Férey, *J. Am. Chem. Soc.*, **2008**, *130* (21), 6774–6780, **DOI:** 10.1021/ja710973k

[70] K. S. Park, Z. Ni, A. P. Côté, J. Y. Choi, R. Huang, F. J. U.Romo, H. K. Chae, M. O'Keeffe, and O. M. Yaghi, *PNAS*, **2006**, 103, 27, 10186-10191, doi: 10.1073/pnas.0602439103.

[71] N. Liedana, A. Galve, C. Rubio, C. Téllez, and J. Coronas, *Appl. Mater. Interfaces* **2012**, 4, 5016−5021, dx.doi.org/10.1021/am301365h

[72] D. Cunha, M. Ben Yahia, S. Hall, S. R. Miller, H. Chevreau, E. Elkaïm, G. Maurin, P. Horcajada, C. Serre, *Chem. Mater.*, **2013**, 25, 2767−2776; doi:10.1021/cm400798p

[73] S. D. Vinot, C. Martineau, S. Diaby, M. B. Yahia, S. Miller, C. Serre, P. Horcajada, D. Cunha, F. Taulelle and G. Maurin, *J. Phys. Chem. C* , **2013**, 117, 11694−11704, doi: 10.1021/jp402916y

[74] I. Erucar and S. Keskin, *Ind. Eng. Chem. Res.*, **2016**, 55, 1929−1939, DOI: 10.1021/acs.iecr.5b04556

[75] Y. Inokuma, S. Yoshioka, J. Ariyoshi, T. Arai, Y. Hitora, K. Takada, S. Matsunaga, K. Rissanen and M. Fujita, *Nature,* **2013**, 495, 461–466; doi:10.1038/nature11990.

[76] K. Biradha and M. Fujita, *Angew. Chem. Int. Ed.* **2002**, *41*, 3392-3395.

[77] a) Y. Inokuma, S. Yoshioka, J. Ariyoshi, T. Arai, M. Fujita *Nat. Protoc.,* **2014**, *9*, 246-252. b) M. Hoshino, A. Khutia, H. Xing, Y. Inokuma and M. Fujita, *IUCrJ,* **2016**, 3, 139–151; http://dx.doi.org/10.1107/ S2052252515024379.

[78] T. R. Ramadhar, S.L. Zheng, Y. S. Chen and J. Clardy, *Acta Cryst*., **2015**, A71, 46–58; doi:10.1107/S2053273314019573

[79] K. Ikemoto, Y. Inokuma, K. Rissanen and M. Fujita, *J. Am. Chem. Soc.*, **2014**, *136* (19), 6892–6895; **doi:** 10.1021/ja502996h

[80] V. Duplan, M. Hoshino, W. Li, T. Honda and M. Fujita, *Angew. Chem. Int. Ed.*, **2016**, 55, 4919 –4923; doi: 10.1002/anie.201509801

[81] A. B. Cuenca, N. Zigon, V. Duplan, M. Hoshino, M. Fujita and E. Fernàndez*, Chem. Eur.J.*, **2016**, 22,4723 –4726; doi: 10.1002/chem.201600392.

[82] S. Yoshioka, Y. Inokuma, M. Hoshino, T. Satob and M. Fujita, *Chem. Sci.*, **2015**, 6, 3765-3768; **DOI:** 10.1039/C5SC01681A

[83] a) Y. Matsuda, T. Mitsuhashi, S. Lee, M. Hoshino, T. Mori, M. Okada, H. Zhang, F. Hayashi, M. Fujita and I. Abe*, Angew. Chem. Int. Ed*., **2016**, 55, 5785 –5788; DOI: 10.1002/ anie.201601448; b) Y. Inokuma, T. Ukegawa, M. Hoshinoac and M. Fujita, *Chem. Sci*., **2016**, 7, 3910–3913; doi: 10.1039/c6sc00594b; c) N. Zigon, M. Hoshino, S. Yoshioka, Y. Inokuma and M. Fujita, *Angew. Chem. Int. Ed* , **2015**, 54, 9033 –9037; doi: 10.1002 /anie.201502302

[84] S. Urban, R. Brkljača, M. Hoshino, S. Lee and M. Fujita, *Angew. Chem. Int. Ed*., **2016**, 55, 2678 –2682, doi: 10.1002/anie.201509761.

[85] S. Yoshioka, Y. Inokuma, V. Duplan, R. Dubey and M. Fujita, *J. Am. Chem. Soc*., 2016, 138, 10140−10142, doi: 10.1021/jacs.6b05817

[86] E. V. Vinogradova, P. Müller and S. L. Buchwald, *Angew.Chem. Int. Ed*., **2014**, 53, 3125 –3128; DOI: 10.1002/anie.201310897

[87] A. G. O’Brien, A. Maruyama, Y. Inokuma, M. Fujita, P. S. Baran and D. G. Blackmond, *Angew. Chem. Int. Ed.*, **2014**, 53, 11868 –11871; doi: 10.1002/anie.201407948.

[88] C. Duan, M. Wei, D. Guo, C. He and Q. Meng, *J. Am. Chem. Soc.*, **2010**, *132* (10), pp 3321–3330; **doi:** 10.1021/ja907023c.

[89] Hamilton, B. D.; Ha, J. M.; Hillmyer, M. A.; Ward, M. D. , *Accounts of Chemical Research* **2012,** *45* (3), 414-423.

[90] Jiang, Q.; Ward, M.D. *Chem. Soc. Rev*., **2014**,43, 2066-2079.

[91] Ha, J. M.; Wolf, J. H.; Hillmyer, M. A.; Ward, M. D., *Journal of the American Chemical Society* **2004,** *126* (11), 3382-3383.

[92] Ha, J. M.; Hamilton, B. D.; Hillmyer, M. A.; Ward, M. D., . *Crystal Growth & Design* **2009,** *9* (11), 4766-4777.

[93] Hamilton, B. D.; Weissbuch, I.; Lahav, M.; Hillmyer, M. A.; Ward, M. D. , *Journal of the American Chemical Society* **2009,** *131* (7), 2588-2596.

[94] A. V. Uskov, D. Yu. Nefedov, E. V. Charnaya, J. Haase, D. Michel, Yu. A. Kumzerov, A. V. Fokin,and A. S. Bugaev, *Nano Lett.,* **2016**, 16, 791−794; doi: 10.1021/acs.nanolett.5b04841

[95] K. P. Nartowski, J. Tedder, D. E. Braun, L. Fàbiàna and Y. Z. Khimyak, *Phys. Chem. Chem. Phys.,* **2015**, 17, 24761-24773, doi: 10.1039/c5cp03880d

[96] B. D. Hamilton, M. A. Hillmyer and M. D. Ward, *Crystal Growth & Design,* **2008**, *Vol. 8, No. 9,* 3368–3375*, doi:* 10.1021/cg800326a

[97] M.W. Holladay, M.J. Dart and J.K. Lynch, *J. Med. Chem.,* **1997**, 40, 4169-4194.

[98] G.K. Lloyd, M. Williams, *J. Pharmacol. Exp. Ther.,* **2000**, 292(2), 461-467.

[99] H. Casanova, P. Araque and C. Ortiz, *J. Agric. Food Chem*., **2005,** 53, 9949-9953

[100] M. Tomizawa and J. E. Casid, *Annu. Rev. Pharmacol. Toxicol.*, **2005**, 45, 47–68 doi: 10.1146/annurev.pharmtox.45.120403.095930

[101] A. J. Rogers, L. D. Denk, and P. M. Wax, *The Journal of Emergency Medicine*, **2004**, Vol. 26, No. 2, pp. 169–172, doi:10.1016/ j.jemermed.2003.05.006

[102] Isman, *Phytoparasitica,* **1997**, 25, 339-344.

[103] Davide Capucci Ph.D Thesis, "*Stabilization of APIs and nutraceuticals through co-crystallization and molecular confinement*", XXVIII cycle, University of Parma

[104] K. Fukawa, S. Harada, N. Kasai, M. Toda, K. Mori, F. Toda, *Bull. Chem. Soc. Jpn.*, **1989**, 62, 2714.

[105] S. Jana, P. A. G. Cormack, A. R. Kennedy, D. C. Sherrington, *J. of Mat. Chem.*, **2009**, 19, 3427-3442.

[106] E. Sanna, E. C. E. Adán, A. Bauzá, P. Ballester, A. Frontera, C. Rotgera and A. Costa, *Chem. Sci*., **2015**, 6, 5466, doi: 10.1039/c5sc01838b

[107] S. Ma, D. Sun, M. Ambrogio, J. A. Fillinger, S. Parkin and H.C. Zhou, *J. Am. Chem. Soc.,* **2007**, 129(7), 1858-1859; doi: 10.1021/ja067435s

[108] D. Sun, S. Ma, Y. Ke, D. J. Collins and H.C. Zhou, *J. Am. Chem. Soc*., **2006**, 128, 3896-3897, doi: 10.1021/ja058777l

[109] L. Han, L. Qin, L.P. Xu and W.N Zhao, *Inorg. Chem.*, **2013**, *52* (4), pp 1667–1669 **DOI:** 10.1021/ic301707h

[110] H. Furukawa, Y. B. Go, N. Ko, Y. K. Park, F. J. U. Romo, J. Kim, M. O'Keeffe and O. M. Yaghi, *Inorg. Chem*., **2011**, 50, 9147–9152; dx.doi.org/10.1021/ic201376t.

[111] B. Jasiewicz, M. Hoffmann, A. Gasowska, R. Jastrza and K. M. bJaskóla, *Acta Chim. Slov.,* **2014,** *61,* 137–144

[112] For a comparison with NMR spectra of free nicotine see: S. Berger and D. Sicker, *Classics in Spectroscopy,* 2009, WILEY-CH; ISBN: 978-3-527-32516-0

[113] K. Simis, M. Lei, A.T. Lu, K.C. Sharma, R.L. Hale, R. Timmons, J. Cassella, *Drug Development and Industrial Pharmacy*, 2008, 34, 936–942; doi: 10.1080/03639040802149061

[114] Oxford Diffraction, CrysAlis CCD, and CrysAlis RED. Abingdon, UK: Oxford Diffraction Ltd.; **2008**

[115] Sheldrick, G; Shelz97, *Program for structure refinement*, University of Goettingen, Germany, **1997**

[116] Dolomanov, O.V.; Bourhis, L.J.; Gildea, R.J.; Howard, J.A.K.; Puschmann, H., OLEX2:

A complete structure solution, refinement and analysis program, *J. Appl. Cryst.,* **2009**, *42*, 339-341.

[117] A. Dhakshinamoorthy, M. Alvaro and H. Garcia, *Chem. Commun.,* **2012**, 48, 11275–11288; DOI: 10.1039/c2cc34329k

[118]K. Manna, T. Zhang, and W. Lin, *J. Am. Chem. Soc.*, **2014**, *136* (18), 6566–6569 **DOI:** 10.1021/ja5018267

[119] F. Carson, E. M. Castro, R. Marcos, G. G. Miera, K. Jansson, X. Zou and B. M. Matute, *Chem. Commun*., **2015**, 51, 10864.

[120] J. B. DeCoste, G. W. Peterson,. B. J. Schindler, K. L. Killops, M. A. Broweb and J. J. Mahleb, *J. Mater. Chem. A*, **2013**, 1, 11922.

[121] P. G. Yot, K. Yang, F. Ragon, V. Dmitriev, T. Devic, P. Horcajada, C. Serre and G. Maurina, *Dalton Trans*., **2016**, 45, 4283.

[122] S. Pullen, H. Fei, A. Orthaber, S. M. Cohen, S. Ott, *J. Am. Chem. Soc.*, **2013**, 13; 135(45): 16997–17003

[123] K. Sasan, Q. Lin, C.Y. Mao and P. Feng, *Chem. Commun.,* **2014**, 50, 10390, DOI: 10.1039/c4cc03946g

[124] J. Canivet, S. Aguado, Y. Schuurman, and D. Farrusseng, *J. Am. Chem. Soc*. **2013**, 135, 4195−4198; dx.doi.org/10.1021/ja312120x.

[125] S. A. Burgess, A. Kassie, S. A. Baranowski, K. J. Fritzsching, K. Schmidt-Rohr, C. M. Brown and C. R. Wade*, J. Am. Chem. Soc*., **2016**, 138, 1780−1783; DOI: 10.1021/jacs.5b12366

[126] T. Toyao, M. Saito, S. Dohshi, K. Mochizuki, M. Iwata, H. Higashimura, Y. Horiuchi and M. Matsuok, *Chem. Commun.,* **2014**, 50, 6779; DOI: 10.1039/c4cc02397h

[127] D. Merki and X. Hu, *Energy Environ. Sci.*, **2011**,4, 3878-3888, **doi:** 10.1039/C1EE01970H

[128] D. Brazzolotto, M. Gennari, N. Queyriaux, T. R. Simmons, J. Pécaut, S. Demeshko, F. Meyer, M. Orio, V. Artero, C. Duboc, *Nature Chem*., **2016**, doi:10.1038/nchem.2575

[129] H. Ogata, K. Nishikawa and W. Lubitz, *Nature*, **2015**, 520, 571–574, doi:10.1038/nature14110

[130] A. Volbe, M.H. Charon, C. Piras, C. Hatchikian, M. Frey, J.C .Fontecilla-Camps, *Nature*. **1995**, 373, 580; doi:10.1038/373580a0.

[131] R. Hidalgo, P. A. Ash, A.J. Healy, K. A. Vincent, *Angew Chem Int Ed Engl.* **2015**, *24*, 7110. doi: 10.1002/anie.201502338

[132] a) M. Gennari, M. Orio, J. Pecaut, F. Neese, M-N. Collomb, C. Duboc, *Inorg. Chem*., **2010**, *49*, 6399-6401. b) Gennari, Duboc et al., *Inorg. Chem.*, **2011**, 50, 3707.

[133] H. Zhu, H. Liu, I. Zhitomirsky, S. Zhu, *Materials Letters*, **2015**, 142, 19–22.

---

[134] A. Dome´nech, H. Garcia, M. T. Domenech-Carbo, and F. Llabres-i-Xamena**,** *J. Phys. Chem. C,* **2007,** *111,* 13701-13711

[135] A. Dome´nech, H H. Garcia, M. T. Domenech-Carbo, and F. Llabres-i-Xamena, *Electrochemistry Communications,* **2006,** 8 ,1830–1834

[136] D. Feng, K. Wang, J. Su, T. F. Liu, J. Park, Z. Wei, M. Bosch, A. Yakovenko, X. Zou, and H. C. Zhou, *Angew. Chem. Int. Ed*., **2014**, 54, 149–154

[137] S. Brunauer, L. S. Deming, W. E. Deming, E. Teller, *J. Am. Chem. Soc.*, **1940**, *62* (7), 1723–1732 , doi:10.1021/ja01864a025

[138] C. F. Macrae, I. J. Bruno, J. A. Chisholm, P. R. Edgington, P. McCabe, E. Pidcock, L. Rodriguez-Monge, R. Taylor, J. van de Streek and P. A. Wood, *"Mercury CSD 2.0 - New Features for the Visualization and Investigation of Crystal Structures"*, *J. Appl. Cryst.*, **2008**, 41, 466-470, doi: 10.1107/S0021889807067908.

[139] A. Betard and R. A. Fischer, *Chem. Rev.*, **2012**, 112, 1055–1083; doi: 10.1021/cr200167v.

[140] J. H. Cavka, S. Jakobsen, U. Olsbye, N. Guillou, C. Lamberti, S. Bordiga and K. P. Lillerud, *J. Am. Chem. Soc*., **2008**, *130*, 13850–13851.

[141] H. Fei, S. Pullen, A. Wagner, S. Ott and S. M. Cohen, *Chem. Commun.*, **2015**, 51, 66-69.

[142] Hod, Deria,Bury, Mondloch, Kung, So, Sampson, Peters, Kubiak, Farha, Hupp, *Nature Commun*., **2015**, 6, n. 8304; doi:10.1038/ncomms9304

[143] I. Hod, W. Bury, D. M. Karlin, P. Deria, C. W. Kung, M. J. Katz, M. So, B. Klahr, D. Jin, Y. W. Chung, T. W. Odom, O. K Farha, J. T. Hupp, *Adv. Mater.,* **2014**, 26, 6295-6300

[144] Izutsu, K. *Acid–Base Dissociation Constants in Dipolar Aprotic Solvents* (Blackwell Scientific, 1990).

[145] P. R. Castillo and St. L. Buchwald, *Chem. Rev*., **2016**, 116, 12564−12649, DOI: 10.1021/acs.chemrev.6b00512

[146] a) I. P. Beletskaya, A. V. Cheprakov, *Organometallics* , **2012**, 31 (22), 7753−7808; b) C. Fischer, B. Koenig, *Beilstein J. Org. Chem.* , **2011**, 7, 59−74.

[147] B. Schlummer, U. Scholz, *Adv. Synth. Catal*. **2004**, 346, 1599–1626, DOI:10.1002/adsc.200404216

[148] C. C. Mauger, G. A. Mignani, *Org. Proc. Res. Dev.*, **2004**, *8* (6), 1065–1071, **doi:** 10.1021/op049832y

[149] C. Fischer, B. Koenig, *Beilstein J. Org. Chem.* **2011,** *7,* 59–74. doi:10.3762/bjoc.7.10

[150] D. G. Brown, J. Boström, *J. Med. Chem*. **2016**, 59, 4443−4458, doi:10.1021 /acs.jmedchem.5b01409

---

[151] B. Bhattacharya, D. Ghoshal, *CrystEngComm*, **2015** 17, 8388.

[152] Z. J. Lin, J. Lü, M. Hong, R. Cao, *Chem. Soc. Rev.*, **2014**, 43, 5867-5895

[153] L. Sarkisov, R. L. Martin, M. Haranczyk, B. Smit, *J. Am. Chem. Soc.*, **2014**, 136, 2228-2231

[154] G. Férey, C. Serre, *Chem. Soc. Rev*. **2009**, 38, 1380.

[155] C.H. Lee, H.Y. Huang, Y.H. Liu, T. T. Luo, G.H. Lee, S. M. Peng, J. C. Jiang, I. Chao, K. L. Lu*, Inorg. Chem*. **2013**, 52, 3962–3968.

[156] a) S. Y. Yun, Y. K. Lee, S. W. Lee, *Bull. Korean. Chem. Soc*. **2009**, 30, 1899; doi:10.5012/bkcs.2009.30.8.1899; b) D. Min, H. S. Hush, S.W. Lee, *Polyhedron,* **2008**, 27, 2083, doi:10.1016/j.poly.2008.03.024

[157] R. Grunker, I. Senkovska, R. Biedermann, N. Klein, M. R. Lohe, P. Muller and S. Kaskel, *Chem. Commun.* **2011**, 47, 490–492.

[158] Y. E. Cheon, J. Parka, M. P. Suh, *Chem. Commun.* **2011**, 36, 5436-5438.

[159] B. P. Fors, P. Krattiger, E. Strieter, S. L. Buchwald, *Org. Lett.* **2008**, Vol. 10, No. 16, 3505-3508.

[160] United States Environmental Protection Agency, *Report* (1988), (EPA/600/8-88/019; Order No. PB88-179452/GAR), 46 pp. ; b) Bi W, Hayes RB, Feng P, Qi Y, You X, Zhen J*, et al.* 1992. Mortality and incidence of bladder cancer in benzidine-exposed workers in China. *Am J Ind Med* 21(4): 481-489. ATSDR. 2001. *Toxocological Profile for Benzidine*. Agency for Toxic Substances and Disease Registry. http://www.atsdr.cdc.gov/toxprofiles/tp62.pdf. c) Lowry LK, Tolos WP, Boeniger MF, Nony CR, Bowman MC. 1980. Chemical monitoring of urine from workers potentially exposed to benzidine-derived azo dyes. *Toxicol Lett* 7(1): 29-36.

[161] Q. R. Fang, D. Q. Yuan, J. Sculley, J. R. Li, Z. B. Han, H.C. Zhou, *Inorg. Chem.* **2010**, 49, 11637–11642.

[162] N. Wei, M. Y. Zhang, X. N. Zhang, G. M. Li, X. D. Zhang, Z. B. Han, *Cryst. Growth Des.* **2014**, *14* (6), 3002–3009.

[163] W. Qingli, D. Caifeng, Z. S. Sheng, L. Nian, *Asian Journal of Chemistry* **2006**, 18, (3), 1895-1902.

[164] S. L. Huang, Y. J. Lin, Z. H. Li, and G. X. Jin *, Angew. Chem. Int. Ed.* **2014**, 53, 11218–11222.

[165] Faming Zhuanli Shenqing Gongkai Shuomingshu (2009), 13pp. CODEN:CNXXEV; CN101550165

[166] G. Mukherjee, K. Biradha, *Cryst. Growth Des*. **2014**, 14, 419–422, doi: 10.1021/cg401858s

[167] R. Yang, L. Li, Y. Xiong, J. R. Li, H. C. Zhou, C. Y. Su, *Chem. Asian J.* **2010**, 5, 2358-2368.

---

[168] K. Biradha, M. Sarkar and L. Rajput, *Chem. Commun.*, **2006**, 4169–4179, doi: 10.1039/b606184b

[169] J.L.C. Rowsell, O.M. Yaghi, *Microporous and Mesoporous Materials* 73, **2004**, 73, 3–14, doi:10.1016/j.micromeso.2004.03.034

[170] O.M. Yaghi, M. O'Keeffe, N.W. Ockwig, H.K. Chae, M. Eddaoudi, J. Kim, *Nature* , **2003**, 423, 705, doi:10.1038/nature01650.

[171] X.L.Wang, X. T. Sha, G.C. Liu, N.L. Chen, C. H. Gong,and Y. Qu, *Z. Anorg. Allg. Chem.,* **2015**, 641, (7), 1274–1281

[172] X. Wang, H. Lin, B. Mu, A. Tian and G. Liu, *Dalton Trans.*, **2010**, 39, 6187–6189, DOI: 10.1039/c0dt00302f

[173] B. Q. Ma, K. L. Mulfort, and J. T. Hupp*, Inorg. Chem*. **2005**, 44, 4912-4914; DOI: 10.1021/ic050452i

[174] For catenation and topological analysis: L. Carlucci, G. Ciani, D. M. Proserpio, *Coordination Chem. Rev.*, **2003**, 247-289, doi: 10.1016/S0010-8545(03)00126-7

[175] Zn-dabco: a) H. Chun, H. Jung and J. Seo, *Inorg. Chem.*, **2009**, 48, 2043-2047, b) Hyungphil Chun, *J. Am. Chem. Soc.,* **2008**, 130 (3), 800–801 DOI: 10.1021/ja0776778; c) Zn-py-dmf: S. Wang, S. Xiong, Z. Wang and J. Du, *Chem. Eur. J.*, **2011**, 17, 8630 – 8642, DOI: 10.1002/chem.201100226

[176] a) Cu based: L. F. Ma, B. Liu, L. Y. Wang, C. P. Lic and M. Du, *Dalton Trans.*, **2010**,39, 2301-2308; DOI: 10.1039/B920308G; b) Mn based: H. Chen, D. Xiao, J. He, Z. Li, G. Zhang, D. Sun, R. Yuan, E. Wang and Q.L. Luo, *CrystEngComm*, **2011**,13, 4988-5000; DOI: 10.1039/C1CE05254C

[177] G. N. Reiner, L. F. Fraceto, E. de Paula, M. A. Perillo, D. A. García, *J. Biomaterials and Nanobiotechnology*, **2013**, 4, 28-34 doi:10.4236/jbnb.2013.43A004

[178] G. N. Reiner, L. D. Marìn, N. Olguìn, S. S. Redondo, M. S. Borzone, E. R. Farré, C. Sunol, D. A. Garcìa, *Cell Biochem Biophys*, **2013**, 67, 515–525; DOI 10.1007/s12013-013-9537-4

[179] M. T. Baker, M. Naguib, *Anesthesiology* , **2005**, 10 , 103, 860-876.

[180] WHO Model List of Essential Medicines, *World Health Organization*. October 2013. p. 6.

[181] T.Y. Euliano, J.S. Gravenstein, "A brief pharmacology related to anesthesia". *Essential anesthesia: from science to practice*, 2004 , Cambridge, UK: Cambridge University Press. p. 173. ISBN 0-521-53600-6.

[182] K. A. Woll, B. P. Weiser, Q. Liang, T. Meng, A. M. Wu, B. Pinch, W. P. Dailey, W. D. Gao, M. Covarrubias and R. G. Eckenhoff, *ACS Chem. Neurosci.,* **2015**, 6, 927–935, DOI: 10.1021/acschemneuro.5b00078

[183] H. Zhang, W. Wang, Z. Zhao, Y. Ge, J. Zhang, D. Yu, W. Chai, S. Wu, L. Xu, *The Anatomical Record*, **2010**, 293, 12 1985–1990

[184] Flavouring Group Evaluation 22: Ring-substituted phenolic substances from chemical groups 21 and 25, *The EFSA Journal,* 2006, 393, 1-78.

[185] I. M. Helander, H. L. Alakomi, K. L. Kala, T. M. Sandholm, I. Pol, E. J. Smid, L. G. M. Gorris and A. V. Wright, *J. Agric. Food Chem*, **1998**, *46,* 3590-3595.

[186] I. H. N. Bassolé and H. R. Juliani, *Molecules*, 2012, *17*, 3989-4006; doi:10.3390/molecules17043989

[187] F. Nazzaro, F. Fratianni, L. De Martino, R. Coppola and V. De Feo, P*harmaceuticals*, **2013**, 6, 1451-1474; doi:10.3390/ph6121451

[188] a) J. Xu, F. Zhou, B.P. Ji, R. S. Pei and N. Xu, *Letters in Applied Microbiology*, **2008**, 47 174–179, doi:10.1111/j.1472-765X.2008.02407.x b) R. J. W. Lambert, P. N. Skandamis, P.J. Coote and G. J. E. Nychas, *Journal of Applied Microbiology*, **2001**, 91, 453-462

[189] A. Ahmad, A. Khan, F. Akhtar, S. Yousuf, I. Xess, L. A. Khan, N. Manzoor, *Eur J Clin Microbiol Infect Dis* , **2011**, 30-41, doi:10.1007/s10096-010-1050-8

[190] E. Aydın, H. Türkez, M. S. Keles¸ *Cytotechnology,* **2014,** 66, 149–157, doi: 10.1007/s10616-013-9547-5

[191] C. Turek and F. C. Stintzing, *Comprehensive Reviews in Food Science and Food Safety*, **2013**, Vol.12, 40-53, doi: 10.1111/1541-4337.12006

[192] M. L.R. Cabello, S. Pichardo, J.M. Bermúdez, A. Bañosc, C. Núñez, E. Guillamón, S. Aucejo, and A.M. Cameán, Development of PLA films containing oregano essential oil (Origanum vulgare L. virens) intended for use in food packaging, *Food Additives &Contaminants: Part A*, **2016** , 33, 8, 1374-1386, DOI: 10.1080/ 19440049. 2016. 1204666

[193] L.A.S., Rupika, S. Bigger, K. Sonneveld, M.Cran, J. Miltz, , **2007**, Antimicrobial activity of films containing mixtures of thymol and carvacrol. 23rd IAPRI Symposium Windsor UK.

[194] A. Guarda, J. F. Rubilar, J. Miltz, M. Jose Galotto, *International Journal of Food Microbiology*, **2011**, 146, 144–150

[195] I. H. N. Bassolé , and H. R. Juliani, Essential Oils in Combination and Their Antimicrobial Properties, *Molecules* **2012**, *17*, 3989-4006; doi:10.3390/molecules 17043989

[196] D. S. Reddy, D. C. Craig, and G. R. Desiraju, *J. Am. Chem. Soc*. ,**1996**, 118, 4090-4093

[197] K. Prout, J. Fail, R. M. Jones, R. E. Warner and J. C. Emmett, *J. Chem. Soc., Perkin Trans. 2*, **1988**, 265-284, DOI: 10.1039/P29880000265

[198] J. Vaughn, H. Wu, B. Efremovska, D. H. Olson,J. Mattai, C. Ortiz, A. Puchalski,a J. Li and L. Pan, *Chem. Commun.,* **2013**, 49, 5724, DOI: 10.1039/c3cc41236a

---

[199] H. Wang, E. Lashkari, H. Lim, C. Zheng, T. J. Emge, Q. Gong, K. Yam and J. Li, *Chem. Comm.*,**2016**, 52, 2129, DOI: 10.1039/c5cc09634k

[200] A. L. Myers and J. M. Prausnltz, *Thermodynamics of mixed-gas adsorption*, *AIChEJ*., **1965**, 11,121-127.

[201] Q. Yang, C. Zhong, and J. F. Chen, *J. Phys. Chem. C*, **2008**, 112, 1562-1569.

[202] M. Bosch, M. Zhang, and H. C. Zhou, *Advances in Chemistry*, **2014**, doi: 10.1155/ 2014/182327

[203] A. Schaate, P. Roy, A. Godt et al., *Chemistry A*, **2011**, vol. 17, no. 24, 6643-6451.